Applications of Magnetoelectric Sensors

Ying Shen

Dissertation submitted to the faculty of the Virginia Polytechnic Institute and State University in partial fulfillment of the requirements for the degree of
Doctor of Philosophy
In
Materials Science and Engineering

Dwight D. Viehland Chair
Alex O. Aning
Chester J.Weiss
Jiefang Li
Keith L. McLaughlin

January 27, 2014
Blacksburg, Virginia

Keywords: Magnetoelectric, magnetic sensor, gradiometers, application

Applications of Magnetoelectric Sensors

Ying Shen

ABSTRACT

The magnetoelectric (ME) effect is an electric output in response to an applied magnetic field. In a heterostructure configuration where the two-phases are engineered with close interface contact, a giant electric response to a magnetic field has been found, which is designated as the ME voltage (or charge) coefficient α^{ME}. This effect is mediated by a mechanical-coupling between magnetostrictive and piezoelectric phases. In this thesis, I concentrate on application study for ME sensors with respect to noise control and rejection, thermal stability, triple-axis sensor design, array imaging, DC and AC magnetic sources detection and active mode ME sensor development, which is important for future ME sensor device applications.

In most applications, magnetic sensors must be operated in an open environment (i.e., magnetically unshielded). Such environments are contaminated by environmental noise, which can raise the equivalent magnetic noise floor of any magnetic sensor dramatically. In other words, for practical use ME magnetic sensors are fundamentally challenged by the inability to distinguish minute target signals from external noises which have several orders of higher amplitudes than former. As environmental shielding of magnetic sensors is impractical in numerous applications, using two (or more) magnetic sensors in a differential mode configuration is expected to reject/reduce environmental magnetic noise. In Chapter three, I focus on the analysis of the magnetic detection, potentiality to optimize ME gradiometers to be more sensitive for device applications. I evaluate the

efficiency of coherent noise rejection and analyze the capacity of intrinsic noise levels of each sensor by a basic ME differential structure with a digital post processing and in a laboratory environment.

In order to enable ME sensors as a viable competitor for extremely sensitive low-level magnetic field detection, there is a critical need to further enhance its sensitivity especially in unshielded environments for end users. Recent studies have indicated that an array of m ME sensor units, either in serial or parallel mode, can significantly increase the sensitivity by a factor of √m. To extend such approach from single "ME unit" to "ME array," several parameters of ME senor array need to be investigated, like (i)the signal current level, (ii)noise level, and SNR for both parallel and (iii) serial arrangements of ME units into an array, which will be predicted as illustrated in Chapter four.

Previous researchers have demonstrated the possibility to develop multi-axial ME sensors with a performance equivalent to that of a high-end fluxgate multi-axial device, which consumes much less energy than that of fluxgate. My goal is to design an advanced triple-axial sensor of various operational modes, characterize their noise floors and orthogonality between various directions, and test the ability to detect an AC target, all of which are detailed in Chapter five. Estimation of the AC dipole localization was realized with the help of a grid search (GS) algorithm. The results show good convergence and accuracy of object location along three orthogonal directions. Through simulation analysis, the major localization errors were found to arise from sensor calibration.

There are basically two types of magnetic anomaly detection: search and alarm systems. In the search system, magnetic sensors are mounted onto a moving platform looking for ferromagnetic target by surveying specific areas. The target presence is manifest as a special magnetic anomaly signature along the predefined paths passing in the vicinity of the target. However, as the piezoelectric phase in the ME sensor is susceptible to the motion incurred vibrational noise in this approach, right now such search system is not viable for the ME sensor device yet. In contrast, the alarm system makes use of stationary instruments producing an alarm signal when ferromagnetic target passes nearby the magnetic sensor. Here, my approach for localization, detection and identification for dc source, such as vehicle, is based on alarm system, illustrated in

Chapter six. In the present work shown in section 4.2, my investigation covers two types of magnetic sensors, where the first one (e.g. fluxgate) serves as a reference to compare with the second one (ME sensor in alarm mode) two show their detection sensitivity in open environment responding to the moving vehicles. This non-intrusive ME sensor system with a larger sensing range is viable for detection and recognition of vehicle induced magnetic signatures in an outdoor (open) environment. We also show a finite element simulation method capable predicting the magnetic anomaly projection in the geomagnetic field. Furthermore, a magnetic flux distraction effect caused by a nearby metallic material was investigated for Metglas/PMN-PT laminated magnetoelectric (ME) sensors. Taking advantage of this flux distraction, a ME sensor can perform an accurate search for metallic targets of different dimensions and at various distances.

In last chapter, I study the non-linear ME effect based modulation mode sensor which can modulate weak low frequency signals to a higher frequency band width. This results in the mitigation of a strong 1/f noise, which is often quite large at frequencies near or below 1 Hz. I found that the non-linear ME coefficient $\alpha_{\mathrm{nonlin}}^{\mathrm{ME}}$ for ME laminate composites of Metglas/PMN-PT is strongly dependent on the derivative of the piezomagnetic strain coefficient $\partial d_{33}^{m}/\partial H$. Due to this finding, I exploit the magnetic flux concentration effect and show an enhancement of $\alpha_{\mathrm{nonlin}}^{\mathrm{ME}}$ at H_{DC}=0 for a Metglas/PMN-PT heterostructure be 13 $\mathrm{V}/(\mathrm{cm}-\mathrm{Oe}^{2})$ for two Metglas layers ME laminates using a drive signal at f_0=1 kHz, through an optimized Metglas-piezofiber thickness ratio. It was further increased to $\alpha_{\mathrm{nonlin}}^{\mathrm{ME}}$=100 $\mathrm{V}/(\mathrm{cm}-\mathrm{Oe}^{2})$ at f_0=EMR. These findings demonstrate much higher frequency modulation efficiencies with SNR=300 and lower noise floors

ACKNOWLEDGEMENTS

First and foremost, I would like to express my sincere gratitude to my advisor, Dr. Dwight Viehland, for his continuous support of my Ph.D research, for his patience, motivation, enthusiasm, and immense knowledge. His guidance was essential throughout the sometimes-arduous process of researching and writing this thesis. I could not have imagined having a better advisor and mentor for this undertaking. Moreover, his dedication to research will equip me for both career and life.

I would like to express my heartfelt gratitude to Dr Jiefang Li, who is not only a mentor, but a dear friend as well. From the outset, she has been a dedicated, inspirational, supportive and patient role model. I could not be prouder of my academic roots and hope that I can, in turn, pass on the research skills and the vision that she has given to me. In particular, my heartfelt appreciation goes to Passive Sensors Unlimited (PSU) and Dr Jiefang Li for providing datalogger device and quite experiment place. Dr Jiefang Li made enormous contribution to data collection in her farm. Without support from PSU and Dr Jiefang Li this thesis would not have been possible.

This thesis was conducted in cooperation with SAIC; thus, I would like to thank my examiner, Dr. Keith McLaughlin, who gave me significant guidance on my project—particularly in relation to gradiometer sensor design and magnetic anomaly detection. Thank you for helping to shape and guide the direction of this study, especially from a practical perspective, with your thoughtful and instructive comments.

I also like to thank my thesis committee members, Dr. Alex Aning and Dr. Chester Weiss, who routinely provided encouraging and constructive feedback. It is no easy task to review a thesis, and I am grateful for their thoughtful and detailed comments.

My gratitude is also extended to colleagues in our ME sensor group. I would like to thank Dr. Davresh Hasanyan, who shared his deep insights about fundamental research on functional materials. His strong background in theory helped to shape this research and will have a lasting impact on my professional pursuits.

I would like to thank Dr. Liangguo Shen for his immense help on the lock-in circuit design that made my project run more quickly and efficiently. I will always have good memories of working with you.

I also extend my thanks to Dr. Yaojin Wang, Junqi Gao and Menghui Li for their insightful discussions on ME materials and applications. I appreciate their support on sensor fabrication, which was essential to my work on sensor applications. I hope they agree that we worked well together and made significant progress on the development of the ME sensor.

I would like to thank Dr. David Gray and David Berry for their great guidance and important discussions on the experimental setup and magnetic sensor design.

I would not have even contemplated this long road to the doctorate if not for my parents, Guoan Shen and Chuanwang Zhang. They instilled within me a love of creative pursuits, persistence and diligence—all of which finds a place in this thesis. To my parents: THANK YOU! My mother will always be my respected idol and everything to me.

To my dear comrade in the sensor group and my husband, Junqi Gao: Thank you for making me a better person than I otherwise would be. To be able to pursue our Ph.D. degrees together, to stick together through thick and thin, has been an absolute gift. You are my soul mate. Finally, to my darling daughter, Alice: You are truly an angel that came into my life. You motivate me to try to be YOUR role model the way my mother was for me.

TABLE OF CONTENTS

LIST OF FIGURES

LIST OF TABLES

Chapter 1:

INTRODUCTION

1.1 Available Magnetic Sensors

Magnetic sensors are capable of exploiting a wide range of phenomenon associated with both physics and material science. For many decades, magnetic sensors have aided researchers and practitioners to analyze and control literally thousands of functions—ranging from complex theoretical applications to practical use in automobiles, computers and on factory floors. Regardless of their use, the main principle involved in sensing a magnetic field is based on the intimate connection between magnetic and electric phenomena. There are a vast array of common magnetic sensor technologies, including the following: search coil, fluxgate, optically pumped, nuclear precession, SQUID, Hall-effect, anisotropic magnetoresistance, giant magnetoresistance, magnetic tunnel junctions, giant magnetoimpedance, magnetostrictive/piezoelectric composites, magnetodiode, magnetotransistor, fiber optic, magnetooptic, and microelectromechanical systems-based magnetic sensors. Since all of them cannot be assessed within the confines of this dissertation, I will first review some of the critical available magnetic sensors, which will be followed by a discussion of the historical development of magnetoelectric composites—particularly with respect to bulk magnetoelectric sensor device applications.

1.1.1 Hall effect sensor

The Hall effect sensor is by far the most widely used magnetic sensor today. [1] The phenomenon known as the Hall effect was first observed in 1879 by Edwin H. Hall, who sought to prove that a magnet can directly impact an electric current. As illustrated in Figure 1.1(a)[2], when an electric current passes along a thin rectangle of gold, there is a voltage difference across it—as long as there is a strong magnetic field applied perpendicular to the plane of the rectangle. The Hall effect comes into being as a manifestation of the action of Lorentz force on quasi-free carriers in the plate. [2]

$$F = q(E + v \times B) \quad (1)$$

where q is the particle charge, E denotes the electric field that produces the current, v points to the carrier velocity, and B is the magnetic induction. For a given current, the

carrier velocity v is proportional to the carrier mobility, but inversely proportional to the carrier density and the plate thickness. Therefore, Hall effect sensors are mostly realized in the form of low-doped semiconductor thin films, making them very compatible with microelectronic circuits.

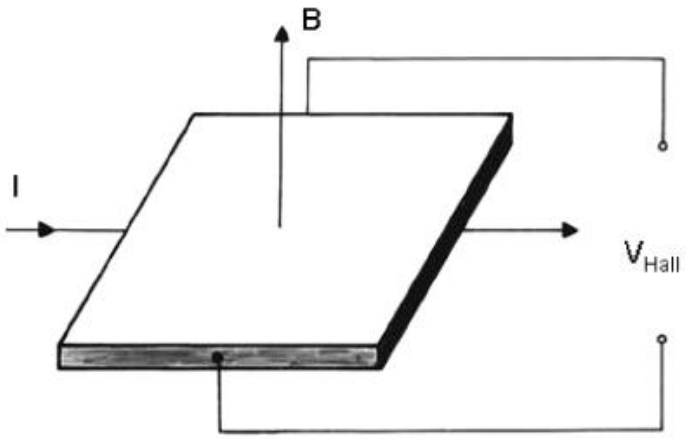

$$V_{Hall} = k\left|\vec{I} \times \vec{B}\right|$$

(a)

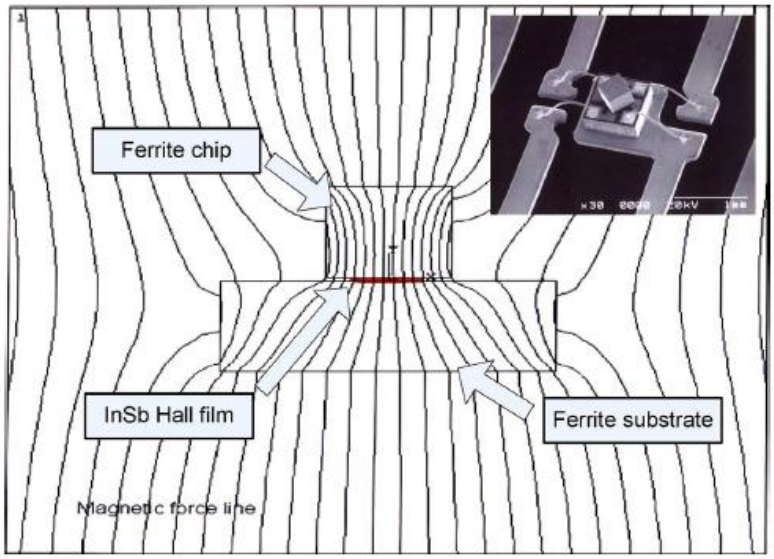

(b)

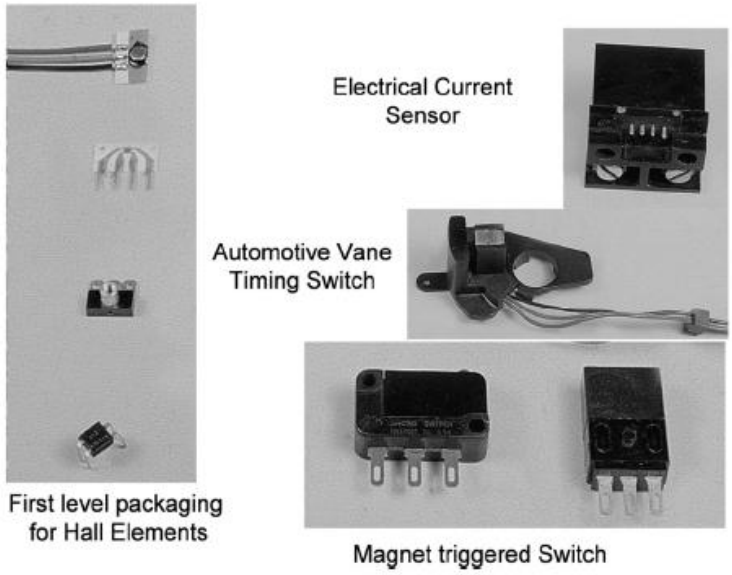

Figure 1.1 (a) Schematic of Hall effect sensor principle; (b) Magnetic force lines of field concentrators for a thin-film Hall sensor; (c) Example of Hall effect sensor products [2,3]

Inexpensive Hall effect sensors are normally made of silicon with a sensitivity of 1 mV/mT for a 1 mA current. Higher sensitivity can be achieved by using thin film Ш-V semiconductors, for example InSb (typ. 5 mV/mT) and InAs (typ. 2 mV/mT). Figure 11(b) depicts an off-the-shelf InSb Hall sensor with an integrated ferrite concentrator (Asahi Kasei, BW series), where the InSb thin-film sensor is sandwiched between a ferrite chip and ferrite substrate. [3] A Hall effect sensor made of silicon-on-insulator technology can reach a noise floor of 1 μT/√Hz with a dimension of only 80 μm wide and 50 nm thick.[4] Furthermore, a promising micro-Hall effect sensor with an active area of 2.4 μm×2.4 μm provided by COMS possesses a noise of 300 nT/√Hz at 1 Hz. [5]

Due to their favorable basic characteristics, simple operating principles and compatibility with a variety of microelectronics, Hall effect sensors have found hundreds of uses in low-cost position sensor applications, as shown in Figure 1.1(c). Moreover, with the ongoing development of high-quality materials and ever-improving fabrication methods, Hall effect sensors will continue to be vital for the microelectronics industry. For example, one application of a Hall sensor is depicted in Figure 1.2[6], where an exchange biased permalloy planar Hall sensor can be used to detect micro- and nanomagnetic beads later utilized for bio-applications. Specifically, the sensor response

to an applied incident magnetic field has been measured both in the presence and absence of commercially available 2 mm and 250 nm magnetic beads.

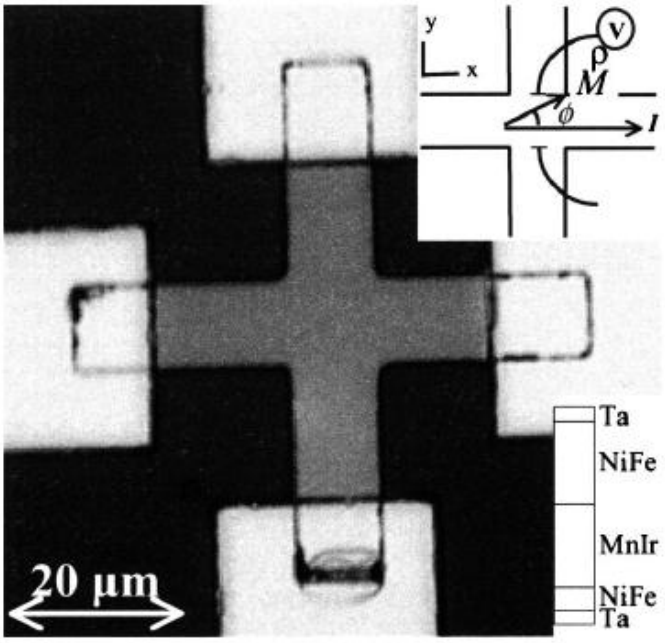

Figure 1.2 Schematic prototype for the planar Hall sensor. The cross is made of exchange-biased permalloy. Current leads are made of 03 mm thick Al. The top inset shows the planar Hall sensor geometry. The magnetic field to be detected is applied in the detection plane, along the y direction. In this plane, the current is applied in the x direction and the voltage, Vy, is measured in the y direction. The bottom inset illustrates the cross-sectional layer structure of the sensor.[6]

The future use of the Hall effect sensor is dependent on further improvements in increasing its sensitivity and decreasing offset. Additionally, it is well known that noise is a limiting factor in low-level magnetic measurements, where 1/f is the most problematic. In the frequency range of 0.1-10 Hz, the noise equivalent magnetic induction is about 1 µT. [1]

1.1.2 Fluxgate sensor

The basic fluxgate is comprised of two ferromagnetic cores wrapped with two coils, a drive and a sense coil, illustrated in Figure 1.3. It takes advantage of magnetic induction together with the fact that all ferromagnetic material becomes saturated at high fields.

During operation, an AC excitation current I_{exc} at a frequency f_0 is applied onto the primary coil, which can saturate the core at high fields. When the ferromagnetic core is out of saturation, it provides a path of low magnetic resistance to the flux lines of external field E_0 owing to its high relative permeability. When the driven sinusoidal current is increased to a sufficient level, the core reaches its saturation point, resulting in an increase in magnetic resistance. In turn, the core becomes less attractive for any additional magnetic field to pass through it. Thus, the alternate gating of the flux produces a change of flux through the pickup coil windings.[7] Based on Faraday's law of induction, the resultant voltage V_{ind} from the pickup coil is defined as

$$V_{ind} = N\frac{dB \cdot A}{dt} + V_{par} \quad (2)$$

where A denotes the surface area of the core perpendicular to the coils, B refers to the gated field, and N is the number of turns in the secondary coil. V_{par} points to a parasitic voltage component caused by the change of magnetic flux in the core.

From Eq. (2), the factors that govern the sensitivity of the device become obvious. In addition to increasing the number of turns *N* and the ferromagnetic qualities of the core, another efficient way to increase the sensitivity is to enhance the length of the core along the direction of the external field. The sensitivity of fluxgate ranges from 10^{-2} to 10^{7} nT for measuring DC and low-frequency AC fields (up to 10 kHz) with a resolution of approximately 0.1-10 nT.

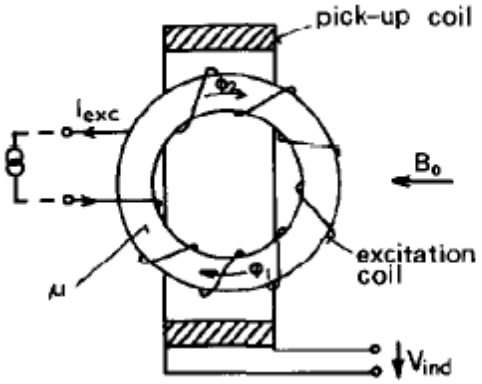

Figure 1.3 Schematic illustration of the operating principles of a fluxgate. The excess magnetic flux abstracted and expulsed by the soft magnetic core when it is driven by excitation current out of and into saturation.[7]

The fluxgate has shown itself to be a robust device with high sensitivity and reliability, which makes it desirable for use in many fields. Figure 1.4 shows a triple-arm fluxgate used as an accurate compass heading. The angle of Earth's magnetic field with respect to the spider is readily determined without ambiguity by exquisitely ratioing the sensed field in each of the three beams.

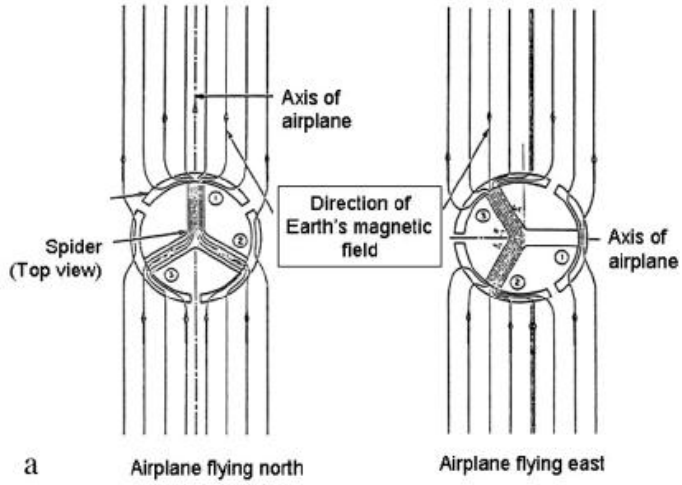

Figure 1.4 (a) Scheme showing how the signals of the triple-arm fluxgate change as the axis are rotated; (b) Aircraft compass system that uses a three-axis fluxgate. [2]

Unfortunately, the cost of the fluxgate is relatively high in comparison to the general magnetic sensor market. Therefore, if the fluxgate could be successfully miniaturized and simplified to a level allowing incorporation of microelectronics circuit technology, it would significantly decrease cost, thereby enhancing its performance-cost standing in the magnetic sensor market.

1.1.3 Magnetoresistor

Magnetioresistors are the second most commonly used magnetic sensors in market; these devices utilize a change in resistance caused by an external magnetic field. Values for magnetoresistance (MR) are defined by $\Delta R/R$ where R is the value at H=0. MR is typically measured in two ways: (1) by the percentage change in the resistance per Oe, and (2) by the voltage change out per volts per Oe. [8]$\Delta R/R$ is usually small, resulting in small changes in the DC voltage, which means that a bridge circuit or other methods are required to minimize the DC offset.

There are two distinct types of magnetoresistors: the anisotropic magnetometer (AMR) and the giant magnetometer (GMR).

1.1.3.1 Anisotropic magnetometer

Permalloy, which is a nickel-iron magnetic alloy, is employed in an AMR. This device can exhibit anisotropic magnetoresistance, which is associated with the angle between the magnetization and the direction of the current flow. [9] The resistance of permalloy decreases as the direction of magnetization rotates away from the direction of an applied current flow until it reaches its lowest point—when the magnetization is perpendicular to the direction of the current flow, as shown in Figure 1.5. [10]

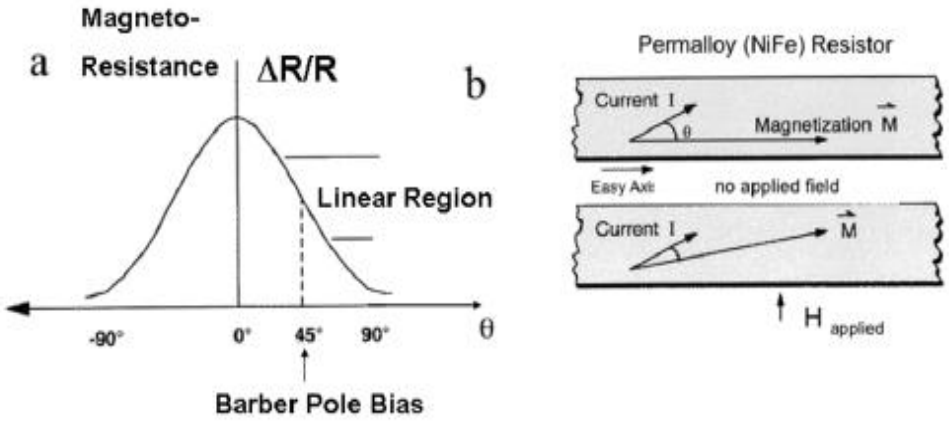

Figure 1.5 AMR sensor (a) magnetoresistance as a function of angle between magnetization and the current flow; (b) difference in θ due to the exposure to a magnetic field. [2]

In order to adjust the linear relationship between induced magnetoresistance and applied current, AMR sensors generally use a “barber pole” structure, in which aluminum stripes sputtered on permalloy strips deflect the direction of the current by 45 °, as shown in Figure 1.6(a). [3]

An integrated sensor is normally comprised of four permalloy resistors sputter-deposited on a silicon substrate (Figure 1.6). A voltage arises from a two-legged current path, known as a bridge, if the resistance of one path is different from the other. However, inherent resistance differences among the four resistors can produce an offset voltage, which is a problem that can be addressed by a set/reset method of changing the direction of magnetization in the bridge. When the applied field is in set/reset mode, the bridge output produces the same amplitudes of magnetization—but as opposite signs, as illustrated in Figure 1.6(b). Thus, one can rectify this issue by subtracting the voltage reading when the sensor is in the reset manner from the analogous value obtained in the set mode.

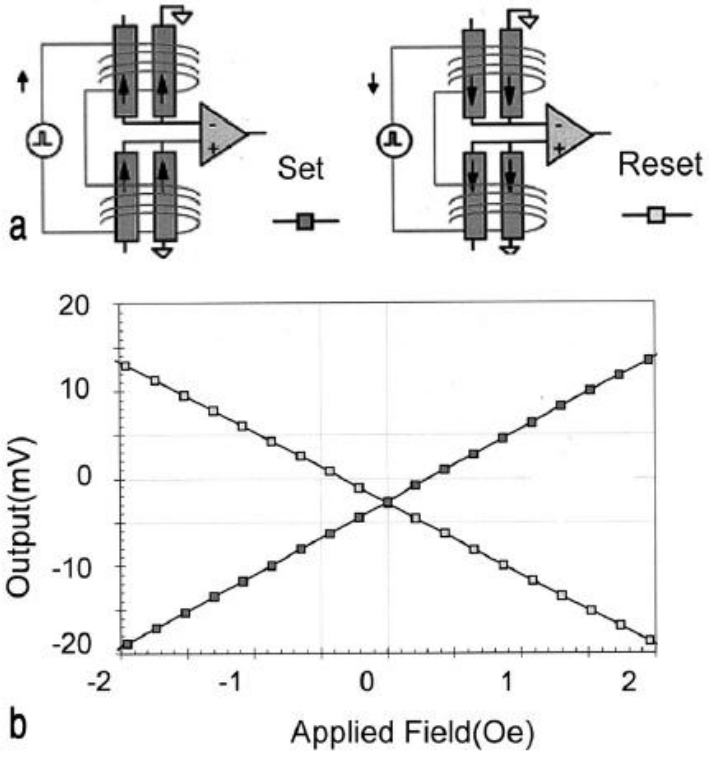

Figure 1.6 (a) Set and reset modes by changing current flows in the bridge in AMR; (b) output signals as a function of the applied magnetic field in set/reset modes. [2]

1.1.3.2 Giant magnetometer

GMR is a four-layer structure that consists of two thin ferromagnets—namely, an antiferromagnet and a ferromagnet that is pinned—as well as a thin conductor and a free ferromagnet (see Figure 1.7). The antiferromagnet (M2) is used to inhibit rotation of the upper ferromagnetic, known as the hard ferromagnet; conversely, the unpinned ferromagnet (M1) is termed the soft ferromagnet.[11] When the magnetizations of the two ferromagnets are parallel to each other, electrons can move very easily—either parallel to the layers or perpendicular to the layers, resulting in slight resistivity. It should be noted that the electrons undergo less scattering in moving from an electronic band structure state in one of the ferromagnets and into a similar (or identical) electronic band structure state in the other ferromagnet. In contrast, when the magnetization of the two ferromagnets are antiparallel, the electrons experience greater resistivity.[12]In fact, it has been reported that the difference in resistivity between parallel and antiparallel magnetizations can be as large as 12.8% at room temperature. [13]

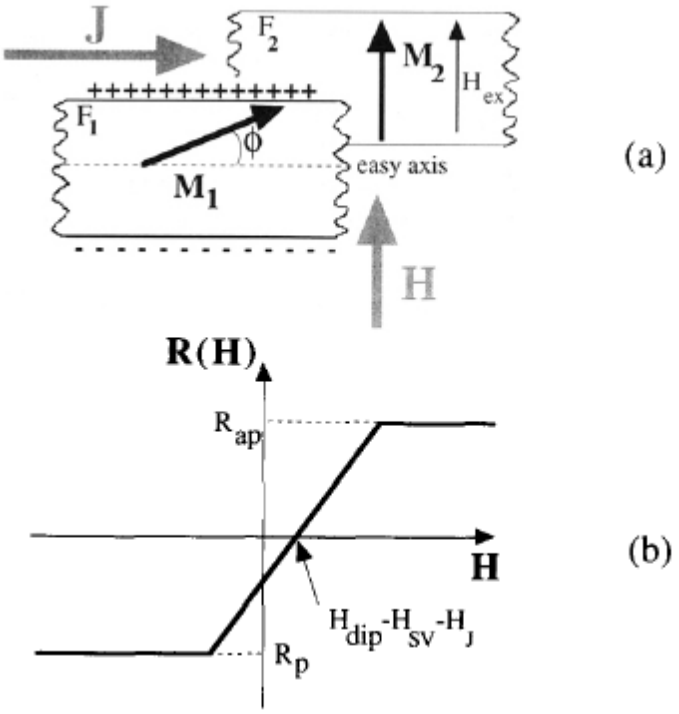

Figure 1.7 Orientation of the magnetization of both pinned and free ferromagnets in a GMR under different fields. M 1 and M 2 are the magnetizations of the two ferromagnetic layers. F 1 is the

nominally free magnetic layer. M 2 is pinned by the exchange anisotropy field (H_{ex}). H_{ex} has been aligned perpendicular to the easy axis of the free layer. ~b is the angle between M 1 and the easy axis of magnetization of F1, J is the sensing current, H is the magnetic field to be sensed.[11]

The sensitivity of a typical magnetoresistor ranges from $5*10^6$ nT to10^3 nT with open-loop readout electronics. Additionally, the minimum detectable field can reach 0.1 nT at limited bandwidths with closed-loop feedback electronics. An advantage of a GMR is that it doesn't demand a set/reset adjustment with spin valves, but this device also tends to be more susceptible to 1/*f* noise in comparison to AMR sensors. [1]To mitigate the sensor noise and offset drift problems, new designs have been introduced that incorporate MR magnetic sensors into the closed loop current sensor, which can deduce the offset drift with temperature changes by a factor of 100.

1.1.4 Superconductor magnetometers

The Superconducting Quantum Interference Device (SQUID) is by far the most sensitive magnetic device, especially at low frequencies (<1 Hz). The SQUID is based on the remarkable interaction between electric currents and magnetic fields when certain superconductors are cooled below their superconducting transition temperature, at which point the superconductor loses all resistance to the flow of electricity. [14] When magnetic flux becomes threaded through a superconductor ring, it produces a current in the ring, which is an exquisitely sensitive indicator of the flux density.[15]

When B.D. Josephson was a graduate student at the University of Cambridge more than 50 years ago, he predicted that periodic variations in a supercurrent could be exploited to measure the current in a superconducting ring—and hence the ambient magnetic field. As he showed, changes in the ring current alter the resonant frequency of the inductively coupled circuit, resulting in periodic changes in the output signal with field variations.[16] The supercurrent flowing through the weak link would be an oscillating function of the magnetic field intensity in the weak link, which can either be a narrow constriction in the superconductor or a point-contact junction. Sensitivity can be improved by coupling the ring to a larger detection coil that is able to collect flux over an area of several square centimeters (Figure 1.8).

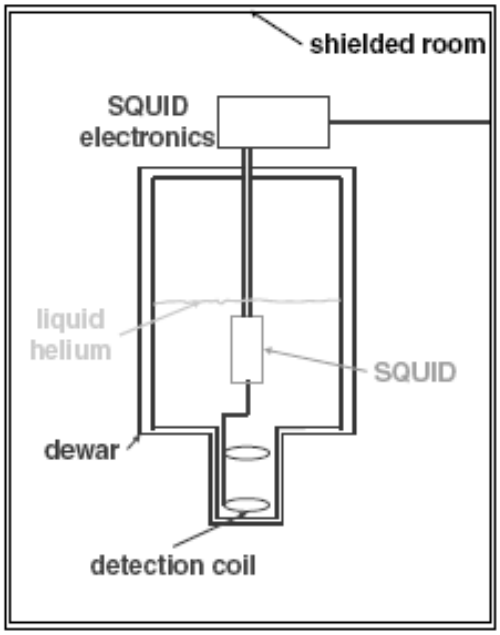

Figure 1.8 Schematic of the SQUID principle.[17]

In short, the SQUID ring functions as a very precise ammeter for measuring the current in the pick-up coil. It should be noted, however, that three components (the SQUID ring, the radio-frequency coil, and the large pick-up coil)must be cooled to the superconducting state. Moreover, the sensitivity of SQUID is limited by the magnetic field noise in the order 10 fT. Although the SQUID itself can be quite small, its need for liquid-helium coolant makes the complete apparatus very bulky and heavy. Most SQUIDs incorporate a low transition temperature (Tc) superconductor Nb operating at below the boiling point of liquid helium 4.2 K. However, the advent of high-Tc superconductors of YBCO operating near the boiling point of liquid nitrogen (77 K) makes higher temperature SQUIDs sound. [14]Unfortunately, SQUIDs that incorporate high-Tc superconductors have yet to display the same high sensitivity as those built with low-Tc superconductors. [17]Specifically, the noise associated with high-Tc operations originates from two sources: 1) higher thermal gradients and variations across the superconductors, and 2) higher Johnson noise in the readout electronics.[2] As noted in the literature, very high sensitive SQUIDs are currently employed in the fields of astronomy [18], geology[19], as well as for use in medical applications.[20]

1. 2 Multiferroic Magnetoelectric (ME) Composites

1.2.1 ME effect

Magnetoelectric (ME) effect is the induction of polarization by an applied magnetization, or vice versa, where the magnetoelectric response is signaled by the appearance of an electric polarization *P* upon applying a magnetic field H.[21, 22]

$$\Delta P = \alpha_{\mathrm{ME}} \Delta H \quad (1)$$

This is called the direct ME effect, where *P* is the electric polarization and α_{ME} is the ME voltage (or charge) coefficient. Thus, a voltage output can be produced by applying a magnetic field on a material, via an ME coupling. Fifty years ago, the ME effect was observed as an intrinsic effect in single crystals of some natural materials. For example, Cr_2O_3 crystals had the largest value with $\alpha_{\mathrm{ME}} \sim 20$ mV/cm-Oe.[23] Although the intrinsic ME effect exists in single-phase compounds, the underlying problem is that they exhibit low Curie temperatures (below room temperature), and a high inherent ME coupling has not yet been observed in the single-phase compounds, especially above room temperature.

In 1976, van Suchtelen first proposed that a giant ME effect could be found in multiferroic ME composites that combine ferroelectric and ferromagnetic phases together at room temperature.[24] Multiferroic materials result from coupling between magnetism and ferroelectricity, which enables a dynamic interaction between these order parameters. In turn, this interaction results in a broader class of multifunctional, or smart, materials that combine several useful properties in the same substance to produce new phenomena that are more than just the sum of the individual parts.[25, 26] For example, one can envisage a magnetoelectric (ME) interaction which could lead to spectacular cross-coupling effects if it induces electric polarization in a magnetically ordered state. Such achievement would result in many promising applications, including magnetic field sensors, logic data-storage memory devices and so on.[27, 28] As shown in Figure 1.9, these ME laminates are engineered from magnetostrictive layer(s) elastically bonded to a piezoelectric one. Thus, a charge is created in the core piezoelectric layer by a strain induced in the magnetostrictive foils excited by an incident magnetic field.

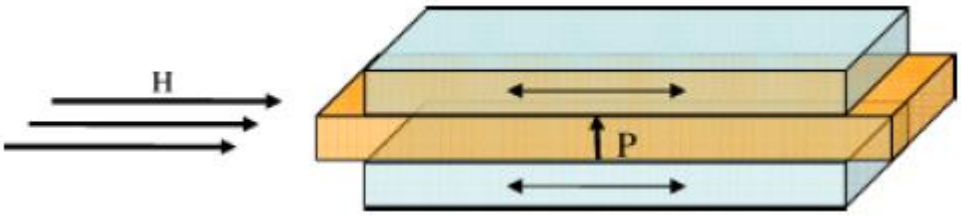

Figure 1.9 Configuration of multiferroic magnetoelectric laminates. [29]

Therefore, the realization of such ME multiferroic composites makes use of the ME effect promised by bulk ME composites to thin films for applications, such as sensors, transducers, filters, oscillators, phase shifters, memory devices, and so on.

1.2.2 Thin films ME composites

Though research and understanding of multiferroic ME films is relatively limited compared with bulk ME composites, the investigation of multiferroic ME nanostructured films has recently been accelerated by advances in thin-film growth techniques [30, 31] and theoretical calculations [32]. Different nanostructures of 0-3 type particulate films, 2-2 type layered heterostructures, and 1-3 type vertical heterostructures have been prepared via physical deposition techniques, such as PLD (Plasma layer deposition), MBE (molecular beam epitaxy), sputtering, spin coating and MOCVD (metal-organic chemical vapor deposition). So far, based on these techniques, various ferroelectric films (BTO, PTO, PZT and BFO) and magnetic films [CFO, NFO, Fe_3O_4, $La_{1-x}SrMnO_2$ (LSMO)] have been developed and studied intensely.

Thin film multiferroic composites have been demonstrated to have several outstanding advantages that different phases could be combined at atomic-level. By precise control of the lattice matching, epitaxial or superlattice composite films can be designed. However, there are still some questions remaining to be solved, like if the ME coupling remains strain-mediated as in bulk composites, if a large ME response from a ME thin films can be realized, and so on. These key issues need to be clearly established.

1.2.3 Bulk ME composites

For bulk ME composites, BaTiO3, PZT, PMN-PT, PVDF are usually chosen as the piezoelectric phase, and ferrites usually as the magnetostrictive phase. There are three types configurations for the bulk composites: 0-3 type particulate composites of

piezoelectric and magnetic oxide grains; 2-2 type laminate ceramic composites consisting of piezoelectric and magnetic oxide layers; and 1-3 type fiber composites with fibers of one phase embedded in the matrix of another phase, as shown in Figure 1.10.

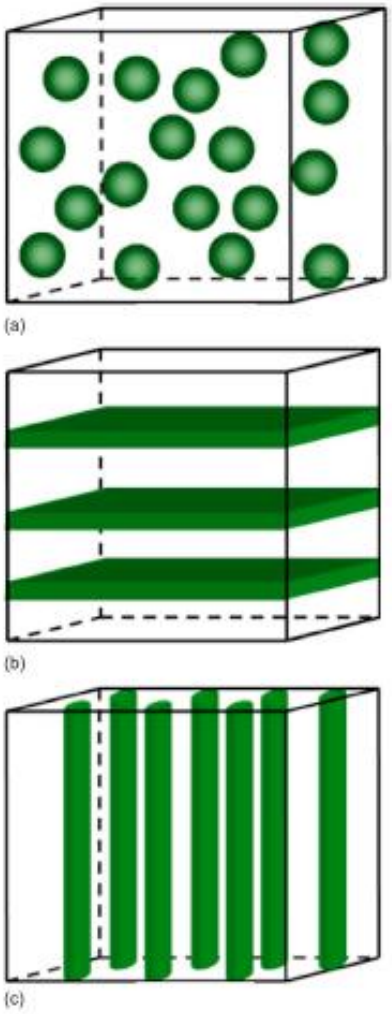

Figure 1.10 Schematic illustration of three main bulk ME composites configurations: (a) 0-3 particulate composites, (b) 2-2 laminate composites, and (c) 1-3 rod composites.[33]

At Philips laboratories, the first work on in-situ formation of ME ceramic composites was based on particulate ceramic composites with a low α_{ME} of around 1-4 mV/cm-Oe. But, the ferrites are conductive or semi-conductive, which could deteriorate the insulation of the composites and cause leakage problems. In contrast, the 2-2 type laminate composites can effectively address such problem with alternating ferrite and piezoelectric oxide layers to gain a much larger ME coefficient. In 2006, Dong et.al proposed a push-

pull mode with laminated Metglas/PZT/Metglas layers to achieve a giant ME effect of 22 V/cm-Oe in a L-L mode, as shown in Figure 1.11. The value of α_{ME} was significantly improved to around 500 V/cm-Oe near the resonant frequency of the laminates.[34]

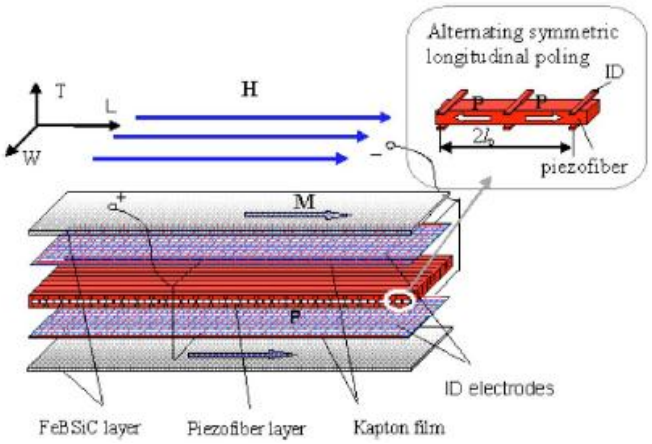

(a)

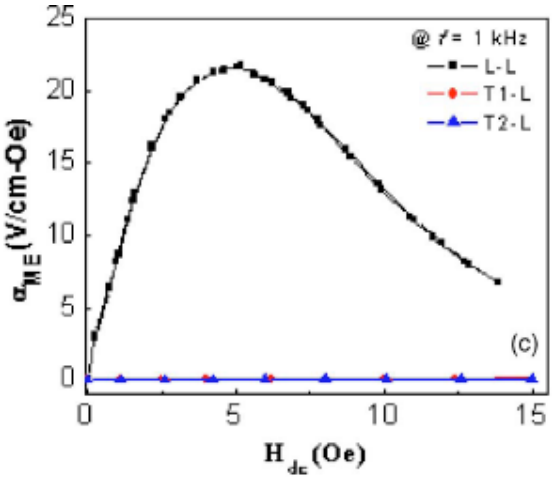

(b)

Figure 1.11 (a) Schematic paragraph of Dong proposed push-pull Metglas/PZT/Metglas laminates composites; (b) ME voltage coefficient of such ME laminates under low magnetic dc bias.[34]

The achievement of such a high ME effect in a two-phase magnetic alloy based ME composites made practical ME device applications promising. However, much work still remains for their real applications. Here, I will cover this topic of ME applications in my thesis.

1.3 ME Magnetic Sensor Devices

Above room temperature, bulk ME composites exhibit a large ME effect exceeding that of single-phase compounds by many orders of magnitude.[13] The achievement of such high ME effects in ME heterostructures promises multifunctional magnetic field sensors, transducers, resonators, memory devices, and so on. The working principle employed by ME heterostructures composites is simple, as the magnetic field input is required to have two parts, a dc bias and an ac probe. Either of the two can be detected by providing the other component. So either DC or AC magnetic field can be sensed by ME sensors in form of electric outputs.

1.3.1. Noise floor and sensitivity

The practical usefulness of a magnetic sensor is judged not only by the output signal of the sensor in response to an incident magnetic field, but as well by the equivalent magnetic noise generated in the absence of an incident field. The realization of ME magnetic sensors has been hindered by the challenge to develop ME composites with a high α_{ME} and a low equivalent magnetic noise. In 2009, my colleagues Das et al. optimized the heterostructures of a core $Pb(Zr,Ti)O_3$ (PZT) fiber layer with 6 layers of Metglas which were shown to detect a magnetic field as small as 0.3 nT.[35] In 2011, investigations by Wang et al to replace the PZT fibers with $0.7Pb(Mg_{1/3}Nb_{2/3})O_3$-$0.3PbTiO_3$ (PMN-PT) single crystal ones have yielded ME laminate composites with a much lower magnetic noise floor of $\leq$ 5 pT/√Hz at 1 Hz, as shown in Figure 1.12.[36] More recently, an ultralow equivalent magnetic noise of 6.2 pT/√Hz at 1Hz was obtained in a bimorph heterostructure sensor unit consisting of longitudinal-magnetized Metglas layers and a transverse-poled Mn-doped $Pb(Mg_{1/3}Nb_{2/3})O_3$-$0.29PbTiO_3$ (PMN-PT) single crystal.[37] However, in a real application environment, the sensitivity and equivalent magnetic noise floor shown above is not accurate enough for understanding how a ME sensor performs, as the noise will always limit the sensitivity and degrade the sensor's signal-to-noise ratio (SNR).

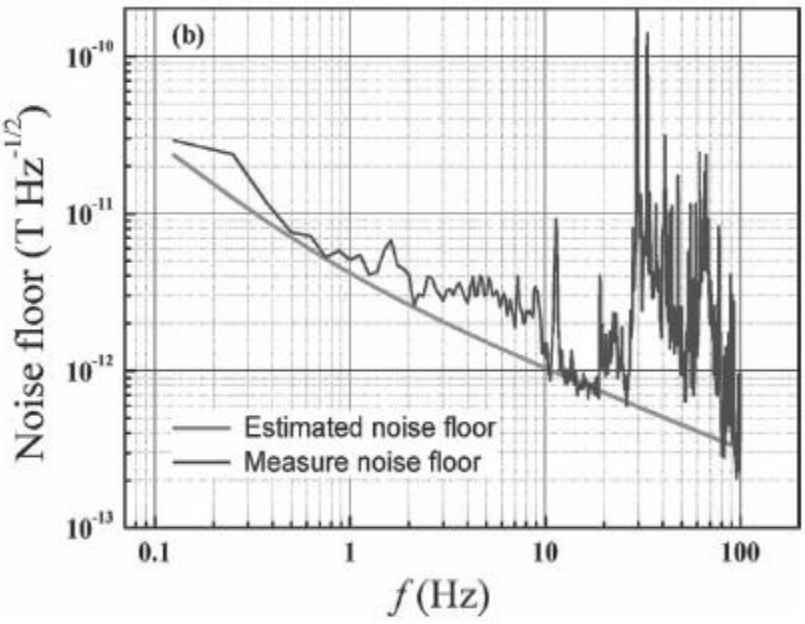

Figure 1.12 Measured and estimated equivalent magnetic noise of the proposed sensor unit.[36]

There are mainly three types of noises in a ME sensor: thermal noise introduced via pyroelectric currents which is caused by the thermal expansion mismatch between piezoelectric and magnetic phases[38], vibration noise introduced via piezoelectric effect, and electric noises from the detecting circuits[39]. Zhai et.al found that ME output signals induced from two reversely-polarized PZT layers have opposite signs, while the simultaneously induced thermal charges are of the same sign, as shown in Figure 1.13. Thus, the thermal induced charges from the ME sensor can be rejected by simply subtracting the total signal from one PZT layer from another one.[38] Besides the thermal fluctuations, the thermal stability of ME sensors is also essential in an open complex environment when temperature changes can occur. However, the stability of ME sensors to temperature changes has not yet been determined, even though in fact that the sensor needs to operate over a broad range of ambient temperatures. Here, I will show my investigation on the thermal stability of ME sensor over a temperature range of $-50 \leq T \leq 50$ ℃, which will be illustrated in Chapter 3.

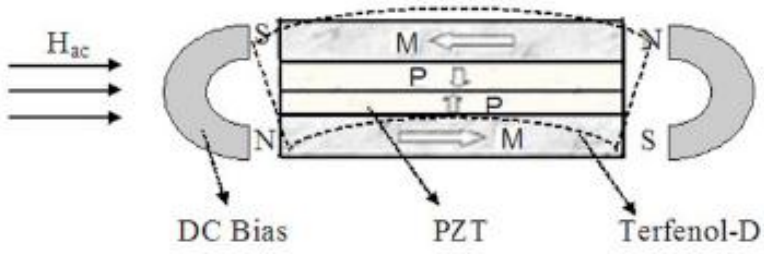

Figure 1.13 Schematic of the symmetric bimorph mode laminate with U shaped dc magnetic bias.[38]

It is well known that a moving ME sensor is susceptible to vibration noises introduced via the piezoelectric effect. Vibration noise severely undermines the sensitivity of ME sensors at static state, and this maybe the most critical issue in the ME sensor application.[20] Compared with the thermal noise, it is difficult to exclude vibration noises by only using vibration isolation platform. A lot of prototypes of magnetic sensors based on these ME composites with ultra-high sensitivity have been proposed. Much work still remains in order to widely commercialize ME composites, such as optimization and integration for ME device systems, noise rejection and SNR enhancement. However, there has been very rare work on these issues. Here, I will show my investigations on noise rejection in Chapter 3.

1.3.2. DC magnetic field sensor

The detection principle of a DC test is quite different from that of an AC one. For an AC sensor, the goal is to improve the ME voltage coefficients by optimizing the DC magnetic bias that can obtain the maximum output signal in response to an incident magnetic field. On the other hand, for a DC sensor, it requires larger voltage changes because the DC magnetic field variations are large in the range of -0.65 gauss to 0.65 gauss. Figure 1.14 presents a typical curve for Metglas/PZT composites, where the optimum α_{ME} at a magnetic DC bias of 8 Oe is related to the AC detection sensitivity, while the slope value of the linear part affects the DC detection sensitivity.

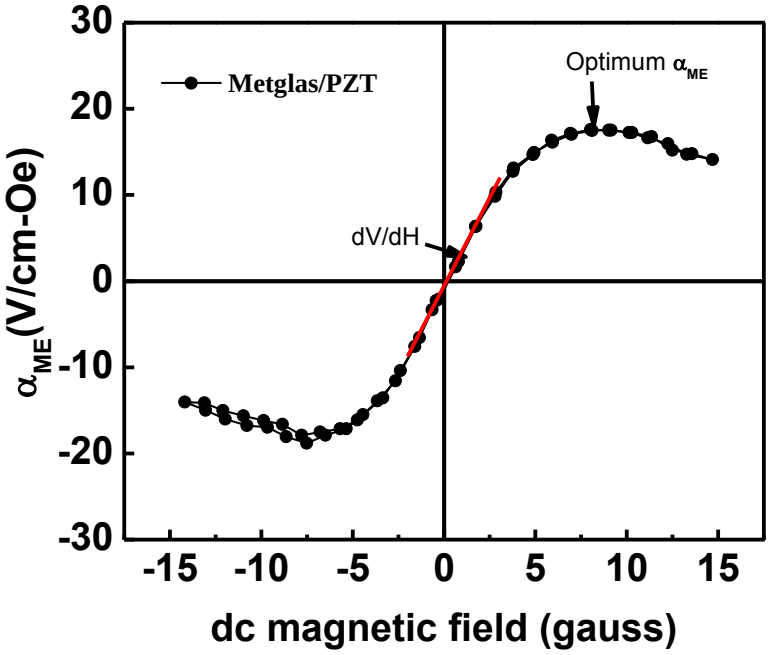

Figure 1.14 α_{ME}-H_{dc} for Metglas/PZT composites

Based on this idea, our previous group members have investigated how to use the DC sensor to sense geomagnetic fields in a laboratory conditions, and potentially to build up an underwater positioning system based on local magnetic field mapping. The motivation for this application is inspired by bio-behaviors in nature. Some researchers have shown that some sea creatures can sense a geomagnetic field and use it for their navigation as shown in Figure 1.15. The results show that they can detect the variations of intensity and inclination angles of the geomagnetic field. This finding offers the potential to develop a new guidance system based on geomagnetic fields.

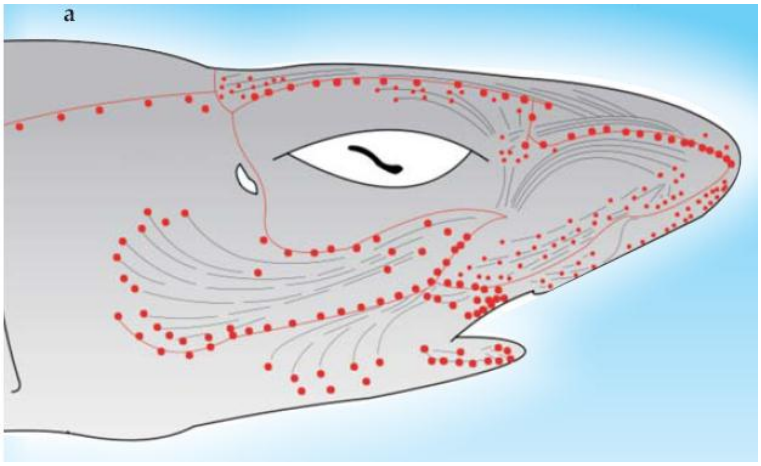

Figure 1.15 Magnetoelectric receptors in shark's head

The DC magnetic field sensitivity was characterized using an active method: an excitation coil was wrapped around the sensor which carried a small AC current provided by the lock-in amplifier to drive the ME sensor. Voltages were then induced in the piezoelectric layer by small changes in H_{dc} which were caused by geomagnetic variance in space. Figure 1.16 presents the comparison of the DC magnetic field sensitivity of two ME composites.

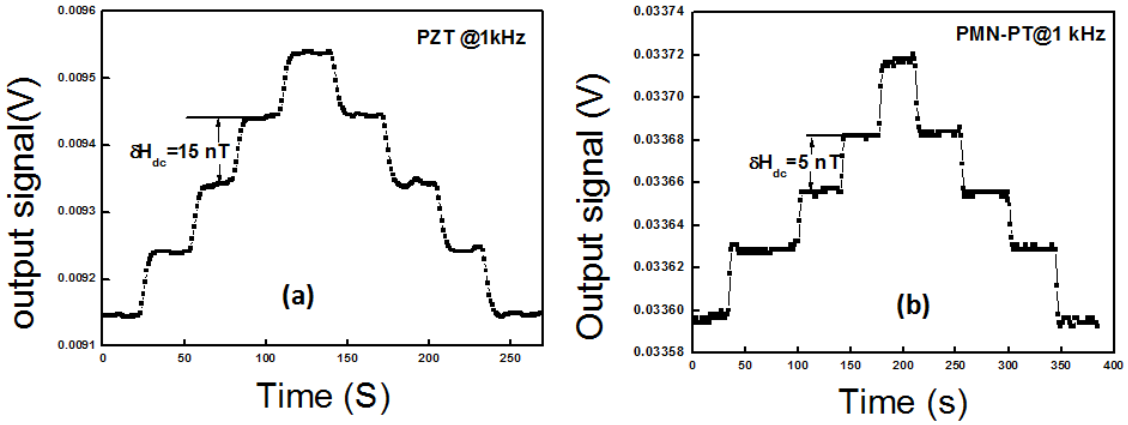

Figure 1.16 DC magnetic field sensitivities for (a) PZT based; (b) PMN-PT based composites.[41]

Gao et. al reported the enhancement for the DC magnetic field sensitivity in ME laminates. It shows the induced output voltages in response to small changes in H_{dc} at

driving frequencies of f=1 kHz with strength H_{ac}=0.1 Oe.[41] It can be seen that DC magnetic field variations as small as H_{dc}=15 nT can be detected for the PZT laminates sample. Figure 1.16 shows similar sensitivity measurements to small changes in H_{dc} for Metglas/PMN-PT laminates. In this figure, one can see that the sensitivity was significantly enhanced relative to the Metglas/PZT ones. The sensitivity to DC magnetic field changes for PMN-PT laminates can be seen to be 5 nT at 1 kHz, which is 3 times higher than that for PZT based ones. Such enhancement in DC field sensitivity is a direct consequence of the higher values of α_{ME} for the Metglas/PMN-PT laminates at small DC bias range. Indeed, the achievement of such improvement in DC sensitivity can be attributed to the fact that the value of slope was much larger for Metglas/PMN-PT than Metglas/PZT over the range of -5 Oe <H_{dc}< 5 Oe.

1.3.3 AC magnetic field sensor

The ME composites can be used as a magnetic probe for detecting AC fields. For example, Dong et. al demonstrated that push-pull ME Terfenol-D/PMN-PT/Terfernol-D three-layer laminates have a linear response to H_{ac} at driving frequencies of f=1 kHz and 77.5 kHz over a wide range of fields from 10^{-11}< H_{ac}<10^{-3} T as shown in Figure 1.17.[42] Furthermore, driving with a H_{ac} near the laminates' resonant frequency should contribute to a significant enhancement in sensitivity to small AC magnetic field variations.

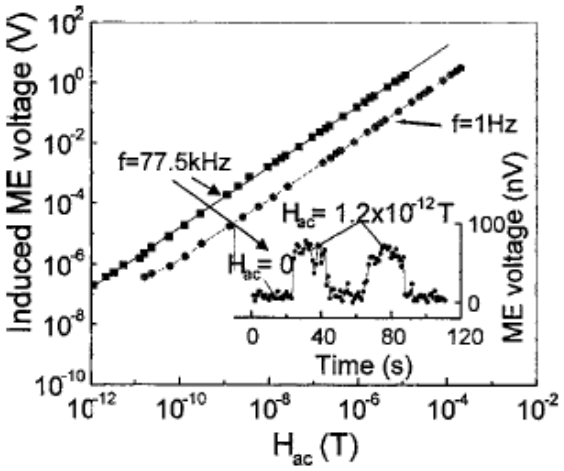

Figure 1.17 The induced ME voltage as a function of magnetic field over the range of 10^{-12}<Hac<10^{-3} T at drive frequencies of *f* =1 Hz and *f* =77.5 kHz (resonance condition); inset of the figure shows the change in the ME voltage as a function of time, in response to a minute magnetic field variation of 1.2×10^{-12} T.[42]

Since some specific applications require extremely low frequency detection, an important consideration for the design of magnetic sensors is the frequency bandwidth of detectable magnetic fields. For example, the magnetoencephalography (MEG) measurements span a frequency range from about 10 mHz to 1 kHz.[43] Gao et.al have presented a quasi-static charge amplifier method to detect the extreme low frequency response of Metglas/PMN-PT laminated composites as shown in Figure 1.10 (a). Using this technique, the ME effect can be used to detect magnetic field changes at a frequency less than 10^{-2} Hz, and ME charge coefficients show good stability over wide frequency range from10 mHz to 1 kHz. Thus, a quasi-static magnetic sensor has been developed based on ME composites which can work at frequencies down to 10 mHz, with equivalent magnetic noise floors of 3 nT/√Hz as shown in Figure 1.18 (b).[44]

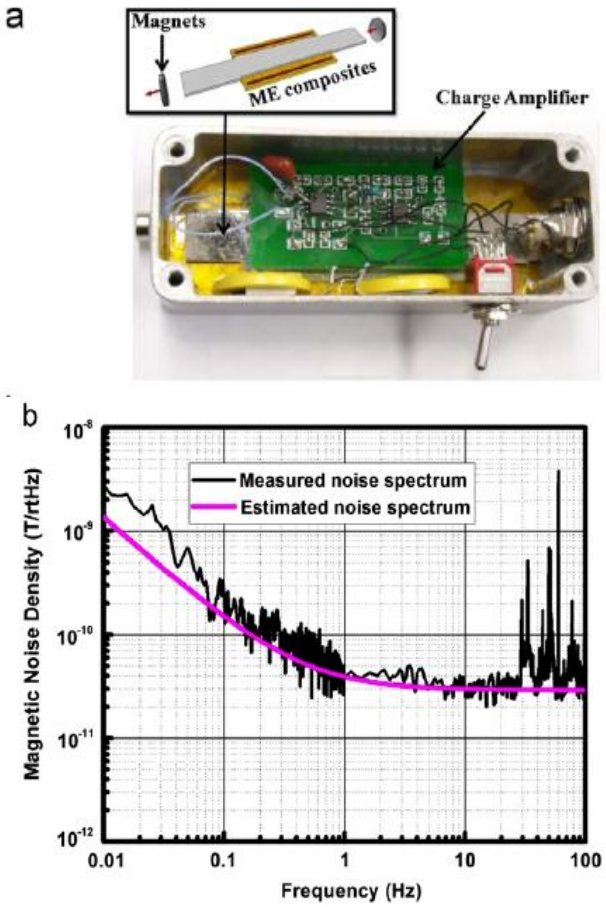

Figure 1.18 (a) Photograph of a low-frequency magnetic sensor detection unit; (b) estimated and measured equivalent magnetic noise of the sensor.[44]

Many prototypes of magnetic sensors based on the ME effect have been developed with ultrahigh sensitivity. However, much work still remains to be done with the purpose to commercialize ME composites products, such as the design and integration of bi-axis and triple-axis vector sensor systems, thermal stability of ME composites, and SNR of the system in an open environment where noises are dominant in low frequency domains.

1.4 Summary of This Section

There is a need for portable magnetic sensors that are highly sensitive, compact, operated at room temperature and use little power. However, there are no available technologies that can fulfill all these requirements. Despite the fact that a SQUID can detect small magnetic fields, it demands extremely low operating temperatures, making it usable only under controlled environments. Most applications for detecting magnetic

anomalies have used fluxgate sensors, which have a minimum detectable signal level of 0.01–1 nT at quasi-static frequencies.

Recently ME laminated composites consisting of layers of magnetostrictive Metglas and piezo-fibers have been developed for sensitive passive magnetometer applications at room temperature. Though plenty of prototypes of ME magnetic sensors based on bulk ME composites with very high sensitivity have been proposed in literatures, a lot of work still remains in terms of widely commercialize the ME magnetic sensor devices, such as rejection of external noises, design of ME sensors or array with high SNR, thermal stability, and triple-axis system optimization and integration. These are purposes of my thesis.

References:

[1] R. S. Popovic, J. A. Flanagan, and P. A. Besse, "The future of magnetic sensors," *Sensor and Actuators A*, vol. 56, pp. 39-55, 1996.

[2] J.Lenz and A. S. Edelstein, "Magnetic Sensors and Their Applications," *Ieee Sensors Journal*, vol. 6, 2006.

[3] P. Ripka, "Advances in Magnetic Field Sensors," *Ieee Sensors Journal*, vol. 10, p. 11081116, 2010.

[4] L. Portmann, "A SOI CMOS Hall effect sensor architecture for high temperature applications (up to 300 ℃)," *Sensors, 2002. Proceedings of IEEE*, vol. 2, pp. 1401-1406, 2002.

[5] P. Kejik, G. Boero, M. Demierre, and R. S. Popovic, "An integrated micro-Hall probe for scanning magnetic microscopy," *Sensors and Actuators A: Physical*, vol. 129, pp. 212-215, 2006.

[6] L. Ejsing, M. F. Hansen, A. K. Menon, H. A. Ferreira, D. L. Graham, and P. P. Freitas, "Planar Hall effect sensor for magnetic micro- and nanobead detection," *Applied Physics Letters*, vol. 84, p. 4729, 2004.

[7] P. Ripka, "Review of fluxgate sensors," *Sensors and Actuators A: Physical*, vol. 33, pp. 129-141, 1992.

[8] T. McGuire, "Anisotropic magnetoresistance in ferromagnetic 3d," *IEEE Transactions on Magnetics*, vol. 11, pp. 1018 - 1038 1975.

[9] D. J. Mapps, "Magnetoresistive sensors," *Sensor and Actuators A*, vol. 59, pp. 9-19, 1997.

[10] S. Tumanski, *Thin Film Magnetoresistive Sensors*. Bristol, U.K: Institute of Physics, 2001.

[11] B. Dieny, "Giant magnetoresistance in spin-valve multilayers," *Journal of Magnetism and Magnetic Materials*, vol. 136, pp. 335-359, 1994.

[12] P. P. Freitas and etal., "Spin valve sensors," *Sensor and Actuators A*, vol. 81, pp. 2-8, 2000.

[13] M. J. Carey and etal., " Spin valves using insulating cobalt ferrite exchange-spring pinning layers " *Applied Physics Letters*, vol. 81, pp. 1044-1046, 2002.

[14] R. Kleiner, D. Koelle, F. Ludwig, and J. Clarke, "Superconducting quantum interference devices State of the art and application," *PROCEEDINGS OF THE IEEE* vol. 92, pp. 1534-1548, 2004.

[15] B. Deaver and W. Fairbank, "Experimental Evidence for Quantized Flux in Superconducting Cylinders," *Physical Review Letters*, vol. 7, pp. 43-46, 1961.

[16] B. D. Josephson, "Possible new effects in superconducive tunneling," *Physics Letter*, vol. 1, pp. 251-253, 1962.

[17] V. Pizzella, S. D. Penna, C. D. Gratta, and G. L. Romani, "SQUID systems for biomagnetic imaging," *Superconductor Science and Technology*, vol. 17, pp. 79-114, 2001.

[18] P. L. Richards, "Bolometric Detectors for Measurements of the Cosmic Microwave Background," *Journal of Superconductivity*, vol. 17, pp. 545-550, 2004.

[19] H.-G. Meyer, R. Stolz, A. Chwala, and M. Schulz, "SQUID technology for geophysical exploration," *physica status solidi (c)*, vol. 2, pp. 1504-1509, 2005.

[20] J. P. Wikswo, Jr. , "SQUID magnetometers for biomagnetism and nondestructive testing important questions and initial answers," *Ieee Transactions on Applied Superconductivity*, vol. 5, pp. 74-120, 1995.

[21] S. Cheong and M. Mostovoy, "Multiferroics a magnetic twist for ferroelectricity," Nat Mater, vol. 6, 2007.

[22] J. Ma, J. Hu, Z. Li, and C.-W. Nan, "Recent Progress in Multiferroic Magnetoelectric Composites: from Bulk to Thin Films," Advanced Materials, vol. 23, pp. 1062-1087, 2011.

[23] D. N. Astrov, " Magnetoelectric effect in antiferromagnetic Cr2O3," Sov. Phys. JETP, vol. 13, 1961.

[24] J. v. d. Boomgaard, A. M. J. G. V. Run, and J. v. Suchtelen, "Magnetoelectricity in Piezoelectric–Magnetostrictive Composites," Ferroelectrics, vol. 10, p. 295, 1976.

[25] W. Eerenstein, N. D. Mathur, and J. F. Scott, "Multiferroic and magnetoelectric materials," Nature, vol. 442, pp. 759-65, Aug 17 2006.

[26] S. W. Cheong and M. Mostovoy, "Multiferroics: a magnetic twist for ferroelectricity," Nature Materials, vol. 6, pp. 13-20, 2007.

[27] Y. H. Chu, L. W. Martin, M. B. Holcomb, M. Gajek, S. J. Han, Q. He, N. Balke, C. H. Yang, D. Lee, W. Hu, Q. Zhan, P. L. Yang, A. Fraile-Rodriguez, A. Scholl, S. X. Wang, and R. Ramesh,

"Electric-field control of local ferromagnetism using a magnetoelectric multiferroic," Nat Mater, vol. 7, pp. 478-82, Jun 2008.
[28] C. Ederer and N. A. Spaldin, "Magnetoelectrics A new route to magnetic ferroelectrics," Nature Materials, vol. 3, p. Nature Materials, 2004.
[29] J. Zhai, Z. Xing, S. Dong, J. Li, and D. Viehland, "Magnetoelectric Laminate Composites: An Overview," Journal of the American Ceramic Society, vol. 91, pp. 351-358, 2008.
[30] H. Zheng, J. Wang, S. E. Lofland, Z. Ma, L. Mohaddes-Ardabili, T. Zhao, L. Salamanca-Riba, S. R. Shinde, S. B. Ogale, F. Bai, D. Viehland, Y. Jia, D. G. Schlom, M. Wuttig, A. Roytburd, and R. Ramesh, "Multiferroic BaTiO3-CoFe2O4 Nanostructures," Science, vol. 303, pp. 661-3, Jan 30 2004.
[31] H. Zheng, F. Straub, Q. Zhan, P. L. Yang, W. K. Hsieh, F. Zavaliche, Y. H. Chu, U. Dahmen, and R. Ramesh, "Self-Assembled Growth of BiFeO3–CoFe2O4 Nanostructures," Advanced Materials, vol. 18, pp. 2747-2752, 2006.
[32] C.-W. Nan, G. Liu, Y. Lin, and H. Chen, "Magnetic-Field-Induced Electric Polarization in Multiferroic Nanostructures," Physical Review Letters, vol. 94, 2005.
[33] C.-W. Nan, M. I. Bichurin, S. Dong, D. Viehland, and G. Srinivasan, "Multiferroic magnetoelectric composites: Historical perspective, status, and future directions," Journal of Applied Physics, vol. 103, p. 031101, 2008.
[34] S. Dong, J. Zhai, J. Li, and D. Viehland, "Near-ideal magnetoelectricity in high-permeability magnetostrictive/piezofiber laminates with a (2-1) connectivity," Applied Physics Letters, vol. 89, p. 252904, 2006.
[35] J. Das, J. Gao, Z. Xing, J. F. Li, and D. Viehland, "Enhancement in the field sensitivity of magnetoelectric laminate heterostructures," Applied Physics Letters, vol. 95, p. 092501, 2009.
[36] Y. Wang, D. Gray, D. Berry, J. Gao, M. Li, J. Li, and D. Viehland, "An Extremely Low Equivalent Magnetic Noise Magnetoelectric Sensor," Advanced Materials, vol. 23, pp. 4111-4114, 2011.
[37] Y. Wang, J. Gao, M. Li, D. Hasanyan, Y. Shen, J. Li, D. Viehland, and H. Luo, "Ultralow equivalent magnetic noise in a magnetoelectric Metglas/Mn-doped Pb(Mg1/3Nb2/3)O3-PbTiO3 heterostructure," Applied Physics Letters, vol. 101, p. 022903, 2012.
[38] J. Zhai, Z. Xing, S. Dong, J. Li, and D. Viehland, "Thermal noise cancellation in symmetric magnetoelectric bimorph laminates," Applied Physics Letters, vol. 93, p. 072906, 2008.
[39] Z. Xing, J. Li, and D. Viehland, "Noise and scale effects on the signal-to-noise ratio in magnetoelectric laminate sensor/detection units," Applied Physics Letters, vol. 91, p. 182902, 2007.
[40] Y. Shen, J. Gao, L. Shen, D. Gray, J. Li, P. Finkel, D. Viehland, X. Zhuang, S. Saez, and C. Dolabdjian, "Analysis of the environmental magnetic noise rejection by using two simple magnetoelectric sensors," Sensors and Actuators A: Physical, 2011.
[41] J. Gao, D. Gray, Y. Shen, J. Li, and D. Viehland, "Enhanced dc magnetic field sensitivity by improved flux concentration in magnetoelectric laminates," Applied Physics Letters, vol. 99, p. 153502, 2011.
[42] S. Dong, J. Zhai, F. Bai, J.-F. Li, and D. Viehland, "Push-pull mode magnetostrictive/piezoelectric laminate composite with an enhanced magnetoelectric voltage coefficient," Applied Physics Letters, vol. 87, p. 062502, 2005.
[43] J. Vrba and S. E. Robinson, "Signal processing in magnetoencephalography," Methods, vol. 25, pp. 249-71, Oct 2001.
[44] J. Gao, Y. Wang, M. Li, Y. Shen, J. Li, and D. Viehland, "Quasi-static (f<10−2Hz) frequency response of magnetoelectric composites based magnetic sensor," Materials Letters, vol. 85, pp. 84-87, 2012.

Charpter 2:

PURPOSE OF THIS THESIS

In recent years, there have been great advancements in the development of magnetic field sensors. AMR (anisotropic magneto-resistance) sensors have become the standard for off-the-shelf devices with integrated flipping and feedback coils for use in medium-accuracy applications such as compasses for vehicles. GMR (giant magneto-resistance) sensors are widely used in angular sensing. Furthermore, significant enhancements have been found in sensitivity improvements in resonance magnetometers. However, these achievements are still in the laboratory phase, which is still far behind the classical completed ones. Thus, the development of magnetic sensors has proven to be slow. Most fascinating breakthroughs on nanosensors with pico-tesla resolution have turned out to be a bubble.

For sake of application, the need for improved sensors is ubiquitous in aspects of smaller size, lower power consumption, and lower cost for similar or improved performance. In many applications, sensor size is an issue and considered as the only selection criterion, either because of the need for spatial resolution or because of the weak point-like sources. However, there is always a tradeoff between the size of a sensor and its other parameters, such as sensitivity. In addition, for applications, which do not limit in a small detection distance, parameters such as sensitivity become more important. However, in other more demanding cases, the linearity, temperature coefficients and even cross-field sensitivity become more important than noise. Therefore, for each application, one needs to make a tradeoff between sensitivity, size, power and cost. These requests also lead to the possible improvement approaches for the next generation of magnetic sensors which are:

1) Extreme sensitivity ($<<nT/\sqrt{Hz}$ and $<pT/m/\sqrt{Hz}$) at low frequencies (10^{-3} Hz), to resolve weaker mobile anomalies and utilize detector mobility to sample space;

2) Low power consumption–passive if possible–to foster deployment longevity;

3) Ambient temperature operation;

4) Small size, to promote portable imaging array systems.

Next, I will focus on these requirements to illustrate the property of ME sensors and gradiometers. I will show the objective and significance of my study in terms of three aspects:

1) Increase of rejection efficiency, and lowering of gradiometer noise under various conditions;
2) Arrays of sensors, how sensors in arrays interact, 1D and 2D image;
3) Localization, detection, and identification of AC source ;
4) Localization, detection, and identification of DC source ;
5) Modulation mode sensor to transfer low frequency signal to high frequency to eliminate 1/*f* noise.

Chapter 3:

INCREASE OF NOISE REJCTION EFFICIENCY FOR ME GRADIOMETER

3.1. Introduction

A gradient is obtained by finding the difference between two magnetometer readings which are separated by a base-line in space.[1, 2] After normalized with respect to the separation, the difference gives rise to a gradient along the baseline, provided that the magnetometers' axes are aligned with sufficient accuracy. There are three gradients in terms of the three vector components for a given line direction, and there are three linear independent directions, resulting in nine gradients in 3D. All gradients can be expressed into a matrix named a magnetic gradient tensor:

$$G^B = \begin{pmatrix} G_{xx}^B & G_{xy}^B & G_{xz}^B \\ G_{yx}^B & G_{yy}^B & G_{yz}^B \\ G_{zx}^B & G_{zy}^B & G_{zz}^B \end{pmatrix} \quad (3.1)$$

As the gradient tensor is symmetric and traceless, $\nabla \cdot B = 0$ and $\nabla \times B = 0$ give four constraints on the nine tensor components.[3] Five orthogonal functions are sufficient for the various procedures of signal processing need for efficient detection. [4] A prototype man-portable magnetic gradiometer is shown in Figure 3.1.

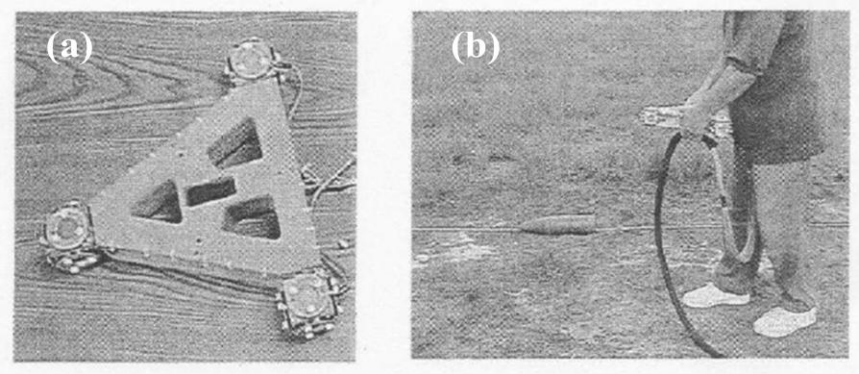

Figure 3.1 (a) Picture of a magnetic gradiometer; (b) man-portable gradiometer localizing ordnance. [3]

Magnetic gradiometers of various types are widely used for detection and characterization of ferromagnetic objects, varying from SQUID operating at liquid helium or liquid nitrogen temperature[5], fluxgate operating at room temperature[6], optically pumped devices[7], to on-chip anisotropic magnetoresistors (AMRs)[8] as shown in Figure 3.2(a)-(d).

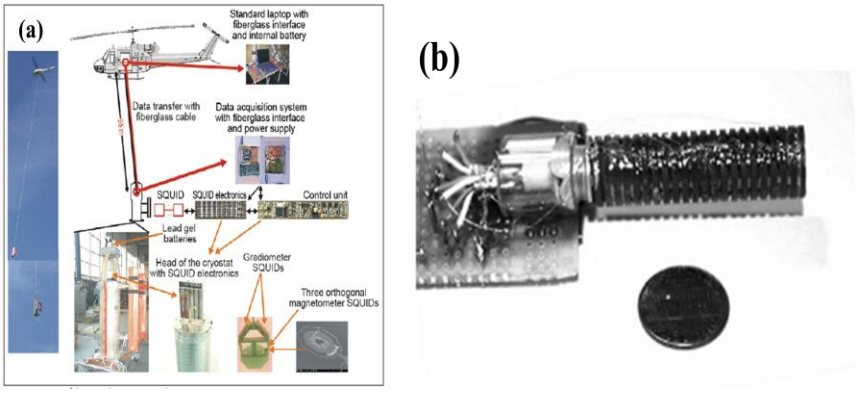

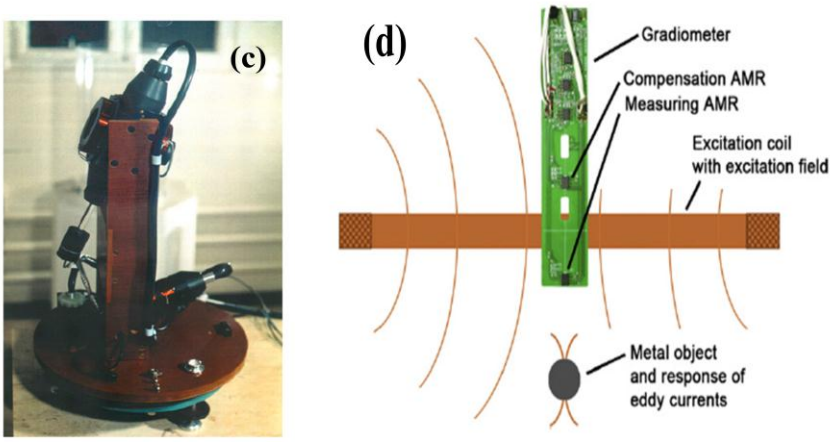

Figure 3.2 (a) Setup of airborne SQUID system; (b) The fluxgate gradiometer shown with 1-cent coin; (c) A photograph showing the optically pumped magnetic sensor unit used in our work; (d) AMR Gradiometer combined with the excitation coil form the detector head. The compensating and measuring sensors of the gradiometer are symmetrically placed on both sides of the excitation coil.

The gradiometer is desirable for discerning nearby sources and locating small anomalies as gradients decrease with distance more rapidly than field strength. This way, the target in the vicinity can be preferentially detected. A further advantage is that the gradiometer can offer a high degree of immunity from diurnal and minor magnetic storm activity in the ambient magnetic field, making small and weak magnetic targets recognizable. Direct measurement of the target-anomaly vector is hampered by the huge Earth-field vector (50 μT) and environmental noise which is always at least two orders larger than the target. Indeed, the environmental noise can be simply extracted by cross-correlating ambient-noise recordings from any two magnetometers. As shown in Section 3.2, two ME sensors are used that allow taking the difference between the outputs to efficiently null off the correlated noises. With gradiometer measurements, the noise floor is decreased, making small and weakly magnetic target recognizable, as illustrated in Section 3.3.

3.2 ME Gradiometer to Reject Environmental Noise

In most applications, magnetic sensors must be operated in an open environment (i.e., magnetically unshielded). Such environments are contaminated by environmental noise, which can raise the equivalent magnetic noise floor of any magnetic sensor dramatically.

In other words, for practical use ME magnetic sensors are fundamentally challenged by the inability to distinguish minute target signals from external noises which have several orders of higher amplitudes than former. As environmental shielding of magnetic sensors is impractical in numerous applications, using two (or more) magnetic sensors in a differential mode configuration is expected to reject/reduce environmental magnetic noise. Recent studies have indicated that such configurations are capable of rejecting common noise sources that are coherently shared between two sensors spatially separated by a baseline.[9, 10] However, there has been rare experimental mention so far on differential gradiometry measurements using ME sensors to reject environmental noises that are coherently shared between two sensors.

Here, we focus on the analysis of the magnetic detection, potentiality to optimize ME gradiometers to bemore sensitive for device applications. We evaluate the efficiency of coherent noise rejection and analyze the capacity of intrinsic noise levels of each sensor by a basic ME differential structure with a digital post processing and in a laboratory environment.

3.2.1 Experimental Setup

The ME laminate composite used in this experiment (*cf.* Figure 3.3) was a tri-layer Metglas/PZT/Metglas fiber with a multi push-pull mode configuration. Thin interdigited electrodes deposited on Kapton® sheets were attached to the top and bottom surfaces of a $4\ \text{cm} \times 1\ \text{cm} \times 180\ \mu\text{m}$ PZT (CTS, Albuquerque, NM) fiber bundle using a two-part epoxy. The interdigited electrode pattern allows for symmetric poling of the piezoelectric fibers in a back-to-back pattern along their length axis [11]. Three layers of $8\ \text{cm} \times 1\ \text{cm} \times 22\ \mu\text{m}$ Metglas foils (Vitrovac 7600F, Vitrovac Inc. Hanau, German) were then affixed to the top and bottom surfaces of the Kapton® electrodes using the same epoxy as for the piezoelectric core. Magnetic DC biases were applied by permanent magnets placed at either end of the ME laminates. The ME laminate sensor and bias magnets were packaged in a PVC enclosure and wrapped with thin aluminum sheets to provide a shielding from electromagnetic interference (EMI).

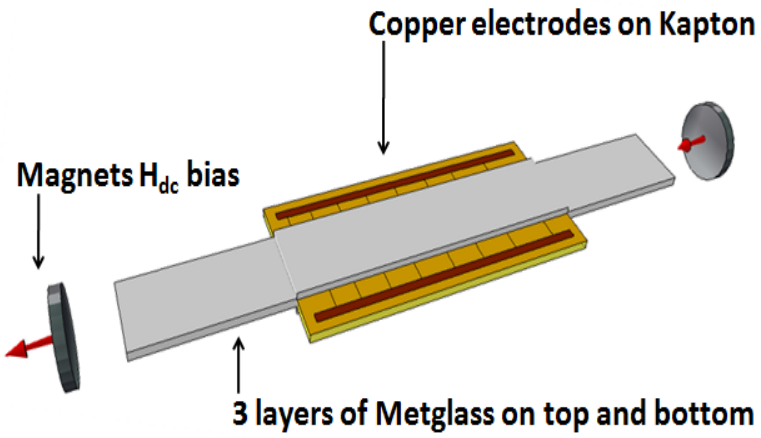

Figure 3.3 Schematic diagram of the Metglas/PZT ME laminate sensor.

Figure 3.4 (a) illustrates the configuration of sensors and signal collection electronics used in our experimentation. Two packaged ME laminate composite sensors and corresponding charge amplifier (CA) circuits were assembled into battery operated sensor detection units which were separated by a baseline of 10 cm. ME laminates were placed parallel to each other and aligned with the geomagnetic field. The charge amplifiers were designed with a transfer function of 1 V/pC and with a frequency bandwidth of 0.6 Hz to 10 Hz [12]. The output signals from the CAs were recorded using a CR5000 Datalogger (Campbell Scientific, Inc.) with a 100 Hz sample rate, a full-scale of 1 V and a dynamic range of 60 dB. Signal processing was carried out using MATLAB scripts. The noise tests were conducted in our lab (at about 10pm) which can be considered as a high magnetic and vibratory disturbance environment.

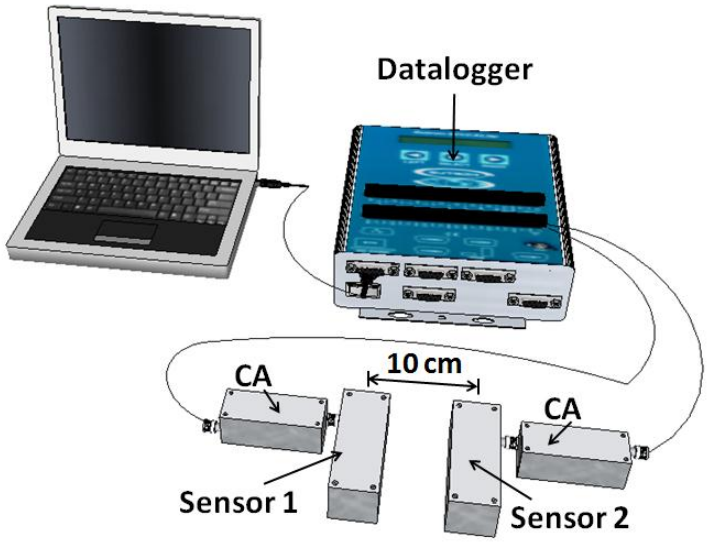

(a)

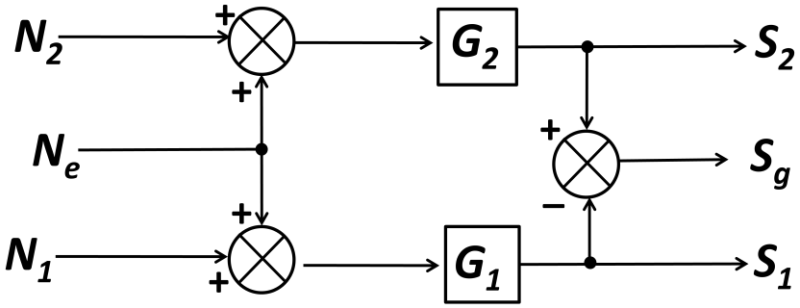

(b)

Figure 3.4 (a) Schematic illustration of sensor pair configuration with associated charge collection and signal processing circuitry; (b) block diagram representation of signal collection showing external (Ne) and internal (N1) and (N2) (for sensor 1 and 2, respectively) equivalent input magnetic noise sources, conversion of charge signals (Ne + Nk) into voltage signals Sk via Gk gain of the sensor k (k={1,2}) and associated to its charge amplifiers, and differential output voltage, Sg.

Each of the two sensors in the parallel array was exposed to the same external magnetic environment. Indeed, we assume spatial homogeneous perturbations in the volume. So, the sensors were exposed to one external noise source, N_e, as shown in Figure 3.4(b). Additionally, each sensor exhibited a random equivalent input magnetic noise of N_1 and N_2, which are considered intrinsic to the detection unit (ME sensors and charge amplifier). All noise sources (N_1, N_2, and N_e) are assumed uncorrelated. The charge produced by the noise signals from each of the two sensors was integrated via a

charge amplifier[12]. The gain of the channel k is G_k, as defined in Figure 3.4(b) and shown in Figure3.5. The resultant voltage signals, S_1 and S_2, were collected by the Datalogger as illustrated in Figure 3.4 (b). Each output can be analyzed and differential output, $S_g(= S_2 - S_1)$, computed.

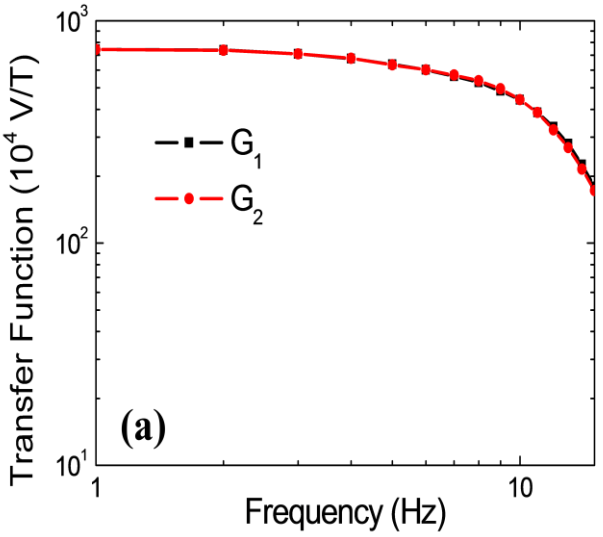

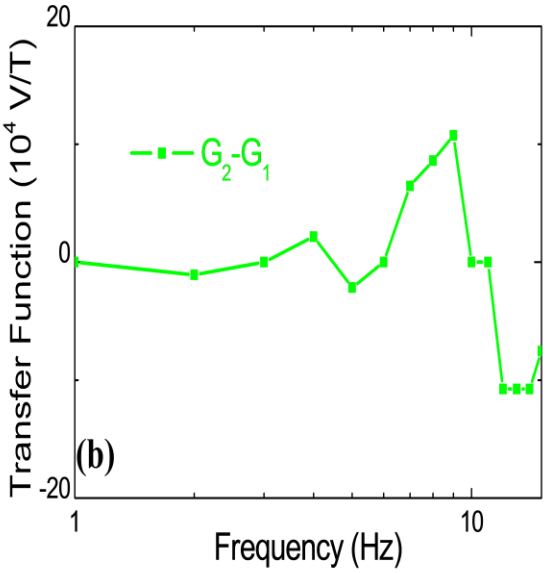

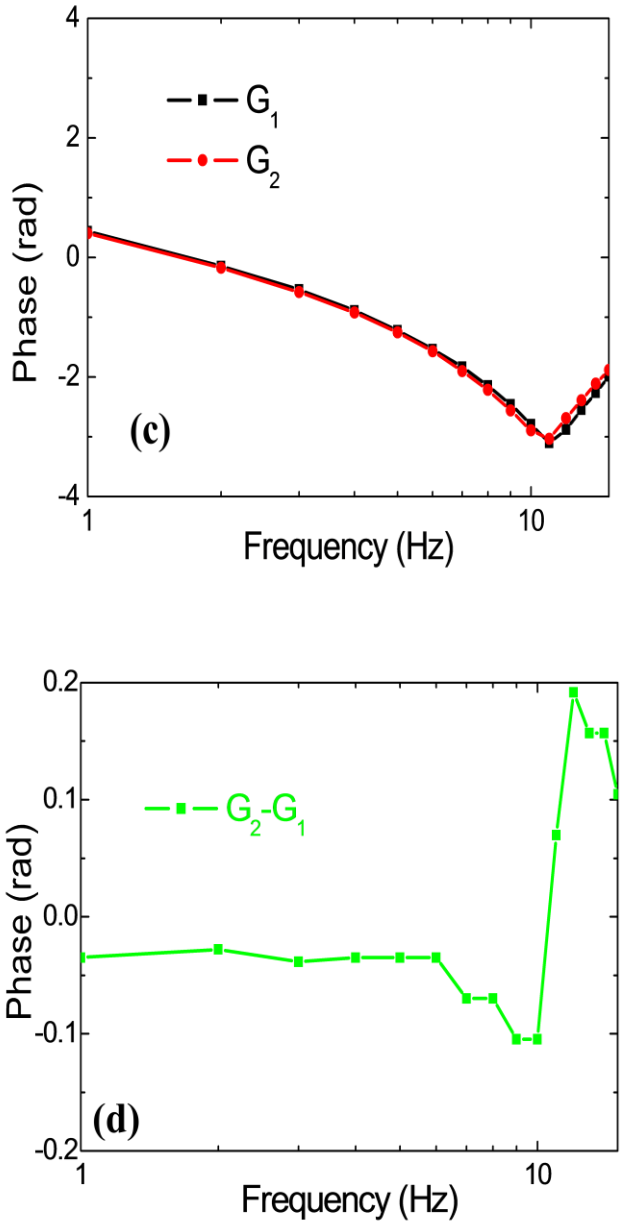

Figure 3.5 Homogenous gain transfer function of (a) sensor 1 G1 (black curve), sensor 2 G2 (red curve) and (b) differential output abs(G2)–abs(G1); phase transfer function of (c) sensor 1 G1 (black curve), G2 sensor 2 (red curve) and (d) differential output abs(G2)–abs(G1).

3.2.2 Theoretical estimation of intrinsic noise source level

Our approach following classical signal processing techniques to estimate instrumental noise based on measuring the coherence of the output signal of two sensors, as given in [13]. The coherence between the outputs, S_1 and S_2, is given by

$$C_{S_1S_2}(f) = \frac{P_{S_1S_2}(f)^2}{P_{S_1S_1}(f)P_{S_2S_2}(f)} \tag{3.2}$$

where $P_{S_1S_1}(f)$ and $P_{S_2S_2}(f)$ are the power spectral density (PSD) of the output voltage signals, S_1 and S_2, respectively. $P_{S_1S_2}(f)$ is the cross spectral density of both signals. The power spectral density and the cross-spectral density are defined by

$$P_{S_iS_j}(f) = \lim_{T\to\infty} E\left[\frac{\left|S_i^*(f,T)S_j(f,T)\right|}{T}\right] \tag{3.3}$$

where S_i and S_j are two signals, T is the length of record, S_i (f, T) is the Fourier transform of signal S_i recorded and S^*_i (f, T) is the S_i (f, T) complex conjugate. $P_{S_iS_j}(f)$ can be estimated [14] by

$$\tilde{P}_{S_iS_j}(f) = \frac{2}{n_d T}\sum_{n=1}^{n_d}\left[S^*_{i,n}(f,T)S_{j,n}(f,T)\right] \tag{3.4}$$

where n_d refers to the number of records averaged, T is the lengthof each record, $S_{i,p}(f, T)$ is the Fourier Transform of the p^{th} record of the signal S_i. $\tilde{P}_{S_iS_j}(f)$ is a very poor estimation when $n_d < 30$: the signal to noise ratio for this estimation, $P_{ij}(f)^2 / E\left[\left(P_{ij}(f) - \tilde{P}_{ij}(f)\right)^2\right]$, is equal to n_d[15]. $C_{S_1S_2}(f)$ can be thought of as the percentage of overlap in the power spectra of signals S_1 and S_2.

The output signal PSD is comprised of external and internal noises, as depicted in Figure 3.2 (b). Our charge amplifiers were designed with a transfer function of G_1 and G_2, respectively. This allows the PSD to be written as

$$P_{S_kS_k}(f) = |S_k|^2 P_{N_kN_k}(f) + |S_k|^2 P_{N_eN_e}(f) \tag{3.5}$$

where $k \in \{1;2\}$. As long as the internal sensor noise is random and incoherent, the cross spectral density of both sensors is proportional to the power spectral density of the coherent environmental noise N_e and is given by

$$P_{S_1S_2}(f) = \left|G_1^*(f)G_2(f)\right| P_{N_eN_e}(f). \quad (6)$$

$G^*_1(f)$ is the $G_1(f)$ complex conjugate, assuming that the internal noise signals from both sensors are incoherent. Also, we assume that they have roughly identical magnitudes

$$P_{N_1N_1}(f) = P_{N_2N_2}(f) = P_{N_iN_i}(f) \quad (3.7)$$

and since the signals arising from the external noise are coherent, the cross spectral density can be expressed as

$$C_{S_1S_2}(f) = \frac{1}{\left(1+\frac{P_{N_iN_i}(f)}{P_{N_eN_e}(f)}\right)^2}. \quad (3.8)$$

Using Equation (3.5), and rearranging Equation (3.8), when the coherence is close to 1 or $P_{N_iN_i}(f) << P_{N_eN_e}(f)$, the internal noise of each sensor can be expressed as

$$P_{N_iN_i}(f) \approx P_{N_eN_e}(f)\left[1-\sqrt{C_{S_1S_2}(f)}\right] \approx P_1(f)\left[1-\sqrt{C_{S_1S_2}(f)}\right]. \quad (3.9)$$

The gains of each channel are closed $(G_1(f) \approx G_2(f))$. Thus, the output noise in the differential configuration can be evaluated by

$$P_{S_gS_g}(f) = \left|G_1(f)\right|^2 \left(2P_{N_iN_i}(f) + \left|\frac{G_2(f)-G_1(f)}{G_1(f)}\right|^2 P_{N_eN_e}(f)\right). \quad (3.10)$$

This noise level is clearly limited by the intrinsic differentiator noise, $2P_{N_iN_i}(f)$, and by $\left|\frac{G_2(f)-G_1(f)}{G_1(f)}\right|^2 P_{N_eN_e}(f)$ value given by the discrepancy between the two sensors (*cf.* Fig. 3). In order to evaluate this last term, the ratio $T_{12}(f)=G_2(f)/G_1(f)$ between $S_2(f)$ and $S_1(f)$ can be used

$$\left|\frac{G_2(f)-G_1(f)}{G_1(f)}\right|^2 = 1+\left|T_{12}(f)\right|^2 - 2\left|T_{12}(f)\right|\cos\left(\arg\left(T_{12}(f)\right)\right). \quad (3.11)$$

Then, for close sensors ($|T_{12}| = 1+\varepsilon$ with $\varepsilon << 1$ and $\arg(T_{12}) = \theta << 1$) and spatial homogeneous external noise sources, the rejection of coherent noise sources can be evaluated by

$$\left|\frac{G_2(f)-G_1(f)}{G_1(f)}\right|^2 \approx \varepsilon^2+\theta^2 . \qquad (3.12)$$

3.2.3 Results

The time-domain signal output traces of a pair of parallel sensors, as well as the time-domain difference between the signals, are given in Figure 3.4. The top graph (a) in this figure shows the output of each charge amplifier circuit, while the bottom graph (b) shows the time-domain difference between the two signals. This test was conducted in an open environment in our lab (unshielded).

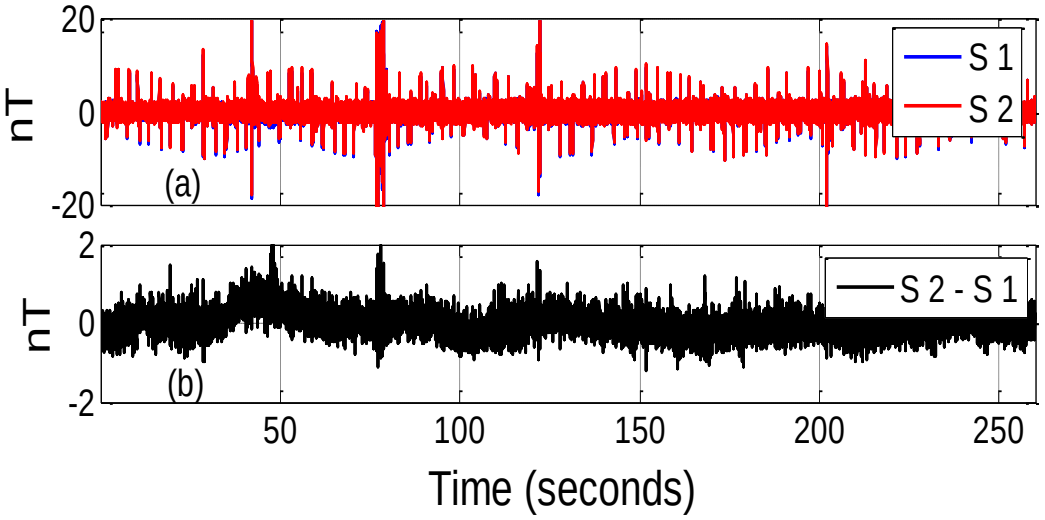

Figure 3.6 Time-domain signal output of two parallel sensor array: (a) output from each sensor (Notice that S2 superimpose S1) and (b) time-domain difference in the two output signals.

The values of $P_{S_1S_1}(f)$ and $P_{S_2S_2}(f)$ estimated from the time-domain data, using Equation (3) and 26,000 number of records averaged, are shown in Figure 6. The data in the figure shows that the sensors have an equivalent background noise level of ~400 pT/√Hz at 1 Hz. The peak at 1.5 - 1.7 Hz, we believe, arises from building vibrations. Next, we estimated the equivalent magnetic noise floor of the differential mode configuration of the ME sensor pair by the difference (S_2 - S_1) by post processing. These results are also shown in Figure 3.7. In this figure, we can see that the equivalent

magnetic noise floor of the sensor pair was about 20× lower than that of the individual sensors. These results demonstrate the ability of this basic sensor differentiator to reject environmental noise, as a common mode. This infers a strong coherence between the output noise of S_1 and S_2.

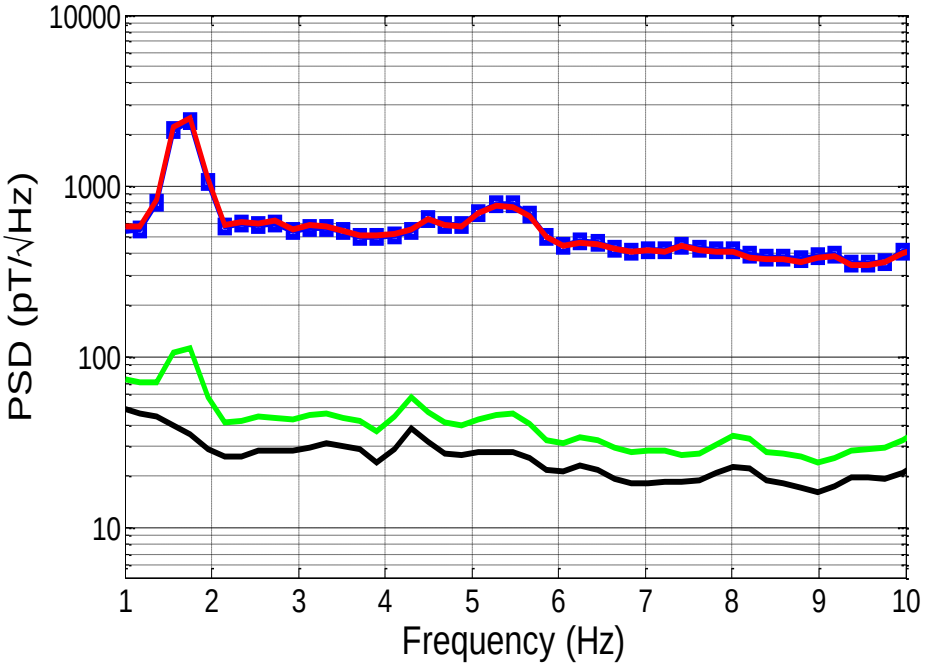

Figure 3.7 Power spectral density curves of S_1 (blue dotted curve), S_2 (red curve) and the signal (S_2 - S_1) (green curve) after post processing. The estimated intrinsic sensor noise (N_1 or N_2) is the black curves.

The upper plot (a) in Figure 3.8 shows the coherence $C_{S_1S_2}(f)$ between sensors 1 and 2. Because of $C_{S_1S_2}(f) \approx 1$, the ratio between S_2 and S_1 helps to evaluate the ratio $T_{12}(f) = G_2(f)/G_1(f)$ as given in (12a). The magnitude of this ratio $|T_{12}(f)|$ gives information about the relative amplitudes of the output signals, while the phase of the transfer function θ_{12} provides information about the time lag between the two output signals. The middle plot (b) in Figure 3.8 originates from the smoothing transfer function amplitude $|T_{12}(f)|$. As can be seen in this Figure 8, the amplitude remained at a near constant level of $T_{12} = 1$, which means that S_1 and S_2 have nearly identical absolute values. The phase angle $\theta_{12}(f)$ is shown in Figure 8 (c).3.

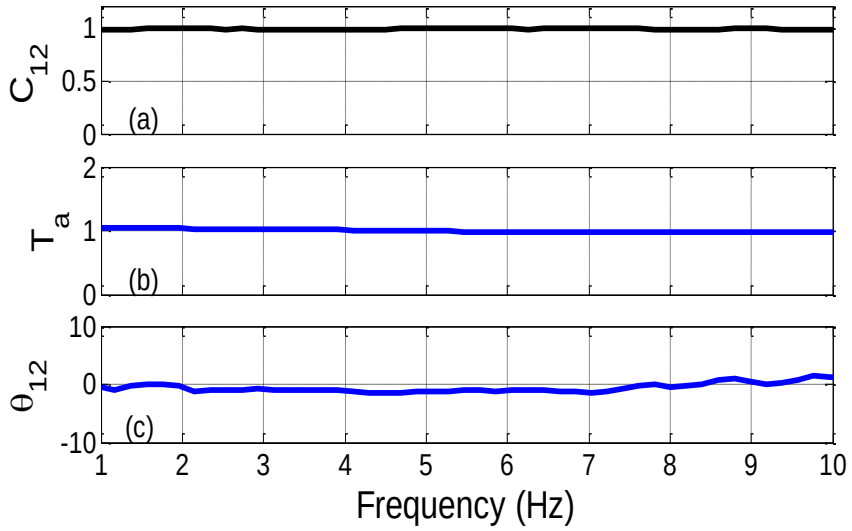

Figure 3.8 (a) Coherence value (top graph), (b) relative amplitude difference and (c) phase shift between S_1 and S_2 outputs.

$$T_{12}(f) = \frac{S_2(f)}{S_1(f)} = \frac{G_2(f)}{G_1(f)} \tag{3.13a}$$

$$Amplitude \equiv |T_{12}(f)| = \frac{|S_2(f)|}{|S_1(f)|} \tag{3.13b}$$

$$Phase \equiv \theta_{12}(f) = ArcTan\left(\frac{\mathrm{Im}(T_{12}(f))}{\mathrm{Re}(T_{12}(f))}\right). \tag{3.13c}$$

The phase value, θ_{12}, was close to 0, but not null. For a phase shift of 3 °or 50 mrad, the rejection factor of the coherent noise evaluated by (Equation 3.12) is around 5%,which are equivalent toa rejection factor of 20. Thus, an external coherent noise level of 50 pT/√Hz is reduced to 2.5 pT/√Hz as measured (*cf.* figure 3.7).

In Figure 3.9, we show signal amplitude contours as a function of time and frequency for S_1, S_2, T_{12} and θ_{12}. In Figure 3.9 (a) and 3.7 (b), one can clearly see fluctuations in S_1 and S_2 as a function of time. Such fluctuations are characteristics of environmental noises. However, in Figure 3.9 (c) and 3.7 (d), the amplitude and phase

contours are much more stable for the differential mode as expected. Accordingly, if a small AC magnetic signal is applied, then it will be more easily distinguishable. Clearly, the ME elements as simple magnetic sensors show their ability to reject magnetic noise source in open environment with respect of presented experimental area. Results foreshadow the development of gradiometers. Indeed, the dynamic range and spatial rejection has not been considered in this work.

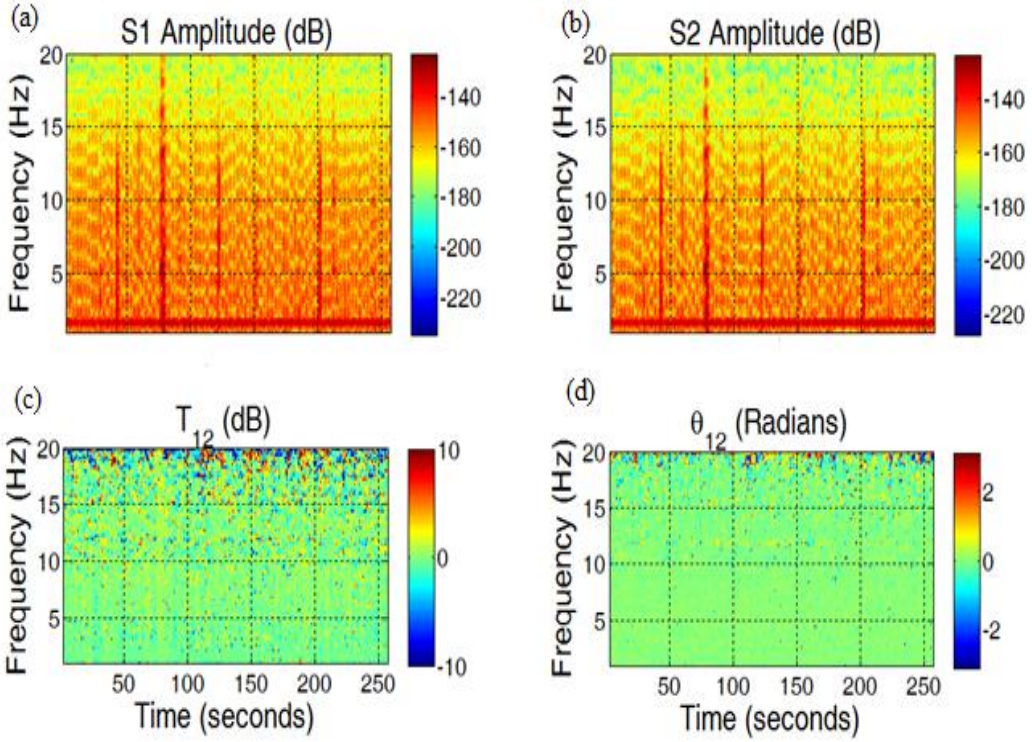

Figure 3.9 Example of contour diagrams of signal amplitudes for (a) S_1, (b) S_2 sensors, (c) T_{12} and (d) signal phase θ_{12} as a function of time and frequency.

In order to compare these results to the intrinsic noise of the ME differentiator output, we performed measurements of the equivalent magnetic noise of the individual ME sensors in a magnetically shielded environment. The mu-metal chamber was also placed on a vibration isolation platform. The output signals were acquired and recorded by a datalogger in units of V/√Hz, which was converted into units of T/√Hz using the transfer functions of each sensor. This yields

$$Conversion\ factor = \frac{\alpha_{ME}\left(pC/Oe\right)}{1\left(pC/V\right)} \qquad (3.14a)$$

and

$$Noise\ floor\left(T/\sqrt{Hz}\right) = \frac{Noise\ floor\left(V/\sqrt{Hz}\right)}{Conversion\ factor} \times 10^{-4}. \qquad (3.14b)$$

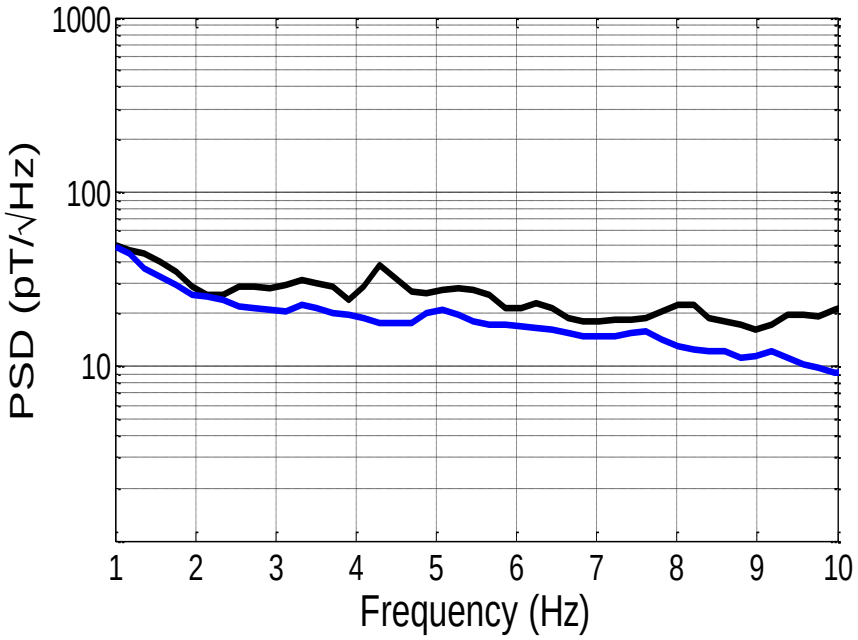

Figure 3.10. Magnetic spectral noise density curve (blue) of S_1 in a magnetic shielding chamber compare to the estimated intrinsic magnetic spectral noise density of the differentiator (black).

A representative result of these measurements is shown in Figure 3.10. In this figure, the noise floor can be seen to be about 20 pT/√Hz for $2 < f < 5$ Hz, increasing some and decreasing slightly at lower and higher frequencies, respectively. It is important to note that the noise floor for the individual sensors was close to the estimated internal noise floor of the differentiator (see Figure3.7).

These results clearly demonstrate that the rejection efficiency of the system is, in the given area and associated to the sensed magnetic field range, about a factor of 20 and

mainly limited by the incoherent noise and phase shift discrepancy between the individual ME sensors.

3.2.4 Summary of this section

A functional ME differentiator has been shown to be capable to be constructed from a pair of parallel ME sensors. Measurements demonstrated a good coherency between two sensor signals S_1 and S_2, enabling a common mode rejection of environmental noise simply by the difference (S_1 - S_2). The results show that the noise rejection of the system limited by the internal incoherent noise and discrepancy between ME sensors in the given experimental set-up. Advancements in lowering the equivalent magnetic noise floor and phase shift of individual ME sensors will thus be beneficial to ME gradiometer development. Accordingly, my investigation demonstrates the feasibility of a passive, low power battery operated hybrid uncooled environmental magnetic noise rejection system with high sensitivity in an open environment, which is the first step to the development of gradiometers. Further works will be devoted to analyze and characterize this differential measurement as a gradiometric measurement to give the limit of the present design.

3.3 High Detection Sensitivity of Gradiometer

Magnetometers are an important technology for many applications: such as traffic surveillance, detection of unexploded ordnances, metallic contaminant detectors, mapping of Earth's field. [16-19] These applications are based on the magnetometer's ability to sense perturbations (i.e., magnetic anomalies) in background Earth's geomagnetic field. An advantage of ME sensor technology is that it is nearly passive, requiring very little power only for a low noise charge amplifier detection circuit. Thus, ME sensor units are small and passive Magnetometer with the capability of pico-Tesla sensitivity at low frequencies while operated at room temperature.

Although some investigations have shown that ME sensors have pico-Tesla sensitivity, it must be kept in mind that these studies were performed in magnetically shielded chambers mounted on vibration absorbing platforms. A critical issue with respect to real world applications is their performance in an open environment: reduced signal-to-noise ratio (SNR) is maybe the most difficult challenge for ME magnetometer

applications in such situations. [20, 21] To date, there have been no investigations of the performance of ME magnetometer for magnetic target detection in such open environments. To circumvent these difficulties of open environment magnetic detection, we investigated ME tensor Gradiometry. A magnetic gradiometer obtains the difference signal between two magnetometer measurements, and then normalized that difference with respect to the sensor separation: this then excludes homogeneous background noise from the measurements, resulting in a good operational SNR. [1, 2] Here, we present the realization of high detection sensitivity for a Metglas/PMN-PT based ME gradiometer sensor system, via a giant ME effect and gradiometer noise rejection technique.

3.3.1 Experimental procedures

The ME laminate heterostructures used in this study were comprised of one PMN-PT piezoelectric fiber layer epoxy-ed between two Metglas magnetostrictive layers. The four equal ME laminates used in this study were fabricated and characterized in the same method. Both faces of a 4 cm × 1 cm × 200 μm PMN-PT (Ceracomp Co., Ltd., Korea) fiber bundle were affixed with Kapton® patterns of interdigited electrodes that yielded a symmetric poling of the PMN-PT fibers in a back-to-back configuration along their length axes. [22] Using the same epoxy, tri-layers of 8 cm × 1 cm × 22 μm Metglas foils (Vitrovac 7600F, Vitrovac Inc. Hanau, German) were attached onto both sides of the outer surfaces of the Kapton® sheets. [5] The ME sensor charge output was then measured via a low noise charge amplifier (CA) with a gain factor of 1V/pC over 0.6-10 Hz frequency range, yielding a voltage signal proportional to an incident B-field. [9] The ME laminate and charge amplifier circuit were packaged into an electromagnetic interference (EMI) shielded enclosure. Permanent magnets were employed at each end of the enclosure to provide DC magnetic bias H_{dc}.

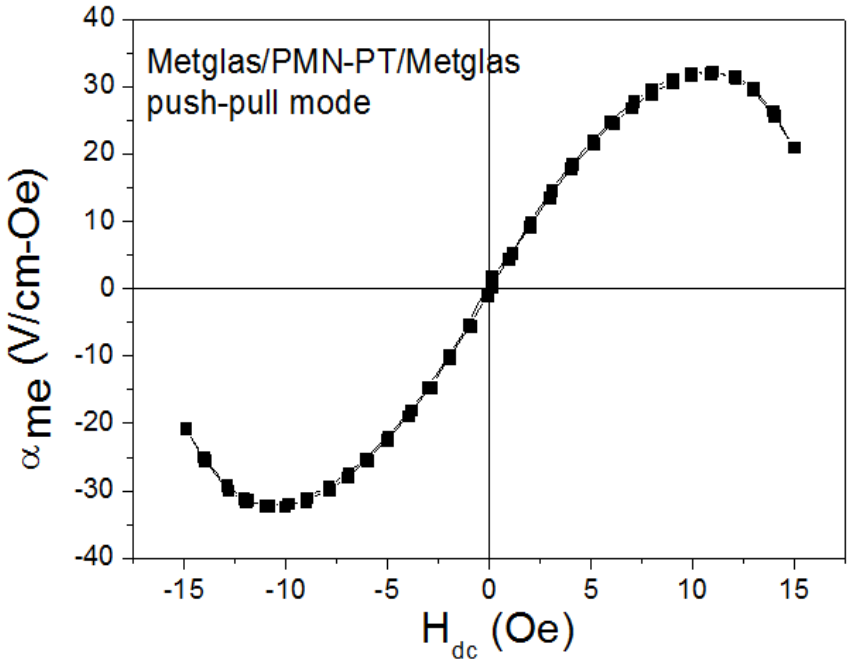

Figure 3.11 The ME voltage coefficient α_{ME} as a function of the static magnetic field H_{dc} for Metglas/PMN-PT.

First, a lock-in amplifier method was used to measure the ME voltage coefficient α_{ME} for Metglas/PMN-PT as a function of H_{dc} applied along the longitudinal axis of the ME laminates. A pair of Helmhotz coils were driven by a lock-in amplifier (SR 850) to produce an AC magnetic field of H_{ac}=1 Oe at f=1 KHz. Figure 3.11 shows α_{ME} as a function of H_{dc} for a Metglas/PMN-PT laminate. The value of α_{ME} increased with increasing H_{dc} reaching a maximum of 32 V/cm-Oe, and then subsequently decreased as H_{dc} was further decreased. The ME charge coefficient of these four laminates were 2010 pC/Oe, 2100 pC/Oe, 2017 pC/Oe and 2240 pC/Oe. Bi-axial ME sensor systems consisting of two single-axis ME sensor units mutually perpendicular to each other in a "+" configuration were constructed, as illustrated in Figure 3.12.

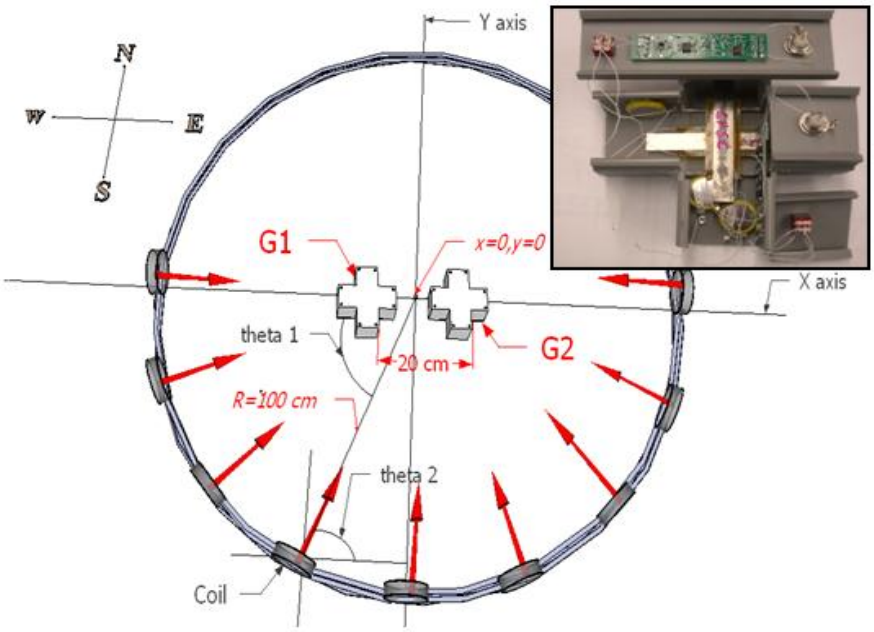

Figure 3.12 Diagram of experimental layout as the coil position is rotated from 0 to 180 degree for our two biaxial ME magnetometers. The inset is a photo of a prototype biaxial ME magnetometer.

Measurements were conducted in an open environment (magnetically unshielded) in our laboratory. Figure 3.12 shows the experimental configuration for the gradiometer measurements. A matched pair of ME gradiometer sensors G 1 and G 2 were oriented parallel to the geomagnetic north with a center-to-center separation distance of D=0.2 m. A magnetic dipole, represented by a solenoid coil driven by a signal generator, produced an AC sine wave signal at 7 Hz. Let $\boldsymbol{R}$ be the 2D x-y plane position where the coil was placed. The coil was rotated along the perimeter of a circle with a radius R= $|\boldsymbol{R}|$=1 m centered on the sensor pair. The radial position of the coil (θ1) and its orientation relative to the x axis (θ2) were controlled such that the magnetic dipole pointed towards the center of the gradiometer array. The field was studied as the coil was rotated from 0 to 180 °. The output signals from the sensors in the time-domain were collected via a CR5000 datalogger and sampled at a rate of 100 Hz and a 1 V dynamic range. The magnetic field strengths at each testing point were recorded in 100 seconds, and a fast Fourier transform (FFT) was then performed via Matlab to calculate the power spectral density (PSD) for the two output signals as a function of frequency.

3.3.2 Results

Figure 3.13 gives the background noise PSD plots of our gradiometer over a frequency range of $1<f<10$ Hz. The data show that the y-component of the sensors ($G1_y$ and $G2_y$) had nearly identical equivalent background noises of 300 pT/√Hz over this bandwidth, increasing some and decreasing slightly at lower and higher frequencies respectively. Direct subtraction of two magnetic sensors output signals can reject the coherent environmental noise source and yield the gradiometer noise floor. [23]In Figure 3.13, the differential noise floor for the y-axis sensors ($G1_y$ - $G2_y$) was determined to be 20 pT/√Hz for $1<f<10$ Hz. One can also see in this figure that the individual sensor noise floor for the x-component sensors ($G1_x$ and $G2_x$) was about 110 pT/√Hz, and their differential output ($G1_x$ - $G2_x$) was about 40 pT/√Hz over the same bandwidth. It is important to note that the equivalent gradiometer noise floor of the y-axis and x-axis sensors were about 23.5dB and 8.8dB respectively lower than that of the corresponding individual sensors. This enables enhanced detection sensitivity by gradiometers, and will contribute to a higher SNR during signal detection.

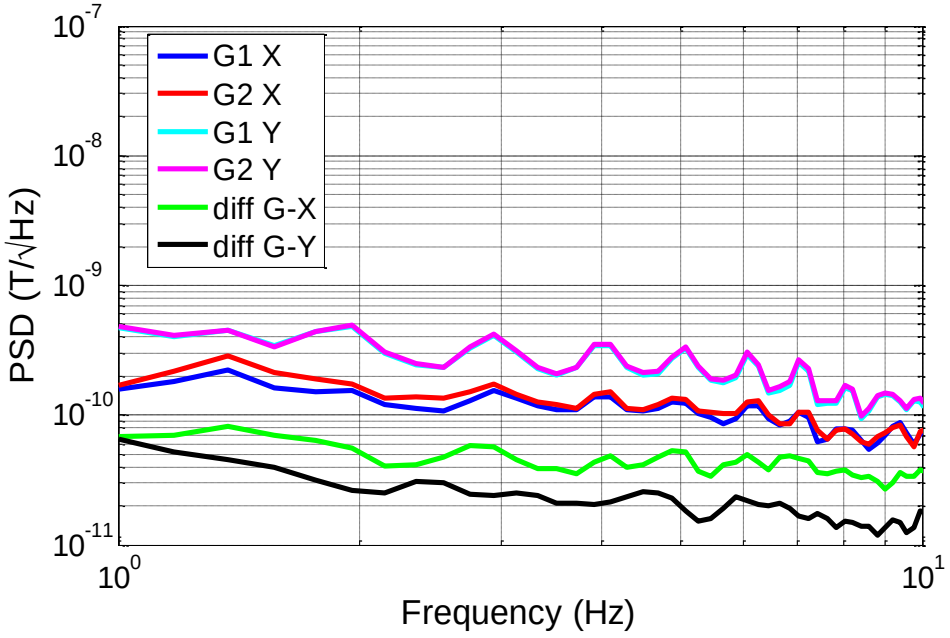

Figure 3.13 Power spectral density curves of the background noise for sensors $G1_x$ and $G2_x$ (blue and red curves respectively), sensors $G1_y$ and $G2_y$ (cyan and pink curves respectively), and gradiometric noise floor signals diff (G_x) and diff (G_y) (green and black curves respectively).

Figure 3.14(a) shows the coherence $C_{x_1x_2}(f)$ between $G1_x$ and $G2_x$ which was slightly lower than unity: the transfer functions $T_{12}(f)$ of S_1 and S_2, which are the Fourier transforms of $G1_x$ and $G2_x$, were evaluated by their relative ratios as defined as: $T_{12}(f)=\frac{S_2(f)}{S_1(f)}$. The smoothing transfer function amplitude $|T_{12}(f)|$ is shown in Figure 3.14(b), can be given as: $Amplitude \equiv |T_{12}(f)| = \frac{|S_2(f)|}{|S_1(f)|}$. The amplitude ratio, $|T_{12}(f)|$, was also close to unity with ± 0.1 variance. Figure 3.14(c) shows phase discrepancy $\theta_{12}(f)$ between S_1 and S_2, which can be estimated as: $Phase \equiv \theta_{12}(f) = ArcTan\left(\frac{\mathrm{Im}(T_{12}(f))}{\mathrm{Re}(T_{12}(f))}\right)$.

For matched sensors, when $|T_{12}| = 1+\varepsilon$ with $\varepsilon << 1$ and $\arg(T_{12}) = \theta << 1$, the coherent noise rejection efficiency is: [23]

$$Rejectionefficiency = \frac{1}{\sqrt{\varepsilon^2+\theta^2}}. \qquad (3.15)$$

In Figure 3.14 (c), we can see that the absolute value of phase shift was about 20 °(or 0.39 rad), which contributes to a rejection efficiency of 7.7dB together with the amplitude ε factor effects. Thus, the equivalent gradiometric noise floor was about 7.7dB lower than that of the individual sensors for $G1_x$ and $G2_x$ (see Figure. 3.13).

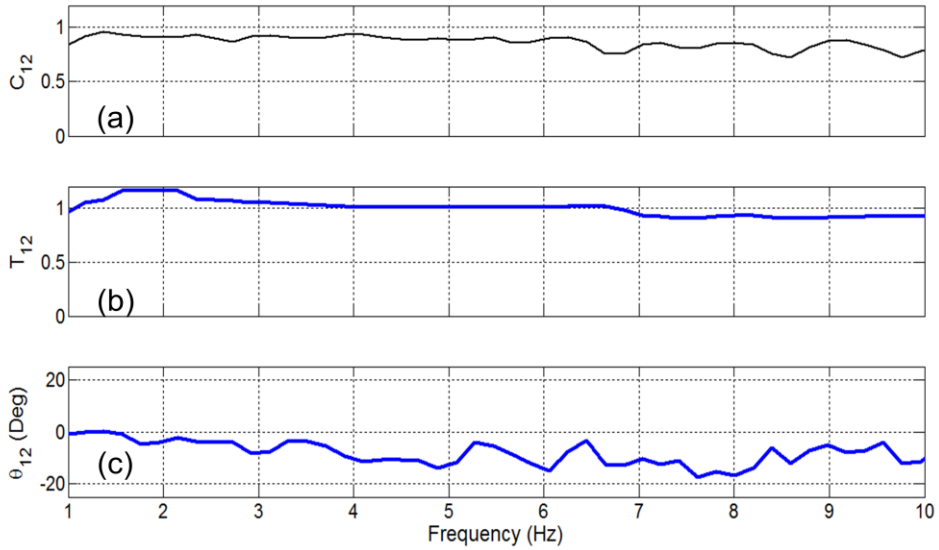

Figure 3.14 (a) Coherence value, (b) relative amplitude difference and (c) phase shift for $G1_x$ and $G2_x$.

The coherence $C_{y_1y_2}(f)$ between the y-axis sensors $G1_y$ and $G2_y$ was analyzed similarly, as shown in Figure 3.15 (a). The value of $C_{y_1y_2}(f)$ remained constant at $C_{y_1y_2}(f)$= 1, indicating better coherence than that of $C_{x_1x_2}(f)$. Figure 3.15(b) shows the absolute amplitude ratio which was also nearly unity, which shows that $G1_y$ and $G2_y$have nearly identical magnetic field strengths. The value of $\theta_{12}(f)$ shown in Figure 3.15(c) reveals a phase shift of $4°$ (0.07 rad). By employing Eq. (4), we can determine that the rejection efficiency for $G1_y$ and $G2_y$was 23dB, which is confirmed by Figure 3.13 which had a gradiometer noise floor of 20 pT/√Hz from an individual sensor noise level of 300 pT/√Hz.

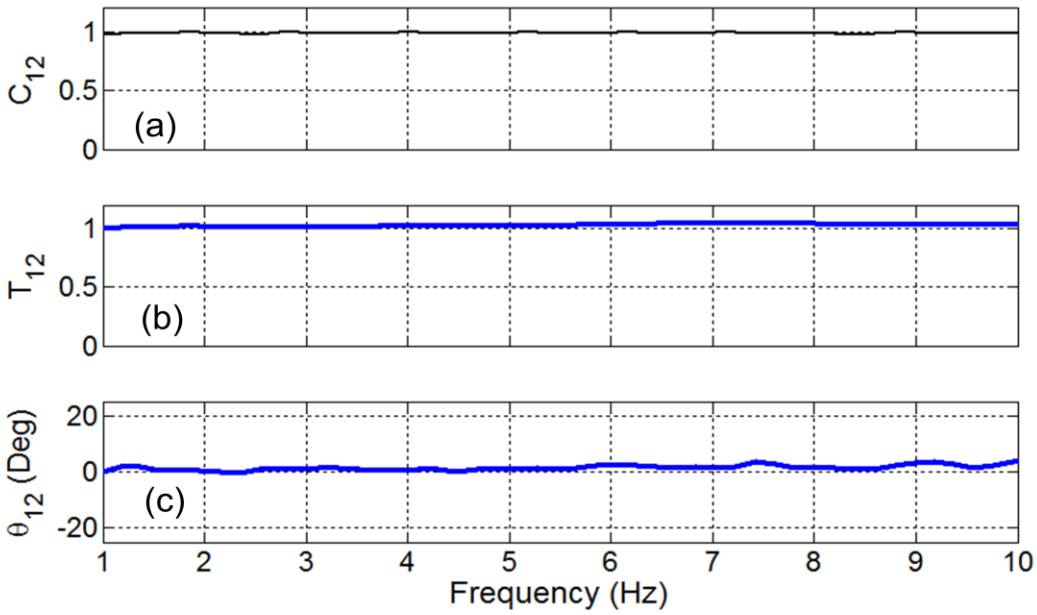

Figure 3.15 (a) Coherence value, (b) relative amplitude difference and (c) phase shift for $G1_y$ and $G2_y$.

At a frequency of *f*=7 Hz, when the angle between the target source and the central point of the gradiometers was θ1=0°, the induced magnetic fields on $G1_x$ and $G2_x$ were maximum as shown in Figure 3.16(a). In this figure, it can be seen that the gradiometer noise floors remained at a level lower than that of the individual sensors. If a small magnetic anomaly was nearby (assuming a magnetic amplitude of 100 pT in the quasi-static frequency domain), it would readily be sensed by the ME gradiometer but not the individual ME sensors. The magnetic strengths of $G1_y$ and $G2_y$ sensors were smaller than that along the x-axis as they are perpendicular to the dipole. Under ideal conditions when the sensor can be treated as a physical point, the $G1_y$ and $G2_y$ sensors should not have a magnetic response to the dipole at θ1=0°. When the dipole was moved to θ1=30°, it can be seen that the induced magnetic fields on the $G1_y$ and $G2_y$ sensors increased whereas that of $G1_x$ and $G2_x$ slightly decreased, as shown in Figure 3.16 (b). For θ1=90°, $G1_y$ and $G2_y$ had nearly the same induced magnetic field strength (*f*=7 Hz) due to a strong coherence to the same source (see Figure 3.16(c)). The induced magnetic field amplitudes on $G1_x$ and $G2_x$ should be the same, due to the same relative distances to the dipole. However, $G1_x$ and $G2_x$ exhibited a discernable variance in the output signals, resulting from an inherent difference due to variations in sensors phases (see Figure. 3.14). The

magnetic fields at other points (θ1= 45°, 60°, 120°, 135°, 150° and 180°) were also recorded and signal processing conducted to compute the PSD amplitude.

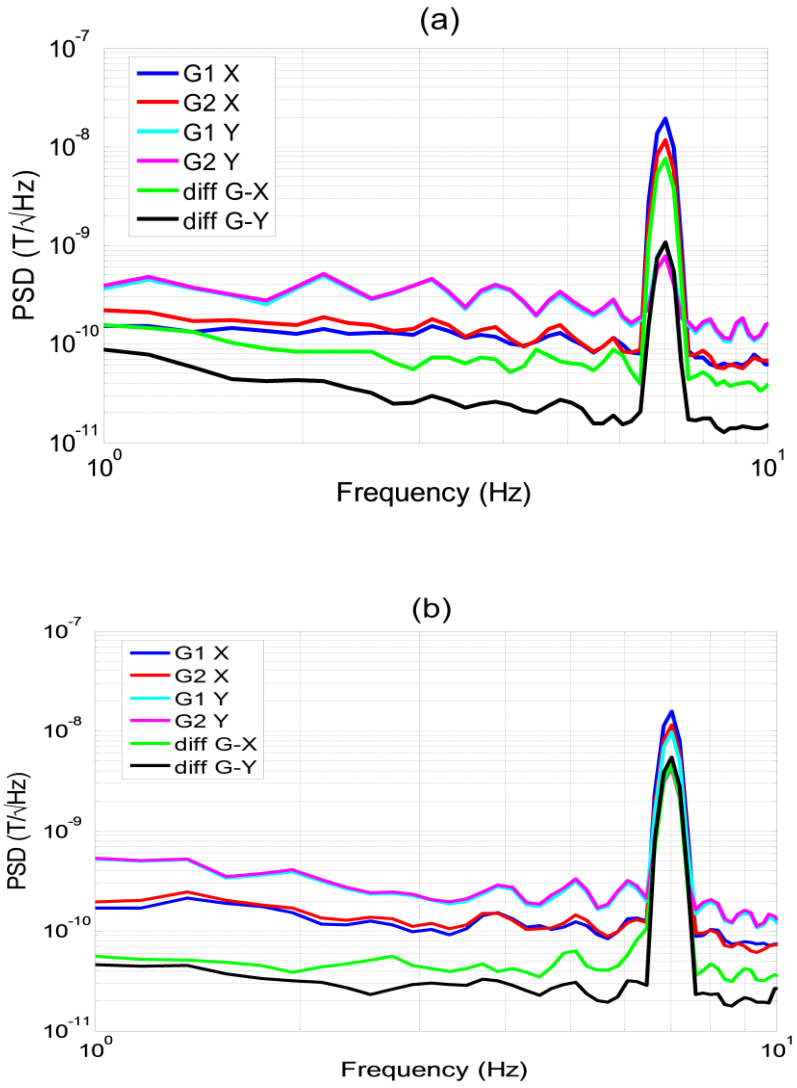

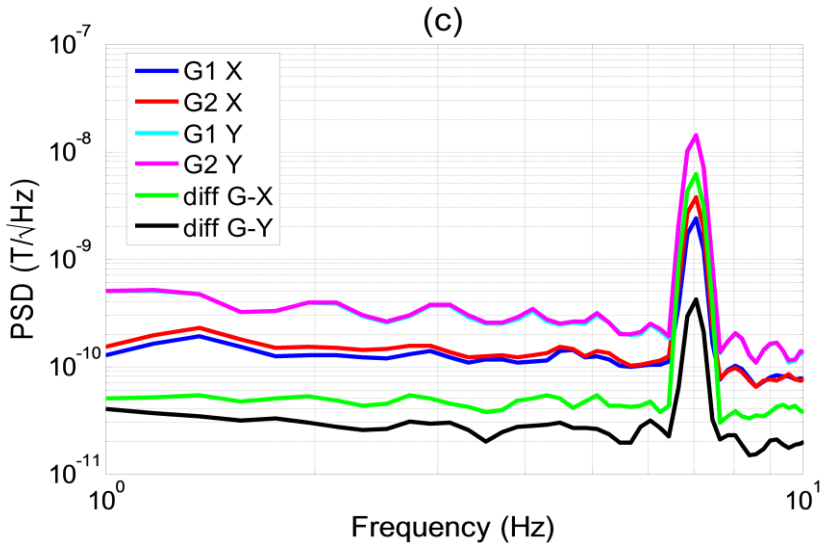

Figure 3.16 Power spectral density curves at (a) θ1=0°, (b) θ1=30°, (c) θ1=90° for sensor $G1_x$ and $G2_x$ (blue and red curves respectively), sensors $G1_y$ and $G2_y$ (cyan and pink curves respectively), and gradiometric noise floor signals diff (G_x) and diff (G_y) (green and black curves respectively).

With the purpose to determine the precision of our 2-axis gradiometers ability to locate a target, the induced field intensity on the sensors and gradiometer were studied, and the results compared with predictions by Matlab. Figure 3.17(a) shows the comparison between the observed RMS magnetic signals for the x-axis sensors ($G1_x$ and $G2_x$) and their predicted counterparts (P ($G1_x$) and P ($G2_x$)). From the data we can see that the observed results of $G1_x$ and $G2_x$ match well with the predicted values. The RMS difference between the observed gradiometer noise floor diff (G_x) and the predicted gradiometer noise floor diff P(G_x) was 1.41 nT. The baseline of the gradiometer is 0.2m, so the x-axis gradiometer sensors error was about 7.05 nT/m. The ratio of the 1.41nT error and the 19.44 nT average field, when the dipole was parallel to the x-axis sensors, yields an error estimate of 7.2 %. The evaluation for the y-axis sensor errors were estimated similarly as shown in Figure 3.17(b). The obtained gradiometer noise floor had a typical sine waveform with a 0.603 nT error relative to the simulation representing a gradiometer error of y-axis sensors of 3 nT/m. This error of 0.603 nT with an AC source field of 14.15 nT vertical to the baseline of the sensors (dipole moment parallel to y-axis sensors) yields a relative error of 4.2 %.

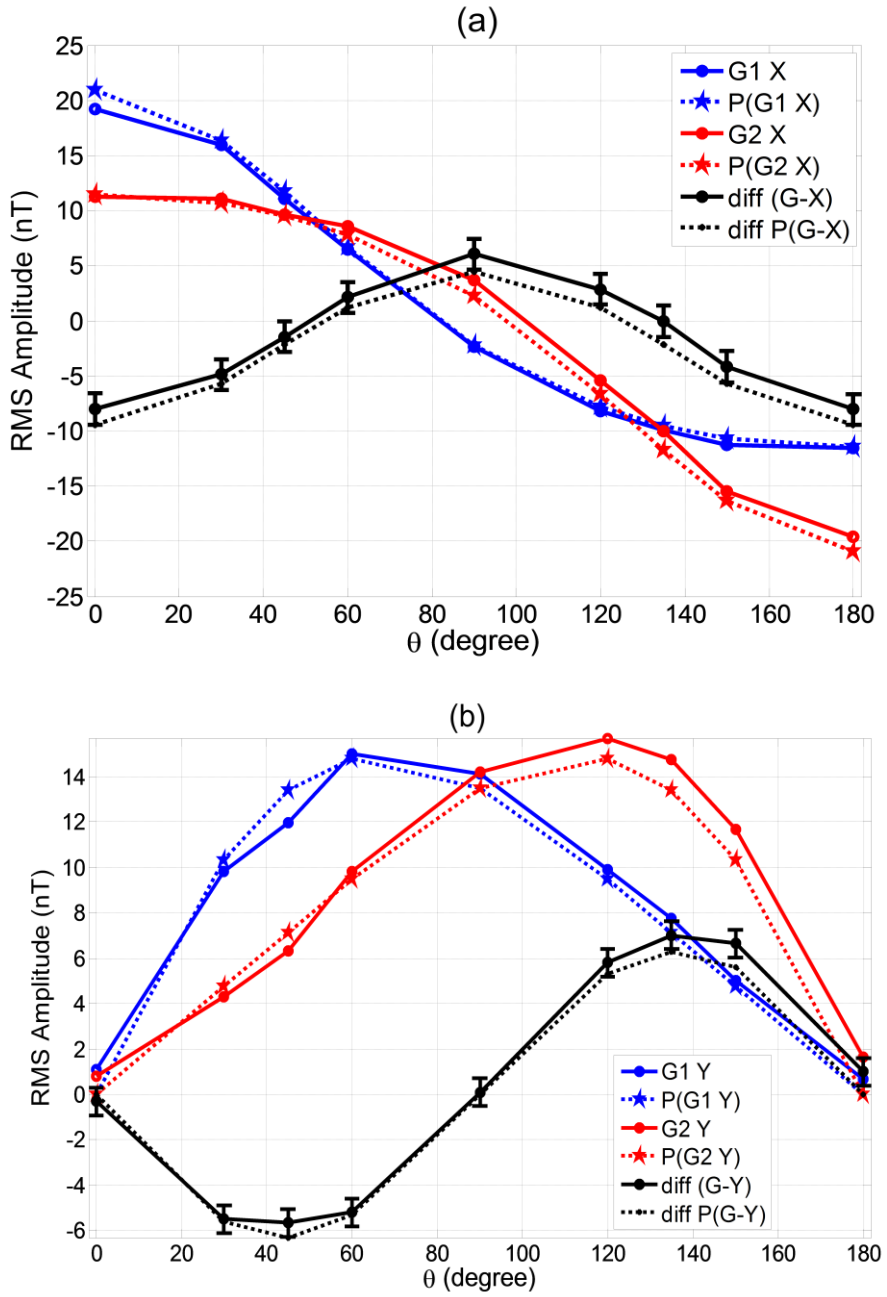

Figure 3.17 RMS values for (a) sensors $G1_x$ and $G2_x$ with observed amplitudes (blue and red solid curves with solid cycle marker respectively), predicted amplitudes (blue and red doted curves with star marker respectively), measured gradiometric noise floor signals diff (G_x) (solid back curve with variance bar), and predicted gradiometric noise floor diff P (G_x) (dotted back curve); (b) sensors $G1_y$ and $G2_y$ with observed amplitudes (blue and red solid curves with solid cycle marker respectively), predicted amplitudes (blue and red doted curves with star marker respectively), measured

gradiometric noise floor observed signals diff (G_y) (solid back curve with variance bar), and predicted gradiometric noise floor diff P (G_y) (dotted back curve).

3.3.3 Summary of this section

A bi-axial ME gradiometer sensors consisting of Metglas/PMN-PT fiber laminates are viable for AC magnetic dipole detection with high detection sensitivity. Gradiometric noise analysis showed that a direct gradiometer noise rejection method can remove the homogenous environmental noise between two parallel sensors orientated in the same direction, leading lower detection limit. Experimental results have confirmed the predictions, and we show that the ME sensors are capable of precisely detecting magnetic targets with a measurement error of only 7.2% and 4.2% along the x- and y-components of the gradiometer.

Reference:

[1] R. E. Bracken and P. J. Brown, "Reducing Tensor Magnetic Gradiometer Data for Unexploded Ordnance Detection," *Scientific Investigations Report,* 2005.

[2] A. V. Veryaskin, "Magnetic gradiometry a new method for magnetic gradient measurements," *Sensor and Actuators A* vol. 91, pp. 233-235, 2001.

[3] W. M. Wynn, "Magnetic dipole localization with a tensor gradiometer: A rigorous analysis including relative motion."

[4] A. S. B. Ginzburg, L. Frumkis, B.Z. Kaplan, N. Salomonski, "Investigation of advanced data processing technique in magnetic anomaly detection systems," presented at the 1st International Conference on Sensing Technology, Palmerston North, New Zealand, 2008.

[5] R. Stolz, V. Zakosarenko, M. Schulz, A. Chwala, L. Fritzsch, H.-G. Meyer, and E. O. KÖstlin, "Magnetic full-tensor SQUID gradiometer system for geophysical applications," *The Leading Edge,* vol. 25, 2006.

[6] M. Janosek, P. Ripka, F. Ludwig, and M. Schilling, "Single-core fluxgate gradiometer with simultaneous gradient and homogeneous feedback operation," *Journal of Applied Physics,* vol. 111, p. 07E328, 2012.

[7] E. Pulz, K.-H. Jäckel, and H.-J. Linthe, "A new optically pumped tandem magnetometer principles and experiences," *Measurement Science and Technology,* vol. 10, pp. 1025-1031, 1999.

[8] J. Vyhnánek, M. Janošek, and P. Ripka, "AMR gradiometer for mine detection," *Sensors and Actuators A: Physical,* 2012.

[9] B. Ullrich, G. Kaufmann, R. Kniess, H. Zoellner, M. Meyer, and L. Keller, "Geophysical Prospection in the Southern Harz Mountains, Germany: Settlement History and Landscape Archaeology Along the Interface of the Latène and Przeworsk Cultures," *Archaeological Prospection,* vol. 18, pp. 95-104, 2011.

[10] J. McGuirk, G. Foster, J. Fixler, M. Snadden, and M. Kasevich, "Sensitive absolute-gravity gradiometry using atom interferometry," *Physical Review A,* vol. 65, 2002.

[11] J. Das, J. Gao, Z. Xing, J. F. Li, and D. Viehland, "Enhancement in the field sensitivity of magnetoelectric laminate heterostructures," *Applied Physics Letters,* vol. 95, p. 092501, 2009.

[12] Z. P. Xing, J. Y. Zhai, S. X. Dong, J. F. Li, D. Viehland, and W. G. Odendaal, "Modeling and detection of quasi-static nanotesla magnetic field variations using magnetoelectric laminate sensors," *Measurement Science and Technology,* vol. 19, p. 015206, 2008.

[13] J. Bendat and A. Piersol, *Random Data: Analysis and Measurement Procedures*, 4th ed.: WILEY, 2010.

[14] L. K. J. V. J. Briaire, "Uncertainty in Gaussian noise generalized for cross-correlation spectra," *J. Appl. Phys,* vol. 84, pp. 4370 - 4374, 1998.

[15] P. Welch, "The Use of Fast Fourier Transform for the Estimation of Power Spectra: A Method of Time Averaging over Short Modified Periodograms," *IEEE Trans. Audio and Electroacoustics,* vol. 15, pp. 70-73, 1967.

[16] T. H. A. Salem, J.K. Asahina, K. Ushijima "Detection of unexploded ordnance (UXO) using marine magnetic gradiometer data," *Exploration Geophysics,* vol. 36, pp. 97-103, 2005.

[17] E. Sifuentes, O. Casas, and R. Pallas-Areny, "Wireless Magnetic Sensor Node for Vehicle Detection," *IEEE Sensors Journal* vol. 11, 2011.

[18] S. Tanaka, T. Akai, M. Takemoto, Y. Hatsukade, T. Ohtani, Y. Ikeda, S. Suzuki, S. Adachi, and K. Tanabe, "Application of SQUID to magnetic contaminant detection," *Physica C: Superconductivity,* vol. 470, pp. 1507-1510, 2010.

[19] A. Chwala and T. M. R. IJsselsteijn, N. Oukhanski, T. Schüler, V. Schultze, R. Stolz, and H. G. Meyer, "Archaeometric prospection with high-Tc SQUID gradiometer," *IEEE TRANSACTIONS ON APPLIED SUPERCONDUCTIVITY,* vol. 13, 2003.

[20] J. Gao, J. Das, Z. Xing, J. Li, and D. Viehland, "Comparison of noise floor and sensitivity for different magnetoelectric laminates," *Journal of Applied Physics,* vol. 108, p. 084509, 2010.

[21] F. Li, F. Zhao, Q. M. Zhang, and S. Datta, "Low-frequency voltage mode sensing of magnetoelectric sensor in package," *Electronics Letters,* vol. 46, p. 1132, 2010.

[22] J. Zhai, Z. Xing, S. Dong, J. Li, and D. Viehland, "Detection of pico-Tesla magnetic fields using magneto-electric sensors at room temperature," *Applied Physics Letters,* vol. 88, p. 062510, 2006.

[23] Y. Shen, J. Gao, L. Shen, D. Gray, J. Li, P. Finkel, D. Viehland, X. Zhuang, S. Saez, and C. Dolabdjian, "Analysis of the environmental magnetic noise rejection by using two simple magnetoelectric sensors," *Sensors and Actuators A: Physical*, vol. 171, pp. 63-68, 2011.

Chapter 4:

ME SENSOR ARRAY IMAGING

4.1 Introduction

In order to enable ME sensors as a viable competitor for extremely sensitive low-level magnetic field detection, there is a critical need to further enhance its sensitivity especially in unshielded environments for end users. Recent studies have indicated that an array of m ME sensor units, either in serial or parallel mode, can significantly increase the sensitivity by a factor of √m. [1] To extend such approach from single "ME unit" to "ME array," the signal current level, noise level, and SNR for both parallel and serial arrangements of ME units into an array will be predicted.

4.1.1 Parallel mode

ME sensor units were employed and connected in a parallel fashion. Given that the signal responses of all these ME sensors are harmonic to the applied magnetic field *H* with the same ME charge coefficient, impedance and noise level, the response current signals can be directly added from each ME senor response, as follows:

$$I_{sP} = mj\omega\alpha_0(\omega)e^{-j\theta}H \quad (4.1)$$

The inherent noise, however, is not harmonic, and the terms cannot be simply added. While assuming that all the noise sources are uncorrelated, the total noise must be evaluated by a root-square sum of all noise contributions as [4, 5]

$$i_{nP} = \sqrt{i_{n1}^2 + i_{n2}^2 + \cdots\cdots + i_{nm}^2} = \sqrt{m}i_n (4.2)$$

The equivalent model is shown in Figure 4.1, which results in the SNR of ME array in parallel as

$$SNR_P = \frac{\sqrt{m}j\omega\alpha_0(\omega)e^{-j\theta}H}{i_n} (4.3)$$

The above analysis shows that the signal current increases by a factor of m, but the noise current increases by $\sqrt{m}$. Together, they increase the SNR of parallel mode by a factor of $\sqrt{m}$.

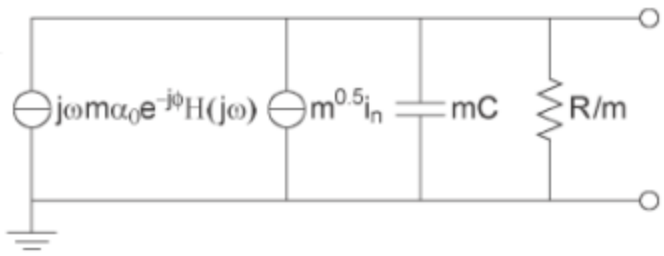

Figure 4.1 Equivalent circuit of ME array in parallel mode and (b) serial mode. [1]

4.1.2 Serial mode

In this case, the voltage source model was used for convenience in analysis. The total voltage responses acquired are as follows: [1]

$$V_{ss} = mj\omega\alpha_0(\omega)e^{-j\theta}H \cdot R/(1 + j\omega RC) \quad (4.4)$$

According to [4, 5], the voltage noise level must be computed as:

$$v_{nS} = \sqrt{v_{n1}^2 + v_{n2}^2 + \cdots\cdots + v_{nm}^2} = \sqrt{m}i_nR/(1 + j\omega RC) \quad (4.5)$$

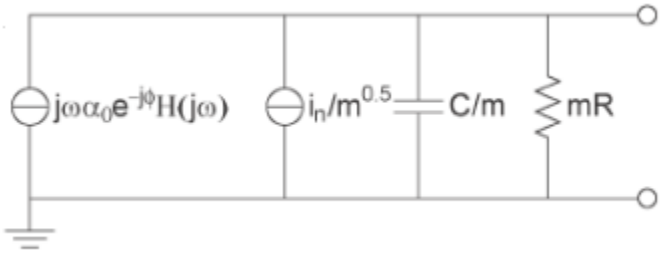

Figure 4.2 Equivalent circuit of ME array in serial mode. [1]

This voltage source model can be converted into a current source model by the Norton Theorem as shown in Figure 4.2. The signal current (I_{ss}) and noise current level (i_{nS}) are:

$$I_{ss} = j\omega\alpha_0(\omega)e^{-j\theta}H \quad (4.6)$$

$$i_{nS} = \frac{i_n}{\sqrt{m}} \quad (4.7)$$

Finally, the SNR is:

$$SNR_S = \frac{\sqrt{m}j\omega\alpha_0(\omega)e^{-j\theta}H}{i_n} \quad (4.8)$$

Eq. (4.6), (4.7) and (4.8) show that the signal current is unchanged by a serial arrangement of ME sensors, while the noise current is decreased by a factor of $\sqrt{m}$ which results in SNR being increased by a factor of $\sqrt{m}$.

This option opens up the possibility to employ ME sensor arrays (MESA) for efficient surveying of ranges. However, even if mitigation of sensor self-noise and enhanced sensitivity of the MESA can be achieved, external noise from the environment may prohibit MESA from detecting object signals in environments where shielding is impractical. One simply cannot shield out external noise without masking the signal in the environment. Rather, one can only optimize the detection for some specific measuring performances.

Here, we show a 4×4 MESA with higher sensitivity than a single sensor. When operated in an open environment, the magnetic noise of the four units in the array system were optimized reaching a noise floor of 15-16.8 pT/√Hz at *f*=1 Hz owing to their strong coherence, which was similar to that in a shielded environment. After making amplitude and phase corrections, a 22 dB common mode rejection was achieved between the array units and an optimizing beam. After employing an inverse variance weighting method, the noise floor for the array was found to be 8.2 pT/√Hz at *f*=1 Hz, yielding a noise rejection efficiency of 27 dB.

4.2 Integration

4.2.1 Single unit

A schematic of the ME tri-layer Metglas/PZT/Metglas laminate used for detection is shown in Figure 4.3. Five 180 μm PZT fibers (CTS, Albuquerque, NM) of length 4 cm and width 0.2 cm were oriented parallel to the longitudinal axis of the laminate. Thin interdigitated (ID) copper electrodes deposited of Kapton® sheets were attached to the top and bottom surfaces of the PZT fiber bundle using a two-part epoxy to obtain a push-pull mode configuration. [6] The ID electrode pattern allowed for symmetric poling of the piezoelectric fibers in a back-to-back pattern along their length axis. [7] Tri-layer 22 μm thick Metglas foils (Vitrovac 7600F, Vitrovac Inc. Hanau, German) were then cut to the widths and lengths of about 8 cm × 0.4 cm and affixed to the top and bottom surfaces of the Kapton® electrodes using the same epoxy as the piezoelectric core.

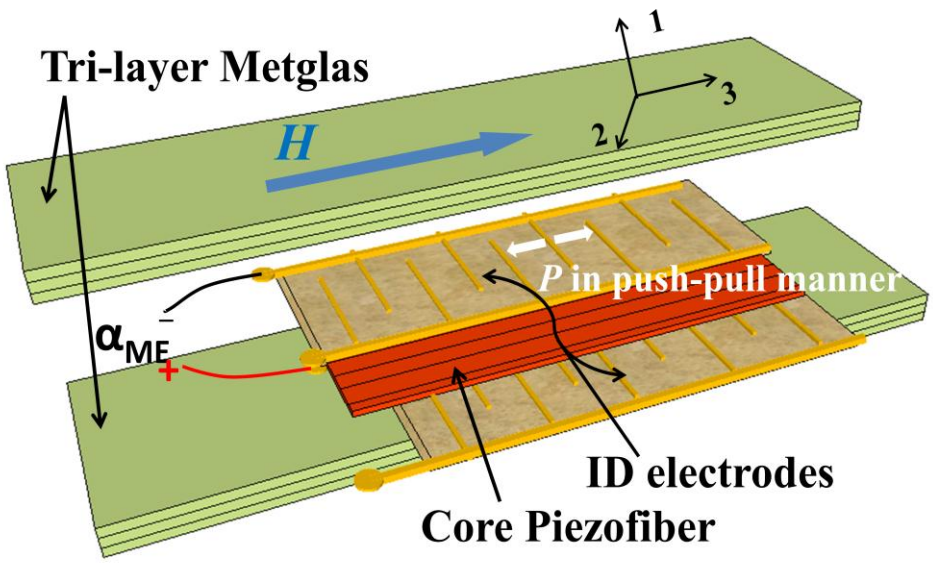

Figure 4.3 Schematic diagram of the Metglas/PZT ME laminate composite

The ME laminate composites and charge amplifier (CA) detection circuit were assembled into battery operated sensor detection units (see Figure 4.4 (a)) which were wrapped with thin aluminum sheets for shielding electric field interference. Permanent magnets placed at either end of the ME laminates were used to apply the H_{dc} bias along the longitudinal axis to the Metglas layers. Incorporation of the magnets allowed us to achieve the maximum ME value as well as the highest sensitivity to minute magnetic field AC variations. The transfer function of the CA is shown in Figure 4.4 (b). It had a frequency bandwidth of 0.6 Hz to 10 Hz, with a gain of about 1 V/pC in band.

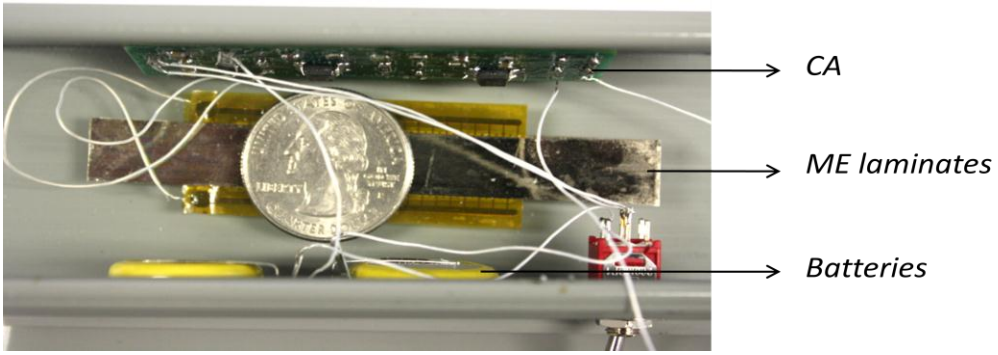

(a)

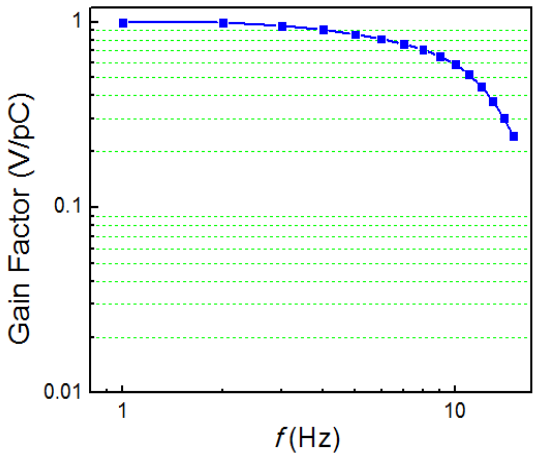

(b)

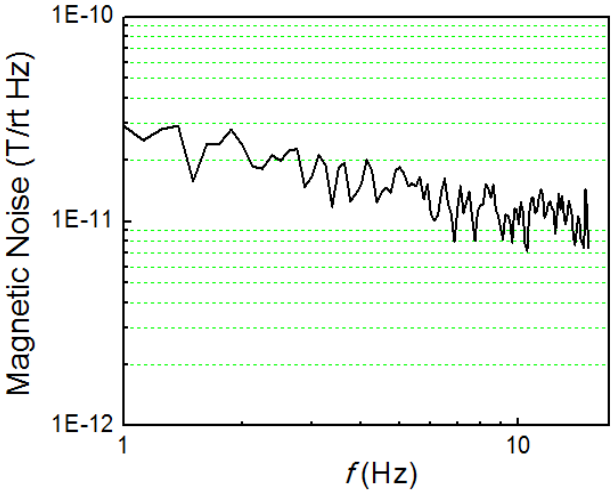

(c)

Figure 4.4 (a) Photograph of the prototype ME magnetometer; (b) Homogenous gain transfer function of ME composite (blue curve); (c) Equivalent magnetic spectral noise density curve (blue) of ME magnetometer in a magnetic shield.

The magnetic field sensitivity and equivalent input noise of the ME magnetometer system were characterized in a magnetically shielded environment at quasi-static frequencies (≤ 10 Hz). Sensor units were placed in a magnetically shielded mu-metal chamber which was lying on a vibration isolation platform. The output signals were acquired and recorded by a CR5000 Datalogger (Campbell Scientific, Inc.) in units of V/√Hz, which was subsequently converted into units of T/√Hz using the transfer function for each sensor.

$$Conversion\ factor = \frac{\alpha_{ME}\left(pC/Oe\right)}{transfer\ function\left(pC/V\right)} \tag{4.9a}$$

$$Noise\ floor\left(T/\sqrt{Hz}\right) = \frac{Noise\ floor\left(V/\sqrt{Hz}\right)}{Conversion\ factor} \times 10^{-4}. \tag{4.10b}$$

Figure 4.4 (c) shows the magnetic spectral noise density as a function of frequency. We can see that the ME sensor has a background noise less than 20 pT/√Hz at f>1Hz. This demonstrates that ME laminate sensors can achieve high levels of sensitivity at room temperature and in a passive mode of operation.

4.2.2 Array configuration

Figure. 4.5 (a) illustrates a schematic of the configuration of a 4×4 MESA comprised of four single ME sensor units (as shown in section 2.2.1), where each unit is composed of four ME laminates attached onto the walls of the solid plastic housing. The baselines between up-down and left-right sensors were both optimized to be 4 cm. Permanent magnets placed at either end of the four-sensor unit were used to apply the H_{dc} bias along the longitudinal axes to the Metglas layers of each unit. The ME laminate composites were made of tri-layer of Metglas/PZT-fiber/Metglas with a multi push-pull mode configuration. Each surface of a core 4 cm × 1 cm × 180 μm PZT (CTS, Albuquerque, NM) fiber bundle was affixed with thin interdigited (ID) electrodes deposited on Kapton® sheets by a two-part epoxy. The ID electrode pattern allows for symmetric poling of the piezoelectric fibers in a back-to-back pattern along their length axes. [8] Three layers of 8 cm × 1 cm × 22 μm Metglas foils (Vitrovac 7600F, Vitrovac Inc. Hanau, German) were then coupled to the upper and lower surfaces of the Kapton® electrodes using the same epoxy as for the piezoelectric laminate. Four ME laminate composites and charge amplifier (CA) detection circuit were assembled into battery operated sensor detection units wrapped with thin aluminum sheets for shielding electric field interference. We designed CAs with a transfer function of 1 V/pC and a frequency bandwidth of 0.6 <f < 10 Hz. A picture of a 4×4 MESA unit is shown in the inset of Figure 3(a), which consisted of four four-sensor units supported by a foam platform.

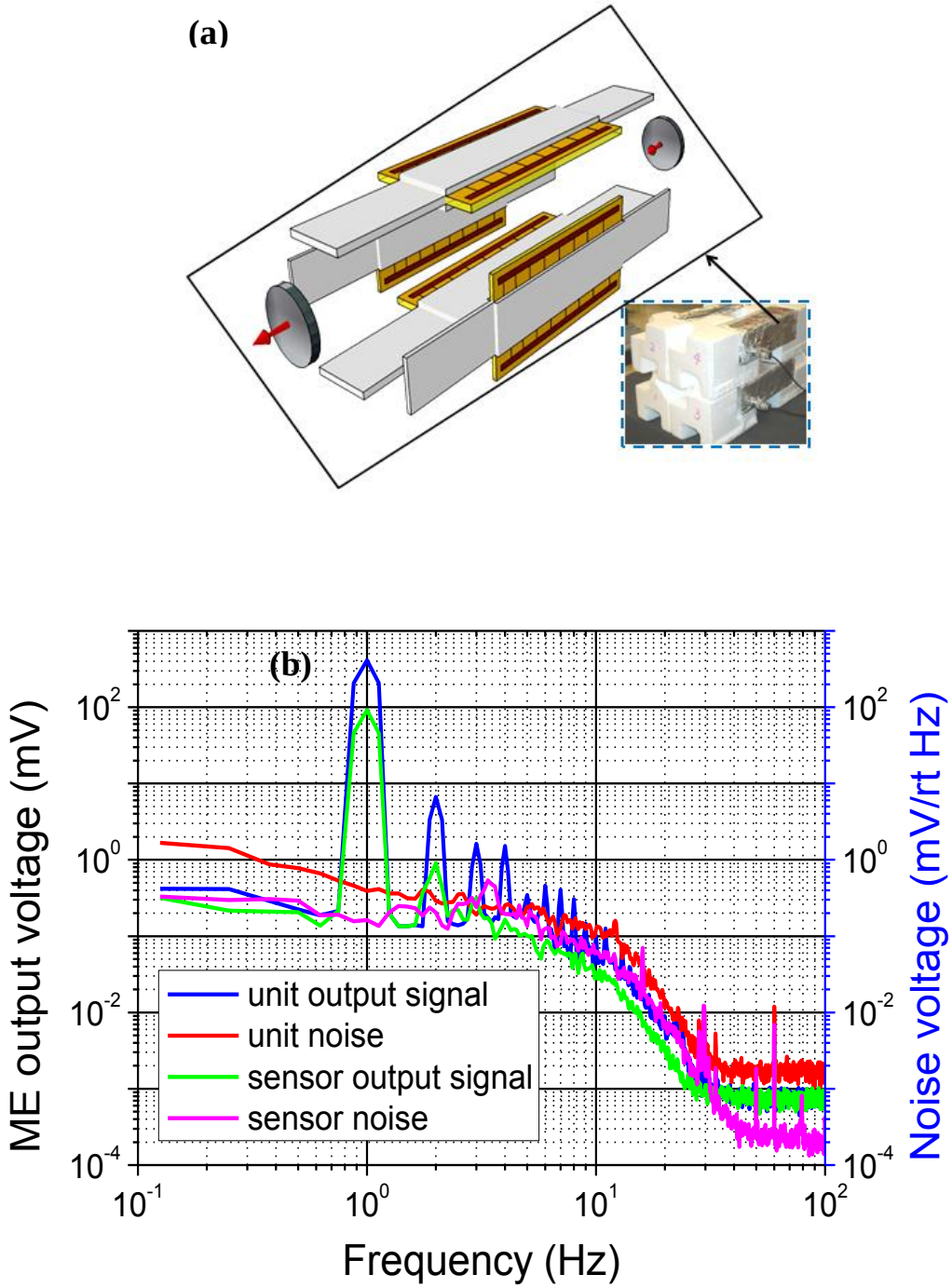

Figure 4.5 (a) Schematic representation of four-sensor unit model, including permanent magnetic H_{dc} bias. Insert: Picture of a four four-unit array mounted on a foam platform. (b) 4×4 MESA and single sensor ME output signal in response to a 1 Hz, 10 nT incident AC magnetic field and background voltage noise without intentional excitation.

The magnetic field sensitivity of a ME four-sensor unit was calculated using the transfer function by

$$Magnetic\ field\ sensitivity = \frac{V_{noise-f}}{V_{noise-ME}} * H_{ac-f} * SNR\ ; \qquad (4.11)$$

where $V_{\text{noise-}f}$ is the voltage noise of individual sensors at the frequency of interest (f=1 Hz), $V_{\text{noise-}ME}$ is the self-noise voltage output, $H_{\text{ac-}f}$ is an applied incident magnetic field driven by a custom-built Helmholtz coil, and SNR equals the minimal acceptable signal-to-noise ratio of 2. The sensitivity measurements were performed in a magnetically shielded mu-metal chamber which was also mounted onto a vibration isolation platform. Figure. 4.5(b) shows that at f=1 Hz the sensor unit had a background voltage noise of 0.4 mV/√Hz, and a 414 mV output signal in response to the 10 nT incident field. Based on equation (1), the sensitivity of the 4×4 MESA was determined to be 19.3 pT at 1 Hz. Following the same measurement procedure, individual sensors exhibited a background noise of 0.16 mV/√Hz and a 86.5 mV response signal, resulting in a 37 pT sensitivity at 1 Hz as shown in Figure. 4.5(b). These results demonstrate that the sensitivity enhancement between single sensor and four-sensor units is a factor of 2.

4.3 Signal Processing for Array Sensitivity

Figure. 4.6(a) shows a 300 second time history signal output from a four sensor unit which was placed in an open environment in our lab (unshielded). Note that the single 4 sensor units differ in signal amplitude by 10-15%. The signal output of each charge amplifier circuit were seemly superimposed on each other due to common environmental noise cluster sources. The Welch averaged power spectral density (PSD) of the output voltage signals are given in Figure. 4.6(b). From this figure, one can see that the units had a background equivalent magnetic noise level of 200 pT/√Hz at f=1 Hz, even though the sensor units had a sensitivity of 19.3 pT at f=1 Hz in a shielded environment. A beam was defined as the mean of a four sensor unit over a time series after post signal processing.

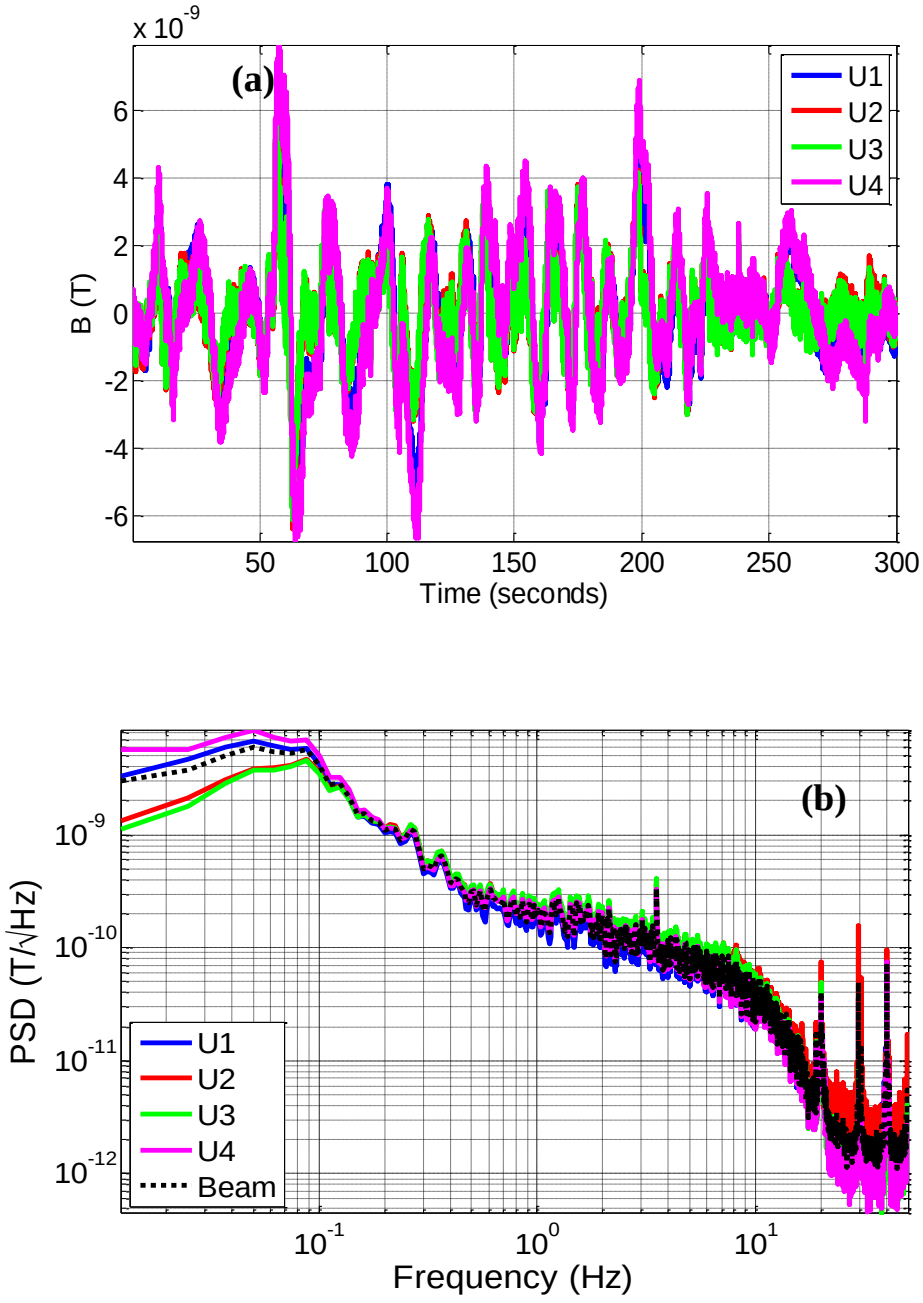

Figure 4.6 (a) Time-domain signal output of four four-sensor units; and (b) power spectra density of each unit and their averaged time-series beam after post processing

The unit self-noise was then estimated based on measuring the coherence of the output signals of each unit and the beam.[9, 10] These results are shown in Figure. 4.7(a), which implies that the units and their beam have a strong coherence at a near constant level of $C(f) \approx 1$over the frequency range of 0.6 <*f*< 7 Hz. A transfer function $T_{i,b}(f)$ (*i*=1, 2, 3

and 4) was then estimated for each unit to the initial beam. The magnitude of the transfer function represents the relative amplitudes ratios of the output signals, while the phase of the transfer function yields information about the time lag between the two output signals. [10]

Figure. 4.7(b) shows the phase and amplitude of the transfer function that matches each unit to the beam. The upper plot in Figure4.7(b) shows that the smoothing transfer function amplitude $|T_{i,b}(f)|$ varies between sensor units on the order of ±5 dB over the 1 <f< 10 Hz bandwidth. In the lower plot of Figure4.7(b), the phase variability between units is on the order of ± 0.5 radians (~28 degrees) for 1 <f< 10 Hz. It should be noted that units 2 and 3 had several strong phase variability peaks above 5 Hz. The units were previously adjusted for an average amplitude transfer function of unity in the 0.5 <f < 2 Hz bandwidth, as the equivalent noise floor in the low frequency domain was of more concern.

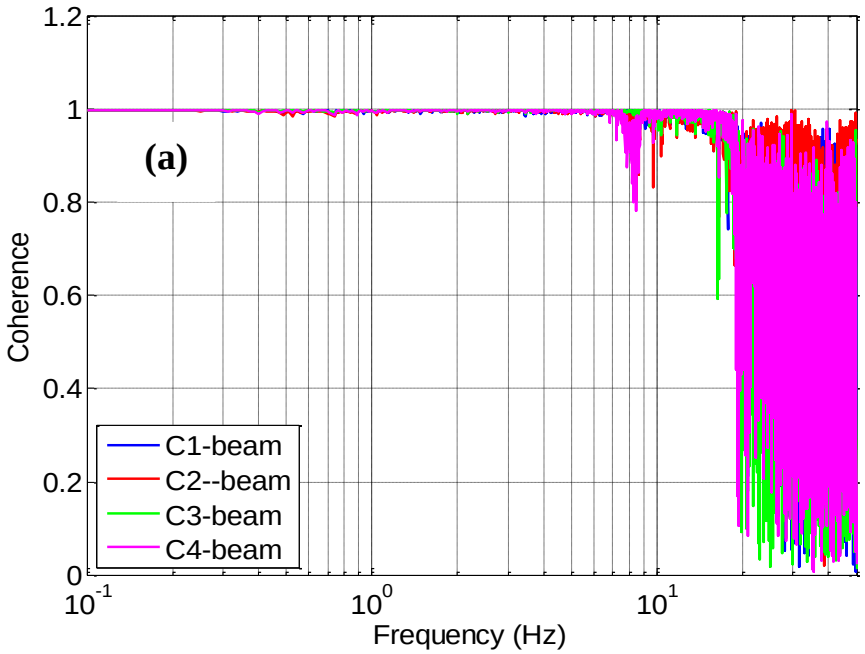

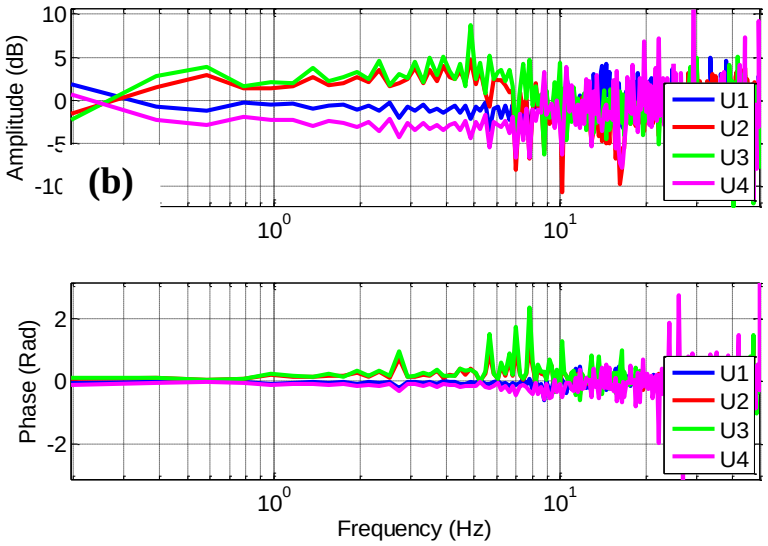

Figure 4.7 Coherence value between unit and beam over the frequency range of 0.6<*f*<7 Hz. (b) Amplitude and phase calibrations of the transfer function that matched each unit to the beam over frequency domain of 1<*f*<10 Hz.

Figure. 4.8(a) shows estimates of the Welch averaged self-noise from the coherence between each unit and the beam. The four units displayed close values of self-noise estimations at *f*=1 Hz. Unit 1 had the lowest self-noise density of 15 pT/√Hz; and units 2, 3 and 4 had self-noise level of 16.8 pT/√Hz at *f*=1 Hz. The Welch averaged spectra of the beam is also shown for reference. The results clearly indicate that there is a 22 dB common mode rejection between the beam and the units as measured with a Welch averaged spectra. Our approach was to estimate the array rms noise based on a root-square sum of all noise contributions, as given in [4, 5]. We estimated the array rms noise as

$$N_{n,array} = [N_1^2 + N_2^2 + \cdots N_n^2]^{1/2} . \qquad (4.12)$$

By employing an inverse variance weighting algorithm, the higher noise units were assigned a reduced weight and the lower noise ones were given an enhanced weight. So the normalized noise level for the array was:

$$N_{n,array} = [(N_1 W_1)^2 + (N_2 W_2)^2 + \cdots (N_n W_n)^2]^{1/2} ; \quad (4.13)$$

where the weight of each unit was defined as:

$$W_n = \frac{N_i^{-2}}{\sum_{i=1}^{n}(N_i^{-2})} . \qquad (4.14)$$

A representative result of the array noise is also shown in Figure. 4.8(a). The noise density can be seen to be about 8.2 pT/√Hz at f=1 Hz, which represents a 27 dB environment uniform noise reduction from 200 pT/√Hz.

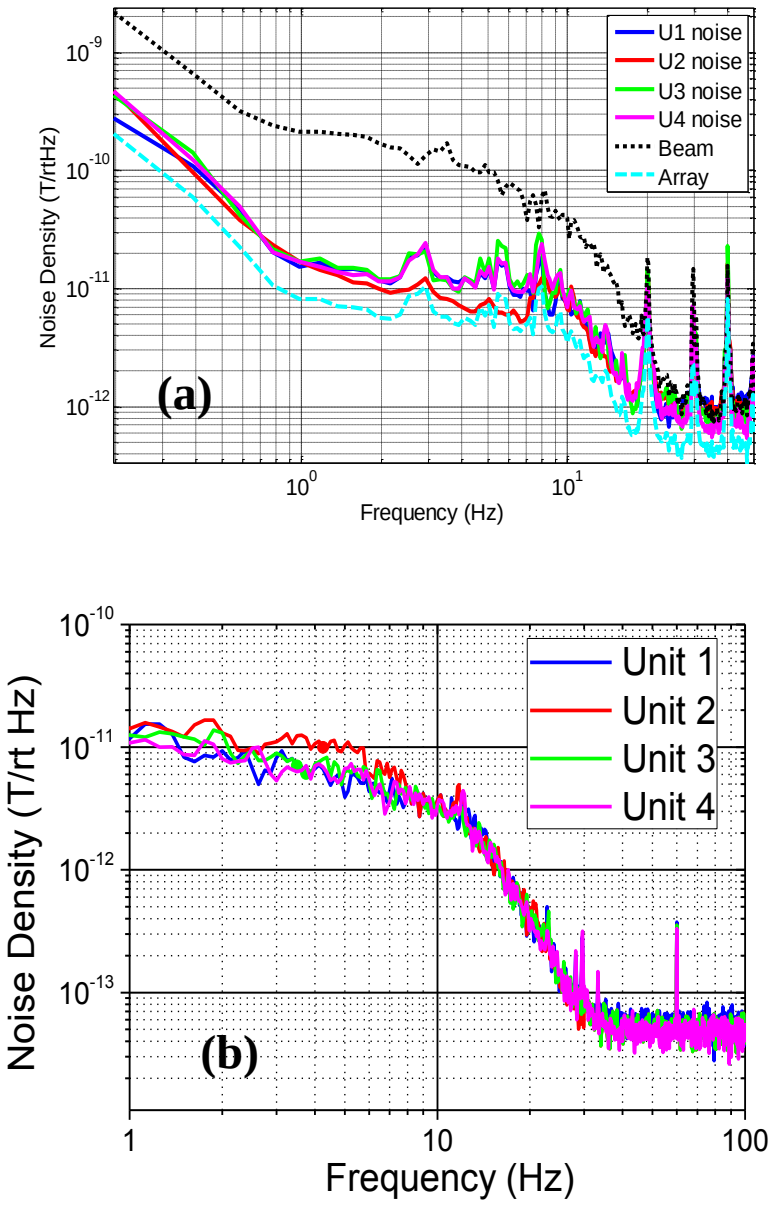

Figure 4.8 (a) Welch averaged self-noise as estimated from coherence between each unit and the beam. The Welch averaged spectra of the beam (dominated by the external noise) is shown for reference. There is a 22 dB common mode rejection between the beam and the units. The estimated 4×4 array noise based on inverse variance weighing is shown at 8.2 pT/√Hz at 1 Hz. (b) Noise density of units in a magnetic shielding chamber. Measured and estimated magnetic self-noise of four units match well at f=1 Hz.

Finally, we measured the intrinsic noise of these ME sensor units in a zero-Gauss vibration isolated chamber. In Figure. 4.8(b), the noise floor can be seen to be about 10−14 pT/√Hz at f=1 Hz. This is close to the estimated self-noise amplitudes of each sensor unit measured in an unshielded environment. The findings imply that such optimization efficiency of magnetic noise, in an open environment for the given 4×4 sensor array, is about a factor of 22 dB which is in good agreement with measurements performed in a zero-Gauss, vibration-isolated environment.

Therefore, an optimization of the magnetic noise has been performed to achieve the best possible equivalent magnetic noise for ME sensor array in open environment detection yielding about 8.2 pT/√Hz at f=1 Hz. Such optimization holds considerable promise for low cost, modest size, energy efficient, room temperature ME sensor applications in open environments for minute target signal detection. Next work will be devoted to analyze and characterize this differential measurement as a ME sensor imager as shown in following section.

4.4 ME Array Imager

The passive ME magnetic sensor for sensing hazardous objects in a non-constrained environment is based on sampling the Earth's magnetic field distortions caused by a metallic anomaly. Magnetic sensors are able to measure these properties without physical contact and have become the eyes of many industrial and navigation control systems.[11, 12] When ME sensors are properly placed in the vicinity of unstructured crowds, the magnetic field of moving metallic hazardous items can be fully discovered. A database of magnetic signatures has to be established and extracted the unique features to anticipate the invisible targets. Researchers have found that magnetic field profiles depend on several parameters, such as the object's mass, length, distance to the sensor, and moving orientation.[13, 14] However, there has been no experimental report so far on the dependence of magnetic field signatures on such key parameters.

Here, we study the magnetic characteristic of metallic objects theoretically and experimentally first. Then, the 4×4 MESA imager was employed and demonstrated its capability for non-intrusive target imaging detection in uncontrolled environment.The

results point to a ME sensor array as an attractive alternative for the security detection of suspicious metallic items carried covertly.

4.4.1 Theory

The moving metallic object can be treated as a magnetic dipole. Anderson used the known equation for the spatial distribution of a dipole as given in Equation 1:[15]

$$\vec{B} = \frac{\mu_0}{4\pi} * \left[\left(\frac{3(\vec{m}\cdot\vec{r})\vec{r}}{r^5}\right) - \frac{\vec{m}}{r^3}\right] \qquad (4.15)$$

The geometry relevant to the Anderson representation is shown in Figure 4.9. If we choose the time origin at the CPA, the position of the sensor relative to the dipole source is defined by

$$\vec{r} = \vec{r_0} + \vec{v}t \quad (4.16)$$

Combining equation (1) and (2) to work with the projection of the dipole magnetic field vector $\vec{B}$ along a prescribed direction $\hat{u}$:

$$\begin{aligned}\vec{B}\cdot\hat{u} = \frac{\mu_0 m}{4\pi r_0^3} * \Bigg[&\left(\frac{1}{(1+\theta^2)^{\frac{5}{2}}}\right)(3*(\hat{m}\cdot\hat{r_0})(\hat{r_0}\cdot\hat{u}) - \hat{m}\cdot\hat{u}) \\ &+ \left(\frac{\theta}{(1+\theta^2)^{\frac{5}{2}}}\right)\left(3*(\hat{m}\cdot\hat{r_0})(\hat{v}\cdot\hat{u}) - 3(\hat{m}\cdot\hat{v})(\hat{r_0}\cdot\hat{u})\right) \\ &+ \left(\frac{\theta^2}{(1+\theta^2)^{\frac{5}{2}}}\right)(3*(\hat{m}\cdot\hat{v})(\hat{v}\cdot\hat{u}) - \hat{m}\cdot\hat{u})\Bigg] \qquad (4.17)\end{aligned}$$

Where a dimensionless time parameter θ has been introduced as:

$$\theta = \frac{\vec{v}t\cdot\vec{r_0}}{\vec{r_0}\cdot\vec{r_0}} = \frac{(\vec{v}\cdot\vec{r_0})t}{r_0^2} = \frac{vt}{r_0} \quad (31)$$

Equation 30 can be further simplified by the reassignment of terms.

$$\begin{aligned}\vec{\boldsymbol{B}}\cdot\hat{\boldsymbol{u}} = \frac{\boldsymbol{\mu_0 m}}{\boldsymbol{4\pi r_0^3}} * \Bigg[&\left(\frac{\mathbf{1}}{(\mathbf{1}+\boldsymbol{\theta}^{\mathbf{2}})^{\frac{5}{2}}}\right) * \boldsymbol{C_0} + \left(\frac{\boldsymbol{\theta}}{(\mathbf{1}+\boldsymbol{\theta}^{\mathbf{2}})^{\frac{5}{2}}}\right) * \boldsymbol{C_1} + \left(\frac{\boldsymbol{\theta}^{\mathbf{2}}}{(\mathbf{1}+\boldsymbol{\theta}^{\mathbf{2}})^{\frac{5}{2}}}\right) \\ &* \boldsymbol{C_2}\Bigg] \qquad (\mathbf{4.18})\end{aligned}$$

where

$$\begin{cases} C_0 = 3 * (\hat{m} \cdot \hat{r_0})(\hat{r_0} \cdot \hat{u}) - \hat{m} \cdot \hat{u} \\ C_1 = 3 * (\hat{m} \cdot \hat{r_0})(\hat{v} \cdot \hat{u}) - 3(\hat{m} \cdot \hat{v})(\hat{r_0} \cdot \hat{u}) \\ C_2 = 3 * (\hat{m} \cdot \hat{v})(\hat{v} \cdot \hat{u}) - \hat{m} \cdot \hat{u} \end{cases}$$

The rest of the terms can be grouped together for a final form resembling Equation 32 with three functions f_0, f_1 and f_2 that are called Anderson functions.

$$\vec{B} \cdot \hat{u} = \frac{\mu_0 m}{4\pi r_0^3} * [f_0 * C_0 + f_1 * C_1 + f_2 * C_2] (4.19)$$

where

$$f_n = \frac{\theta^n}{(1+\theta^2)^{\frac{5}{2}}} for n = 0, 1, 2 \ .$$

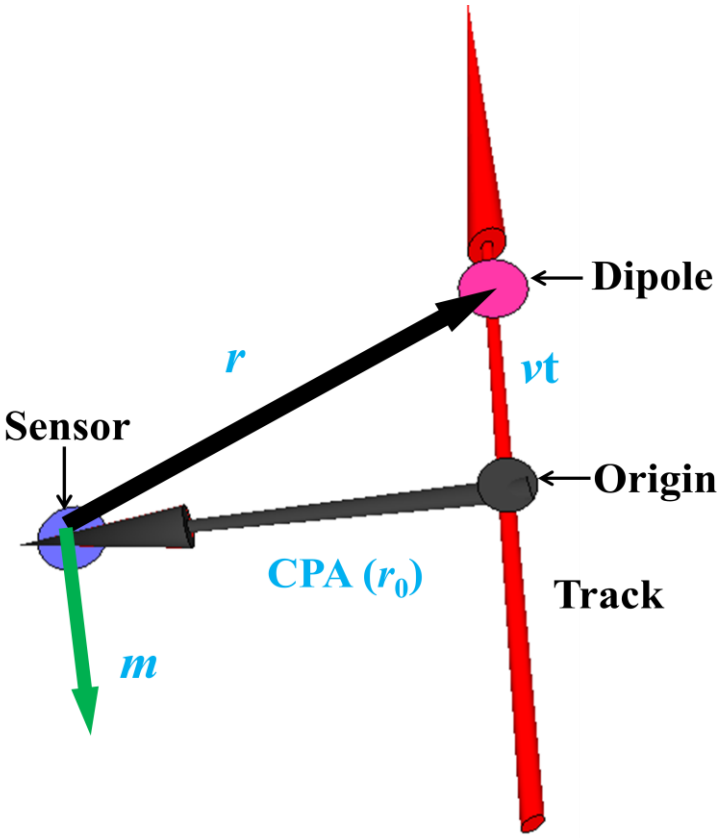

Figure 4.9 Schematic illustration of the Anderson function representation.

Thus, inserting the direction ($\hat{u}$), the velocity vector ($\hat{v}$), the moment of the dipole (m) and the closet path approaching to the track (r_0) into the coefficient equations, a field

component in any of the orthogonal directions can be found.[16] If the velocity vector $\hat{v}$ is not time dependent, the projection of magnetic field $\vec{B}$ in direction $\hat{u}$ is depend only on relative position of the sensor and dipole (moving object).

4.4.2 Experiment

A bi-axis ME sensor was used in this study comprised of two single-axis ME sensor units, where the sensors mutually perpendicular to each other in a plane to enable measurement of the two magnetic fields B_x and B_y. The output signal from ME sensor was directly collected by a Datalogger (Campbell Scientific, Inc.) with 100 Hz sample rate and a 5 V full-scale. And the post signal processing was conducted via Matlab. Firstly, we evaluated the effects of some critical parameters onto the magnetic signatures, such as CPA, moving direction, and velocity as analyzed in section 2.4.1. A small 0.5 cm diameter metallic cylinder with 8 cm height was used as the target and placed onto a remote-control non-metal vehicle. The well-costumed vehicle can move with controlled velocity and through a track with fixed CPA to the sensor.

4.4.2.1 Effects of CPA

The CPA has been used as one of the feature extraction technique as described in [17]. Here, for comparison purpose, the effects of relative distance between sensor and target were studied by different CPA at 40cm, 50cm, 60cm and 70cm. The target moving direction was set from right-to-left with respect to the sensor and the moving velocity was controlled at constant speed v=0.55 m/s. Magnetic field strengths of sensor's two orthogonal direction componnets B_x and B_y are plotted in Figure 4.10(a) through (d) at these designed CPAs. From Figure 4.10(a), one can see that the induced magnetic field strengths were largest at the cloest CPA=40cm; obviously the strengths discreased as the CPA increased from 50cm, 60cm to 70cm in both components. As expected from Anderson funtions, these CPA effect data can be effectively used as a discriminating feature for concealed target detection.

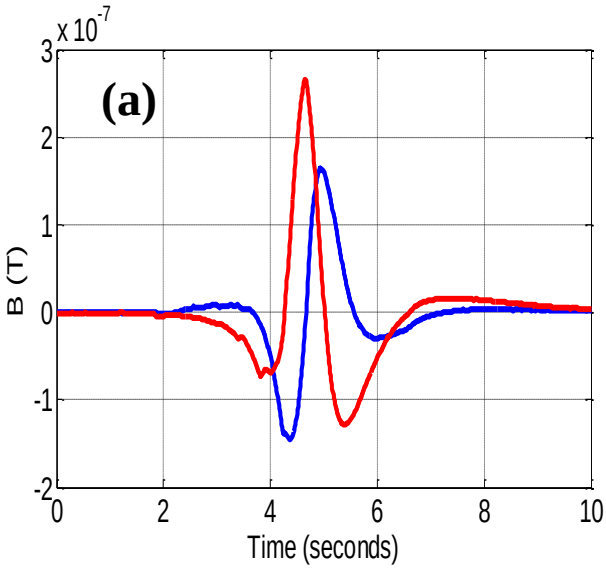
x 10^-7
(a)
B (T)
Time (seconds)

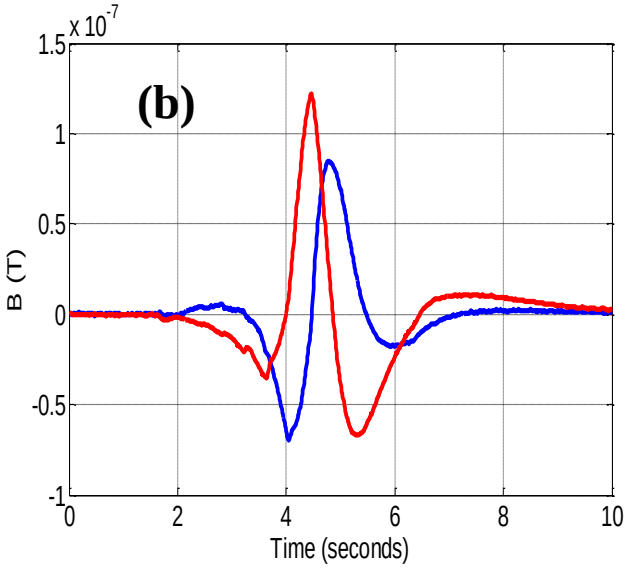
x 10^-7
(b)
B (T)
Time (seconds)

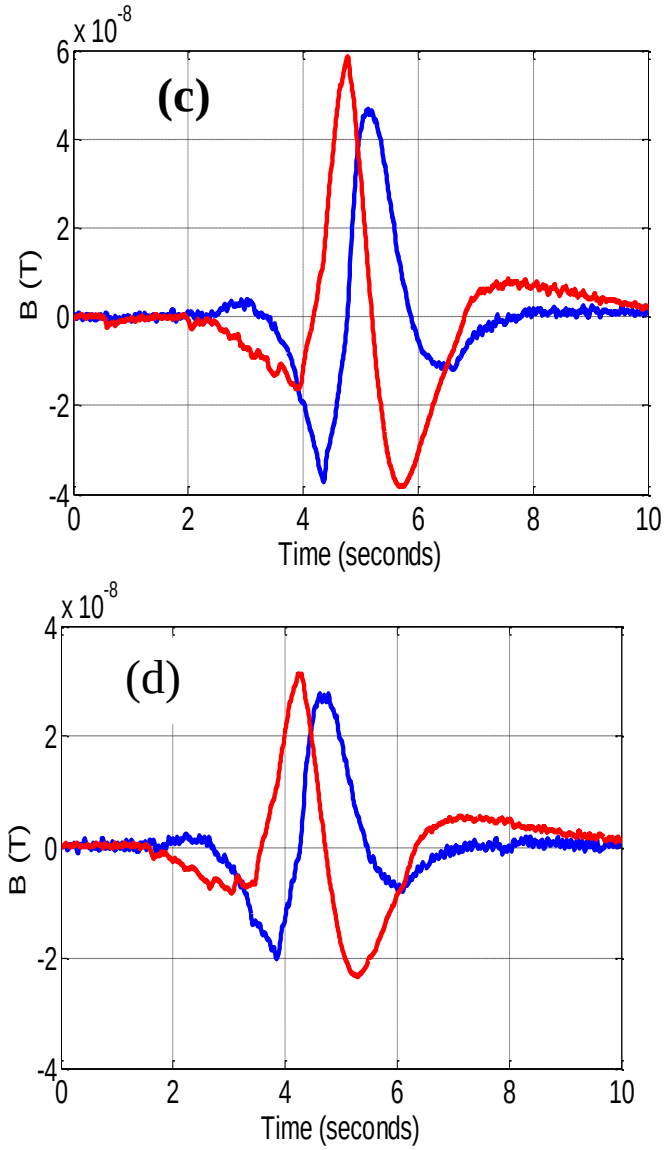

Figure 4.10 (a) Magnetic field components in two orthogonal directions B_x (blue curve) and B_y (red curve) sensed by a ME sensor for a nearby moving metallic target at different CPA=40cm (b) 50cm, (c) 60cm and (d) 70cm when velocity equals 0.55 m/s and moving direction was set from right-to-left with respect to the sensor.

4.4.2.2 Effects of moving direction

We next characterized the magnetic signal waveforms by changing the moving direction. Figure 4.11 shows the results when the target was moving from left-to-right at CPA=40cm and the same velocity v=0.55 m/s. Comparing figure 4.10(a) and figure 4.11, one can clearly see that withi the same CPA there are discernable differences in component shapes and behaviors, specifically for x-component. There is a reversal in the

occurrence in x-component waveforms,while signature reversal doesn't occur for y-component with a change in moving direction. The differences in the waveforms can be attributed to different orientations of target induced magnetic moment on sensor's components. These evidences are illustrating how the signatures of the x- and y-component vary with object travelling directions.

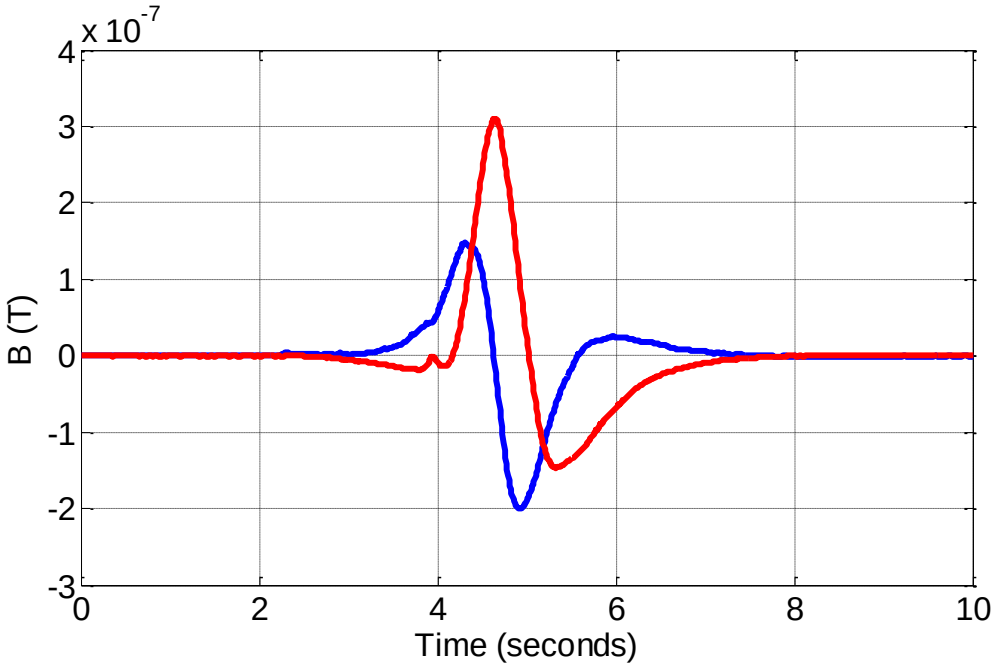

Figure 4.11 Magnetic field components in two orthogonal directions B_x (blue curve) and B_y (red curve) sensed by a ME sensor for a nearby moving metallic target at fixed CPA=40cm when velocity equals 0.55 m/s and moving direction was set from left-to-right with respect to the sensor.

4.4.2.3 Effects of velocity

The effects of object moving velocity were examined by varyig velocity while keeping other parameters fixed. Figure 4.12 (a), (b) and (c) show the velocity results at CPA=30cm when velocity=0.29, 0.43 and 0.55 m/s respectively. The moving direcion was kept constantfrom right-to-left relative to the sensor. Comparing three graphs in Figure 4.12, one can see that the magnetic signal shows the same amplitudes and wavelet shapes by increasing velocity. However, one can also see that the signature peaks and troughs become narrow and sharp when the moving velocity increased. These results correlate well with the Anderson function, implying the maximum induced signal

strength of the moving object is inrelavent to the target speed, which is only dependent on the CPA. However, the target approaching velocity would change the time rate of the magnetic flux density purtubations received by the sensor, thus resulting in different waveform shapes of the induced magneitc signatures in time history. It is important to note that the width of the wavelet is inversely proportional to the time rate of changing of the magnetic flux density on the senosr. The results indicate that the velocity is effective as a discriminating feature for the target detection.

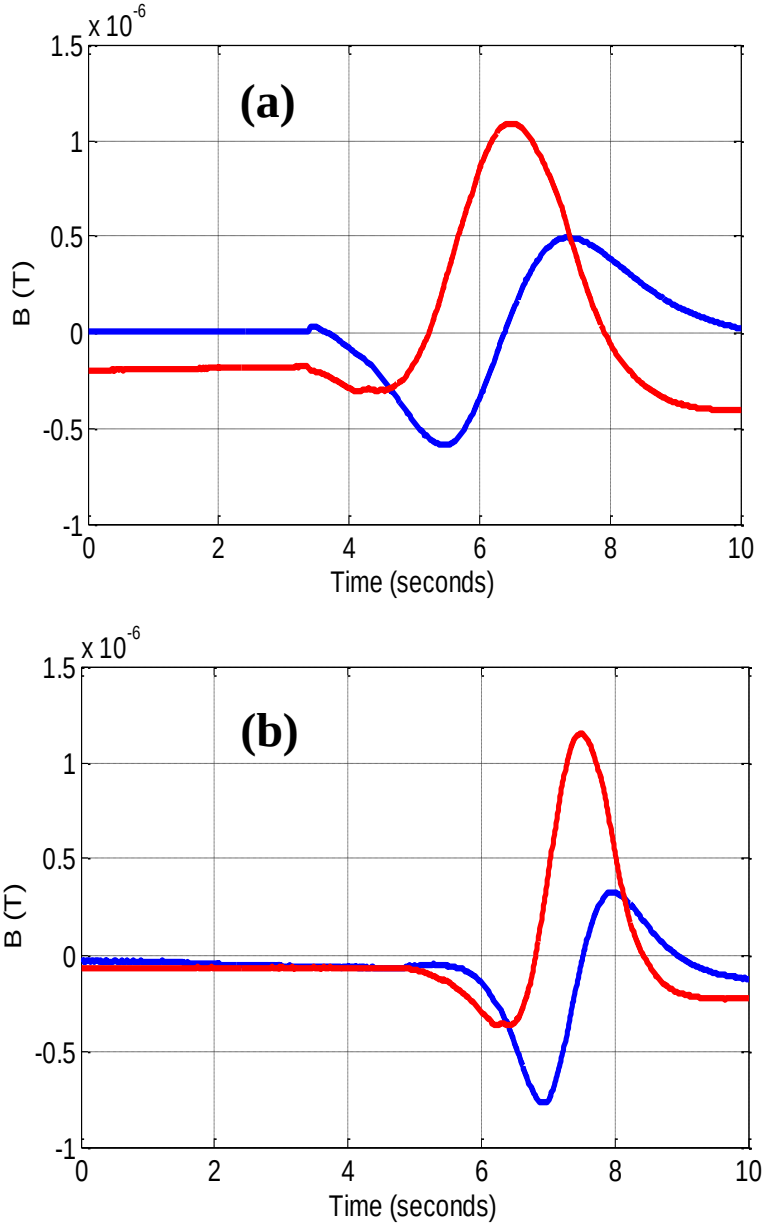

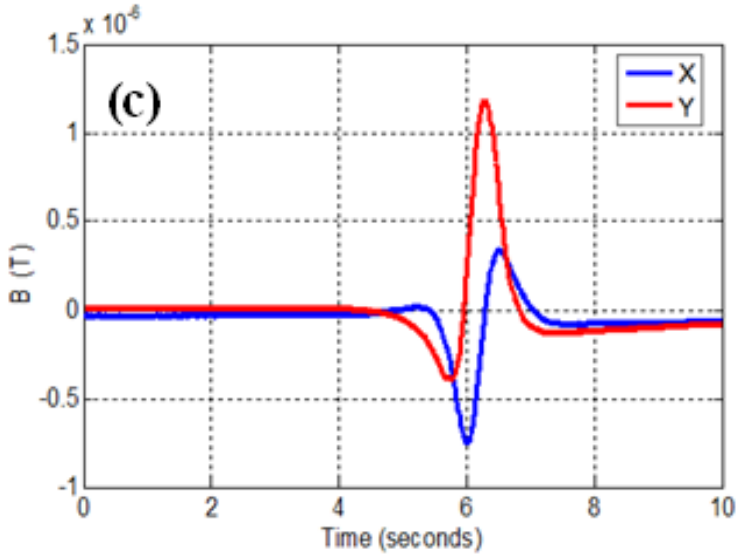

Figure 4.12 (a) Magnetic field components in two orthogonal directions B_x (blue curve) and B_y (red curve) sensed by a ME sensor for a nearby moving metallic target at fixed CPA=30cm when moving at different velocities v= 0.29 m/s, (b) 0.43 m/sand (c) 0.55m/s.

4.4.2.4 Object detection by ME array imager

A superior approach that we have begun pursuing was to integrate several sensors to form an array imaging system. We employed four single-axis ME sensor to construct an array imager for a hinded scissor item detection test in our lab. Figure 4.13(a) shows the overall system set up comprised of four individual sensors (S1, S2, S3 and S4) mounted on a bracket and separated by 40cm along vertical direction. The scissor was concealed around the carrier's waist who was walking along a path 80cm away from the nearby array imager. The four output channels of the array imager were connected to the datalogger and the resultant imaging was presented in Figure 4.13(b) during the person passing by the detector in a time range of 10seconds. The signal captured by thearray provides a magnetic signature, an unique spectrum, for that object as shown in Figure 4.13(c). It notes that S3 illustrates a strongest response singal due to the smallest CPA between the object and S3. Obviously, the second and third strongest signal strengths were observed in S2 and S3 respectively; while S1 presents the smallest response caused by the longest CPA. Figure 4.13(c) also implies that the carrier's approaching orientation was from rigt-to-left owing to our analysis above for the effect of moving direction. It can also be found that the carrier's moving velocity was relatively slow by comparing the

width of magnetic signature peakes to the analysed data in Figure 10. A more accurate velocity prediction can be made after establishing a database of magnetic signatures to extract the unique features. Figure 4.13(b) and (c) both indicate that the person should carry a hidden metallic item which had a horizontal position close to S3, specificly at a spot above S3 slightly, which is close to the actual scenario shown in Figure 4.13(a).

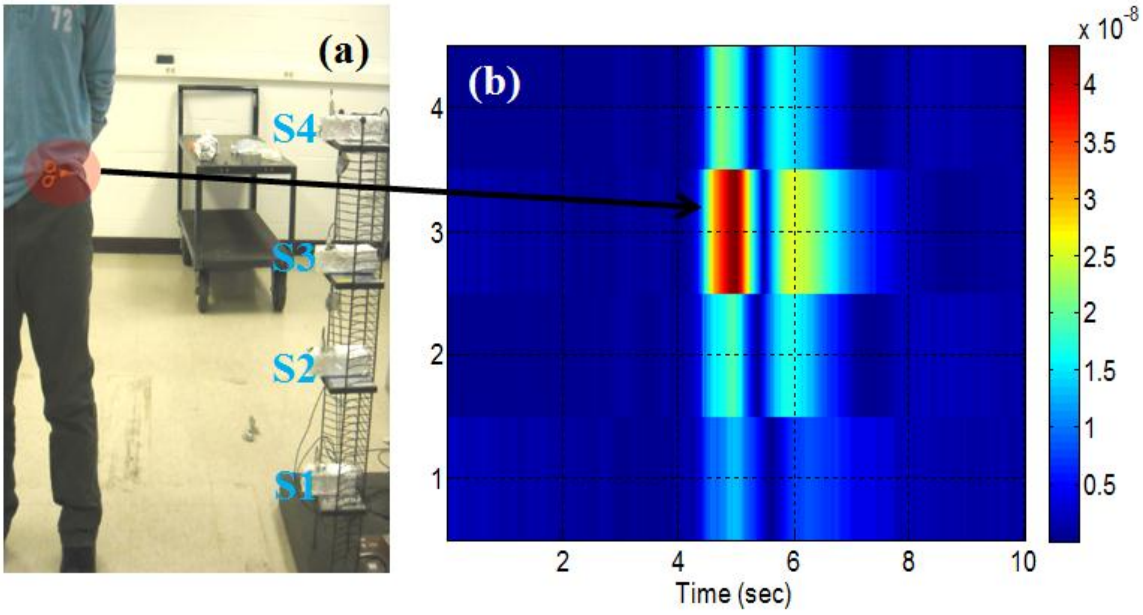

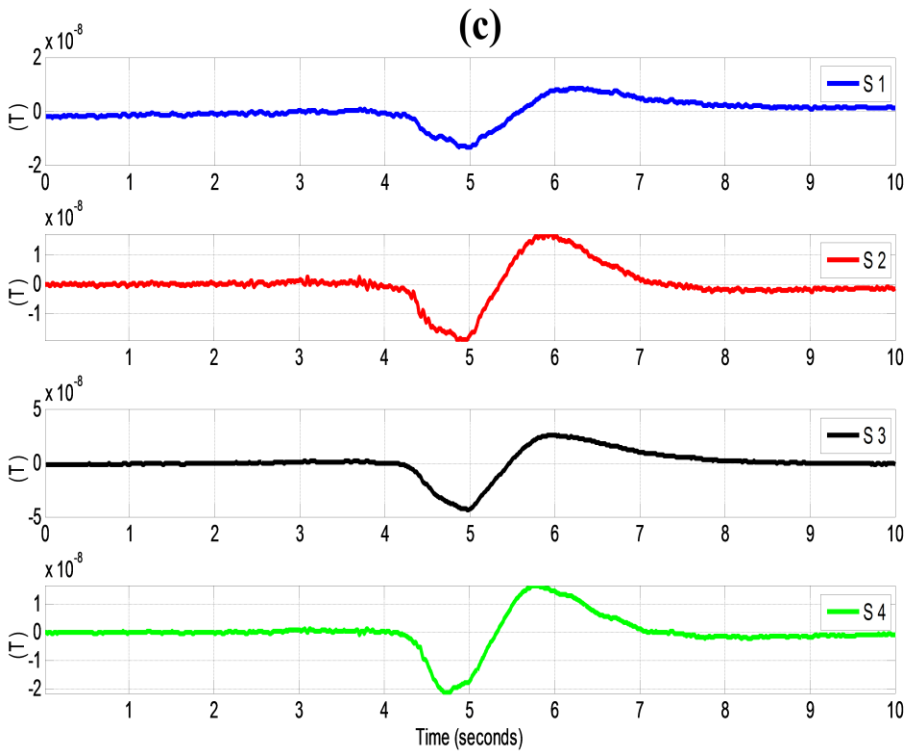

Figure 4.13 (a) Picture of the overall imaging system set up comprised of four individual sensors (S1, S2, S3 and S4) placed on a bracket and separated by 40cm along vertical direction; the scissor was concealed around the carrier's waist who was walking on a path 80cm away from the nearby sensor bracket, (b) resultant imaging spectrum presnted by the ME sensor array during the person passing by the detector in a time range of 10s, (c) magnetic filed signatures detected by the four individual sensors.

A simple repeatability test for the item was conducted where the scissor was located on the shoulder of the carrier for the same walking path and moving direction. Figure 4.14(a) shows the imaging result illustrating the horizontal positon of the concealed threat should be close to or above S4 due the maximum amplitdues which should be produced by the smallest CPA. The other information about moving direction and velocity can be captured from the magnetic signature waveform as shown in Figure 4.14(b).

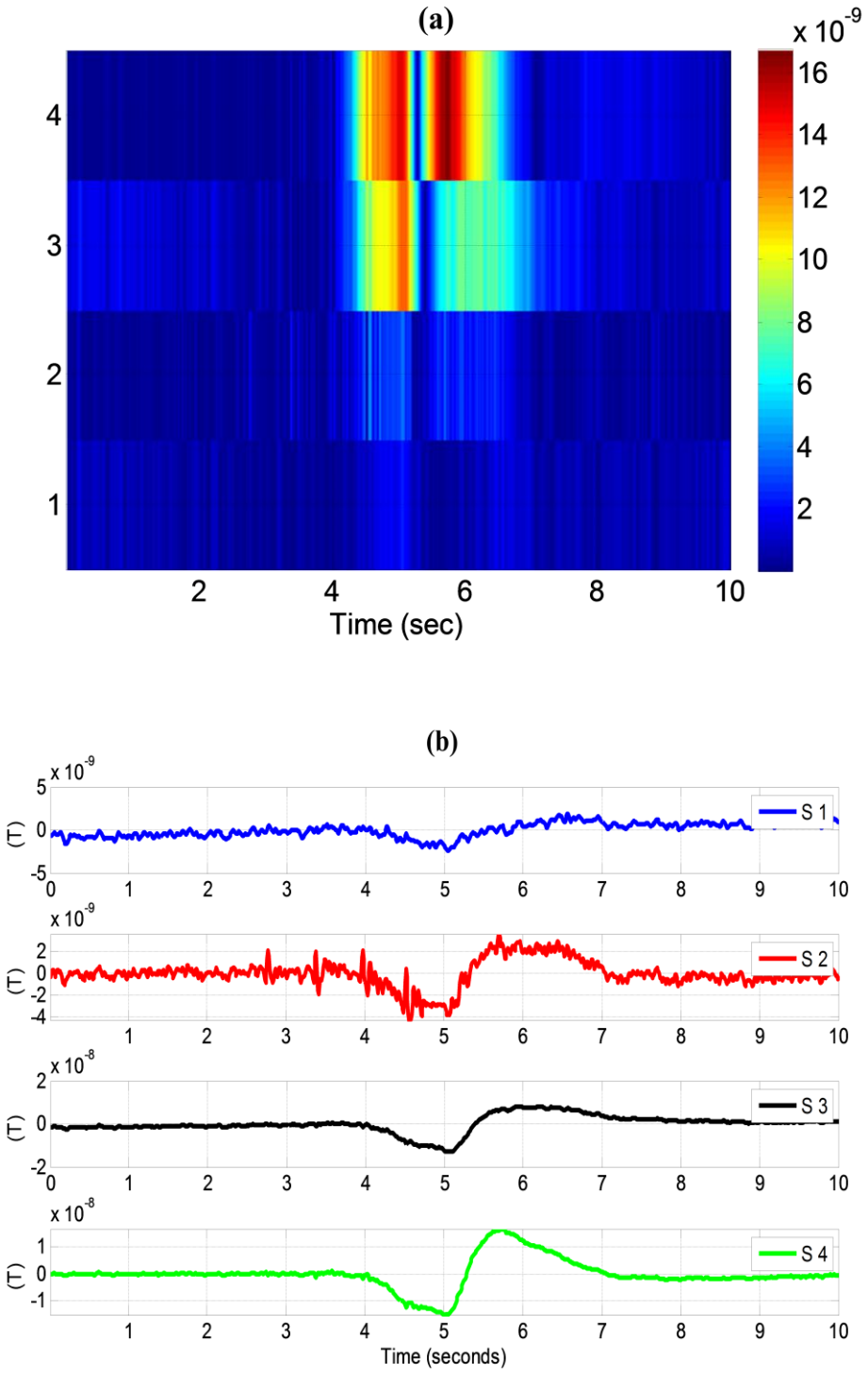

Figure 4.14 (a) Resultant imaging spectrum presnted by the ME sensor array during the person passing by the detector in a time range of 10s, (b) magnetic filed signatures detected by the four individual sensors when the scissor was concealed onto the carrier's shoulder.

It indicates that more accurate localization could be achieved by incorporating more sensors and making them closely spaced to increase spacial resolution. Figure 4.13 and 4.14 underlie the basis of the ME sensor array based system to perfrom efficient measurements for non-invasion detection and localization. The ME sensor imager technology holds a promising potential for reducing the size, complexity, cost, and specifically in uncontrolled environment without a walk through portal.

4.5 Summary of This Section

It has been found that after adjusting the incoherent noise and phase shift discrepancy between each unit to a beam, the self-noise estimation for each sensor can achieve the lowest possible level. This was also demonstrated by measurements in a controlled shielded environment. Maxwell function indicates that a distortion generated by a magnetic dipole (target) decreases fast as distance increase and usually drops in intensity with the cube of the distance from the object. For multiple sensors or sensor array, several sensors are separated by a certain baseline gives rise to the ME sensor array detector by examining the various detected signal obtained by each sensor unit with respect to the same target.

A 4×4 ME Sensor Array (MESA) comprised of four single ME sensor units was developed, which were made of tri-layer of Metglas/PZT-fiber/Metglas with a multi push-pull mode configuration. The magnetic equivalent noise for the 4×4 magnetoelectric (ME) sensor array unit has been optimized. Such optimization holds promise for practical sensor application in open (unshielded) environments. The self-noise estimation for the array unit was about 15-16.8 pT/√Hz at f=1 Hz, as estimated by the coherence between each unit and their beam. To verify the efficiency of this optimization technique, self-noise tests were also performed in a magnetic shielding chamber and shown to be close to that of units in an open environment. After employing a noise optimization method, the 4×4 array can achieve a 27 dB common mode noise rejection and an equivalent magnetic noise floor of 8.2 pT/√Hz at f=1 Hz.

Such passive-mode sensor with ME effect was very sensitive and viable for detecting minute magnetic field abnormality. An anderson function was employed to analyze the magnetic field signatures which were shown to be dependent on several essential parameters. Such effects were verified by ME sensor experimentally which were in good

agreement with the theory. An array imager was developed and demonstrated its capability for non-intrusive target imaging detection in uncontrolled environment.

References:

[1] Z. P. Xing, J. Y. Zhai, J. Q. Gao, J. F. Li, and D. Viehland, "Magnetic-Field Sensitivity Enhancement by Magnetoelectric Sensor Arrays," *Ieee Electron Device Letters*, vol. 30, pp. 445-447, May 2009.

[2] Z. Xing, J. Li, and D. Viehland, "Modeling and the signal-to-noise ratio research of magnetoelectric sensors at low frequency," *Applied Physics Letters*, vol. 91, p. 142905, 2007.

[3] C.-W. Nan, M. I. Bichurin, S. Dong, D. Viehland, and G. Srinivasan, "Multiferroic magnetoelectric composites: Historical perspective, status, and future directions," *Journal of Applied Physics*, vol. 103, p. 031101, 2008.

[4] W. M. Leach, "Fundamentals of low-noise analog circuit design," *Proceedings of IEEE*, vol. 82, pp. 1514-1538, 1994.

[5] C. D. Motchenbacher and J. A. Connelly, *Low-Noise Electronic System Design*: New York: Wiley-Interscience, 1993.

[6] J. Zhai, Z. Xing, S. Dong, J. Li, and D. Viehland, "Detection of pico-Tesla magnetic fields using magneto-electric sensors at room temperature," *Applied Physics Letters*, vol. 88, p. 062510, 2006.

[7] J. Das, J. Gao, Z. Xing, J. F. Li, and D. Viehland, "Enhancement in the field sensitivity of magnetoelectric laminate heterostructures," *Applied Physics Letters*, vol. 95, p. 092501, 2009.

[8] J. Gao, D. Gray, Y. Shen, J. Li, and D. Viehland, "Enhanced dc magnetic field sensitivity by improved flux concentration in magnetoelectric laminates," *Applied Physics Letters*, vol. 99, p. 153502, 2011.

[9] J. Bendat and A. Piersol, *Random Data: Analysis and Measurement Procedures, 4th ed*, 2010.

[10] Y. Shen, J. Gao, L. Shen, D. Gray, J. Li, P. Finkel, D. Viehland, X. Zhuang, S. Saez, and C. Dolabdjian, "Analysis of the environmental magnetic noise rejection by using two simple magnetoelectric sensors," *Sensors and Actuators A: Physical*, vol. 171, pp. 63-68, 2011.

[11] A. Haoui, R. Kavaler, and P. Varaiya, "Wireless magnetic sensors for traffic surveillance," *Transportation Research Part C: Emerging Technologies*, vol. 16, pp. 294-306, 2008.

[12] J. Wolff, T. Heuer, H. Gao, M. Weinmann, S. Voit, and U. Hartmann, "Parking monitor system based on magnetic field sensors," presented at the IEEE Intelligent Transportation Systems Conference, Toronto, Canada,, 2006.

[13] R. Lao and D. Czajkowski, "Magnetoresistors for Automobile Detection and Traffic Control," *IEEE Sensors*, vol. 13, pp. 70-73, 1996.

[14] A. Agurto, Y. Li, G. Y. Tian, N. Bowring, and S. Lockwood, "A Review of Concealed Weapon Detection and Research in Perspective," presented at the Proceedings of the 2007 IEEE International Conference on Networking, London, UK, 2007.

[15] C. E. Baum, *Detection and identification of visually obscured targets* vol. xvii. Philadelphia, PA: Taylor & Francis, 1999.

[16] B. Ginzburg, L. Frumkis, and B.-Z. Kaplan, "An efficient method for processing scalar magnetic gradiometer signals," *Sensors and Actuators A: Physical*, vol. 114, pp. 73-79, 2004.

[17] T. Phan, B. W. Kwan, and L. J. Tung, "Manetoresistor for vehicle detection and identification," *Computational Cybernetics and Simulationapos*, vol. 10, pp. 3839-3843, 1997.

Chapter 5:

DETECTION AND LOCALIZATION OF AC SOURCES BY TENSOR ME SENSOR

5.1 Introduction

Many triple-axial magnetometer technologies have been exploited and have shown promising merits in application. The practical application includes determining the position of a magnetic object by measuring the three-component magnetic field of the object, such as applications in geophysics [1], vehicle detection [2], detection of a dipole [3], and human movement [4]. Detection for the AC source is one of the important applications for magnetometers. There is a need for portable magnetic sensors that are highly sensitive, compact, operated at room temperature and use little power. However, there are no available technologies that can fulfill all these requirements. Despite the fact that a SQUID can detect small magnetic fields, it demands extreme low operating temperatures making it usable only under controlled environments. Most AC source detection have used fluxgate sensors, which have a minimum detectable signal level of 0.01 to 1 nT at quasi-static frequencies. [5-7]

Recently, our group members have developed a bi-axial sensor which is shown in Figure 5.1(a). The sensor is comprised of Metglas/PZT-fiber layers laminated together, where the two sensors were placed mutually perpendicular to each other in a "+" configuration. This particular structure is able to effectively prevent the individual sensor from interacting with each other. The bi-axial sensor was rotated in Earth's plane, as shown in Figure 5.1(b),and it shows the angular dependence of V_{ME} which proves the potential to make multi-axial sensors.

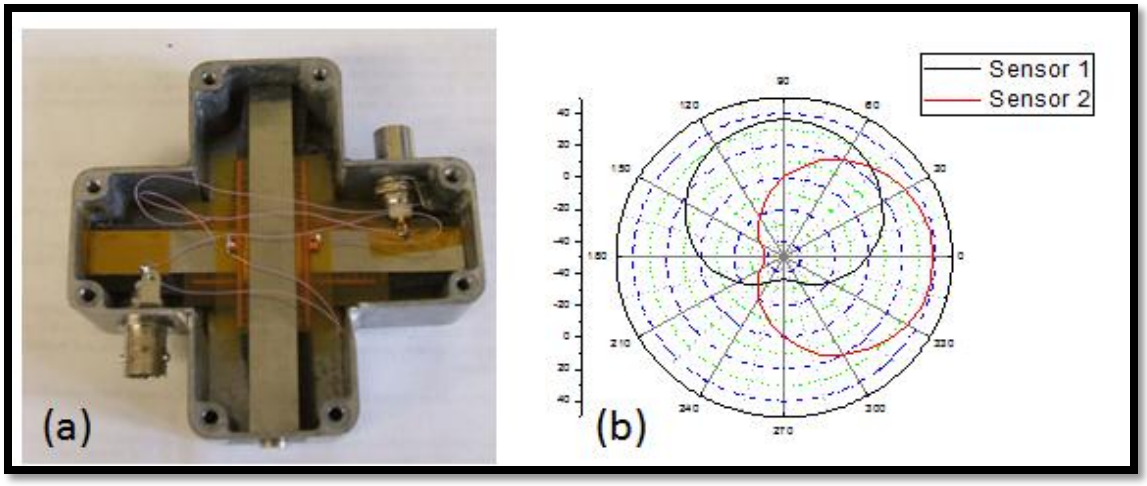

Figure 5.1 (a) Photo of our bi-axial ME magnetic sensor; and (b) output voltage from our bi-axial ME magnetic sensor when it is rotated in Earth's plane.

Previous researchers have demonstrated the possibility to develop multi-axial ME sensors with a performance equivalent to that of a high-end fluxgate multi-axial device, which consumes much less energy than that of fluxgate. There are several advantages associated with a triple-axial sensor:

1) A decrease in the number of sensors needed in a system because sensor components are integrated;

2) Ease and simplicity of formulation as the field of the three-axis components are measured almost at one-point;

3) An integrated magnetic field sensor can be applied resulting in an increasing in the position accuracy.

My goal is to design an advanced triple-axial sensor of various operational modes, characterize their noise floors and orthogonality between various directions, and test the ability to detect an AC target, all of which are detailed in Section 5.3. Estimation of the AC dipole localization was realized with the help of a grid search (GS) algorithm. The results show good convergence and accuracy of object location along three orthogonal directions. Through simulation analysis, the major localization errors were found to arise from sensor calibration.

To date, ME laminated composites of magnetostrictive Metglas foils and piezoelectric $Pb(Zr,Ti)O_3$ or PZT have been widely investigated in various operational modes and

optimized for use in magnetic field detection applications.[8-10] Highly sensitive, room temperature, and passive magnetic field sensors have been developed based on ME laminates. Such magnetic sensors have been shown to have noise floors on the order of pT/√Hz for Metglas/PZT foil laminates. The limiting equivalent magnetic noise sources of ME sensors have been shown to be thermal polarization and DC resistance, both of which are temperature dependent. However, the stability of ME sensors to temperature changes has not yet been determined, in spite of the fact that the sensors need to operate over a broad range of ambient temperatures around 25 ℃, when they are used in open environments. It is unknown if the ME voltage coefficient (α_{ME}) and equivalent magnetic noise floor are decreased or increased with temperature. Such changes in the environment could potentially degrade sensor performance. Therefore, I first examined the thermal stability for the ME laminate in a temperature range of -50 °C ≤ T ≤ 50 °C, as shown in Section 5.2. The parameters which control the noise floor of ME sensors, such as capacitance, tan δ and ME charge coefficient, were characterized. The results show the noise floor was thermally stable around 30 pT/√Hz (f =1 Hz) over the studied temperature range. To demonstrate the relative invariance of ME sensors at different temperatures over the range studied, a simulation based on a noise model was conducted, where the predicted and measured equivalent magnetic noise floors were found to agree well.

5.2 Thermal Stability

An investigation of the temperature dependent properties of Metglas/PZT ME sensors was conducted in the temperature range of -50 °C ≤ T ≤ 50 °C. To fabricate ME sensors in a multi push-pull mode configuration, we obtained PZT fibers (CTS, Albuquerque, NM) and Metglas foils (Vitrovac 7600F, Vitrovac Inc. Hanau, German). The dimensions of the piezoelectric core were 4 cm × 1 cm × 180 μm, which consisted of a PZT fiber bundle affixed to thin interdigited (ID) electrodes deposited on Kapton® sheets by a two-part epoxy. The electrode pattern allowed for a symmetrical polling of the piezoelectric fibers in a back-to-back manner along their length axes.[8] Three layers of Metglas foils cut into dimensions of 8 cm × 1 cm × 22 μm were then attached to the upper and lower surfaces of the Kapton® electrodes using the same epoxy.

Figure 5.2 shows the ME voltage (α_{ME}) and charge (α_{me}) coefficients of the Metglas/PZT-fiber sensor as a function of DC magnetic field H_{dc} at room temperature.

Along the longitudinal axis of the laminates, a constant AC magnetic excitation of H_{ac}=0.1 Oe was driven at f=1 kHz by a pair of Helmholtz coils. An electromagnet was used to generate a H_{dc} along the same axis, and the induced ME voltage signal was directly measured by a lock-in amplifier (Standford Research, SR-850), and the ME charge signal was collected via a charge meter (Kistler type 5015) and measured by the same lock-in amplifier. From this figure, it can be seen that both α_{ME} and α_{me} are nearly zero at H_{dc} = 0; exhibited a near linear dependence on increasing DC biases for H_{dc}< 5 Oe; reached a maximum value of α_{me}=1350 pC/Oe at an optimal bias of H_{dc}≈8 Oe; and then decreased as H_{dc} was further increased.

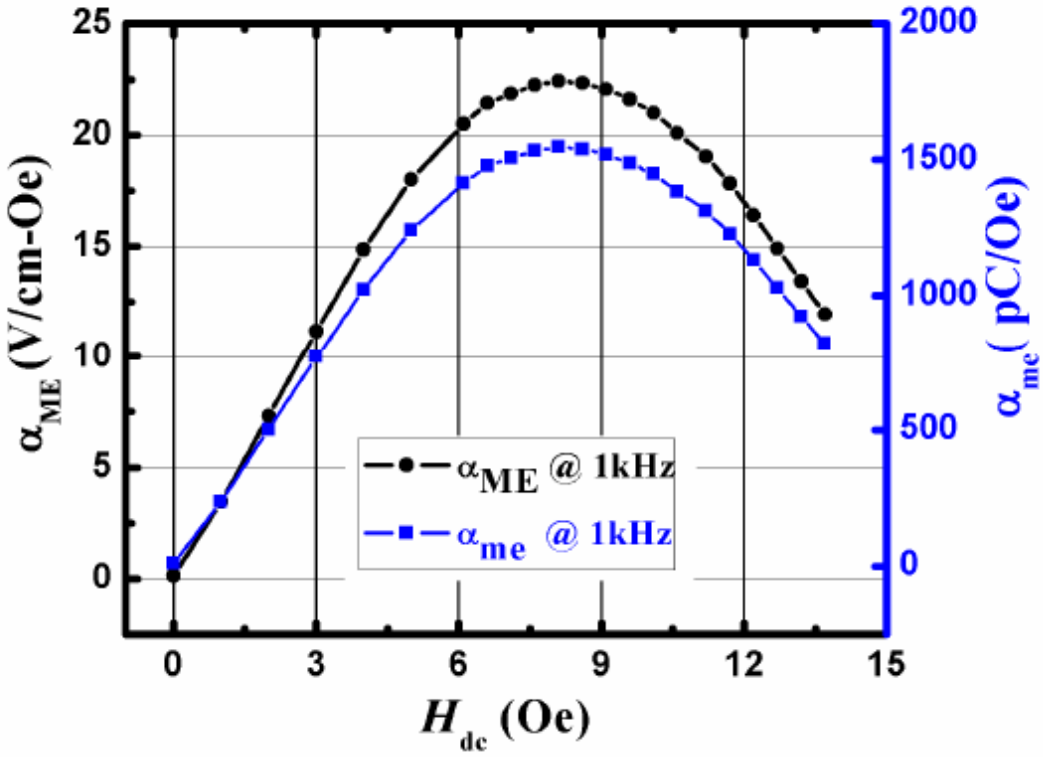

Figure 5.2 ME voltage coefficient α_{ME} (black curve) and ME charge coefficient α_{me} (blue curve) as a function of dc magnetic field H_{dc} for a Metglas/PZT laminate composites at room temperature.

Since the sensitivity of ME composites is mainly limited by the charge noise density (N_c) and the ME charge coefficient, the sensitivity can be estimated as [10, 11]:

$$Sensitivity\ \left(\frac{T}{\sqrt{Hz}}\right) = \frac{N_c\left(\frac{C}{\sqrt{Hz}}\right)}{\alpha_{me} \times 10^8 \left(\frac{C}{T}\right)}\ ; \qquad (5.1)$$

where,

$$N_c = \sqrt{\frac{4kTC\ tan\ \delta}{2\pi f} + \frac{4kT}{(2\pi f)^2 R}}\ ;$$

and where C is the capacitance of the PZT fibers, tan δ is the dielectric loss factor of the piezoelectric core ID electrode layer, R is the DC resistance of the PZT core composite, k is the Boltzmann constant (1.38×10^{-23} J/K), and T is the temperature in Kelvin. This equation can be used to predict the equivalent magnetic noise at different temperatures by putting the temperature-dependent values of C, tan δ and α_{me} into (1). It is then straightforward to devise an experimental method by which to measure the sensitivity and equivalent magnetic noise of a ME sensor at different temperatures. Unfortunately, previous reports have focused on room temperature operations. Following the approached outline above, we can experimentally and theoretically study the temperature dependent performance.

We characterized the temperature dependence of the capacitance, dielectric loss factor, and ME charge coefficient. The ME laminate sensor was placed into a small cooler with dry ice to reduce the inner temperature to -50 ℃. The cooler was mounted on a Zero-Gauss, vibration isolation chamber. The temperature was slowly increased from -50 ℃ to 50 ℃, while the dielectric constant and loss factor were measured. Figure 5.3 (a) shows C and tan δ (f=1 kHz) as a function of temperature which was measured by an impedance analyzer (Agilent 4294 A). The capacitance increased modestly with increasing temperature from 589 pF (T = -50 ℃) to = 659.8 pF (T = 50 ℃). However, the value of tan δ was found to be relatively constant at about 0.01 over the temperature range studied, although at 50 ℃ the tan δ was found to be slightly higher. These C and tan δ data are in agreement with previously reported results for the temperature-dependent properties of PZT-based piezoelectric ceramics. For example, PZT-5A ceramics posses a steady increase in C with temperature and tan δ is nearly independent of temperature between -50 °C ≤ T ≤ 50 °C.[12]

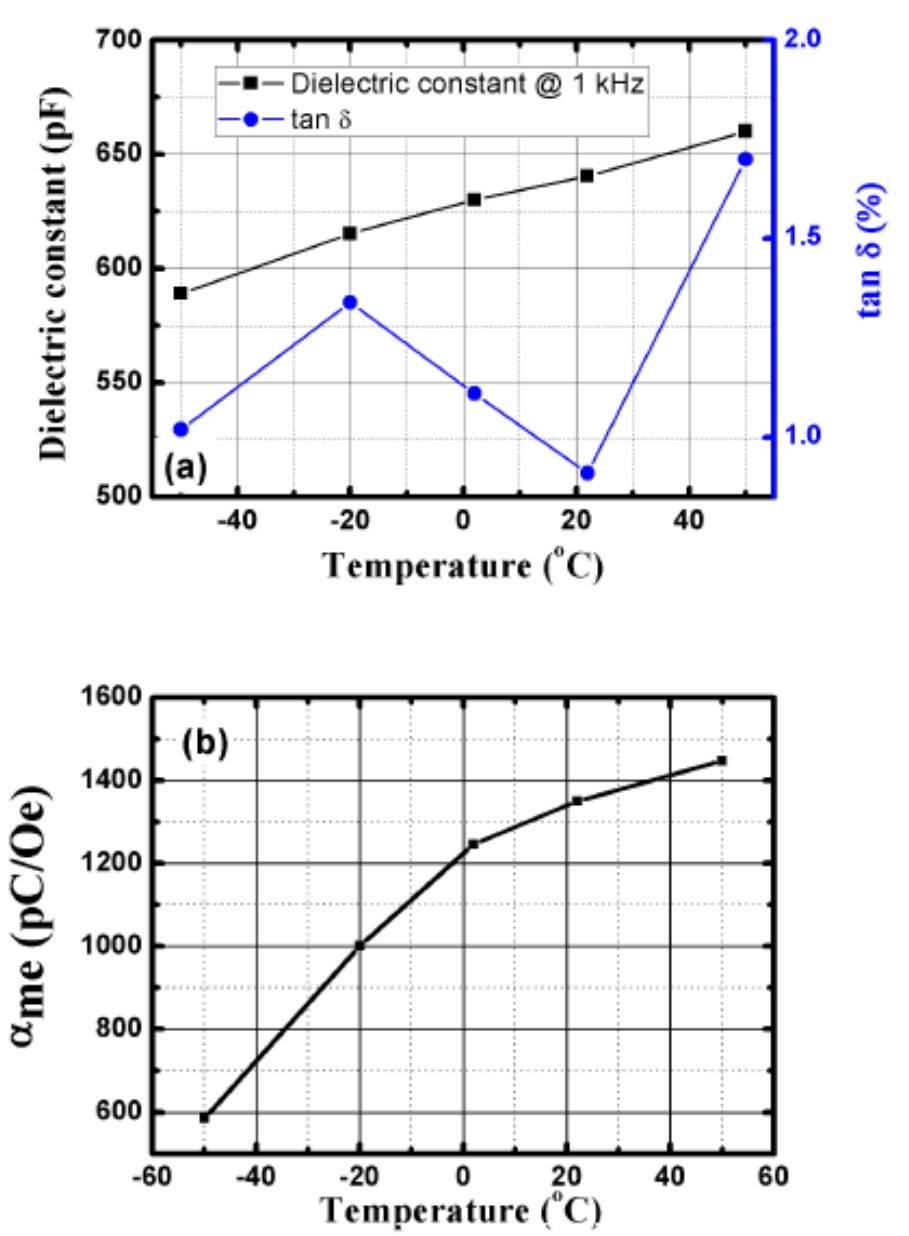

Figure 5.3 (a) Capacitance (black curve) and dielectric loss factor (blue curve) as a function of temperature. Measurements were made at 1 kHz. (b) ME charge coefficient as a function of temperature.

The ME laminates were then integrated into an EMI shielded box with permanent magnets attached at either end of the laminate to provide a DC magnetic biases. Low noise operational amplifier detection circuits were fabricated according to Ref.[13] and assembled into a unit housing with battery support. The sensor detection unit was

designed to operate over the frequency bandwidth of 0.6—10 Hz, with a gain factor of 1 V/pC. Figure 5.3 (b) shows the ME charge coefficient of the ME sensor unit as a function of temperature. The value of α_{me} at various temperatures was obtained previously by measuring the output signal of the ME sensor at different temperatures and then by computing the amplitude ratio between room temperature and the temperature dependent signals. By employing the ratios with respect to room temperature (1350 pC/Oe), the ME charge coefficients at other temperatures were then calculated. During measurement of the output signal, the coil (i.e., controlled source) was located above the cooler shield, centered on the sensor along the longitudinal direction of the laminate. The output signal in response to a constant AC signal was measured using a dynamic signal analyzer while driving the coil at a frequency of f=1 Hz via a lock-in amplifier. Details of the measurement can be found in [14]. In Figure 5.3 (b), one can clearly see with increasing temperature between $-50 \leq T \leq 50$ °Cthat the ME sensor unit gain factor α_{me} increased slightly, which can be attributed to changes in the piezoelectric charge coefficient (d_{33}). [12]

Next, we predicted the ME sensor units equivalent magnetic noise floor as a function of temperature using equations (1) and (2). Figure 5.4 shows the simulated equivalent magnetic noise at different temperatures in the frequency range of $1 < f < 10$ Hz. The values of C, tan δ, $R_{dc}$and α_{me} at different temperatures were pre-measured (see Figures 5.3a and 5.3b) and input into the noise model. In the noise model, the dominate noise source was assumed to be thermal polarization and DC resistance.

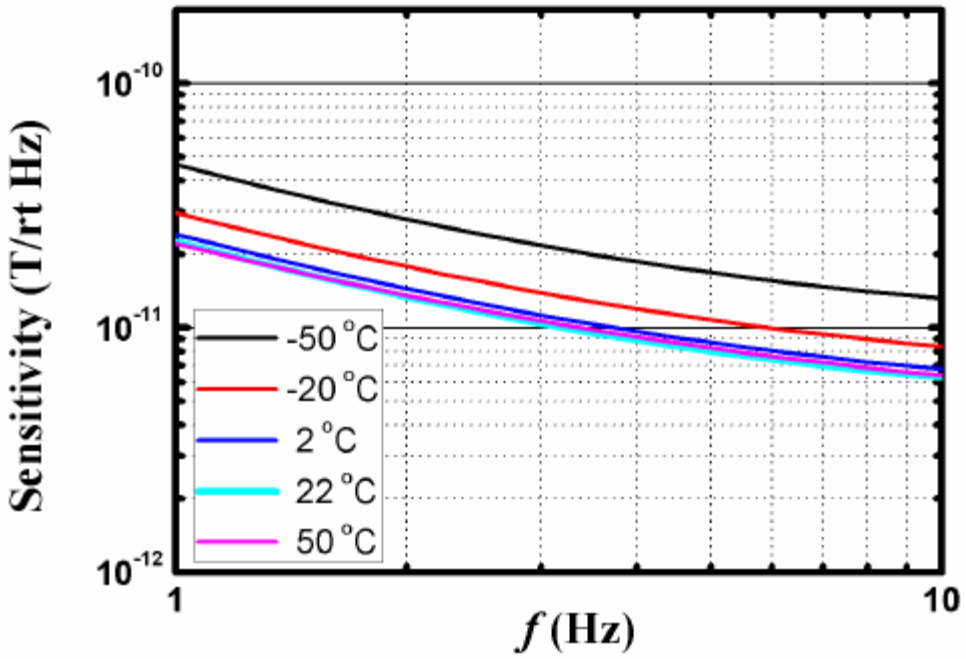

Figure 5.4 Predicted equivalent magnetic noise of the ME sensor unit as a function of temperature over the bandwidth of 1 <*f*< 10 Hz. The simulations were derived from Equations (5.1).

Finally, Figure 5.5 shows the measured equivalent magnetic noise floor of a ME sensor unit over the frequency range of 1 <*f* < 10 Hz at the different temperatures evaluated. These measurements were made by directly connecting the sensor unit to a dynamic signal analyzer (Stanford Research, SR-785). The data reveal that the equivalent magnetic noise floor was relatively invariant to temperature, having a value of 30 pT/√Hz at *f* = 1 Hz between 2 ℃ and 50 ℃. At lower temperatures, the equivalent magnetic noise floor increased to 50 pT/√Hz (-20°C) and 75 pT/√Hz (-50 ℃). Comparisons of Figures 5.4 and 5.5 will demonstrate good agreement between predicted and measured noise floor values. These studies reveal that ME laminate sensor units offer a viable magnetometer technology for applications in a real-world environment when temperature changes occur. We find that the low noise floors of ME sensors persist over the range of ambient temperatures that might be expected during an annual thermal cycle.

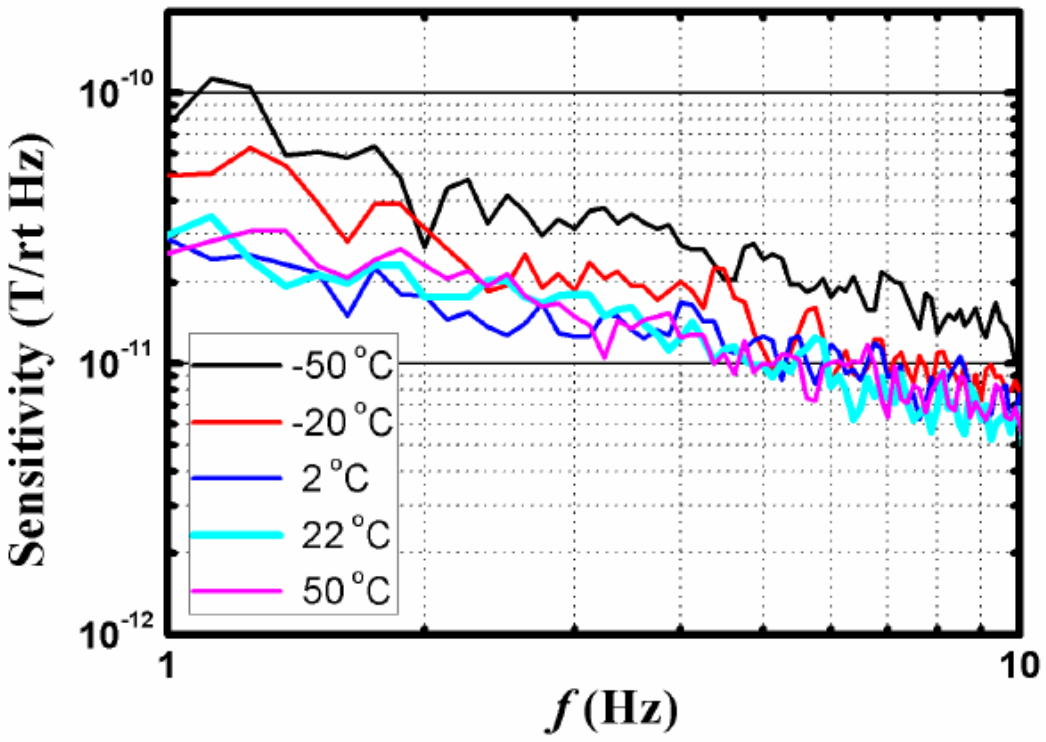

Figure 5.5 Measured equivalent magnetic noise spectra for a ME sensor unitat varioustemperaturesof-50 ℃ (black), -20 ℃ (red), 2 ℃ (blue), 22 ℃ (cyan), and 50 ℃ (pink). Please note that these measurements were done in a zero-Gauss vibration isolated chamber, in the absence of any intentional excitation.

5.3 Triple-axial Sensor for AC Dipole Localization

Recently, ME laminated composites consisting of layers of magnetostrictive Metglas and piezoelectric Pb(Zr, Ti)O_3 (or PZT) fiber have been developed for sensitive passive magnetometer applications at room temperature. Large enhancements in the ME voltage coefficient α_{ME} have been found in these ME laminated heterostructures comprised of piezoelectric and magnetoelectric layers: wherein the ME effect is a product to user, property of elastic forces between layers.[15-17] Incident magnetic fields change the shape of the magnetostrictive phase resulting in a strain on the adjacent piezoelectric phase. The induced strain in turn creates the electric polarization in the piezoelectric phase, resulting in an electric charge in response to an incident magnetic field.[18]

However, to date, the potential for using ME laminates to develop novel ME magnetic sensors for magnetic dipole localization in 3-D space has not yet been studied. Here, we will demonstrate a capacity for ME sensors in these regards while operating at

room temperature in a passive mode. A new grid search (GS) based algorithm is proposed to solve the equations for dipole location.

5.3.1 Detection method

5.3.1.1 Three-axial sensor

The ME laminate composites were made of tri-layers of Metglas/PZT-fiber/Metglas in a multi push-pull mode configuration. [18] Each surface of a core (2.5 cm × 1 cm × 180 μm) piezoelectric $Pb[Zr_xTi_{1-x}]O_3$ (PZT, x~0.52) fiber bundle (3195STD, CTS, Albuquerque, NM) was affixed to thin interdigitated (ID) electrodes deposited on Kapton® sheets by a two-part epoxy. The ID electrode pattern allowed for a symmetric poling of the piezoelectric fibers in a back-to-back pattern along their length axis. [8] Three layers (8 cm × 1 cm × 22 μm) of Metglas foils (7600F, Vitrovac Inc., Hanau, Germany) were then attached to the upper and lower surfaces of the Kapton® electrodes using the same epoxy. Permanent magnets were placed at either end of the ME laminates to provide a dc NdFeB magnetic bias (DA01-N52, K&J Magnetics, Inc) with diameter of 1.6 cm.The static ME charge coefficient α_{me} as a function of dc magnetic field H_{dc} was measured, having an value of α_{me}=1100 pC/Oe at an optimum bias of H_{dc}≈8 Oe according to Ref [19]. Next, we measured the equivalent magnetic noise of the ME laminate over a frequency range of $1<f<10$ Hz, which was found to have a value of less than 30 pT/√Hz at $f \geq 1$ Hz. This shows that ME laminate sensors can achieve high levels of sensitivity in a passive mode of operation.

Figure 5.6 gives a photo of a triple-axis ME detection system, where the upper part is the triple-axis ME sensor and the bottom is the charge amplifier detection electronics enclosed in a plastic solid housing (including batteries). The triple-axis sensors consisted of three ME single-axial sensors that were mutually perpendicular to each other enabling measurement of the three magnetic field components B_x, B_y and B_z. The sensors were placed in their mid-sections with respect to each other to prevent mutual interactions. We used the static charge amplifiers (CAs) designed to have a transfer function of 1 V/pC over the frequency bandwidth of $0.6 <f< 10$ Hz.[13]

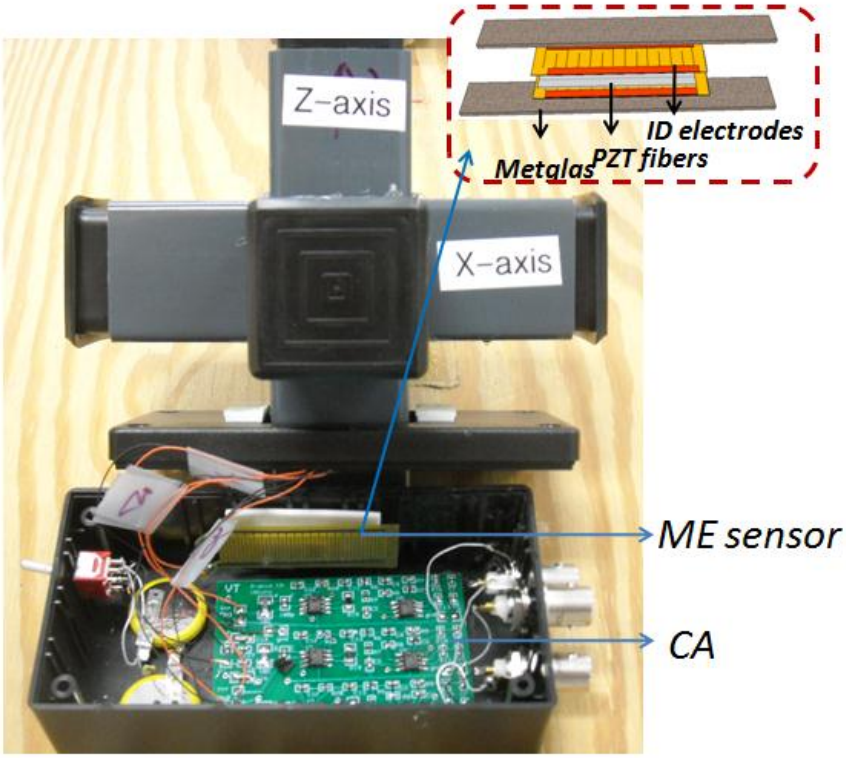

Figure 5.6 Photo of triple-axis ME sensor unit

5.3.1.2 Detection configuration

Figure 5.7 (a) illustrates the configuration of the dipole (illustrated by α, β and γ) and three tri-axis ME sensor devices (denoted as i, j, and k) used in this study. Each triple-axis sensor consisted of three single-axes ME sensor units, where the sensors were mutually perpendicular to each other to enable measuring the three magnetic field components B_x, B_y, and B_z. The corresponding CAs were enclosed in the bottom solid plastic housing of each sensor, including battery support. Triple-axis magnetometers i and j were separated by 40 cm in the x-direction, and the one k was separated from the i-j centerline by 30 cm in the y-direction. A datalogger was utilized to collect output signals from the CAs at 100 samples/sec, with a full-scale of 1 V and a dynamic range of 60 dB. MATLAB scripts were used to perform signal processing. The sensor detection units were placed parallel to each other, and the y-components of the sensors were all aligned with the geomagnetic field.

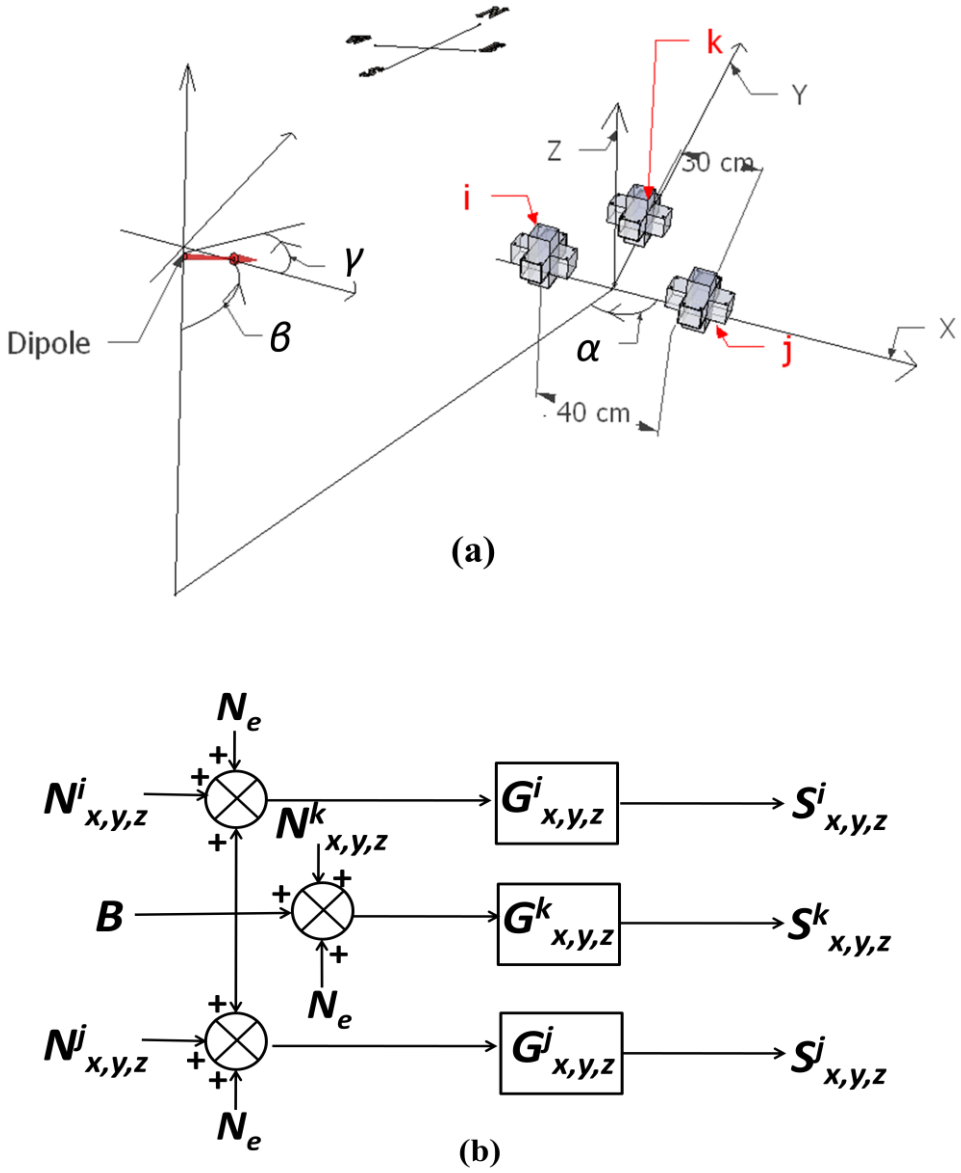

Figure 5.7 (a) Schematic illustration of test layout, where the tensor ME sensors are constructed in three linear orthogonal directions. The baseline between sensor i and j is 40cm and that between sensor k to the central point of sensor i and j is 30cm; (b) Block diagram of signal collection model.

To model the magnetic dipole, a solenoid coil was driven by a signal generator producing an AC sine wave signal B. Please note that the three triple-axis magnetometers (i, j, k) were exposed to the same external noise N_e; and that each one should have incoherent intrinsic noises of $N^i_{x,y,z}$, $N^j_{x,y,z}$, and $N^k_{x,y,z}$ respectively. [20] The dipole signal and noise sources from the nine sensors of the three triple-axis magnetometer were

integrated separately via a CA [21]. A block diagram of the signal collection is shown in Figure 5.7 (b). The gain of each sensor was $G^{i}_{x,y,z}$, $G^{j}_{x,y,z}$, and $G^{k}_{x,y,z}$. The charge signals that were detected were converted into the voltage ones ($S^{i}_{x,y,z}$, $S^{j}_{x,y,z}$, and $S^{k}_{x,y,z}$), which were then recorded by a datalogger.

5.3.2 Theory

The magnetic field B created by a dipole with a moment **M** at distance **R** from the dipole is given as

$$B(x,y,z) = \frac{\mu_0}{4\pi}\frac{3R(M\cdot R) - MR^2}{R^5}\ ; \quad (5.2)$$

Where $\mu_0=4\pi\cdot10^{-7}$ H/m is the permeability of free space, and R is the scaled distance. The tensor matrix form for equation (1) is

$$\begin{vmatrix} B_x \\ B_y \\ B_z \end{vmatrix} = \frac{\mu_0}{4\pi R^3}\begin{vmatrix} 3x'^2-1 & 3x'y' & 3x'z' \\ 3y'z' & 3y'^2-1 & 3y'z' \\ 3z'x' & 3z'y' & 3z'^2-1 \end{vmatrix}\begin{vmatrix} M_x \\ M_y \\ M_z \end{vmatrix}\ ; \quad (5.3)$$

where

$$x' = \frac{x}{R}\ ,\quad y' = \frac{y}{R}\ ,\quad z' = \frac{z}{R},$$

$$R = \sqrt{x^2 + y^2 + z^2}\ . \qquad (5.4)$$

After normalizing, the components of the scalar magnetic moments of ***M*** are

$$M_x = sin\beta cos\gamma M\ , \qquad M_y = sin\beta sin\gamma M\ ,\quad M_z = cos\beta M\ . \qquad (5.5)$$

Where β is the angle between the dipole moment and the z-axis, and γ is that between the dipole moment and the x-axis. Equation (3) can then be rewritten as:

$$\begin{vmatrix} B_x \\ B_y \\ B_z \end{vmatrix} = \frac{\mu_0 M}{4\pi R^3}\begin{vmatrix} 3x'^2-1 & 3xy & 3xz \\ 3yz & 3y'^2-1 & 3yz \\ 3zx & 3zy & 3z'^2-1 \end{vmatrix}\begin{vmatrix} sin\beta cos\gamma \\ sin\beta sin\gamma \\ cos\beta \end{vmatrix}\ . \quad (5.6)$$

If a solenoid has surface area, S, current, I, and N identical turns, its moment strength M takes the form M = INS.

A Grid Search (GS) algorithm provides a robust mathematical approach for determining the maximum likelihood of an objective function. [22] Here, we adopted an iterative GS refinement method to perform a systematic search for a dipole over a defined grid of points. As a first step, a 3-dimentional initial region $\psi = [x_1, x_2] \times [y_1, y_2] \times [z_1, z_2]$

$\in D^3$ was established containing the source and the triple-axis receivers (i, j, and k). The equivalent distance grid can then be defined as [23]

$$\psi = \{(x, y, z)^T \; x = x_1 + \frac{k_x}{n+1}(x_2 - x_1), \quad k_x = 1, \cdots n,$$
$$y = y_1 + \frac{k_y}{n+1}(y_2 - y_1), \quad k_y = 1, \cdots n,$$
$$z = z_1 + \frac{k_z}{n+1}(z_2 - z_1),$$
$$k_z = 1, \cdots n. \; \}. \qquad (5.7)$$

Please note that an evaluation was applied during each mutation and only a single newborn point was re-used in the next iteration. To this end, the problem evolved into searching sub-optimal points statistically among limited possible solutions and restricting their resolutions, rather than solving equation (5.3). Thus the applied GS became an efficient means by scanning regions of feature space to quickly approach an area with the high possibility of leaving an object to be detected. Accordingly we then spent most of the computational time where there was the largest probability of find a dipole.

5.3.3 Results

In order to locate magnetic dipoles by the GS algorithm, a test was performed where a solenoid "dipole" driven at 7 Hz was placed at (0.5m, -1.0m, 0.74m) with (α, β, γ) = (26.58°, 90°, 90°) relative to the origin of the coordinate system. Representative PSD plots of the received sensor signal (RSS) for the three triple-axis gradiometers (i, j, and k) are presented in Figure 5.8 (a), (b) and (c) respectively. The amplitude of the 7 Hz peaks in each the PSD is the dipole that we are trying to localize.

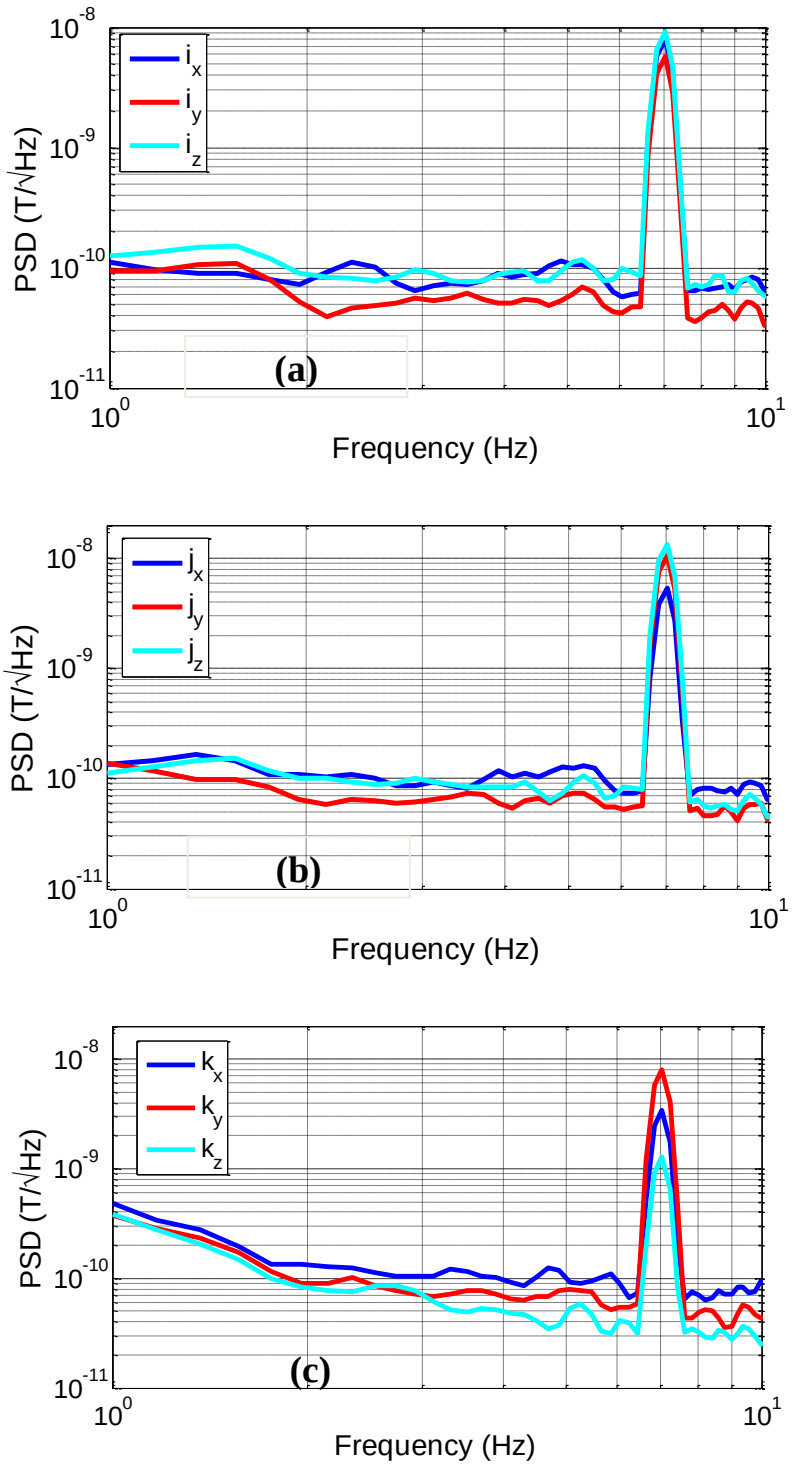

Figure 5.8 Power spectral density of applied AC magnetic dipole at f=7 Hz on (a) sensor i, (b) sensor j and (c) sensor k in x-axis (blue curve), y-axis (red curve) and z-axis (cyan curve)

Execution of the GS algorithm estimation for dipole localization yielded (0.46m, -1.24m, 0.77m). This corresponded to 6.0%, 10% and 13.5% errors in the x, y and z

locations respectively, and error in range of 9.02% relative to the actual position as illustrated in Figure 5.9 (a). Different orientations of the dipoles were considered and tests were performed with changes in (α, β, γ), as illustrated in Figure 5.9 (a), (b) and (c). The results show as the dipole angles change that the accuracy of localization decreased modestly. Figure 5.9 (a), (d) and (e) demonstrate that the accuracy decreases as target distance along the y-direction increases. All the data and localization error were summarized in Table 5.1.

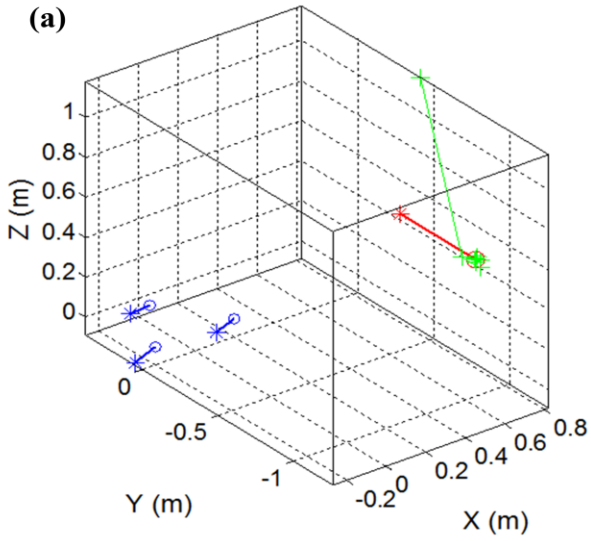

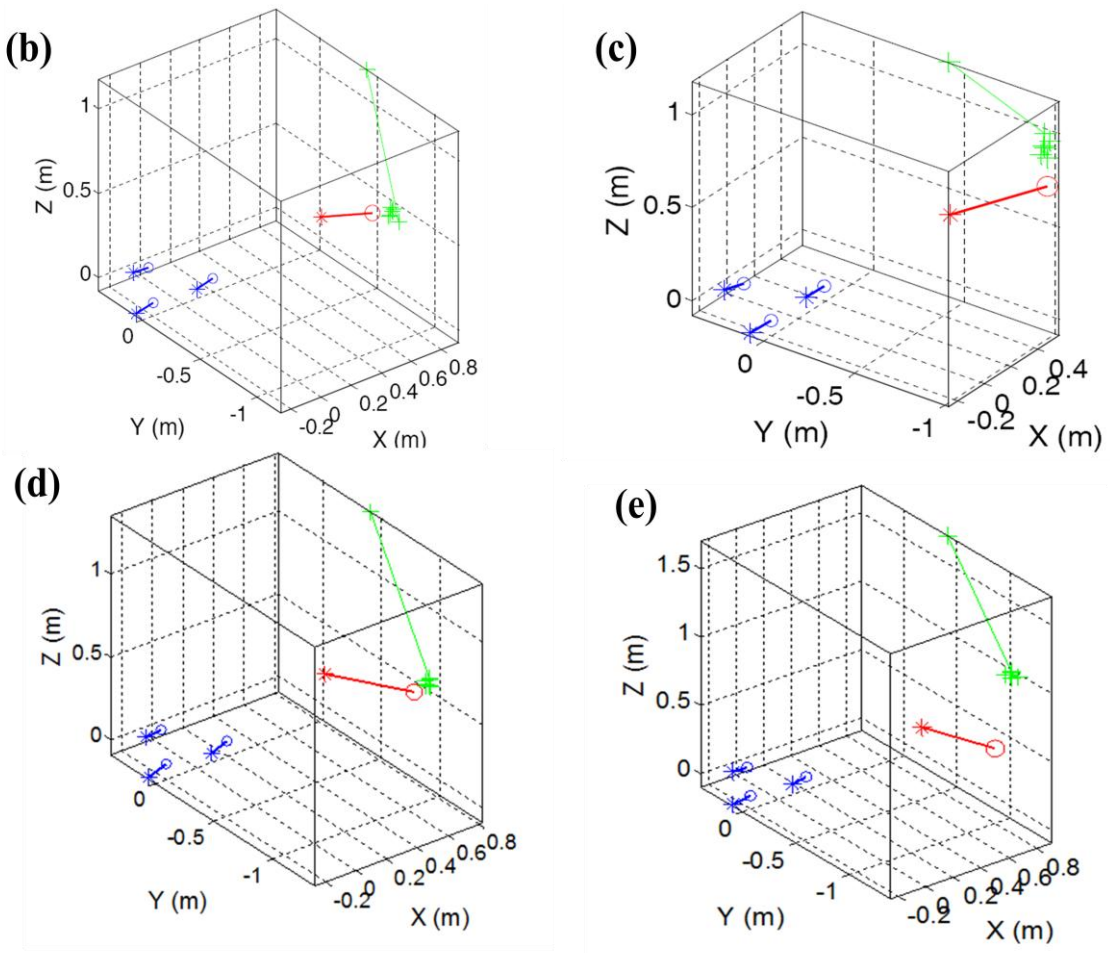

Figure 5.9 Estimation for dipole position (green cross) based on SRR (blue line and star head) by three tensor ME sensors (blue open circles) responding to solenoid dipole (red open circle) with moment direction (red line and star head) with different dipole moment directions as in (a), (b) and (d), and with different distance in y as in (a), (d) and (e).

Table 5.1 Target dipole localization as a function of (α, β, γ) and y

Test	(α, β, γ) in unit of degree	True position (x, y, z) in unit of m	Search position (x, y, z) in unit of m	Localization error in 3-axis	Errors in range
a	*(26.58, 90, 90)*	*(0.5, -1, 0.74)*	*(0.47, -1.10, 0.84)*	*(6%, 10%, 13.5%)*	9.02%
b	*(26.58, 26.58, 90)*	*(0.5, -1, 0.74)*	*(0.49, -1.15, 0.80)*	*(2%, 15%, 8.1%)*	*10.69%*
c	*(26.58, 26.58, 68)*	*(0.5, -1, 0.74)*	*(0.49, -0.98, 0.93)*	*(2%, 2%, 25.7%)*	*7.19%*
d	*(26.58, 90, 90)*	*(0.5, -1.2, 0.74)*	*(0.47, -1.33 0.87)*	*(6%, 11.4%, 18.7%)*	*10.79%*
e	*(26.58, 90, 90)*	*(0.5, -1.4, 0.74)*	*(0.68, -1.26, 1.15)*	*(36%, 10%, 55.4%)*	*10.59%*

Our findings demonstrate that we can use triple-axis ME sensors to locate magnetic dipoles with good precision. The localization was made computationally efficient by use of a GS algorithm. Such efficient localization of magnetic dipole is important to application of passive ME magnetic sensors.

5.3.4 Localization error analysis

In order to analyze the error sources, we then performed simulations to examine the error from the sensor location, the sensor calibration and the geometric sensor configuration respectively when assuming that the dipole was located at (0.5m, -1.0m, 0.74m) with (α, β, γ) = (26.58°, 90°, 90°). First, we simulated the localization accuracy of an ideal scenario using the same sensor location, calibration and configuration as above for the measurements which can be taken as a comparison reference. Figure 5.10 (a) shows the simulation results for a reference corresponding to 1.1%, 0.207% and 0.39% errors in the x, y and z locations. Then, we allowed one element to change each time, while holding the others constant. For example, we investigated the error from the sensor location by supposing the magnetometer i was placed by 1 cm shorter in x-axis at (0.19m, 0m, 0m) instead of (0.2m, 0m, 0m), as shown in Figure 5.10 (b). The simulation yielded a dipole location of (0.52m, -1.03m, 0.74m) with error in the range of 2.12%.

The error from sensor calibration was also determined. Assuming that the x-component sensor of magnetometer i was calibrated with a 10% error arising from either α_{ME} of the ME laminate composite or gain transfer function of the CA. Figure 5.10 (c) shows that the localization errors increased significantly in the x- and z-axis.

In most of sensing system, target localization accuracy relies on the location of the sensor nodes. [24, 25] Accordingly, we considered error from sensors configuration. Suppose magnetometers i and j were separated by a baseline of 20cm in the x-direction with i (-0.1m, 0, 0) and j (0.1m, 0, 0), magnetometer k was placed the position k (0, 0.3m, 0). Figure 6 (d) illustrates that the localization error is a little higher than that of the reference. All the simulation data are summarized in Table 5.2.

Clearly these simulations results demonstrate that measurement errors are likely created by sensor location, sensor calibration and sensor configuration in a given range. These errors add together to affect the target dipole location accuracy. We find that the error mainly results from the sensor calibration error.

Table 5.2 Simulation for target dipole localization with target position at (0.5m, -1.0m, 0.74m) with (α, β, γ) = (26.58°, 90°, 90°).

Simulation	Search position (x, y, z) in unit of m	Localization error ir axis	Errors in rang
Reference	*(0.494, -1.00, 0.737)*	*(1.1%, 0.207%, 0.39%)*	*0.29%*
Sensor location	*(0.52, -1.03, 0.74)*	*(3.8%, 3.3%, 0)*	*2.12%*
Sensor calibration	*(0.62, -1.03, 0.65)*	*(24%, 3.3%, 12.2%)*	*1.37%*
Sensor configuration	*(051, -0.997, 0.734)*	*(2.2%, 0.26%, 0.73%)*	*0.13%*

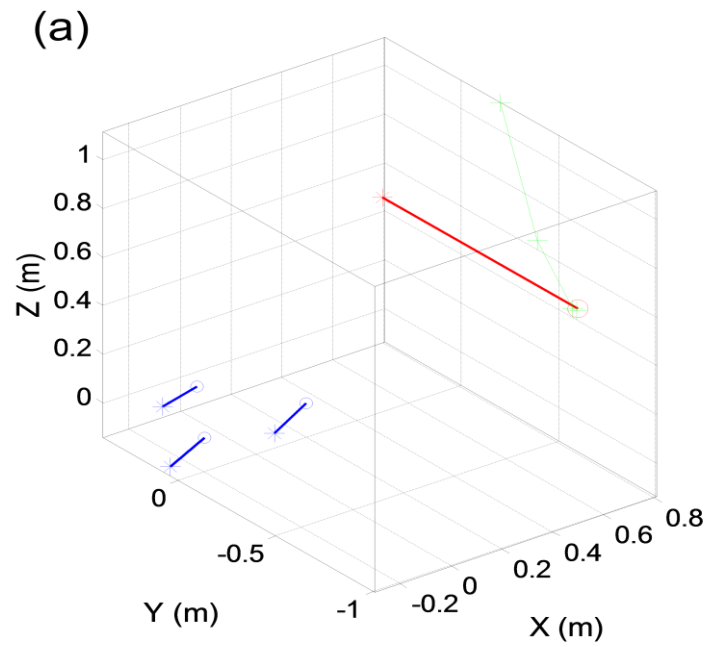
(a)
Z (m)
1
0.8
0.6
0.4
0.2
0
0
-0.5
-1
Y (m)
-0.2
0
0.2
0.4
0.6
0.8
X (m)

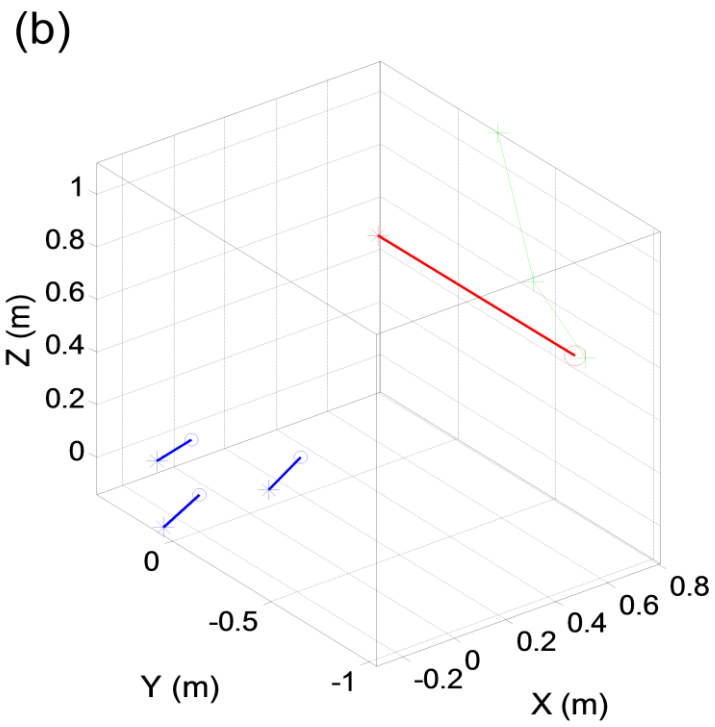
(b)
Z (m)
1
0.8
0.6
0.4
0.2
0
0
-0.5
-1
Y (m)
-0.2
0
0.2
0.4
0.6
0.8
X (m)

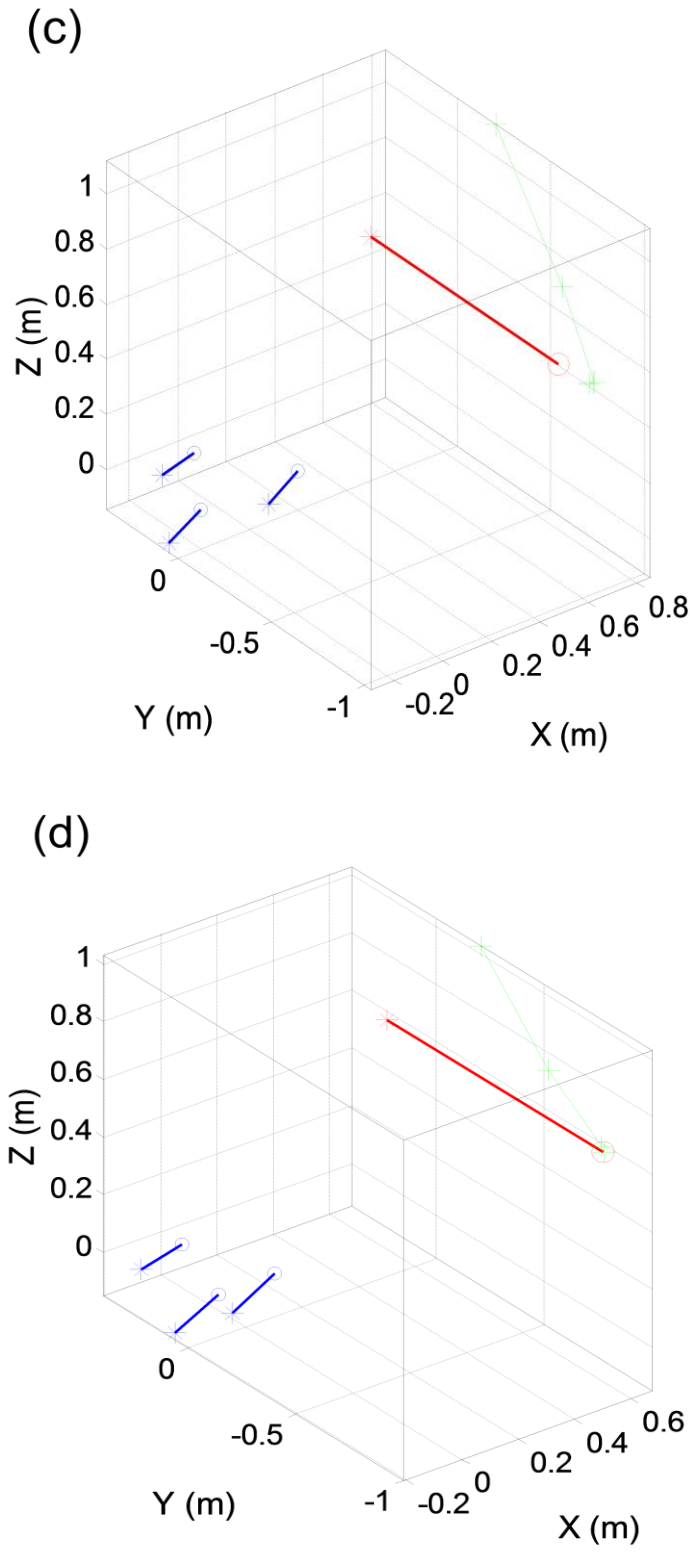

Figure 5.10 Simulations for dipole position when compared with (a) reference to analyze error from (b) sensor location, (c) sensor calibration and (d) sensor configuration

5.4 Summary of This Section

We have investigated the temperature dependence of the performance of ME laminate sensors consisting of Metglas foils bonded to a PZT core. The sensitivity of the sensors to small changes in AC magnetic fields and the equivalent magnetic noise floor were studied over the temperature range of $-50 \leq T \leq 50$ °C. Our results demonstrate that the performance of the sensor was quite stable to temperature changes. The equivalent magnetic noise floor was found to be nearly constant at 30 pT/√Hz (f =1 Hz) over the temperature range investigated. Furthermore, we have applied a noise model to predict the temperature dependent behavior based on input parameters of the C, tan δ, and R_{dc}. We note that good agreement was found between predicted and measured noise floors.

A functional triple-axis ME sensor can be used as magnetometer for AC dipole localization. Measurements demonstrate good localization with various sensing range and dipole moment orientations. Simulation for error sources show that the localization errors of the system are limited mainly by the sensor calibrations. Thus it will be instructive for us to further control error and improve the localization precision. Accordingly, our investigation demonstrates a novel magnetometer having features of being passive and power-efficient, having a room temperature mode of operation, and a feasibility to operate in an open environment.

References:

[1] R. Stolz, V. Zakosarenko, M. Schulz, A. Chwala, L. Fritzsch, H.-G. Meyer, and E. O. KÖstlin, "Magnetic full-tensor SQUID gradiometer system for geophysical applications," *The Leading Edge*, vol. 25, 2006.

[2] S. Y. Cheung, S. C. Ergen, and P. Varaiya, "Traffic Surveillance with Wireless Magnetic Sensors," University of Berkeley2007.

[3] A. S. B. Ginzburg, L. Frumkis, B.Z. Kaplan, N. Salomonski, "Investigation of advanced data processing technique in magnetic anomaly detection systems," presented at the 1st International Conference on Sensing Technology, Palmerston North, New Zealand, 2008.

[4] R. Zhu and Z. Zhou, "A real-time articulated human motion tracking using tri-axis inertial magnetic sensors package," *IEEE TRANSACTIONS ON NEURAL SYSTEMS AND REHABILITATION ENGINEERING*, vol. 12, pp. 295-302, 2004.

[5] R. H. Koch, G. A. Keefe, and G. Allen, "Room temperature three sensor magnetic field gradiometer," *American Institute of Physics*, vol. 67, pp. 230 - 235 1996.

[6] J. E. Fine, "Magnetic Measurements of Military Vehicles at Eglin AFB," Applied Physics Laboratory/Johns Hopkins University,, Laurel, MD2003.

[7] J. Ding, S. Y. Cheung, C. Tan, and P. Varaiya, "Vehicle Detection by Sensor Network Nodes," Institute of Transportation Studies, UC Berkeley2004.

[8] J. Das, J. Gao, Z. Xing, J. F. Li, and D. Viehland, "Enhancement in the field sensitivity of magnetoelectric laminate heterostructures," *Applied Physics Letters*, vol. 95, p. 092501, 2009.

[9] J. Q. Gao, J. Das, Z. P. Xing, J. F. Li, and D. Viehland, "Comparison of noise floor and sensitivity for different magnetoelectric laminates," *Journal of Applied Physics*, vol. 108, Oct 15 2010.

[10] Y. Wang, D. Gray, D. Berry, J. Gao, M. Li, J. Li, and D. Viehland, "An Extremely Low Equivalent Magnetic Noise Magnetoelectric Sensor," *Advanced Materials*, vol. 23, pp. 4111-4114, 2011.

[11] Z. Xing, J. Li, and D. Viehland, "Noise and scale effects on the signal-to-noise ratio in magnetoelectric laminate sensor/detection units," *Applied Physics Letters*, vol. 91, p. 182902, 2007.

[12] M. W. Hooker, "Properties of PZT-Based Piezoelectric ceramics," Langley Research Center, Hampton, Virginia1998.

[13] Z. P. Xing, J. Y. Zhai, S. X. Dong, J. F. Li, D. Viehland, and W. G. Odendaal, "Modeling and detection of quasi-static nanotesla magnetic field variations using magnetoelectric laminate sensors," *Measurement Science and Technology*, vol. 19, p. 015206, 2008.

[14] J. Gao, J. Das, Z. Xing, J. Li, and D. Viehland, "Comparison of noise floor and sensitivity for different magnetoelectric laminates," *Journal of Applied Physics*, vol. 108, p. 084509, 2010.

[15] S. X. Dong, J. Y. Zhai, N. G. Wang, F. M. Bai, J.-F. Li, and D. Viehland, "Fe–Ga/Pb(Mg1/3Nb2/3)O3–PbTiO3 magnetoelectric laminate composites," *Applied Physics Letters* vol. 87, pp. 222504 - 222504-3 2005.

[16] K. Mori and M. Wuttig, "Magnetoelectric coupling in Terfenol-D/polyvinylidenedifluoride composites," *Applied Physics Letters*, vol. 81, p. 100, 2002.

[17] J. Zhai, S. Dong, Z. Xing, J. Li, and D. Viehland, "Giant magnetoelectric effect in Metglas/polyvinylidene-fluoride laminates," *Applied Physics Letters*, vol. 89, p. 083507, 2006.

[18] S. Dong, J. Zhai, J. Li, and D. Viehland, "Near-ideal magnetoelectricity in high-permeability magnetostrictive/piezofiber laminates with a (2-1) connectivity," *Applied Physics Letters*, vol. 89, p. 252904, 2006.

[19] Y. Shen, J. Gao, Y. Wang, J. Li, and D. Viehland, "Thermal stability of magnetoelectric sensors," *Applied Physics Letters*, vol. 100, p. 173505, 2012.

[20] Y. Shen, J. Gao, L. Shen, D. Gray, J. Li, P. Finkel, and D. Viehland, "Analysis of the environmental magnetic noise rejectionby using two simple magnetoelectric sensors," *Sensors and Actuators A: Physical* 2011.

[21] A. Barzilai, T. VanZandt, and T. Kenny, "Technique for measurement of the noise of a sensor in the presence of large background signals," *Review of Scientific Instruments*, vol. 69, 1998.

[22] R. A. Thisted, *Elements of Statistical Computing.*: Chapman and Hall., 1988.

[23] J. Kim, "Iterated Grid Search Algorithm on Unimodal Criteria," Doctor of Philosophy Statistics, Virginia Polytechnic Institute and State University, Blacksburg, 1997.

[24] E. Olson, J. J. Leonard, and S. tELLER, "Robust Range-Only Beacon Localization," *2004 IEEE/OES In Proceedings of Autonomous Underwater Vehicle*, pp. 66 - 75 2004.

[25] J. Liu, Y. Zhang, and F. Zhao, "Robust distributed node localization with error management," in *MobiHoc '06 Proceedings of the 7th ACM international symposium on Mobile ad hoc networking and computing* New York, NY, USA, 2006, pp. 250-261.

CHAPTER 6:

DETECTION AND IDENTIFICATION OF DC SOURCE

6.1 Introduction

The necessity to detect hidden ferromagnetic subjects has led to the development of several detection techniques that feature magnetic anomaly detection. This process relies on the fact that magnetometers (e.g. fluxgate, giant magnetoresistors, optically pumped magnetometers, etc.) are able to sense anomalies in the Earth's magnetic field produced by the object in question.[1-3]

There are basically two types of magnetic anomaly detection systems: search and alarm. In the search system, magnetic sensors are mounted onto a moving platform, which then look for ferromagnetic targets by surveying specific areas.[4]That target is subsequently manifested as a special magnetic anomaly signature along the predefined paths passing in the vicinity of the target. However, due to the fact that the piezoelectric phase in an ME sensor is susceptible to motion-incurred vibrational noise, this search system approach is not currently a viable option. In contrast, the alarm system makes use of a stationary instrument that produces an alarm signal when a ferromagnetic target passes nearby the magnetic sensor. Because the distance between the target and sensor can be assumed to be noticeably exceeding target dimensions, the target magnetic field can be considered to be a dipole model. In other words, the resulting signal is a time-dependent magnetic field that contributes to the mutual motion of the dipole and sensor.

Here, my approach for localization, detection and identification of the DC source (e.g., in a vehicle) is based on the alarm system, described in Section 6.2. Presently, magnetometers of various types have been widely used for detecting and characterizing a dc source by analyzing small anomalies in the Earth's magnetic field. However, there is a conspicuous problem associated with accurately detecting small signals and estimating target parameters in the presence of environmental noise and interference, such as stray electromagnetic signals, vibration, and thermal agitation. In the present work detailed in Section 6.2, my investigation covers two types of magnetic sensors, whereby the first one (i.e., a fluxgate) serves as a reference for comparing findings with the second one (an ME

sensor in alarm mode), with the goal of determining their detection sensitivity in an open environment responding to moving vehicles. This non-intrusive ME sensor system with a larger sensing range is viable for detecting and recognizing vehicle-induced magnetic signatures in an outdoor (open) environment. I also developed a finite element simulation method capable of predicting any likely magnetic anomalies in a geomagnetic field.

As described in Section 6.3, the magnetic flux distraction effect can be employed by an ME sensor and gradiometer to detect and identify a stable DC source with an external driving signal. A magnetic flux distraction effect caused by a nearby metallic material was investigated using Metglas/PMN-PT laminated magnetoelectric (ME) sensors. Taking advantage of this flux distraction, an ME sensor can perform an accurate search for metallic targets of different dimensions and at various distances. Detection results and simulations were in good agreement. The results demonstrate an effective means to employ stationary ME sensors and gradiometers for dc magnetic search applications. Coherence analysis was carried out to confirm that the two ME sensors were not perfectly accordant in amplitude and phase performance, which does not allow the gradiometer to thoroughly reject the common noise.

6.2 Moving DC source detection for vehicle

Vehicle detection, whether non-intrusive or intrusive, is important for an Intelligent Transportation System (ITS), which is an approach that has been initiated in many countries to address increasing traffic congestion problems.[5] The commercial devices for vehicle detection are non-intrusive ones, which are mounted above the surface of roadways such as video image processors, microwave radar, and acoustic and infrared sensors. [6] However, the performance of these systems are easily compromised by adverse weather conditions.

To circumvent these environmental interferences, intrusive methods based on magnetic sensor technologies, such as magnetoresistor and fluxgate magnetometers, have recently been studied for vehicle detection systems due to reduced susceptibility to environmental stresses. [7-9] The principle of magnetic sensors is based on the ability to detect a perturbation (i.e., a magnetic anomaly) to Earth's magnetic field when a ferromagnetic object passes nearby. The most important vehicle source of magnetic fields is the ferromagnetic material used in the construction of engines, axles, gearboxes,

and driveshafts of vehicles. However, presently available magnetometers have a minimum detectable signal of about 0.01-0.2 nT and limited sensing range which requires tunneling under roadway, costing significant installation and maintenance expense. [10, 11]

Laminate magnetoelectric (ME) composites have been investigated as high sensitivity, low noise, room temperature and low power consuming magnetic sensors. [12-15] These ME laminates are engineered from magnetostrictive layer(s) elastically bonded to a piezoelectric one. Thus, a charge is created in the core piezoelectric layer by a strain induced in the magnetostrictive foils excited by an incident magnetic field. Optimized heterostructures of a core $Pb(Zr,Ti)O_3$ (PZT) fiber layer with Metglas have been shown to have magnetic noise floors of $\leq$ 100 pT/√Hz at 1 Hz. [16] Recent investigations to replace the PZT fibers with $0.7Pb(Mg_{1/3}Nb_{2/3})O_3$-$0.3PbTiO_3$ (PMN-PT) single crystal ones have yielded ME laminate composites with a much lower magnetic noise floor of $\leq$ 5 pT/√Hz at 1 Hz. [17] However, an investigation of the potential of ME laminates for moving dc source detection, such as vehicle induced magnetic perturbation, not yet been reported.

6.2.1 Detection system

The ME laminate composites were made of tri-layers of Metglas/PZT-fiber/Metglas in a multi push-pull mode configuration. [18] Each surface of a core (2.5 cm × 1 cm × 180 μm) piezoelectric $Pb[Zr_xTi_{1-x}]O_3$ (PZT, x~0.52) fiber bundle (CTS, Albuquerque, NM) was affixed to thin interdigited (ID) electrodes deposited on Kapton® sheets by a two-part epoxy. The ID electrode pattern allowed for a symmetric poling of the piezoelectric fibers in a back-to-back pattern along their length axis. [16] Three layers (8 cm × 1 cm × 22 μm) of Metglas foils (7600F, Vitrovac Inc., Hanau, Germany) were then attached to the upper and lower surfaces of the Kapton® electrodes using the same epoxy. A schematic is shown in the inset of Figure 6.1 (a). Permanent magnets were placed at either end of the ME laminates to provide a dc magnetic bias as shown in Figure 6.1 (b). The ME charge coefficient α_{me} as a function of dc magnetic field H_{dc} was measured, having an value of α_{me}=1100 pC/Oe at an optimum bias of $H_{dc}\approx$8 Oe according to Ref [19]. Next, we measured the equivalent magnetic noise of the ME laminate over a frequency range of $1<f<10$ Hz, which was found to have a value of less than 30 pT/√Hz

at $f \geq 1$ Hz. This shows that ME laminate sensors can achieve high levels of sensitivity in a passive mode of operation.

The triple-axis sensors consisted of three ME single-axial sensors that were mutually perpendicular to each other enabling measurement of the three magnetic field components B_x, B_y and B_z. The sensors were placed in their mid-sections with respect to each other to prevent mutual interactions. We used the charge amplifiers (CAs) designed to have a transfer function of 1 V/pC over the frequency bandwidth of $0.6 < f < 10$ Hz. [20]

Thin aluminum sheets were used to cover the triple-axis sensors to prevent electromagnetic interference (EMI).An A/D convertor data acquisition device CR5000 Datalogger (Campbell Scientific, Inc., USA) was used to collect output signals from the three tri-axial sensors with a 100 Hz sample rate, a full-scale of 1 V and a dynamic range of 60 dB. [21] Post signal processing was implemented via Matlab. For comparisons purpose, we also used a tri-axial piezoelectric sensor (PE) and a fluxgate magnetometer (Billingsley Aerospace & Defense TFM 100G2, USA).The PE sensor was fabricated using the same material and method as the ME sensor except that the structure is composed only of a core piezoelectric layer engineered with a pair of Kapton ID electrodes, as shown in figure 6.1(c).

6.2.2 Experimental Results

Tri-axial ME, PE and fluxgate sensors were placed on the ground in a line atthe same closest path approach (CPA) as shown in Figure 6.1 (d). The CPA was set equal to 5 meters, with respect to slow-moving vehicle (a standard SUV) passing by in west to east directions. The magnetic field induced by a moving vehicle can be depicted as that of a dipole with good approximation when detection distances are beyond a car length. Figure. 6.1 (e) depicts the three-dimensional components of the magnetic fields in our experimental settings. The x-component is parallel to the line of vehicle moving orientation, y-component is perpendicular to moving direction and z-component is vertical to the roadway surface. It should be noted that this moving magnetic field depends on the vehicle mass, length, shape, distance from the sensor, and orientation with respect to the sensor.

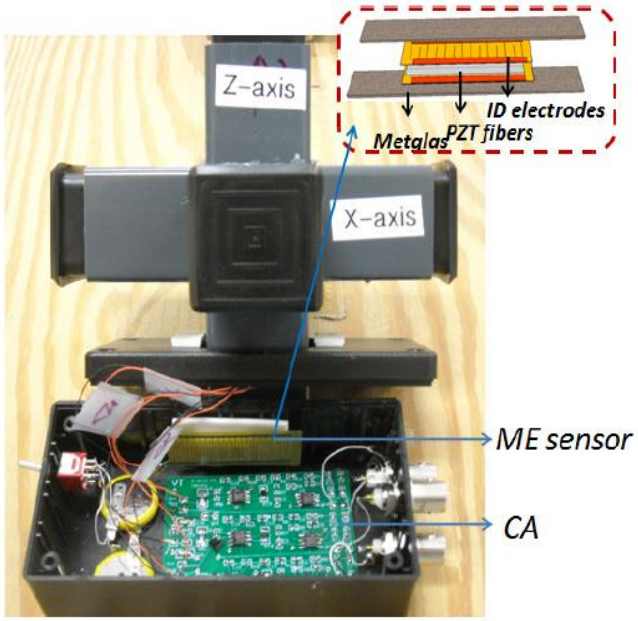
Z-axis
X-axis
ID electrodes
PZT fibers
Metglas
ME sensor
CA

(a)

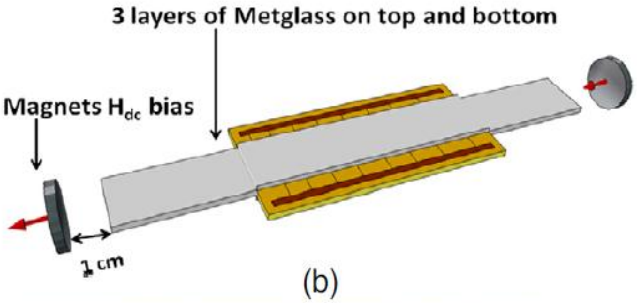
3 layers of Metglass on top and bottom
Magnets H_{dc} bias
1 cm

(b)

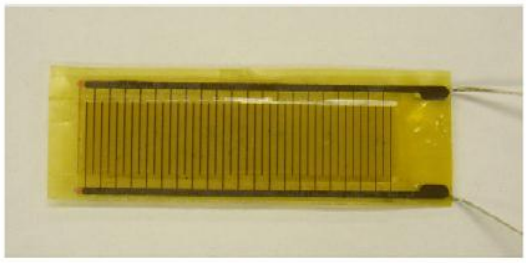

(c)

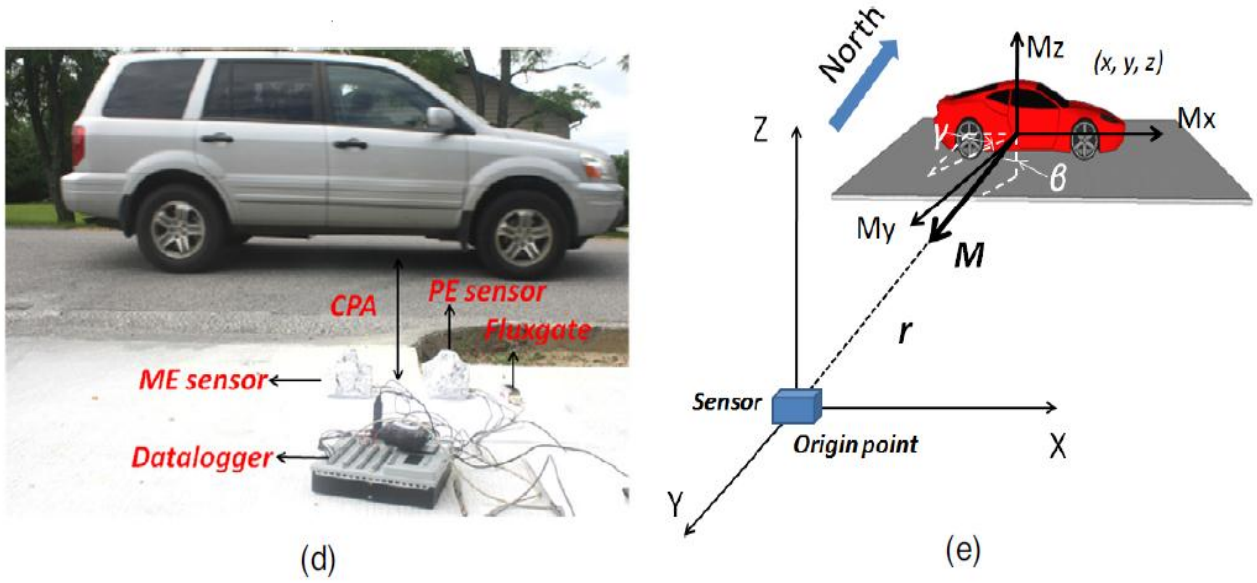

Figure 6.1 (a) Photograph of the prototype triple-layer ME sensor detection unit comprised of ME sensor and charge amplifier. Inset is the configuration of Metglas/PZT/Metglas ME laminates. (b) Schematic graph of the ME sensor with permanent magnets placed at two ends. (c) Photograph of PE sensor, (d) photograph of the vehicle detection system setup. (e) Three-dimensional components of the vehicle-induced magnetic fields to sensor where the x-component is parallel to the line of vehicle motion, the y-component is perpendicular to vehicle motion and the z-component is vertical to the road surface.

In the top and bottom graphs of Figure6.2 (a), ME and fluxgate sensors both exhibit typical magnetic field signals along all three axes in the time domain, which have distinctive waveform features in the time history graph when t = 2.5 s. Please note that the PE sensor did not have notable signal profiles, as can be seen in middle picture of Figure 6.2 (a). By comparing thetop two graphs of Figures 2 (a), one can clearly see that the induced signals from the tri-axial ME sensor near 2.5 sdid not have vibration or acoustic contributions. However, the obtained signal profile for the ME sensor and fluxgate were similar, yielding information about the magnetic signatures of the moving vehicles. Please note that the output signal of the fluxgate had a much smaller amplitude than that of the ME sensor, indicating that fluxgates have a lower sensitivity.

The ME sensor's output signal was then transformed into an equivalent magnetic field using α_{me} of the laminate and the transfer function of the CPA, as shown in Figure 6.2 (b). One can clearly see the induced magnetic field anomaly profile and strength in all

three field components detected by the ME sensor at a CPA=5 m. The values of B_x and B_y show a magnetic anomaly around 150 nT along the x and y directions; whereas B_z has a relatively smaller amplitude of about 100 nT along the z axis.

Similar measurements were performed at CPA = 7, 9, 11 and 13 m. The output signal for all three field components are summarized in Figure 2 (c), which shows that the magnetic field strength decreases with increasing CPA distance for both types of sensors. It should be noted that the ME sensor can discern vehicle signals at a CPA of up to 13 m; whereas for the fluxgate, it was difficult to differentiate target signals from background noise (signal to noise ratio < 2) at a CPA = 11 m, as shown in the inset of Figure 6.2 (c). These results imply that compared to available magnetometer devices, ME sensors are more sensitive and have longer detection ranges that may be reliable for non-intrusive vehicle detector.

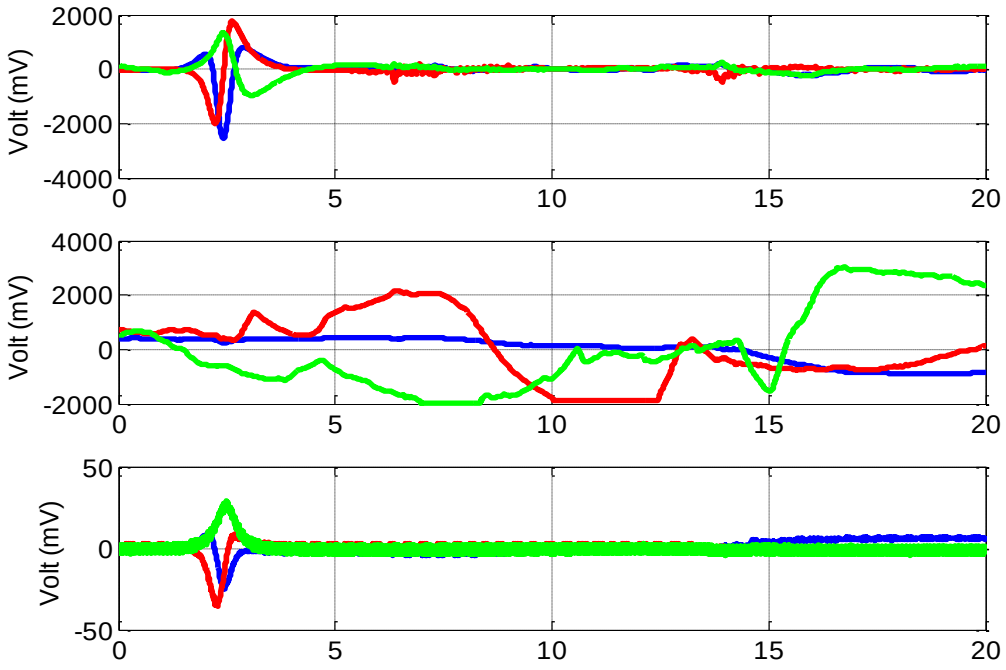

(a)

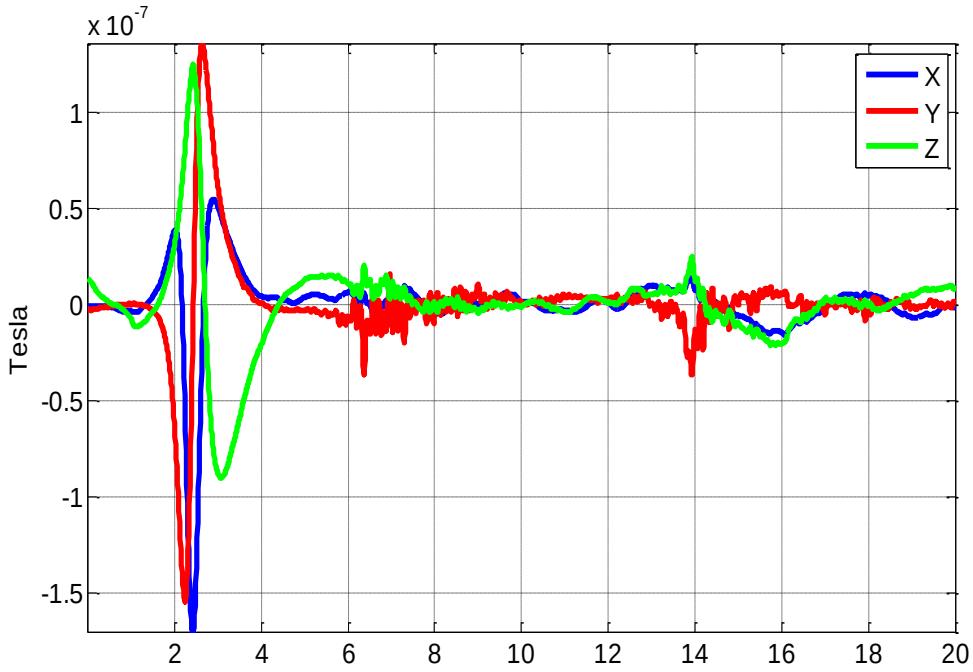
x 10^-7
X
Y
Z
Tesla
1
0.5
0
-0.5
-1
-1.5
2
4
6
8
10
12
14
16
18
20

(b)

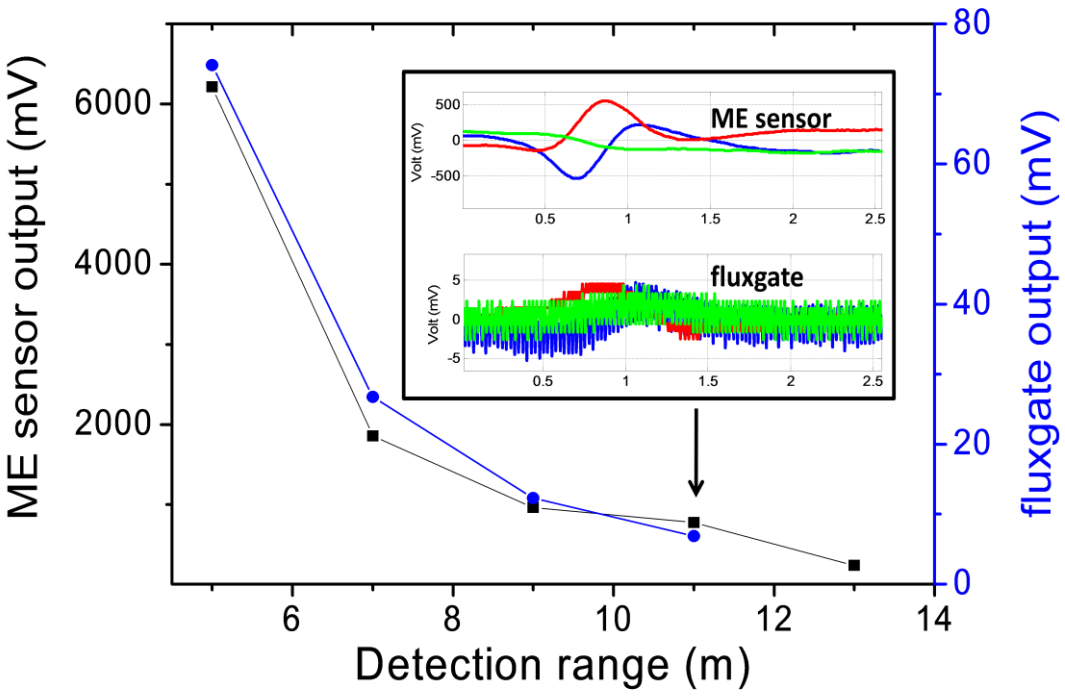
ME sensor output (mV)
fluxgate output (mV)
Detection range (m)
6000
4000
2000
80
60
40
20
0
6
8
10
12
14
ME sensor
fluxgate
Volt (mV)
500
0
-500
5
-5
0.5
1
1.5
2
2.5

(c)

Figure 6.2 (a) Sensor output signals in terms of X (blue curve), Y (red curve) and Z (green curve) component in ME sensor (top), PE sensor (middle) and fluxgate(bottom) at CPA = 5 m, (b) Magnetic perturbation in ME sensor at CPA = 5 m.

6.2.3 Analysis and 3-D simulation

To better understand and estimate the magnetic anomaly disturbance caused by vehicle movement, we developed a finite element 3-D magnetic field simulation which had vehicle dimensions similar to that used in the experiment. Vehicles consist of a large extent of sheet metal, which makes it different to simulate their magnetic signatures using standard finite element analysis because volume meshes of thin extended structures are difficult to generate and tend to become quite large. To circumvent these problems, we modeled the vehicle by creating 2-D face meshes, in addition to the 3-D volume meshes for the surrounding medium, using Comsol 4.2 Multiphysics.

6.2.3.1 Determination of magnetic perturbation

In a current-free region, where

$$\nabla \times H = 0 . \quad (6.1)$$

It is possible to define a scalar magnetic potential φ, such that

$$H = \nabla\varphi . \quad (6.2)$$

Using the constitutive relation between the magnetic flux density and magnetic field

$$B = \mu(H + M) , \quad (6.3)$$

together with the equation

$$\nabla \cdot B = 0 , \quad (6.4)$$

one can be derive an equation for φ, given as

$$\nabla \cdot (\mu\nabla\varphi + \mu M) = 0 . \quad (6.5)$$

The reduced potential formulation used in this model splits the total magnetic potential into external and reduced parts, $\varphi = \varphi_{red} + \varphi_{ext}$, where the reduced potential φ_{red} is the dependent variable. We assume a uniform magnetic permeability of $\mu_r = 100$. Keeping in mind that the magnetization (M) is zero for the materials considered in this model, equation (5) can be written as:

$$\nabla \cdot (\mu\nabla\varphi_{red} + \mu H_{ext}) = 0 . \quad (6.6)$$

To simulate the background geomagnetic field as shown in Figure 6.3, components of the external magnetic field were expressed through the total intensity, given as:

$$H_{ext}(x) = H_{ext} * \cos(\theta) * \sin(\varphi)\,,$$
$$H_{ext}(y) = H_{ext} * \cos(\theta) * \cos(\varphi)\,,$$
$$H_{ext}(z) = -H_{ext} * \sin(\theta)\quad .\qquad (6.7)$$

where θ is the magnetic declination angle and φ is the inclination one. Based on the data provided by NOAA's data center, inclination and declination angles for this location (N 37°16', W 80°25') are approximately θ =65°22' and φ = 8°11', respectively. [22] The magnitude of natural magnetic flux density (B) can then be estimated as 51.48 μT.

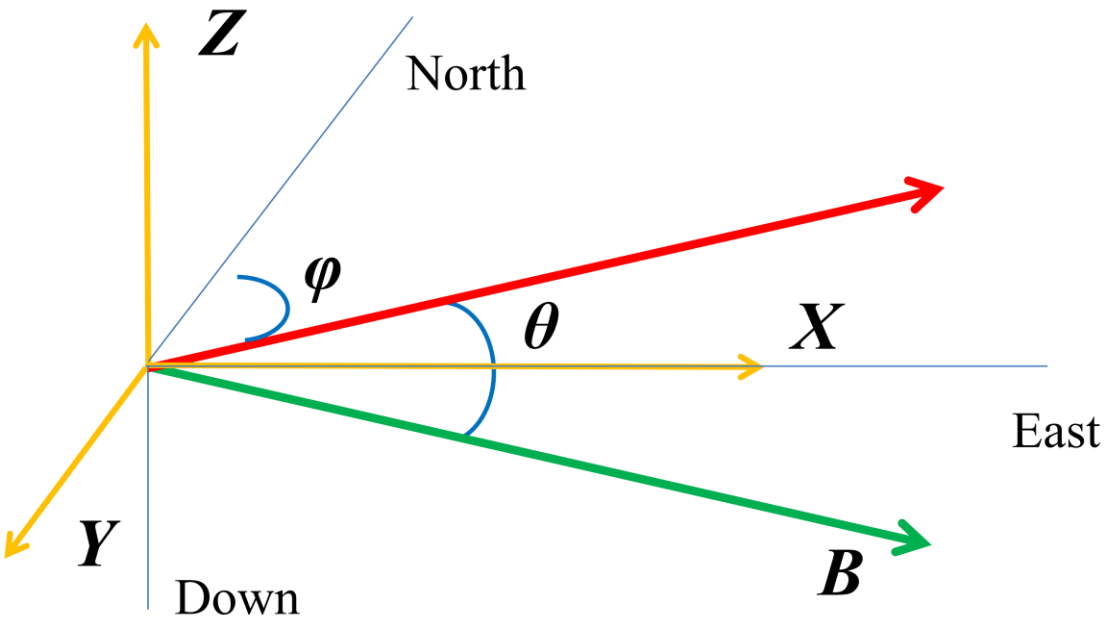

Figure 6.3 *X is* East horizontal field component, *Y* is North horizontal field component, *Z* is vertical field component, positive if directed inside the Earth, B is total field intensity, D is magnetic declination andI is magnetic inclination

Figure 6.4 (a) shows the x-component perturbation due to the inclusion of the vehicle in the background field projecting in a plane along the y-axis. Figures 6.4 (b) and 6.4 (c) show the y- and z-component perturbation fields in the same plane. The magnitude and direction of the tangential magnetic field in the hull of the vehicle is illustrated by arrows. Together, these results give a characteristic field perturbation along

the three orthogonal directions, and provide estimates of the magnetic field strength in its vicinity.

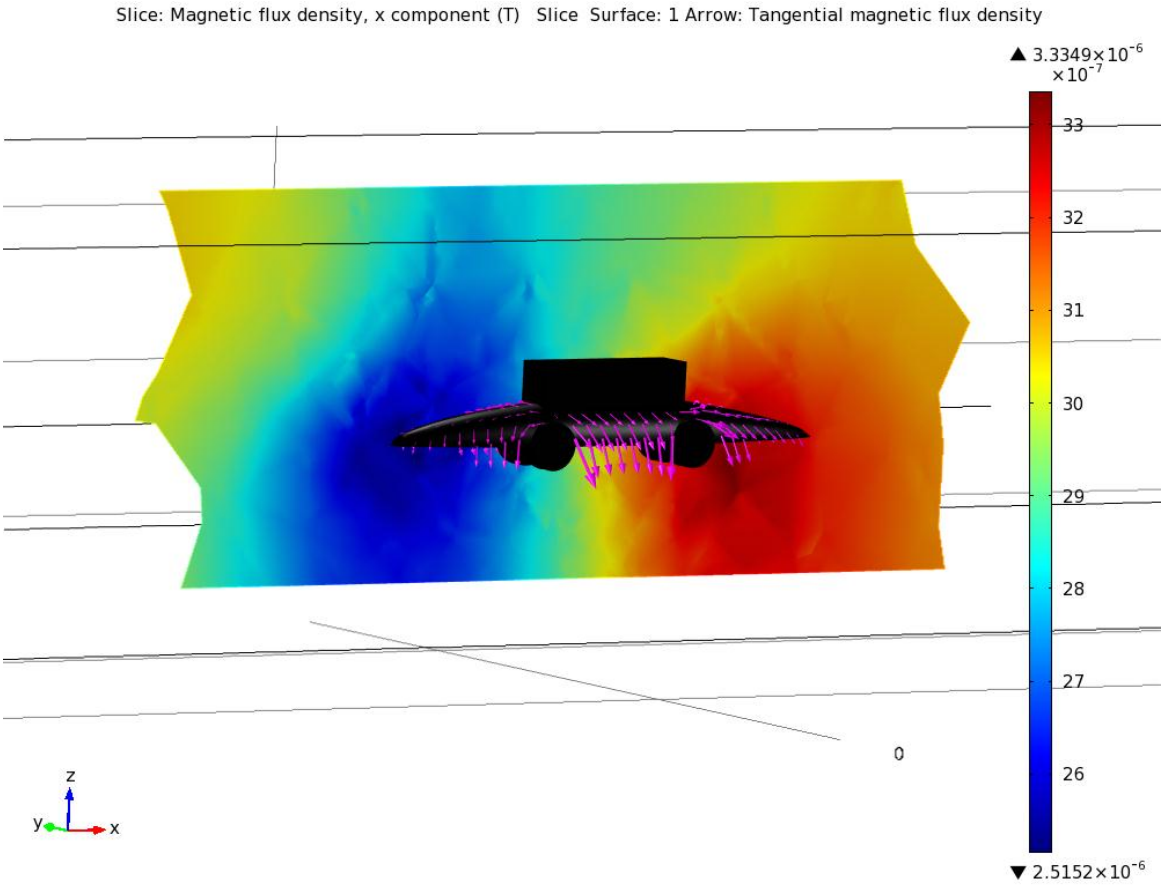

(a)

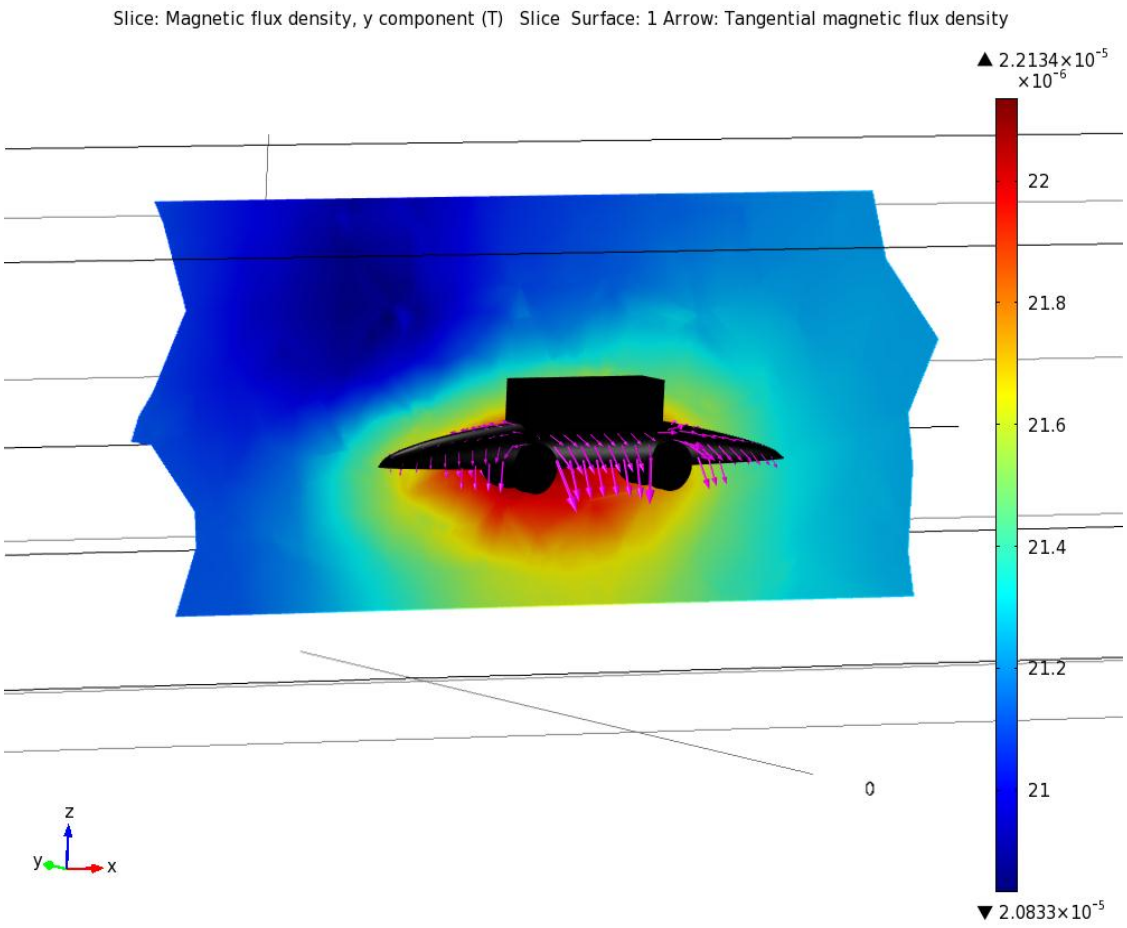
Slice: Magnetic flux density, y component (T) Slice Surface: 1 Arrow: Tangential magnetic flux density
▲ 2.2134×10^-5
×10^-6
22
21.8
21.6
21.4
21.2
21
▼ 2.0833×10^-5
0
z
y
x

(b)

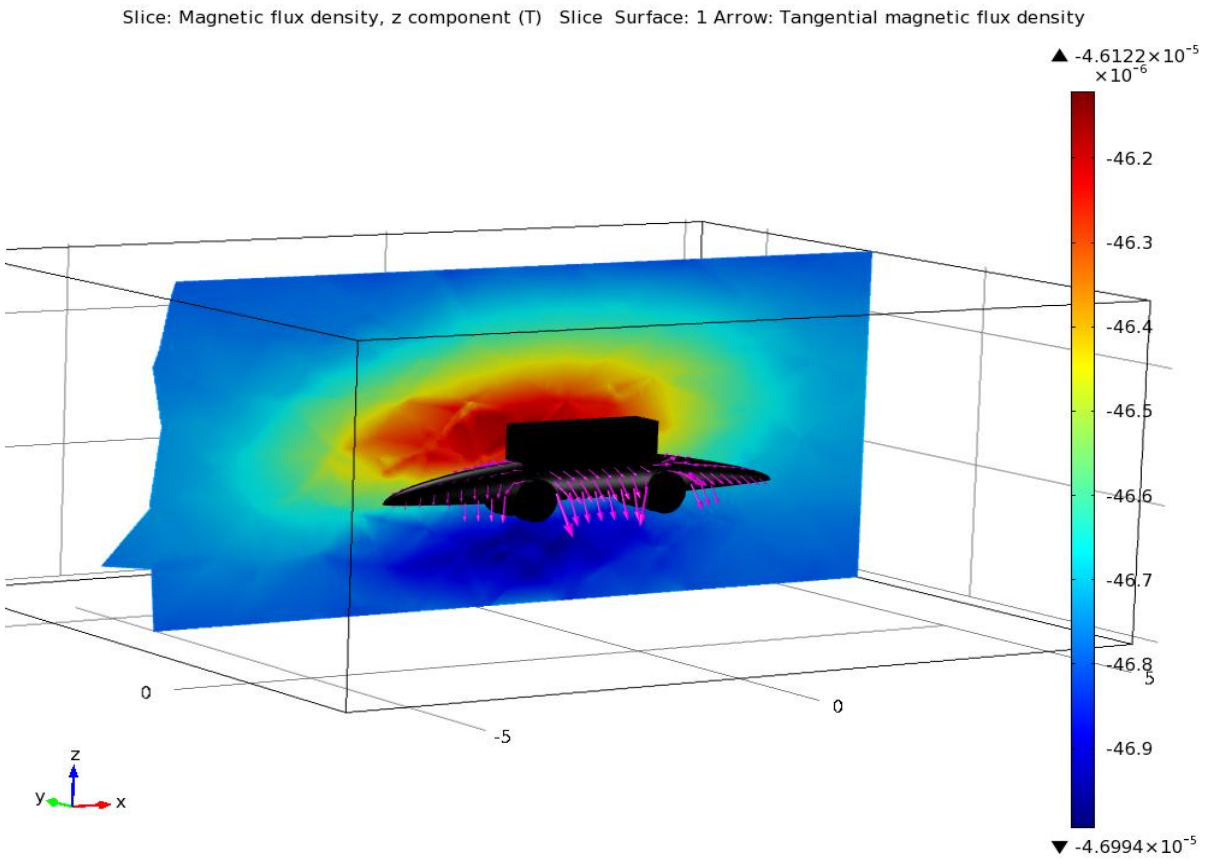

(c)

Figure 6.4 Vehicle induced magnetic field perturbation in (a) x-component, (b) y-component, (c) z-component projected in a plane along y-axis.

6.2.3.2 Magnetic anomaly field at fixed CPA

To mimic our experimental tests at CPA=5m, the vehicle induced magnetic perturbation at y=5 was computed for an x-axis range of -25 m to 25 m, where the z-axis position was set at the same horizontal level as the vehicle (z= -0.3 m). The modeled magnetic perturbation in the x-, y- and z-components are shown in Figures 6.5 (a), 6.5 (b) and 6.5 (c).

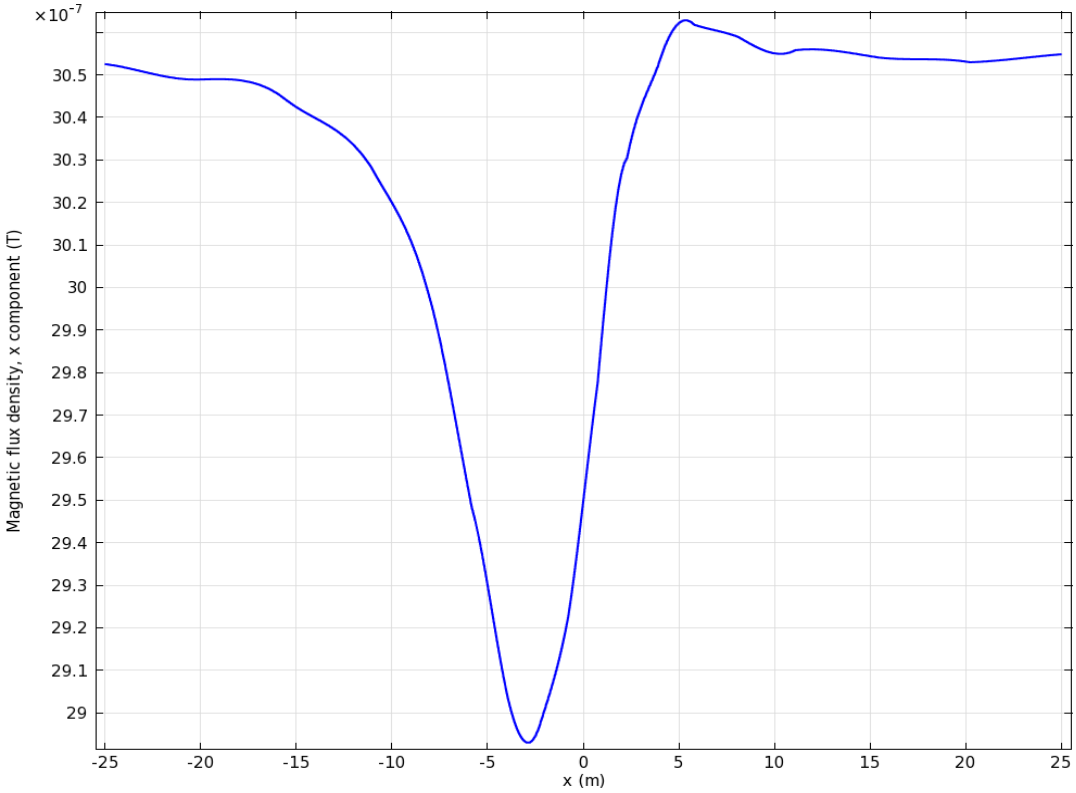
×10^-7
30.5
30.4
30.3
30.2
30.1
30
29.9
29.8
29.7
29.6
29.5
29.4
29.3
29.2
29.1
29
Magnetic flux density, x component (T)
-25
-20
-15
-10
-5
0
5
10
15
20
25
x (m)

(a)

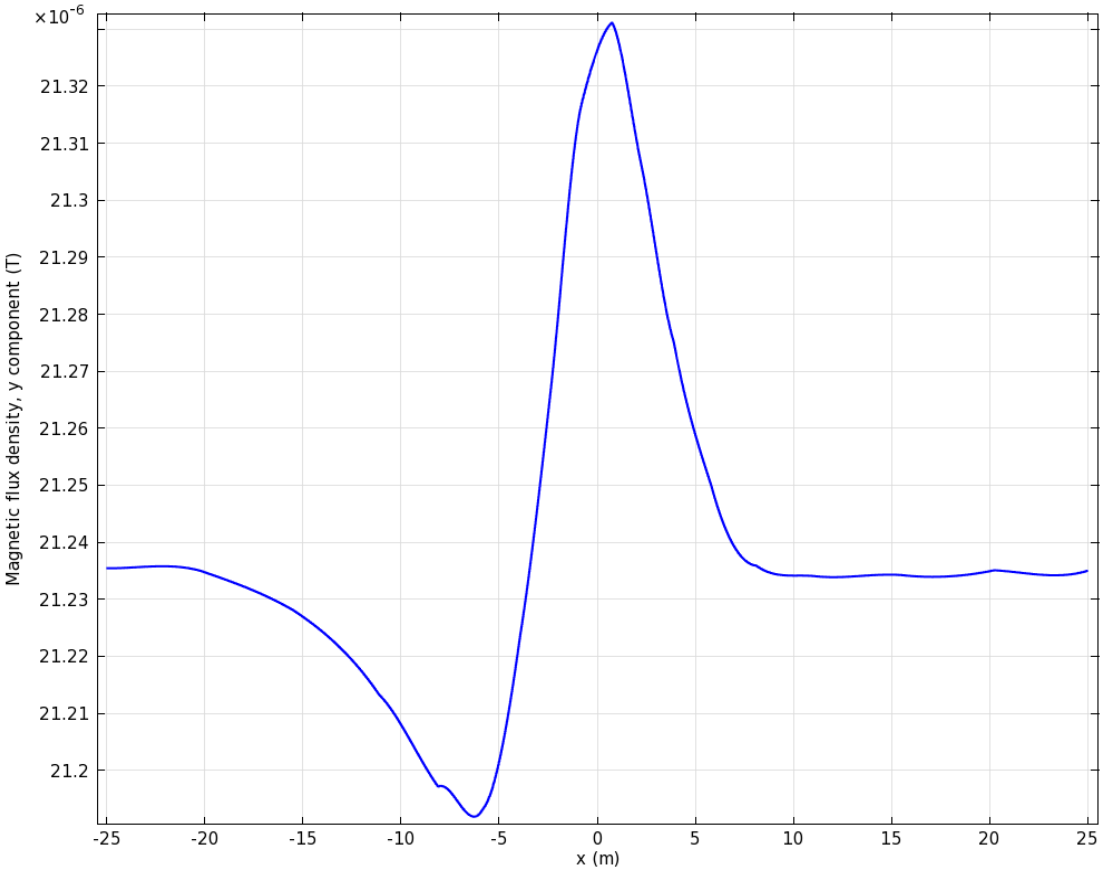
×10^-6
21.32
21.31
21.3
21.29
21.28
21.27
21.26
21.25
21.24
21.23
21.22
21.21
21.2
Magnetic flux density, y component (T)
-25
-20
-15
-10
-5
0
5
10
15
20
25
x (m)

(b)

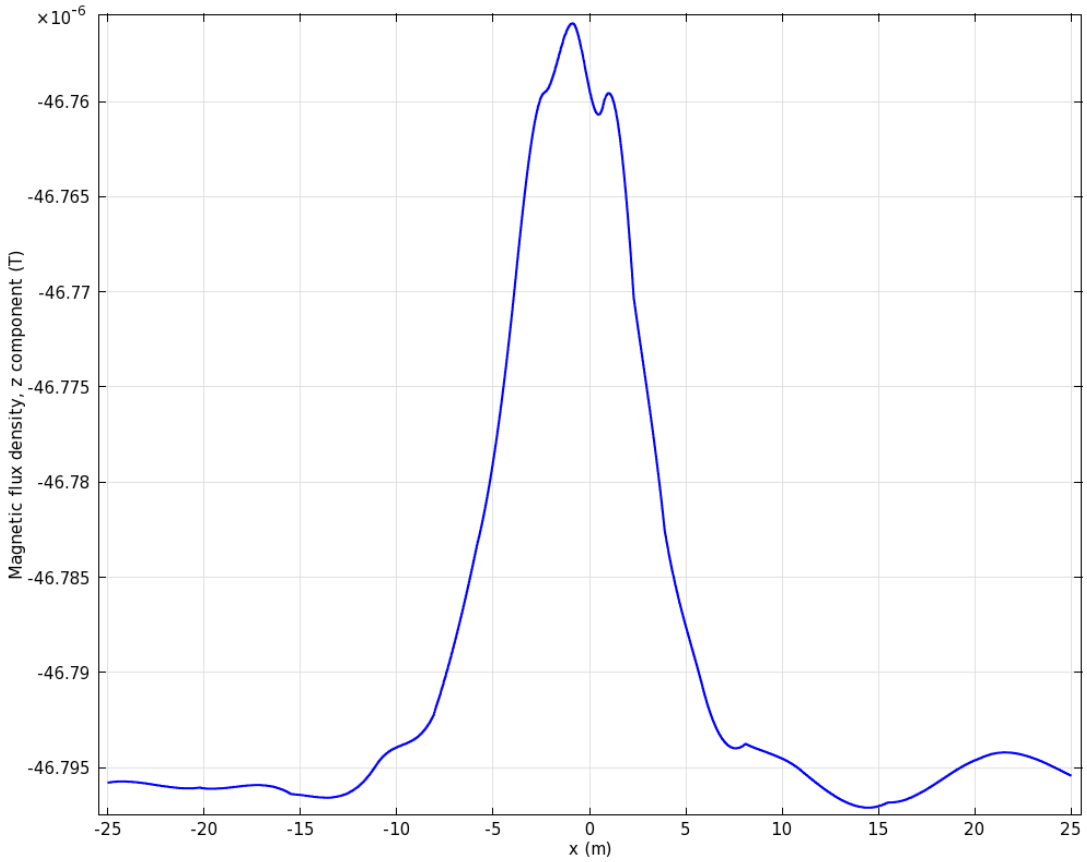

(c)

Figure 6.5 Vehicle induced magnetic field perturbation wave signature in (a) x-component, (b) y-component, (c) z-component at -25m<x<25m, y=5m, z=-0.3m to mimic the test when CPA=5m.

The magnetic perturbation in these three directions was then normalized by the local geomagnetic fields of B_x=3.0526 μT, B_y=21.236 μT, and B_z=46.796 μT. This yielded absolute values of the magnetic field anomaly, as illustrated in Figure 6.6. Comparison of Figure 6.2 (b) and 6.6 will reveal good agreement between measured and predicted magnetic field anomalies induced by the vehicle. Figure 6 shows that the values of B_x, B_y and B_z were about 119 nT, 96 nT, and 30 nT. Some variances between measured and predicted values of the induced magnetic field strength may be due to the relative small detection CPA of 5 m, which was not long compared to the vehicle's length and thus vehicle volume interference might occur. Another possible consideration is that the modeled vehicle was defined with a uniform relative permeability of μ_r=100, which is not the scenario for a real vehicle. These studies reveal that our triple-axis ME laminate

sensor offers a viable magnetometer technology for vehicle sensing applications. We find that the detection resolution of our ME sensor extended over a CPA range larger than 13 m, which might make it promising as a non-intrusive approach to vehicle detection.

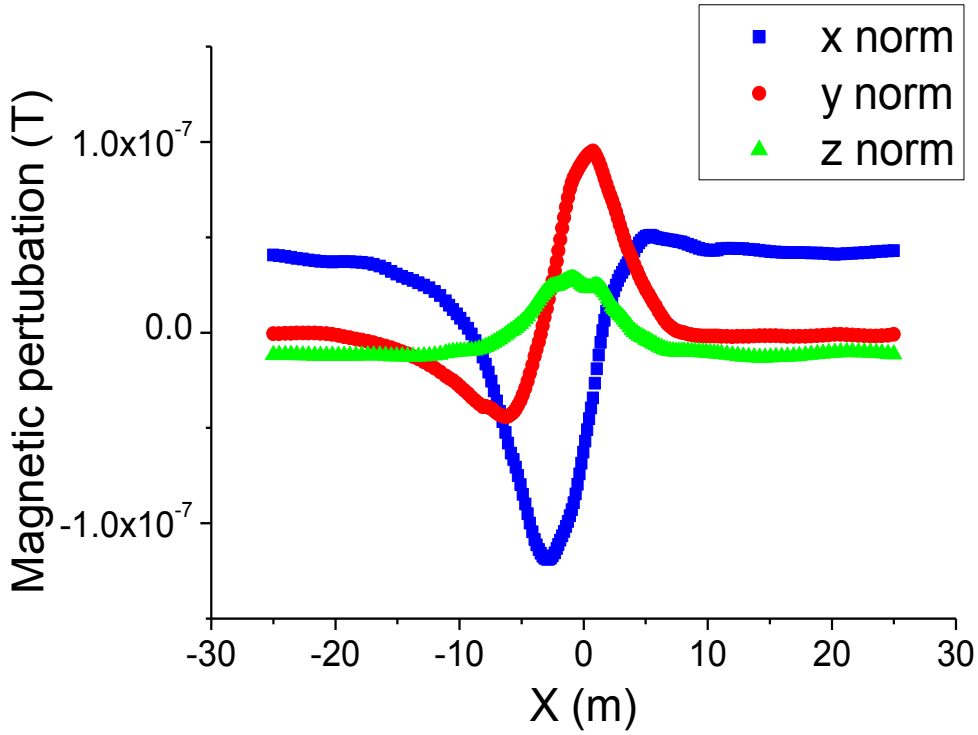

Figure 6.6 Magnetic field anomaly after normalizing with local geomagnetic field at -25m<x<25m, y=5m, z=-0.3m.

6.3 Stable DC Source Detection

6.3.1 Flux distraction effect

ME laminated heterostructures have generally been comprised of two phases: magnetostrictive and piezoelectric phases, where the two different ferroic degrees of freedom interact with each other by elastic forces resulting in a product ME tensor effect. [23] For ME sensors, Metglas is desirable as the magnetostrictive phase: which is due to a large effective piezomagnetic coefficient and low required dc magnetic bias. Metglas/PMN-PT ME laminate sensors with pico-Tesla noise floors at 1 Hz have been

reported, demonstrating an alternative magnetometer technology that is passive and that operates at room-temperature.[24-26]

Metglas results in a significant magnetic flux concentration effect in the ME laminates due to its high relative permeability of μ_r>40,000.[27] In fact, flux concentration has been exploited to enhance the ME coefficient of laminates and resultant magnetic field sensitivity.[27, 28] But flux concentration can be significantly weakened by adjacent high-mu objects, in particular when they are located by an alternating current (AC) magnetic field (H_{ac}) that is excited by a source. This is because a certain amount of the flux that was originally captured by the Metglas would then be shunted to the other high permeability material, producing a flux distraction effect and in-turn an apparent reduced ME response. Furthermore, placing a ME sensor in motion introduces vibration noise via piezoelectricity: this undermines the high sensitivity of its normal stationary state, and is an important issue with regards to applications.[29] Flux distraction of Metglas-based ME sensors could be used to effectively address limitations in detecting dc magnetic targets over a specific survey area, while at the same time allowing the ME sensor to remain stationary. Such a finding could enable ME sensors in different applications, such as non-destructive testing of constructions (or materials), intelligent transportation systems,[30] archeological prospecting and underground natural sources extraction.[31] However, there has been little work in this field of study.

Here, such an AC magnetic flux distraction effect has been investigated. Two essential parameters (the object volume and the distance between sensor and object) that affect flux distraction have also been analyzed. Besides, to exclude the high amplitudes environmental noises, two identical sensors were used to form a gradiometer whose differential output is able to effectively mitigate the environmental noise off and leave the marked gradients. Because two separately placed sensors with certain baseline should have the same level response to the uniform environmental noise, but notable different magnetic field as the magnetic anomaly field drops in intensity fast with the cube of the distance.[21]Thus, a ME gradiometer with a vertical gradient dB_x/dx was developed which can reach a significantly high detection sensitivity of 60 pT/√Hz at quasi-static frequency, especially in open environment. The factor limiting the rejection efficiency was analyzed by a coherent noise test.

6.3.2 Experimental results

Magnetostatic simulation was performed using a finite element model via a Comsol 4.2 AC/DC Module for a coil, ME sensor and a metal plate object. An AC magnetic field H_{ac} was simulated using a solenoid coil driven along the horizontal x-y plane. Assuming a static current density denoted as *J*, the magnetic vector potential *A* must satisfy the vector Poisson equation:

$$\nabla^2 A = -\mu J\ ; \qquad (6.8)$$

where the relative permeability of air is $\mu_{r,air} = 1$ and that of the Metglas-based sensor is $\mu_{r,sensor} = 40000$. Equation (1) can be decomposed into three scalar Poisson equations:

$$\begin{cases} \nabla^2 A_x = -\mu J_x \\ \nabla^2 A_y = -\mu J_y \\ \nabla^2 A_z = -\mu J_z\ . \end{cases} \qquad (6.9)$$

The relations between fields and potentials are then given by:

$$B = \nabla \times A\ . \qquad (6.10)$$

Figure 6.7 (a) shows a simulation schematic diagram for the magnetic flux density of the ME sensor to an magnetic induction field, via 147000 mesh points within a controlled sphere volume. One can see that the flux is relatively intense close to the edges of the coil and decays rapidly with increasing distance from the coil. It can be also seen that the flux concentration effect is quite significant in the ME sensor due to the high permeability of the Metglas layers. The simulated averaged magnetic flux density of the ME sensor was 100.34 nT. Figure 6.7 (b) illustrates the magnetic flux distraction effect caused by the introduction of an adjacent high-mu metal with permeability $\mu_{r,metal} = 200$. One can see that the metal extracts flux density due to its relatively high permeability, leaving the sensor capturing less flux than before (compare with Fig 6.7(a)). Figure 6.7 (c) shows a summary of the volume averaged magnetic flux density of the ME sensor in the presence of a thin metal plate as a function of distance (h) between them for metal plates of different lengths (L) (i.e., fixed width of 4cm and thickness of 0.3 cm). From this figure, it can be seen for L=4 cm that the magnetic field response was nearly unchanged at a value of around 100 nT for h≥10 cm; initially decreased slowly as h decreased; and then decreased more rapidly as h was further decreased to 1 cm. Clearly the magnetic field response decreased with increasing length of metal plate from L=4 cm, 8 cm to 16 cm.

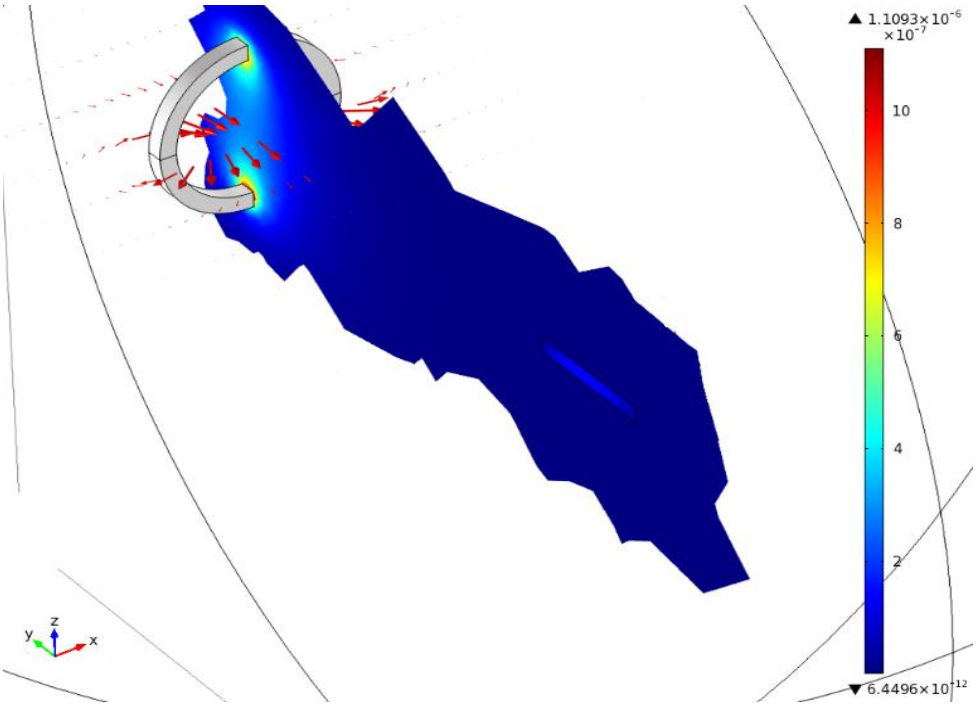
▲ 1.1093×10^-6
×10^-7
10
8
6
4
2
▼ 6.4496×10^-12
z
y
x

(a)

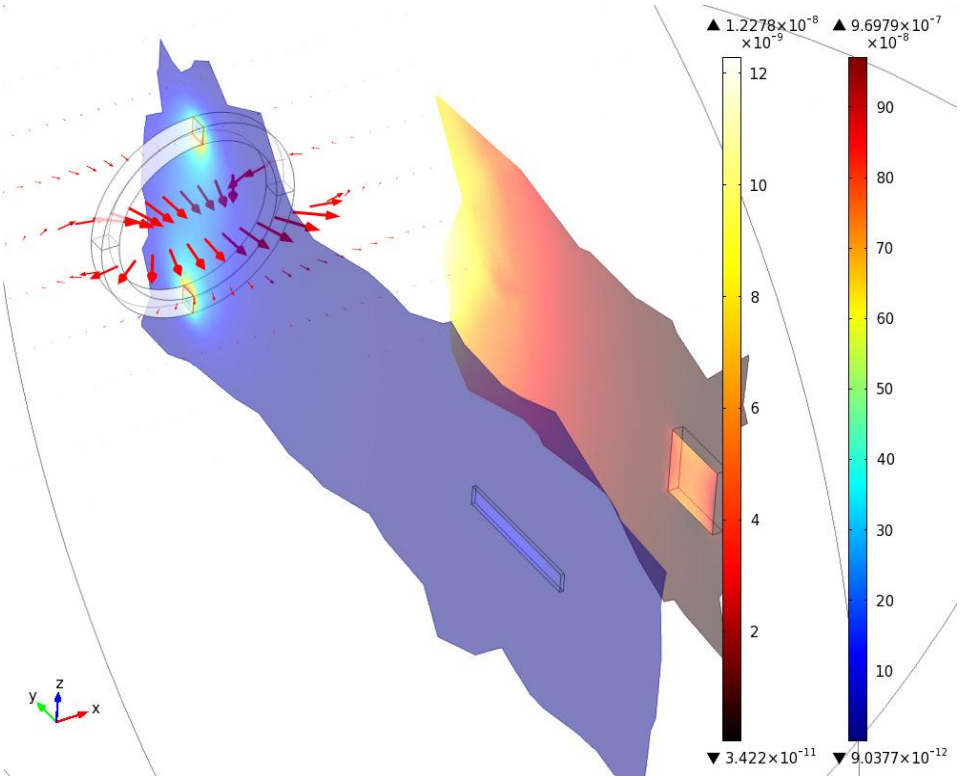
▲ 1.2278×10^-8
×10^-9
12
10
8
6
4
2
▼ 3.422×10^-11
▲ 9.6979×10^-7
×10^-8
90
80
70
60
50
40
30
20
10
▼ 9.0377×10^-12
z
y
x

(b)

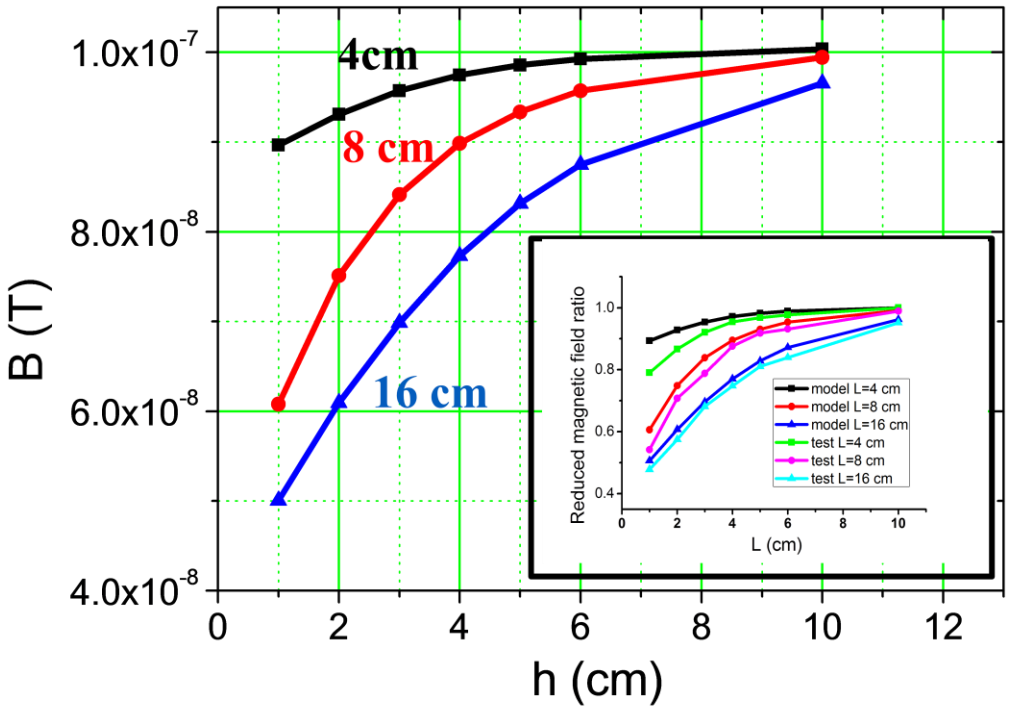

(c)

Figure 6.7 (a) Finite element modeling simulation schematic diagram for magnetic flux density of the ME sensor to an induction magnetic field in the absence of a metal object. (b) Simulation diagram for magnetic flux distraction effect caused by the introduction of an adjacent high-mu metal object. (c) Estimated magnetic field response of a ME sensor as a function of distance h for different length (L) of close metal plates.

A relevant experiment was then conducted with ME laminates composed of six layers of magnetostrictive Metglas laminated onto a core piezoelectric PMN-PT layer. An incident magnetic field induced the Metglas to produce a strain through magnetostriction, which in turn generated a mechanical-strain-induced electric signal in the composite core via piezoelectricity. [13, 18] The core composites were two Kapton interdigitated copper electrodes layers with 500 μm wide digits spaced at 1.5 mm center-to-center (Smart materials, USA) fixed to both top and bottom surfaces of five $40 \times 2 \times 0.2$ mm^3 PMN-PT fibers (Ceracomp, Korean) using epoxy resin (Stycast 1264, USA) to obtain a push-pull geometry. The 25 μm Metglas foils (Vacuumscheltze GmbH & Co. KG, Germany) with

a saturation magnetostriction of about 27 ppm were cut to a surface area of 80×10 mm^2 in order to match the total width of the five PMN-PT fibers. [17] A length of 80 mm was chosen as a trade-off between maximum flux concentration and practical sensor size. [16] Three layers of such Metglas pieces were stacked one on top of each other using the epoxy resin (West system 206, USA) and then two three-layer Metglas stacks were symmetrically attached to the top and bottom sides of the electrode-(PMN-PT)-electrode core using the same epoxy. The laminates were pressed by a vacuum bag method to minimize the epoxy thickness in-between the layers and cured for more than 24 h at room temperature to form the ME laminates.

The ME laminates and charge amplifiers (CAs) circuits were then assembled into a plastic housing enclosure to form ME sensor units. The CAs were designed with a gain transfer function of around 1 V/pC over a frequency bandwidth of 0.6-10 Hz.[32] Two permanent magnets were placed at either end of the ME laminates along the longitudinal axis in order to achieve the maximum ME coefficient as well as the highest sensitivity to minute magnetic field variations. Figure 6.8(a) shows the measured and estimated equivalent magnetic noise floor of the ME laminates for $1<f<100$ Hz in a zero-Gauss, vibration isolation chamber. A very low equivalent magnetic noise of 7.8 pT/√ Hz was found at f=1 Hz was close to the predicted value of 7.2 pT/ √Hz. The prediction method was according to Ref.[19] . It should be noted that the noise floor was about 1 pT/ √Hz at higher frequencies. The very low equivalent magnetic noise makes the ME laminate sensor promising for use in ultralow magnetic field applications.

Figure 6.8 (b) illustrates the configuration of a signal generator (a solenoid coil), ME sensor unit and a target metal plate of the same dimension as the module. The sensor and the metal plate were placed parallel to each other with their core points aligned along the transverse axes. The distance between the sensor and the metal plate was defined as h, and the length of the metal plate was represented by L. A coil located 40 cm away from the sensor was driven at a frequency of 7 Hz by a current density of J=230 A/m^2, generating a constant sinusoid output. A datalogger (Campbell Scientific, Inc., USA) with a 100 Hz sampling rate was employed to collect the signal from the CAs, and the output signal was then processed by Matlab. Experiments were performed in an open lab

environment which can be considered as having high magnetic and vibration disturbances.

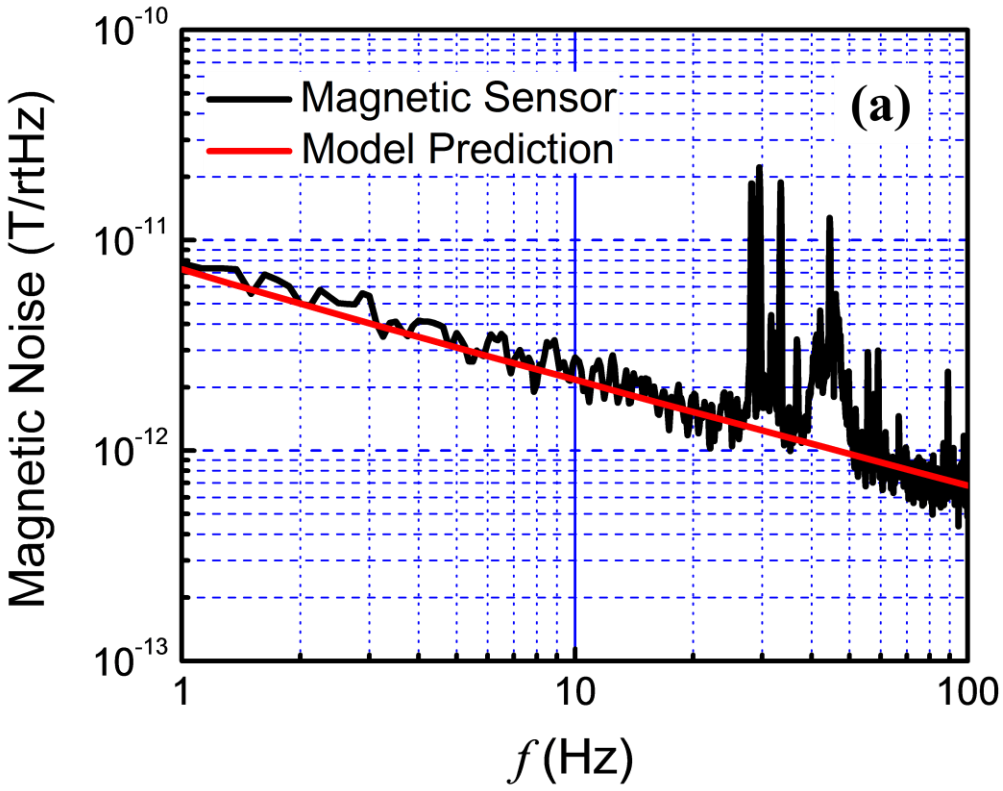

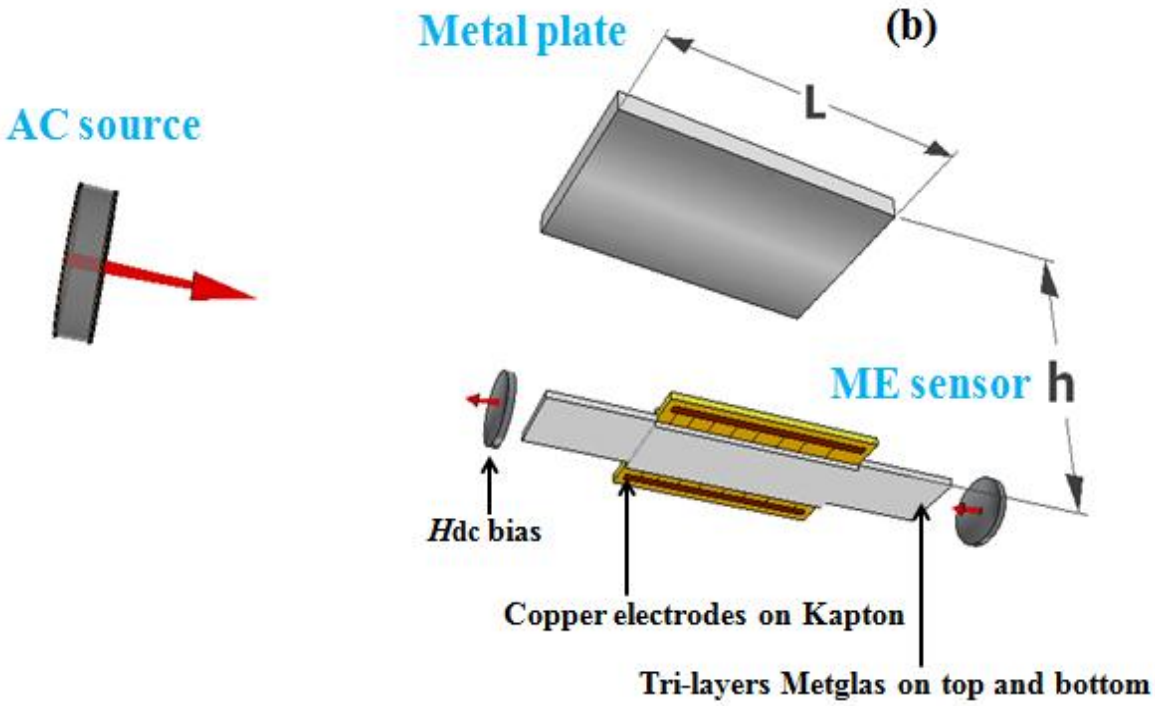

Figure 6.8 (a) Measured and estimated equivalent magnetic noise floor of the ME laminates in the frequency range of 1<*f*<100 Hz taken in a zero-Gauss, vibration isolation chamber. (b) Schematic representation of a signal generator (solenoid coil), ME sensor device and a thin metal plate of length L. The sensor and metal are separated by a distance h.

Figure 6.9(a) shows a sequence of magnetic field responses as a function of h for different lengths (L) of the metal plate. From this figure, it can be seen for L=4 cm that the magnetic field response was nearly unchanged at 101.4 nT at distance h≥10 cm; initially decreased slowly as h was decreased; and then subsequently decreased more rapidly as h was further decreased to 1 cm. It can also be seen that the magnetic field response decreased with increasing length of the metal plate for 4≤ L ≤16 cm in a manner nearly equal to the simulated results (compare with Fig 6.7 (c)). Figure 6.9(b) shows the magnetic field decrement ratio. Results from experiment and simulation can be seen to agree well with each other. The metal object diverts flux density from the ME sensor. This effect was found to decrease as the distance increased between the sensor and object, until the distance was sufficient high that mutual inductance did not occur. It was

also found that the flux distraction was more significant for larger masses of material. These variances in the *B* field observed using highly sensitive ME sensors offer a new magnetometer technology that is promising for use in precise magnetic anomaly field detection to discriminate targets over a specific survey area that have different dimensions (mass) and scopes.

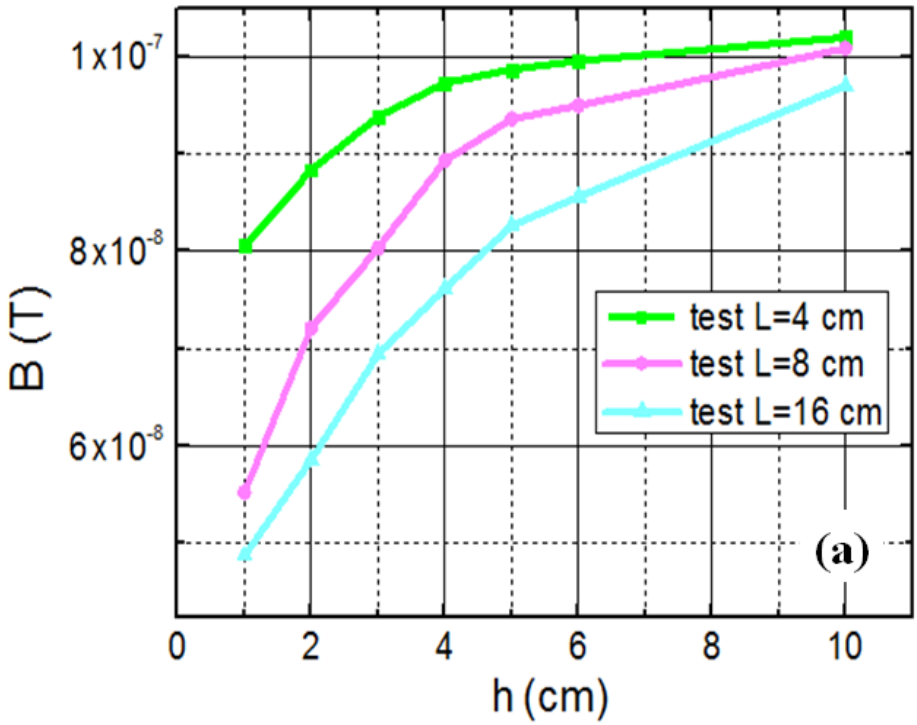

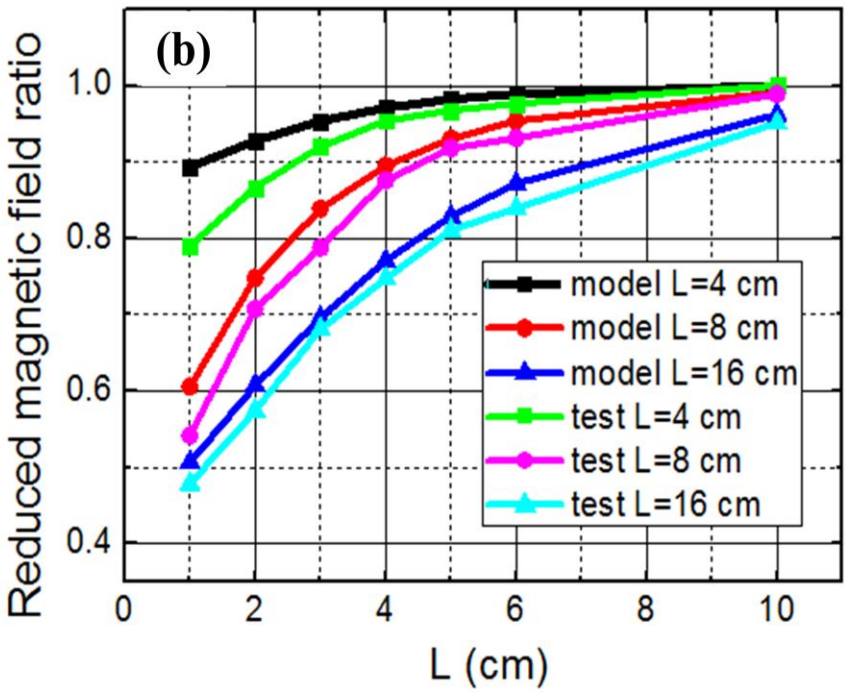

Figure 6.9 (a) The magnetic field response of a ME sensor as a function of distance h for different lengths (L) for nearby metal plates under a constant incident AC magnetic field background produced by a solenoid coil. (b) Magnetic field decrement ratio caused by the magnetic flux distraction effect for experimental and simulated data.

6.3.3 Detection with gradiometer

Two ME sensors S1 and S2 were then arranged with a baseline of 20cm to form a ME gradiometer with a vertical gradient dB_x/dx. The two small ferromagnetic metal targets, with volume size of $4\times4\times0.3$ cm^3 and $8\times4\times0.3$ cm^3, was located close to S1 at distance=2 cm and the distance was gradually increased until the week magnetic field disturbance can't be detected by the gradiometer. Figure 6.10(a) shows a summary of the detection data depicted in Figure 2 for a metal object with dimension of $4\times4\times0.3$ cm^3. This 3D imaging figure provides information that when the target was placed closest to the gradiometer (near S1 for this scenario), the induced amplitudes of gradient is the maximum, around 2.7×10^{-8} (T/m) /√Hz for this case at driven frequency f=1 Hz when distance=2 cm. The gradients decline rapidly, especially in the short distance range, as the distance increases up to disqualify the gradiometer to recognize the minute magnetic field anomaly any more. This phenomenon is a direct consequence of flux distraction

effect that results from the presence of the high permeability metal. At distance=10 cm, one can clearly see that it is the limit for the ME gradiometer to sense the nearby metal target. Figure 6.10(b) shows an equivalent 3D imaging data for the same type of metal object only with larger volume of $8\times4\times0.3$ mm^3 which is as double in length as that in Figure 6.10(a). We can note that the decrease trend in gradient strength looks similar which again proves the fact that the flux distraction effect produced by nearby ferromagnetic material. However, it is important to note that the larger dimension in metal creates more obvious flux distraction effect which is manifest in the gradient strength of 5.5×10^{-8} (T/m) /√Hz at f=1 Hz with the same distance. In addition, one can also clear see that the sensing range extends much further to a distance=20 cm for this bigger plate. The increase in detection resolution can be directly attributed to an increase of the flux distraction effect caused by the bulk mass of the target. This makes ME gradiometer as a viable metal detector and promising in distinguish target size for use in ultra low magnetic field detection.

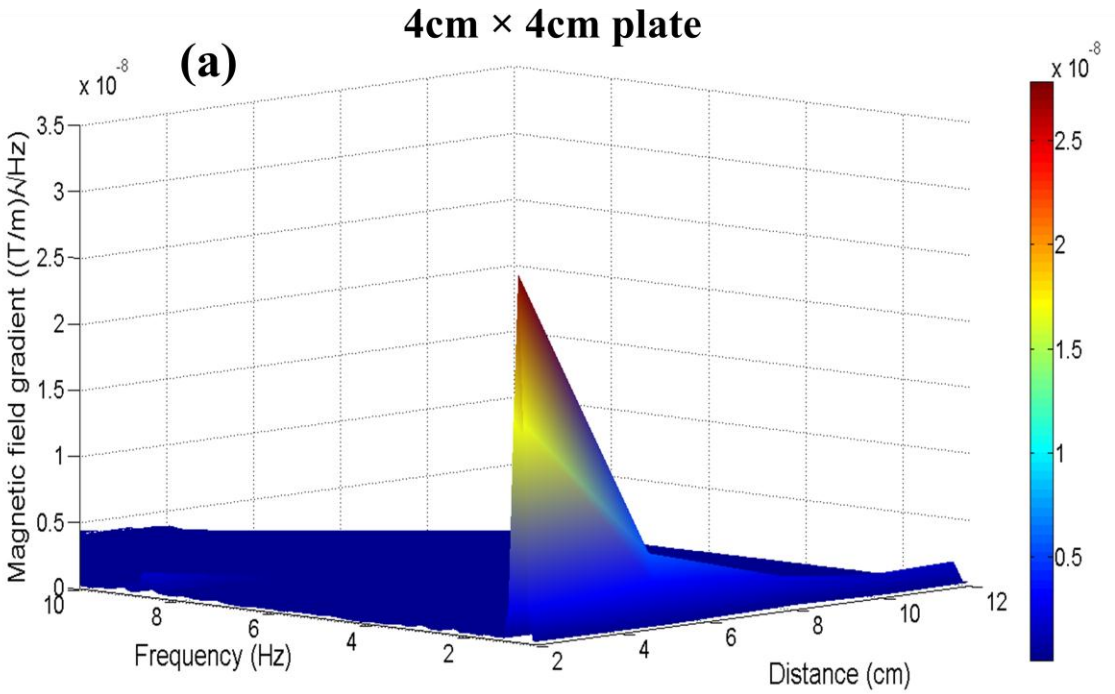

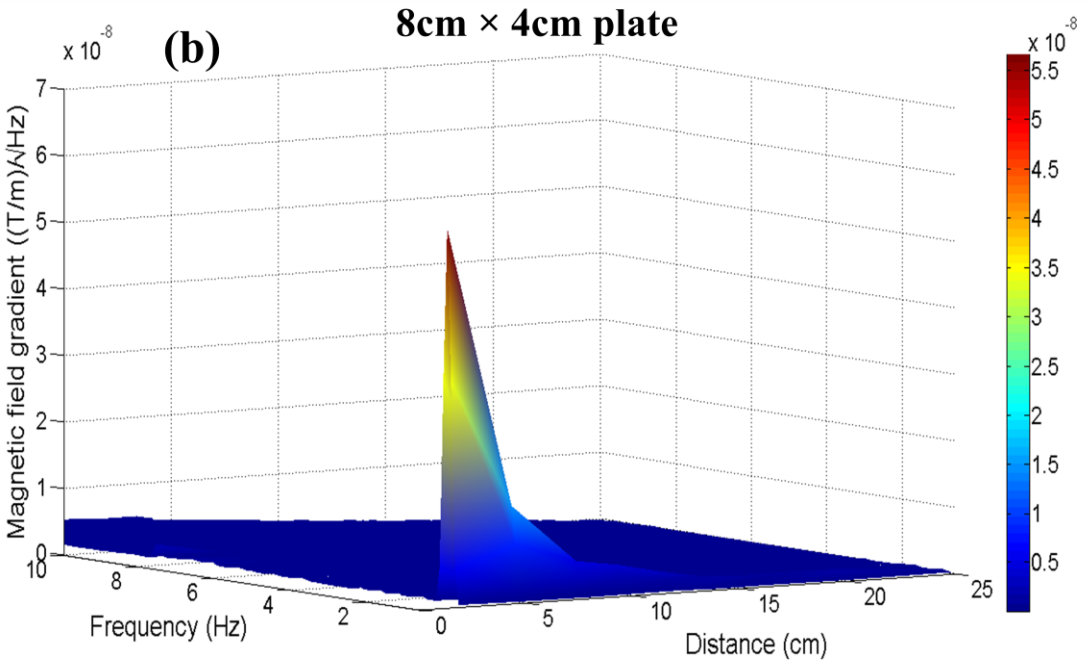

Figure 6.10 3D imaging of magnetic field gradients for (a) a 4×4×0.3 cm^3 metal target and (b) a 8×4×0.3 cm^3 metal target. The gradients decline rapidly, especially in the short distance range, as the distance The gradients decline rapidly, especially in the short distance range, as the distance increases up to disqualify the gradiometer to recognize the minute magnetic field anomaly any more.

We then take the 8×4×0.3 cm^3 plate for example to analyze the differential output (S1-S2) of the gradiometer as a function of metal distance. Figure 6.11(a) shows that (S1-S2) amplitude is maximum of 11 nT/√Hz at f=1 Hz when target is at close quarters which leads to the vertex shown in Figure 6.10(b). The strength of (S1-S2) then drops rapidly to be 60 pT/√Hz as the distance increases to 20 cm when significant differential output can't be detected further. Because a distortion created by a magnetic object usually drops in intensity with the cube of the distance from the object. The maximum distance that such ME gradiometer can detect the object is directly dependent on the sensor's sensitivity and the background nuisance noise. Our findings have demonstrated that ME gradiometer can be exploited for efficient metal detection up to 20 cm (for small 8×4×0.3 cm^3 plate) with limiting factor of detection sensitivity of 60 pT/√Hz, which represents remarkable two orders enhancement of detection sensitivity over previous AMR gradiometer at low frequency. [33]

Here, gradiometer results do not represent a complete elimination of environmental nuisance. To examine the limiting factor suppressing the sensor's detection sensitivity for practical use, we then performed a noise test in open environment for a coherence analysis. The gradiometer was placed with the same original baseline in our lab without the driven signal. Figure 6.11(b) shows the representative power spectral density (PSD) plot of the each sensor which has equivalent background noise level of 0.2 nT/√Hz at frequency bandwidth of $1<f<10$ Hz which is an indicator of the environmental noise. The peaks at 1-3Hz, we believe, result from the building vibration noise. The differential mode noise (S1-S2) of the gradiometer is around 10x lower than that of individual sensor as it can reject environmental noises that are coherently shared between two sensors. It should be noted that the differential noise (S1-S2) is only 50 pT/√Hz at $f=1$ Hz which infers a fair coherence between the two gradiometer outputs S1 and S2.

Figure 6.11(c) shows the coherence analysis between S1 and S2 outputs in terms of their amplitude ratio (S1/S2) and phase discrepancy (S1-S2). The coherence C_{12} gives information about the fraction of power spectrum of signal S1 that also appears in the power spectrum of signal S2. From top graph of Fig. 11(c), one can clearly see that C_{12} remains constant at one unit from frequency $1<f<5$ Hz indicating a good coherent relation between S1 and S2 which is also certified by efficient noise rejection in this range in Figure 10. However, at high frequency range $5<f<10$ Hz, C_{12} drops a little which can be attributed to the decreased amplitude ratio (shown in the middle graph of Fig. 6.11(c)) and phase difference (shown in the bottom graph of Fig. 6.11(c)) in such interval. The amplitude ratio (S1/S2) refers the relative strengths of the two outputs which keeps around 1 at $f<5$ Hz and decrease slightly to 0.9 at $f>5$ Hz. The phase difference represents the time lag between the two signals which points to about 2-6 ° phase drift at the whole frequency bandwidth as can been seen in Figure 6.11(c). These results together indicate that the individual two sensors were not ideally a unit on performance. The small disagreement in amplitude and phase directly leads to discrepancy in sensor response leaving the gradiometer not effectively to null off the common environment noise.

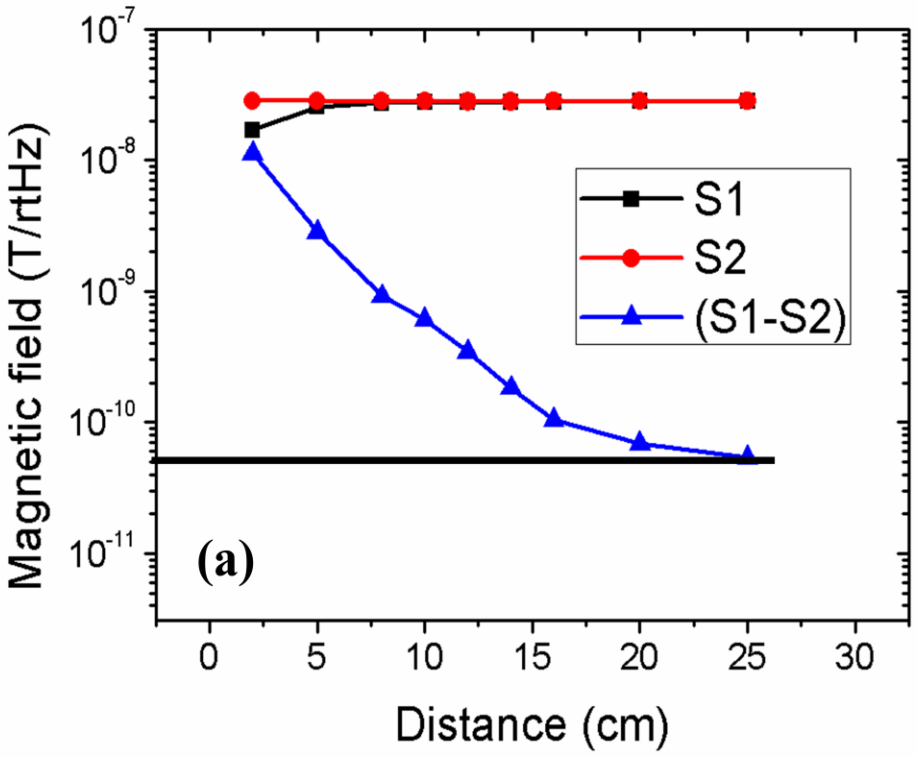
Magnetic field (T/rtHz)
10^-7
10^-8
10^-9
10^-10
10^-11
S1
S2
(S1-S2)
(a)
0
5
10
15
20
25
30
Distance (cm)

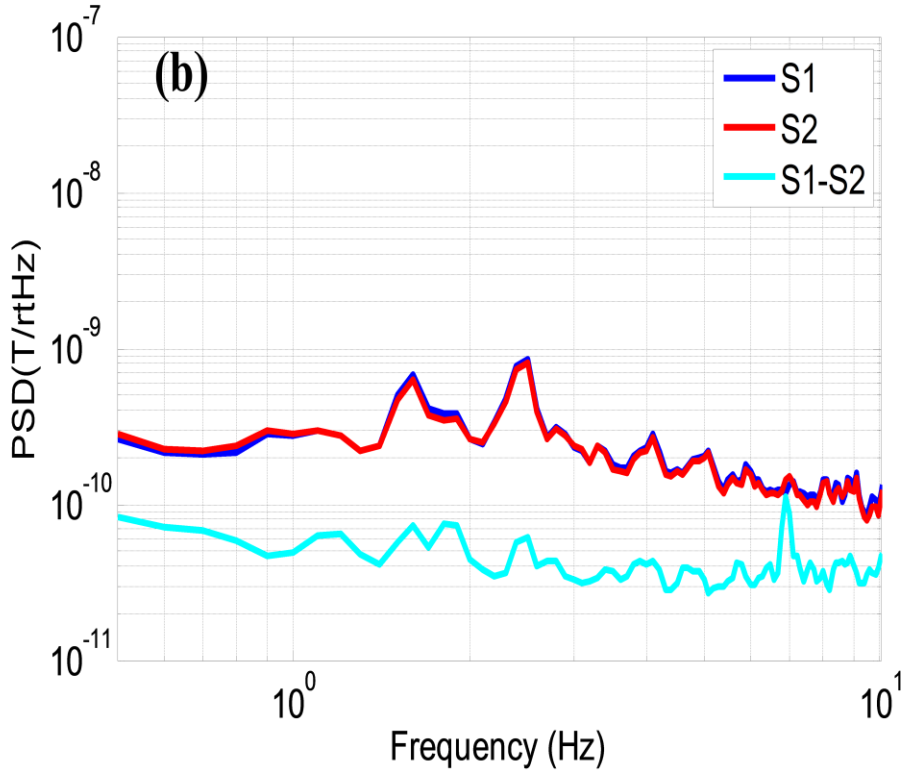
(b)
S1
S2
S1-S2
PSD(T/rtHz)
10^-7
10^-8
10^-9
10^-10
10^-11
10^0
10^1
Frequency (Hz)

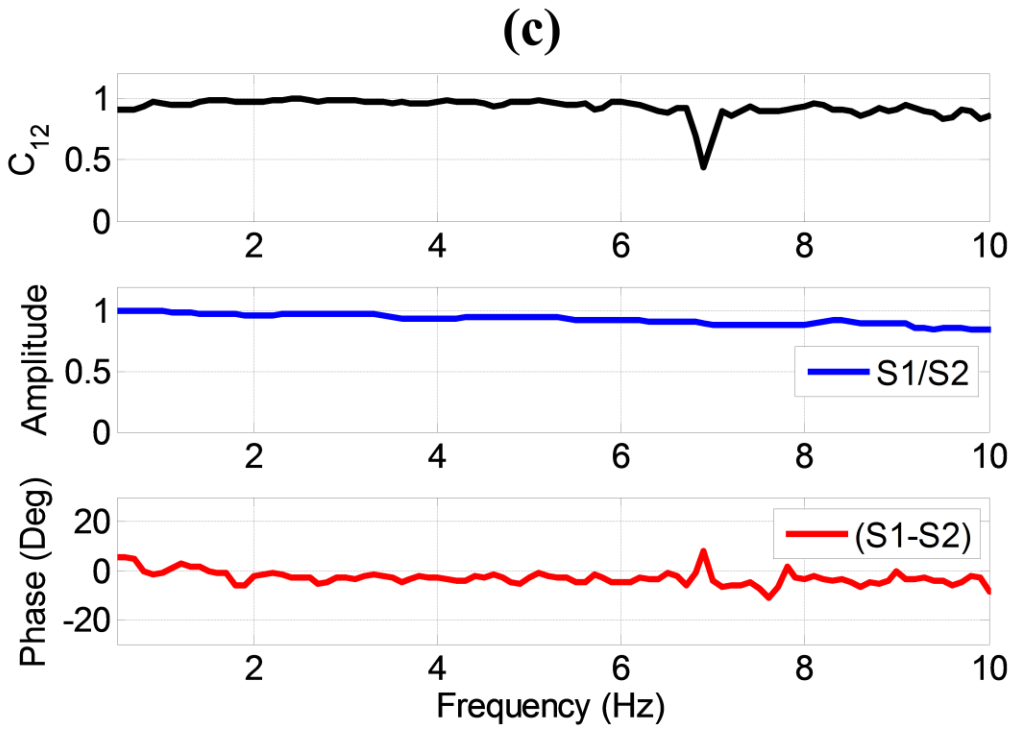

Figure 6.11 (a) Gradiometer differential output (S1-S2) as a function of target distance for the 8×4×0.3 mm^3 metal target. (S1-S2) amplitude is maximum of 11 nT/√Hz at *f*=1 Hz when target is at close quarters. The strength of (S1-S2) then drops rapidly to be 60 pT/√Hz as the distance grows to 20 cm when significant differential output can't be detected further. (b) Power spectra density (PSD) of individual ME sensor which all has an equivalent background noise level of 0.2 nT/√Hz at frequency bandwidth of 1<*f*<10 Hz for external noise. (c) Coherence between S1 and S2 outputs (top graph) in terms of their amplitude ratio (S1/S2) (middle graph) and phase discrepancy (S1-S2) (bottom graph)

6.4 Summary of This Section

In summary, I have investigated a novel triple-axis ME magnetic sensor system for potential non-intrusive vehicle detection. Our results demonstrate that ME sensors are quite sensitive, having detection range larger than 13 m. Furthermore, we developed a 3-D simulation to predict the magnetic anomaly distribution which was dependent on the local geomagnetic field in the vicinity of the vehicle. This simulation model could be used for object detection, tracking and localization. We note that a good agreement was found between measured and predicted magnetic field anomaly signatures. Such ME

sensor technology is a promising apparatus for vehicle detection because it is non-intrusive, low cost, low power consuming, and easily-portable.

By utilizing the high permeability of Metglas, an AC magnetic flux distraction effect was found in ME laminate sensors in response to the presence of adjacent metallic objects. This flux distraction effect was dependent on distance between sensor and object, and the volume of the object. The principle can be employed for dc ferromagnetic dipole detection using Metglas-based ME sensors, and is free of any unwanted motion over a survey area that could introduce vibrational noises sources degrading sensor performance. It has been found both theoretically and experimentally that ME sensors have precise magnetic field variances with respect to minute flux distraction effects resulting from changing target dimensions and distances. After further rejecting the common environmental noise, the ME gradiometers can achieve a very high detection sensitivity of 60 pT/√Hz at quasi-static frequency, which poses it as a viable solution for dc magnetic anomaly detection in a stationary operating mode.

References:

[1] J. Lenz and A. S. Edelstein, "Magnetic sensors and their applications," *IEEE Sensors,* vol. 6, pp. 631-649, 2006.

[2] R. Wiegert, "Magnetic anomaly sensing-based system for tracking a moving magnetic target," 2008.

[3] Y. Ege, O. Kalender, and S. Nazlibilek, "Direction finding of moving ferromagnetic objects inside water by magnetic anomaly," *Sensors and Actuators A: Physical,* vol. 147, pp. 52-59, 2008.

[4] A. S. B. Ginzburg, L. Frumkis, B.Z. Kaplan, N. Salomonski, "Investigation of advanced data processing technique in magnetic anomaly detection systems," presented at the 1st International Conference on Sensing Technology, Palmerston North, New Zealand, 2008.

[5] J. Lan and Y. Shi, " Vehicle Detection and Recognition Based on a MEMS Magnetic," presented at the Proceedings of the 2009 4th IEEE International Conference on Nano/Micro Engineered and Molecular Systems, Shenzhen, China, 2009.

[6] J. Ding, S. Y. Cheung, C. Tan, and P. Varaiya, "Vehicle Detection by Sensor Network Nodes," Institute of Transportation Studies, UC Berkeley2004.

[7] S. Y. Cheung, S. C. Ergen, and P. Varaiya, "Traffic Surveillance with Wireless Magnetic Sensors," University of Berkeley2007.

[8] E. Sifuentes, O. Casas, and R. Pallas-Areny, "Wireless Magnetic Sensor Node for Vehicle Detection," *IEEE Sensors Journal* vol. 11, 2011.

[9] P. Kanathantip, W. Kumwilaisak, and J. Chinrungrueng, "Robust Vehicle Detection Algorithm with Magnetic Sensor," in *Proc. IEEE Symp. Electrical Engineering/Electronics Computer Telecommunications and Information Technology (ECTI-CON)*, 2010, pp. 1060-1064.

[10] J.Lenz and A. S. Edelstein, "Magnetic Sensors and Their Applications," *Ieee Sensors Journal,* vol. 6, 2006.

[11] L. A. Klein, "Sensor Technologies for ITS Sensor Technologies for ITS," in *Transportation Research Board Freeway Operations and Signal Systems Mid-Year Committee Meeting*, Park City Marriott, Park City, Utah, USA, 2002.

[12] S. Dong, J. Zhai, F. Bai, J.-F. Li, and D. Viehland, "Push-pull mode magnetostrictive/piezoelectric laminate composite with an enhanced magnetoelectric voltage coefficient," *Applied Physics Letters,* vol. 87, p. 062502, 2005.

[13] J. Zhai, Z. Xing, S. Dong, J. Li, and D. Viehland, "Magnetoelectric Laminate Composites: An Overview," *Journal of the American Ceramic Society,* vol. 91, pp. 351-358, 2008.

[14] Z. Xing, J. Zhai, J. Li, and D. Viehland, "Investigation of external noise and its rejection in magnetoelectric sensor design," *Journal of Applied Physics,* vol. 106, p. 024512, 2009.

[15] J. Gao, J. Zhai, Y. Shen, L. Shen, D. Gray, J. Li, P. Finkel, and D. Viehland, "Differential-Mode Vibrational Noise Cancellation Structure for Metglas Pb(Zr,Ti)O(3) Fiber Magnetoelectric Laminates," *IEEE Transactions on Ultrasonics, Ferroelectrics, and Frequency Control,* vol. 58, pp. 1541-1544, 2011.

[16] J. Das, J. Gao, Z. Xing, J. F. Li, and D. Viehland, "Enhancement in the field sensitivity of magnetoelectric laminate heterostructures," *Applied Physics Letters,* vol. 95, p. 092501, 2009.

[17] Y. Wang, D. Gray, D. Berry, J. Gao, M. Li, J. Li, and D. Viehland, "An Extremely Low Equivalent Magnetic Noise Magnetoelectric Sensor," *Advanced Materials,* vol. 23, pp. 4111-4114, 2011.

[18] S. Dong, J. Zhai, J. Li, and D. Viehland, "Near-ideal magnetoelectricity in high-permeability magnetostrictive/piezofiber laminates with a (2-1) connectivity," *Applied Physics Letters,* vol. 89, p. 252904, 2006.

[19] Y. Shen, J. Gao, Y. Wang, J. Li, and D. Viehland, "Thermal stability of magnetoelectric sensors," *Applied Physics Letters,* vol. 100, p. 173505, 2012.

[20] Z. P. Xing, J. Y. Zhai, S. X. Dong, J. F. Li, D. Viehland, and W. G. Odendaal, "Modeling and detection of quasi-static nanotesla magnetic field variations using magnetoelectric laminate sensors," *Measurement Science and Technology,* vol. 19, p. 015206, 2008.

[21] Y. Shen, J. Gao, L. Shen, D. Gray, J. Li, P. Finkel, D. Viehland, X. Zhuang, S. Saez, and C. Dolabdjian, "Analysis of the environmental magnetic noise rejection by using two simple magnetoelectric sensors," *Sensors and Actuators A: Physical,* vol. 171, pp. 63-68, 2011.

[22] NOAA, ed. http:id//www.ngdc.noaa.gov/geomagmodels/IGRFGridl.jsp: NOAA'S Geophysical Data Center.
[23] C. Ederer and N. A. Spaldin, "Magnetoelectrics A new route to magnetic ferroelectrics," *Nat Mater*, vol. 3, pp. 849-851, 2004.
[24] J. Gao, Z. Wang, Y. Shen, M. Li, Y. Wang, P. Finkel, J. Li, and D. Viehland, "Self-powered low noise magnetic sensor," *Materials Letters*, vol. 82, pp. 178-180, 2012.
[25] Y. Shen, K. L. McLaughlin, J. Gao, D. Gray, L. Shen, Y. Wang, M. Li, D. Berry, J. Li, and D. Viehland, "AC magnetic dipole localization by a magnetoelectric sensor," *Smart Materials and Structures*, vol. 21, p. 065007, 2012.
[26] Y. Shen, K. McLaughlin, J. Gao, D. Gray, D. Hasanyan, Y. Wang, J. Li, and D. Viehland, "Metglas/ Pb(Mg1/3Nb2/3)O3–PbTi O3 Magnetoelectric Gradiometric Sensor with High Detection Sensitivity," *IEEE Transactions on Ultrasonics, Ferroelectrics and Frequency Control*, vol. 59, pp. 2111-2115, 2012.
[27] Z. Fang, S. G. Lu, F. Li, S. Datta, Q. M. Zhang, and M. El Tahchi, "Enhancing the magnetoelectric response of Metglas/polyvinylidene fluoride laminates by exploiting the flux concentration effect," *Applied Physics Letters*, vol. 95, p. 112903, 2009.
[28] J. Gao, D. Gray, Y. Shen, J. Li, and D. Viehland, "Enhanced dc magnetic field sensitivity by improved flux concentration in magnetoelectric laminates," *Applied Physics Letters*, vol. 99, p. 153502, 2011.
[29] Y. Shen, J. Gao, L. Shen, D. Gray, J. Li, P. Finkel, D. Viehland, X. Zhuang, S. Saez, and C. Dolabdjian, "Analysis of the environmental magnetic noise rejection by using two simple magnetoelectric sensors," *Sensors and Actuators A: Physical*, 2011.
[30] Y. Shen, J. Gao, D. Hasanyan, Y. Wang, M. Li, J. Li, and D. Viehland, "Investigation of vehicle induced magnetic anomaly by triple-axis magnetoelectric sensors," *Smart Materials and Structures*, vol. 21, p. 115007, 2012.
[31] D. S. Parasnis, *Principles of Applied Geophysics*, Fifth ed.: Chapman & Hall, 1997.
[32] Z. Xing, J. Li, and D. Viehland, "Noise and scale effects on the signal-to-noise ratio in magnetoelectric laminate sensor/detection units," *Applied Physics Letters*, vol. 91, p. 182902, 2007.
[33] J. Vyhnánek, M. Janošek, and P. Ripka, "AMR gradiometer for mine detection," *Sensors and Actuators A: Physical*, 2012.

Chapter 7:

MODULATION MODE SENSOR BASED ON NON-LINEAR ME EFFECT

7.1 Introduction

The magnetoelectric (ME) effect is an electric output in response to an applied magnetic field. In a heterostructure configuration where the two-phases are engineered with close interface contact, a giant electric response to a magnetic field has been found, which is designated as the ME voltage (or charge) coefficient α^{ME}.[1-3] This effect is mediated by a mechanical coupling between magnetostrictive and piezoelectric phases.[4, 5]Achieving a substantial value for α^{ME}in an ME heterostructure operated in a passive mode opens the door for developing highly sensitive and low-power consuming magnetometers that operate at room temperature and have sensitivity levels at low frequencies—in fact, approaching those of optically pumped magnetometers.[6,7] The piezomagnetic effect is linear only when the magnetic field and the stress in the magnetostrictive phase vary within a limited range, which is set by a DC magnetic bias (H_{dc}) and/or a mechanical pre-stress. Previous investigations have focused on maximizing α^{ME} near an optimized H_{dc}. Values as high as α^{ME}=61 V/cm-Oe at f=1 Hz have been achieved that have low equivalent magnetic noise levels of 6 pT/rtHz.[1] However, low-frequency vibration and acoustic noise introduced by the piezoelectric effect can significantly raise the noise floor.

Recently, there has been interest in using the non-linear ME effect ($\alpha_{\mathrm{nonlin}}^{\mathrm{ME}}$), as exemplified by a number of research activities in signal processing. For example, non-linear ME interactions have facilitated the development of active mode ME sensors that can modulate weak low frequency signals to a higher frequency bandwidth. This results in the mitigation of a strong 1/f noise, which is often quite large at frequencies near or below 1 Hz.[8-10] Differing the strength of the geomagnetic field scalar along three mutually orthogonal directions can serve as an intelligent switch for the control of this frequency multiplication effect.[11] A DC magnetic field (H_{DC})-controlled frequency

multiplier/doubling effect has been reported in FeBSiC/PZT[12] and Metglas/PZT[13] ME unimorph structures, as illustrated in Figure 7.1.

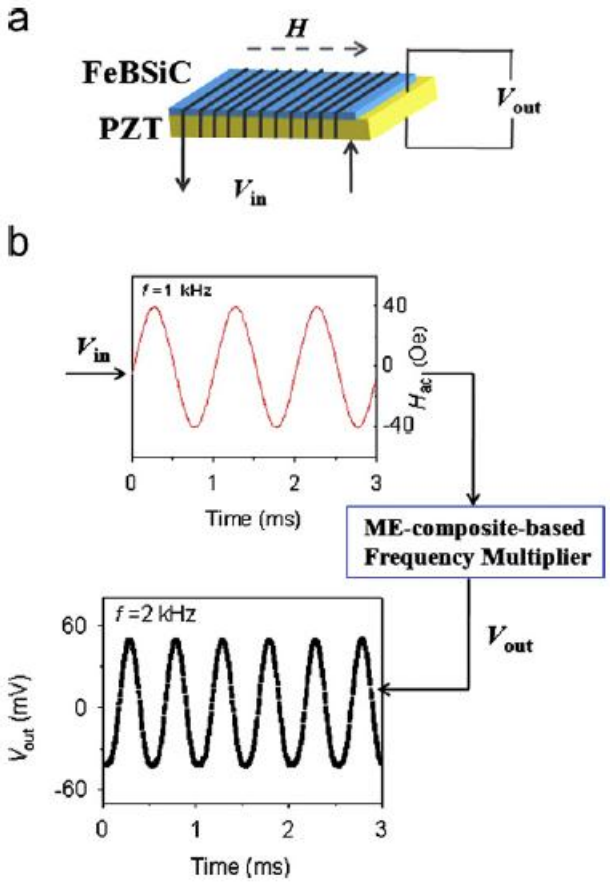

Figure 7.1 (a) Schematic illustration of the ME-composite-based frequency multiplier and (b) representative doubled frequency by this ME frequency multiplier, with the input signal frequency of 1 kHz. [12]

Recently, for Metglas/Pb($Mg_{1/3}Nb_{2/3}$)O_3–$PbTiO_3$ laminates, α^{ME}_{nonlin} was shown to have an optimum value near H_{dc}=0.[14]It shows that for driving frequency f_0=1 kHz (see Fig. 4(c)), a minimum value of the nonlinear ME coefficient α^{ME}_{nonlin}= 0.1 V/cm-Oe^2 was found near H_{dc}=9.5 Oe, whereas a much larger value of α^{ME}_{nonlin} =2.2 V=cm-Oe^2 was found with H_{dc} =2 Oe. Following a similar method—but by increasing f_0=29.5 kHz near the EMR—this maximum value of $\alpha^{ME}_{nonlin.}$ was increased to 25.3 V/cm-Oe^2. These results demonstrate a 253 times higher α^{ME}_{nonlin}, which was achieved by optimizing H_{dc} and f_0.

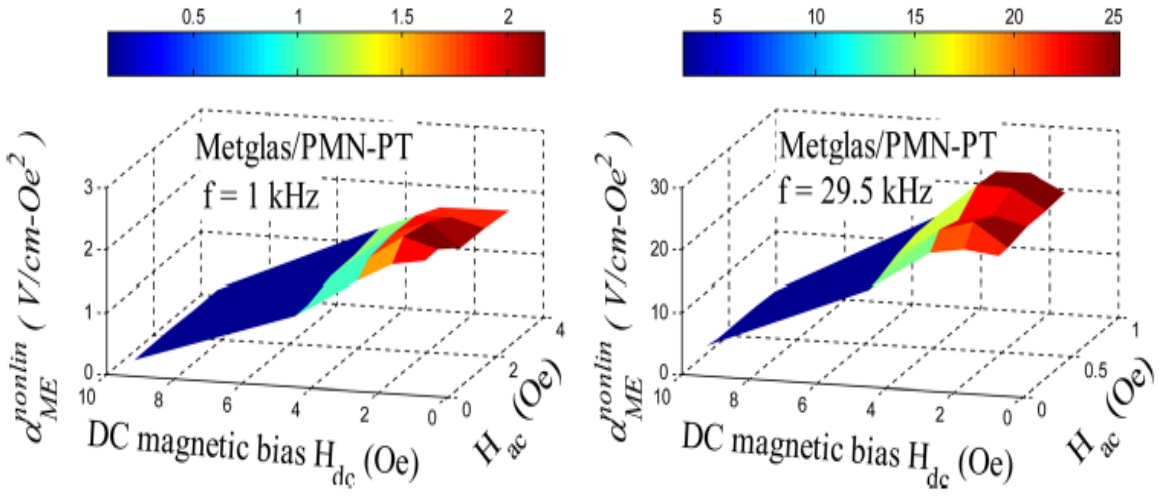

Figure 7.2 The nonlinear ME coefficient α_{nonlin}^{ME} optimization for Metglas/PMN-PT sensor at driving frequency f0=1 and 29.5 kHz respectively.[14]

As discussed in this chapter, I initially investigated the non-linear magnetoelectric (ME) effect of Metglas/Pb($Mg_{1/3}Nb_{2/3}$)O_3–$PbTiO_3$ heterostructures (see Section 7.2). Such an effect holds promise for modulation mode ME sensor applications that require no DC bias. The non-linear ME coefficient was found to be highly dependent on the derivative of the piezomagnetic strain coefficient, which could be augmented by increasing the Metglas length due to magnetic flux concentration. The non-linear ME coefficient was equal to 9.5 $V/(cm - Oe^2)$ at H_{dc}=-1 Oe and 7.5$V/(cm - Oe^2)$ at H_{dc}=0 Oe for a structure with 10cm long Metglas foils. As detailed in Section 7.3, I investigate the non-linear magnetoelectric (ME) response of Metglas/PMN-PT-based sandwiched ME laminate composites of various thicknesses in the magnetostrictive layer. A significant increase in the non-linear ME coefficient under zero DC bias was observed with a decreased Metglas thickness ratio for a fixed number of Metglas layers of n=2. The non-linear ME effect was further improved by driving at the electromechanical resonant frequency. The approach offers the potential to modulate low frequency magnetic signals to higher frequencies, where the noise floor is much lower and the signal-to-noise ratio is significantly higher.

7.2 Piezomagnetic Strain-dependent Non-linear ME Effect

A non-linearity in α^{ME} is known, which is due to a corresponding non-linearity in the magnetostriction of the Metglas layers under a given H_{dc}.[15] Recently, a modulation mode sensor that used a 2nd order ME nonlinearity was reported that was able to transfer low-frequency target signals to higher frequencies.[14] In this method, an exciting carrier signal provided an effective means to reduce 1/f noise, to increase the signal-to-noise ratio (SNR), and to mitigate vibrational noise: that is compared to a conventional passive mode scheme.[8]. The effectiveness of this frequency transfer ability was proportional to the nonlinear ME coefficient $\alpha_{\text{nonlin.}}^{\text{ME}}$ The lack of the need for H_{dc} makes the modulation approach promising. Accordingly, there is a need to understand what causes $\alpha_{\text{nonlin}}^{\text{ME}}$ to vary with $H_{dc.}$ The goal is to find a way to improve $\alpha_{\text{nonlin}}^{\text{ME}}$, especially at H_{dc}=0, that would be enabling for the modulation method to reduce noise by frequency shifting.

7.2.1 Experiment setup

Push-pull tri-layer ME laminates were fabricated by bonding two layers of Metglas on a core $Pb(Mg_{1/3}Nb_{2/3})O_3$–$PbTiO_3$ (PMN-PT) fiber layer.[16] The PMN-PT (Ceracomp, Korea) fibers had a thickness of 200 μm, a length of 4 cm and a width of 1cm. Both top and bottom surfaces of the core composites were fixed to Kapton interdigitated (ID) copper electrode layers (Smart materials, USA) using an epoxy resin (Stycast 1264, USA). The copper electrodes had 500 μm wide digits spaced at a 1.2 mm (center-to-center) distance, enabling the push-pull configuration. The Metglas foils (Vacuumscheltze GmbH & Co. KG, Germany) were 20 μm thick, and were tailored to a length of 8 cm and a width of 1cm.[16] Two tri-layer Metglas foils (epoxied to each other) of such dimensions, were symmetrically attached on both sides of the core composite using an epoxy resin (West system 206, USA). To minimize the epoxy thickness in-between the layers, the laminates were then pressed by a vacuum bag method and cured for more than 24 hours at room temperature. [17]

A 0.074 Oe exciting signal of H_{ac}*sin(2π f_0)t (f_0=1kHz) was applied to a coil which wound around the laminate along its longitudinal axis that was driven by a dynamic signal analyzer (SR-785, Stanford Research Systems, USA), as illustrated in Figure 7.3. A small AC magnetic signal of 180 nT was imposed as an incident field H_{inc}*sin(2π f_1)t

(f_1=1 Hz) by a Helmholtz coil, which surrounded the laminate and was driven by a signal generator. An induced ME modulation output signal of $H_{inc}H_{ac}\cos[2\pi(f_0 \pm f_1)t]$ was measured by the SR-785. The value of α_{nonlin}^{ME} as a function of H_{dc} is shown in Figure 7.4 (a), which can be defined as [14]

$$\alpha_{nonlin}^{ME} = \frac{E}{H_{inc} \times H_{ac}}\left(\frac{V}{cm - Oe^2}\right); \quad (7.1)$$

where H_{inc} is an incident field (to be measured) of a low characteristic frequency f_1,H_{ac} is the driving or modulation high-frequency field at f_0, and E is the ME voltage output of a cross-modulation frequency at $f_0 \pm f_1$.

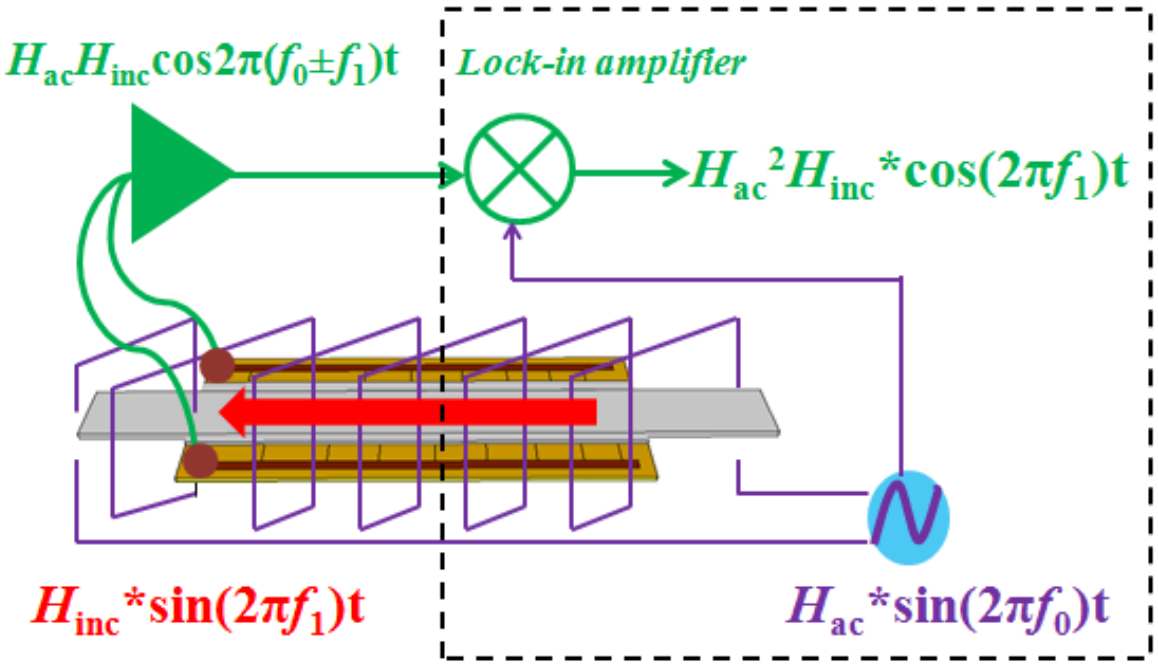

Figure 7.3 Schematic illustration of the ME-composite-based modulation. Carrier signal H_{ac}*sin(2π f_0)t was applied by a driving coil which was wound around the laminate; incident field H_{inc}*sin(2π f_1)t was applied through a Helmholtz coil surrounded the ME laminate. The induced modulation signal is $H_{inc}H_{ac}\cos[2\pi(f_0 \pm f_1)t]$, which can be multiplied with the driving signal $H_{ac}\sin(2\pi f_0 t)$ again via a lock-in amplifier circuits to recover the original incident signal f_1 as $H_{inc}H_{ac}^2\cos(2\pi f_1)t$.

7.2.2 Results and analysis

In Figure 7.4 (a), the value of $\alpha_{\text{nonlin}}^{\text{ME}}$ can be seen to have multiple peaks with increasing H_{dc}. A value of $4.5\text{V}/(\text{cm}-\text{Oe}^2)$ was found at H_{dc}=0 Oe, which increased to a first maximum near H_{dc}=±2 Oe of about $6.5\text{V}/(\text{cm}-\text{Oe}^2)$ and subsequently decreased with increasing H_{dc} until H_{dc}=±9 Oe. With further increase of H_{dc}, the value of $\alpha_{\text{nonlin}}^{\text{ME}}$ increased to a 2nd peak of α_{nonlin}^{ME}=$7.5\text{V}/(\text{cm}-\text{Oe}^2)$ at H_{dc}=±13 Oe, and then decreased rapidly approaching a value of zero for H_{dc}>±20 Oe. Figure 2 (b) shows the magnetostriction λ and the effective piezomagnetic coefficient d_{33}^{m} (or $\partial\lambda/\partial H$) as a function of H_{dc}. The value ofα^{ME} was strongly dependent on d_{33}^{m}, as can be seen in the inset of this figure. The value of α_{nonlin}^{ME} was also found to be dependent on $\partial d_{33}^{m}/\partial H$.Comparison ofFigs.7.4 (a) and 7.4 (c) will reveal that as $\partial d_{33}^{m}/\partial H$ approached a maximum value of 1.2×10^{-6} Oe^{-2} near H_{dc}=0 Oe that the value of $\alpha_{\text{nonlin}}^{\text{ME}}$ was near its1st peak, and when $\partial d_{33}^{m}/\partial H$was at its 2nd peak near H_{dc}=±13 Oe that α_{nonlin}^{ME} was also at its 2nd peak. Furthermore, when α_{nonlin}^{ME} reached a minimum at H_{dc}=±9 Oe, the value of $\partial d_{33}^{m}/\partial H$ was also at its minimum.

Next, the relationship between α_{nonlin}^{ME} and $d_{33}^{m}$was analyzed. The ME voltage V(t) can be written in a Taylor expansion series as: [10]

$$V(t)=\alpha_0+\alpha_1H(t)+\alpha_2H^2(t)+\alpha_3H^3(t)+\cdots\cdots\ ;\quad (7.2)$$

where α_{i} (i=0, 1, 2⋯⋯) is the Taylor expansion coefficient of ith order. The first order coefficient $\alpha_1={}^{dV}/_{dH}$ equals α^{ME}. When the laminate is excited by H_{ac}*sin(2π f_0)t with a parallel superimposed incident field H_{inc}*sin(2π f_1)t, an effective magnetic field $H(t)=H_{dc}+H_{ac}\sin(2\pi f_0t)+H_{inc}\sin(2\pi f_1t)$is induced. This induced ME output can be measured by an AC-coupling method, where the DC component of the signals is removed. Thus, the 2nd order cross-term $\alpha_2'H_{inc}H_{ac}\cos[2\pi(f_0\pm f_1)t]$ becomes significant, where the new summed parameter α_2' equals $\alpha_{\text{nonlin}}^{\text{ME}}$ based on its definition (see Eq. (7.1)). The Taylor series also has a definition for the 2nd order coefficient $\alpha_2'={}^{dV^2}/_{d^2H}$ of:

$$\alpha_{\text{nonlin}}^{\text{ME}}=\alpha_2'=\frac{dV^2}{d^2H}=\frac{d\alpha_1}{dH}=\frac{d\alpha^{ME}}{dH}.\quad (7.3)$$

Eq (7.3) indicates that $\alpha_{\text{nonlin}}^{\text{ME}}$ should be proportional to the derivative strength of α^{ME}, which agrees well with experiment results. Comparison of figure 7.4 (a) and the inset of figure 7.4 (c) illustrates this. The values of $\alpha_{\text{nonlin}}^{\text{ME}}$ and $\partial\alpha^{ME}/\partial H$ have similar functional forms with H_{dc}: both have a first peak around zero DC bias, decrease to a minimum at H_{dc}=±9 Oe, and subsequently increase to a second peak near H_{dc}=±13 Oe. Since α^{ME} is proportional to d_{33}^{m}[18] (see Fig 7.4(b)), equation (7.3) reduces to:

$$\alpha_{\text{nonlin}}^{\text{ME}} \propto \frac{\partial d_{33}^{m}}{\partial H}. \quad (4)$$

This equation shows that $\alpha_{\text{nonlin}}^{\text{ME}}$ should be proportional to $\partial d_{33}^{m}/\partial H$. Eq (4) is verified by the data in figure 7.4 (a) and figure 7.4 (c), as again the functional forms of $\alpha_{\text{nonlin}}^{\text{ME}}$ and $\partial d_{33}^{m}/\partial H$ with H_{dc} are similar.

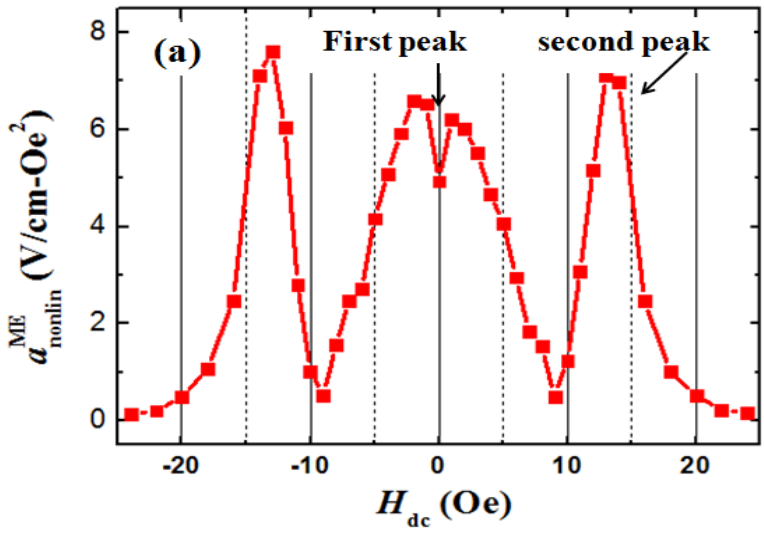

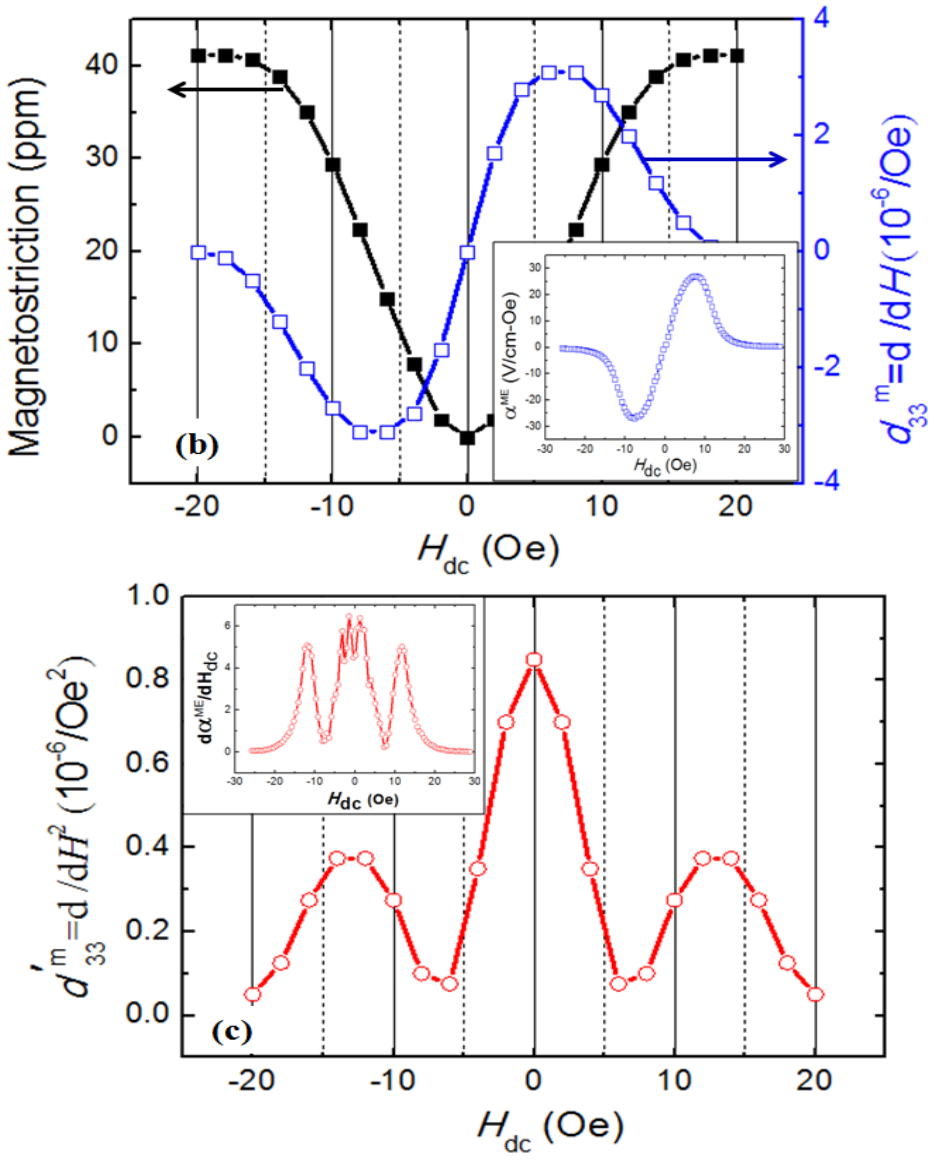

Figure 7.4 (a) Non-linear ME voltage coefficient α_{nonlin}^{ME} of 8cm-long Metglas/PMN-PT laminate composites projected on H_{dc}. (b) Magnetostriction strain λ (black curve) and piezomagnetic coefficient d_{33}^{m} (blue curve) as a function of H_{dc}. The inset is the first order ME coefficient α^{ME} curve which is shown to be highly-dependent on the piezomagnetic coefficient td_{33}^{m}. (c) Derivative strength of d_{33}^{m} as a function of H_{dc}. The inset is the derivative strength of ME coefficient α^{ME}. It indicates that α_{nonlin}^{ME} has a differential dependence of d_{33}^{m} on magnetic bias H_{dc} that is$\partial d_{33}^{m}/\partial H$.

A magnetic flux concentration effect was then found to enhance α_{nonlin}^{ME}. Figure 7.5 (a) shows the value of α_{nonlin}^{ME} for laminates with different Metglas lengths (L=6cm and 10cm) as a function of H_{dc}. In this figure, it can be seen for L=6cm, that the peaks in

$\alpha_{\mathrm{nonlin}}^{\mathrm{ME}}$ became wider than the one with 8cm-Metglas foils (see Figure 2a): in particular, the 2nd peak was shifted toa higher bias of H_{dc}=±20 Oe, and the minimum between the two peaks was increased to H_{dc}=±12 Oe. It can also be seen that the peak values were significantly decreased. In contrast, for L=10cm, the peak values of $\alpha_{\mathrm{nonlin}}^{\mathrm{ME}}$ were notably increased: the peak value was 9.5 $\mathrm{V/(cm-Oe^2)}$ at H_{dc}=-1 Oefor the1st peak, which represents an enhancement of a factor of 4x for $\alpha_{\mathrm{nonlin}}^{\mathrm{ME}}$ over previous reports using a 1 kHz driving signal. [14]It should also be noted under H_{dc}=0that the value of$\alpha_{\mathrm{nonlin}}^{\mathrm{ME}}$ wasincreased to 7.5 $\mathrm{V/(cm-Oe^2)}$: this is in comparison to that of 2.5 $\mathrm{V/(cm-Oe^2)}$ for L=6 cm and 4.8 $\mathrm{V/(cm-Oe^2)}$ for L=8cm. In addition, for L=10cm, the peaks of $\alpha_{\mathrm{nonlin}}^{\mathrm{ME}}$ with H_{dc} were sharper and occurred at lower biases. These trends of change in $\alpha_{\mathrm{nonlin}}^{\mathrm{ME}}$ can be attributed to the difference in d_{33}^{m} for different Metglas lengths, as shown in Figure 7.5 (b). In this figure, for L=6cm, one can see that the maximum d_{33}^{m} occurred near H_{dc}=±12 Oe; whereas for L=10cm, the d_{33}^{m} peak value was shifted to H_{dc}=±6 Oe. This resulted in an increased slope of $\mathrm{d_{33}^{m}}$ with H_{dc}, especially near H_{dc}=0 as highlighted in the figure. These results demonstrate that α_{nonlin}^{ME} is notably-dependent on $\partial d_{33}^{m}/\partial H$, and that the values of both can be increased by flux concentration.

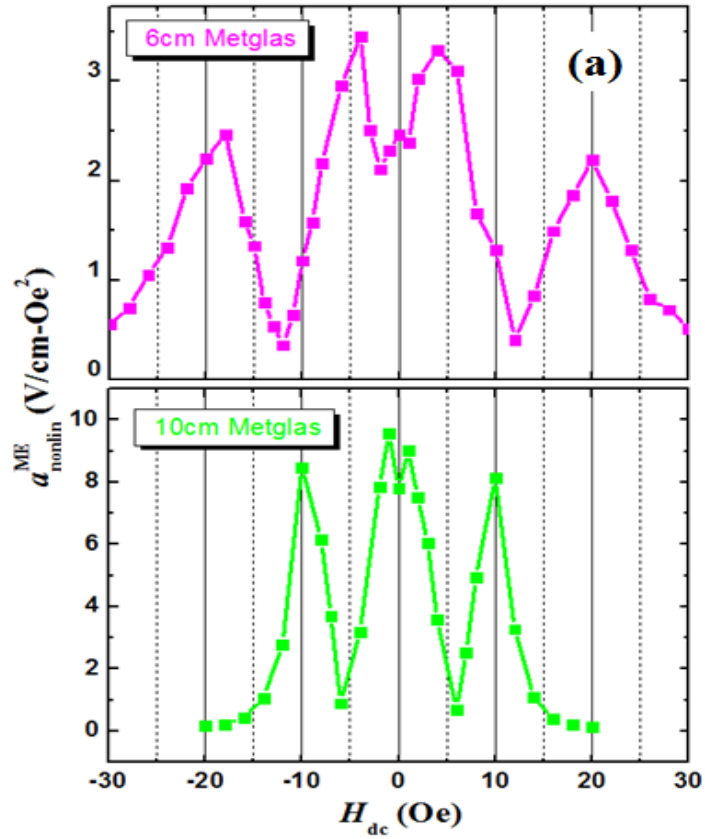
6cm Metglas
(a)
10cm Metglas
α^{ME}_{nonlin} (V/cm-Oe^2)
H_{dc} (Oe)

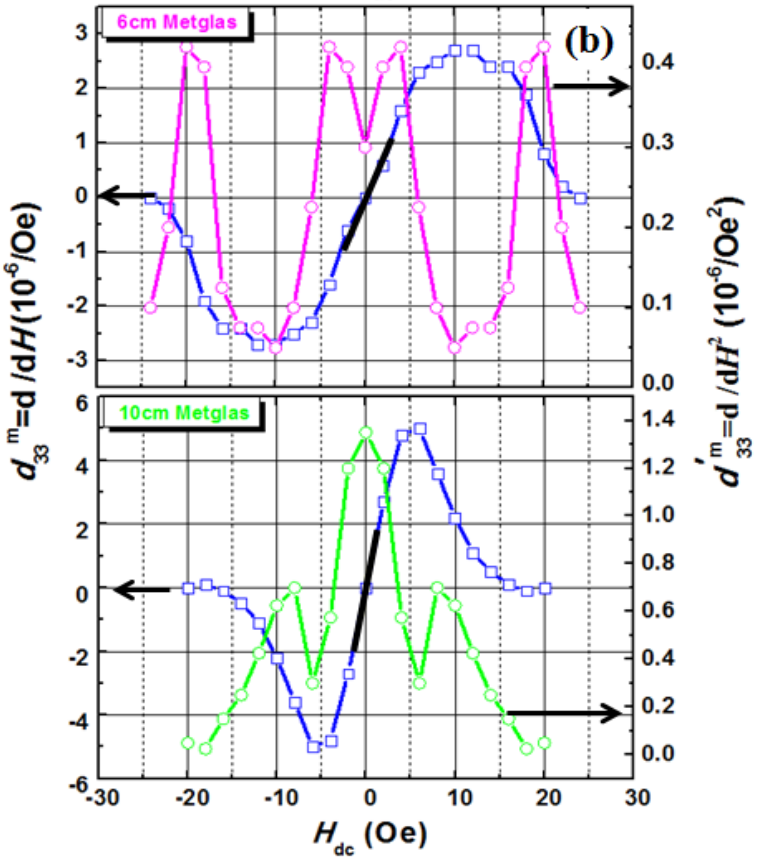
6cm Metglas
(b)
10cm Metglas
d^m_{33}=d /dH(10^{-6}/Oe)
d'^m_{33}=d /dH^2 (10^{-6}/Oe^2)
H_{dc} (Oe)

Figure 7.5 (a) ME non-linear coefficients α_{nonlin}^{ME} for different lengths (6cm and 10cm) Metglas as a function of H_{dc}. (b) Piezomagnetic coefficient d_{33}^{m} and its derivative strength $\partial d_{33}^{m}/\partial H$ of 6cm and 10cm composites. The 10cm composites have much higher $\partial d_{33}^{m}/\partial H$ value than that of 6cm one, particularly under H_{dc}=0 Oe. The slope of $\mathbf{d}_{33}^{\mathbf{m}}$ is highlighted by a bold black line.

When the cross-modulation signal output was demodulated and multiplied with the driving signal $H_{ac}\sin(2\pi f_0 t)$, the original incident signal f_1 can be recovered in the term $H_{inc}H_{ac}^2\cos(2\pi f_1)t$ (see dashed window in Fig 7.3).[10] Following the modulation principle, the demodulation voltage output V_{de} should be linear proportional to the incident field H_{inc}. Accordingly, we measured the sensor output signal after demodulation as a function of H_{inc} using the 8cm ME laminates as given in Figure 7.6 (a). Laminates of length 6cm and 10 cm have similar results that are not shown here. The carrier signal (1 kHz), two cross-modulation signals (999 and 1001 Hz) and the demodulated signal (1 Hz) can be identified. In this figure, it can also be seen as H_{inc} was increased from 18 nT to 180 nT that enhanced cross-modulation signals resulted, which in turn lead to an increased demodulated signal at f_1=1 Hz. In Figure 7.6 (b), the value of V_{de} can be seen to be dependent on H_{inc} with a demodulation transfer function equal to 84 mV/Oe. Note that these data were measured at a constant driving signal of H_{ac} =0.074 Oe for f_0=1 kHz under zero DC bias. The results show that V_{de} is linearly proportional to H_{inc}, in agreement with the modulation principle. Such a linearity of the transfer function is essential for estimating unknown incident fields in applications, where normalization is difficult to perform accurately.

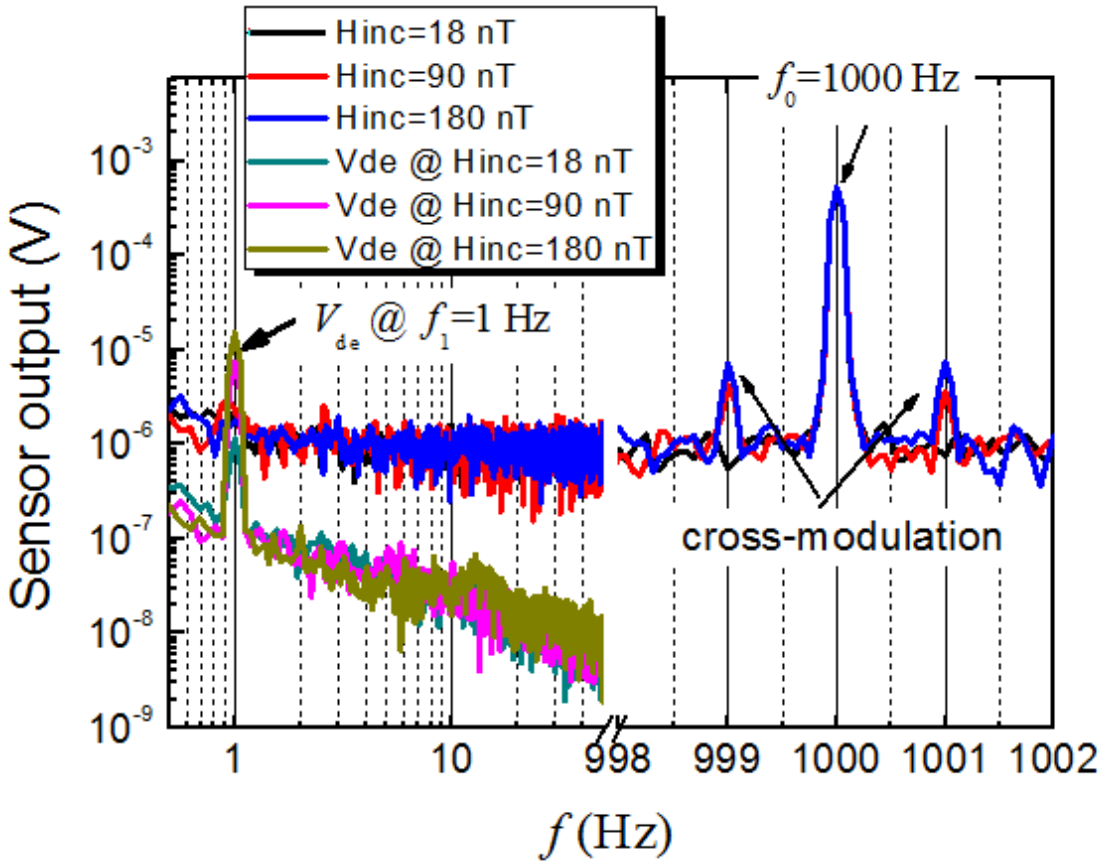
Hinc=18 nT
Hinc=90 nT
Hinc=180 nT
Vde @ Hinc=18 nT
Vde @ Hinc=90 nT
Vde @ Hinc=180 nT
V_{de} @ f_1=1 Hz
f_0=1000 Hz
cross-modulation
Sensor output (V)
10^{-3}
10^{-4}
10^{-5}
10^{-6}
10^{-7}
10^{-8}
10^{-9}
1
10
998
999
1000
1001
1002
f (Hz)

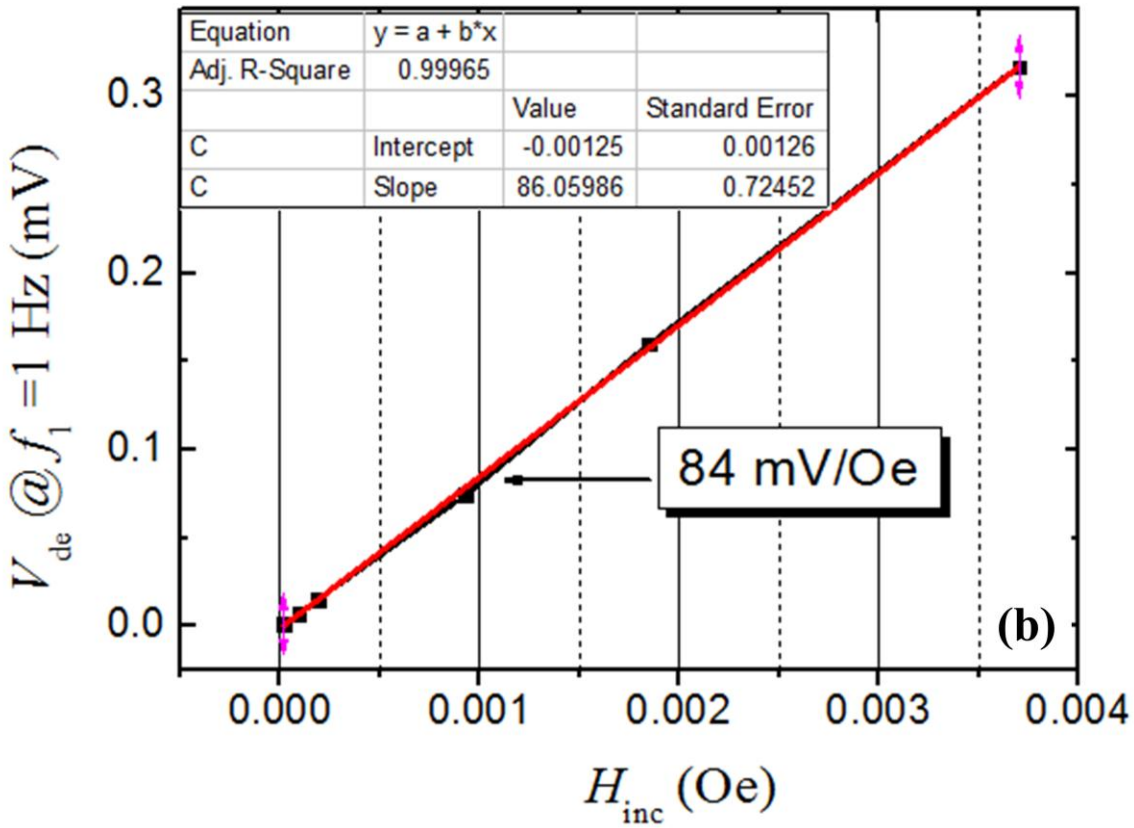

Figure 7.6 (a) Sensor output signals after demodulation as a function of H_{inc} using the 8cm ME composites which contain the carrier signal (1 kHz), two cross-modulation signals (999 and 1001 Hz) and the demodulated signal (1 Hz). The increased H_{inc} from 1.8 nT to 18 nT result in enhanced cross-modulation signals, and finally leaded to an increased demodulated signal V_{de} at f_1=1 Hz. (b) Demodulation output V_{de} is strongly dependent on H_{inc} with demodulation transfer ability function of 84 mV/Oe when driving signal H_{ac} =0.074 Oe.

7.2.3 Summary of This Section

In summary, the non-linear ME coefficient $\alpha_{\text{nonlin}}^{\text{ME}}$ for ME laminate composites of Metglas/PMN-PT has been found to be strongly dependent on $\partial d_{33}^{m}/\partial H$. Adjusting the slope of d_{33}^{m} by a flux-concentration effect provides a way to improve α_{nonlin}^{ME} at H_{dc}=0 Oe. This is important to remove the required H_{dc} for ME sensors, eliminating potential bias interference effects in sensor arrays. The results demonstrate the feasibility to also use the modulation technique to reduce vibration noise by shifting low frequency magnetic signal (f_1) to higher frequencies ($f_0 \pm f_1$). By multiplying cross-modulation signals with the driving signal, an incident signal (f_1) was recovered filtering out low

frequency noises. The demodulated signal V_{de} was found to be linearly proportional to H_{inc}, in agreement with predictions. An increase of the Metglas length resulted in increased values of α_{nonlin}^{ME} to $7.5 V/(cm-Oe^2)$ and to $9.5\ V/(cm-Oe^2)$ at H_{dc}=0 and -1 Oe, respectively.

7.3 Non-linear ME Response Enhancement by Flux Concentration Effect

Due to investigation in section 7.2, we can see that the non-linear ME effect is dependent on the non-linear property of the effective piezomagnetic coefficient (d_{33}^m) that is proportional to H^2 (where H is the applied magnetic field).[19] In piezoelectric/magnetostrictive composites, the induced ME output (V) is proportional to d_{33}^m,[18] resulting in V being proportional to H^2. Thus, when an applied AC magnetic field H_{AC} is superimposed with a DC magnetic field bias H_{DC}, the total effective field in the ME composite is $H = H_{DC} + H_{AC}\sin(\omega_0 t)$, which produces a frequency multiplication effect; by applying another incident AC field $H_{inc,}$ there will be $H = H_{DC} + H_{AC}\sin(\omega_0 t) + H_{inc}\sin(\omega_1 t)$, and the frequency modulation and mixing can be achieved.

Therefore, Enhancement in the value of α_{nonlin}^{ME} is an important issue with regards to the practical use of the non-linear ME effect, i.e., frequency mixing and modulation. There have been limited reports for Metglas/piezo-fiber composites that exhibit α_{nonlin}^{ME}on the order of $2.2\ V/(cm-Oe^2)$ at H_{DC}=2 Oe under a driving signal of f_0=1 kHz, which can be improved to α_{nonlin}^{ME} =$25.3\ V/(cm-Oe^2)$ by simply optimizing f_0 to be the electromechanical resonant (EMR) frequency.[14] Here, I show an enhancement of α_{nonlin}^{ME}at H_{DC}=0 for a Metglas/PMN-PT heterostructure, through an optimized Metglas-piezofiber thickness ratio. Of particular importance, the frequency modulation scheme for the non-linear ME effect can shift low frequency signals to higher frequency ones to achieve a reduced noise floor. With regards to frequency modulation, the value of f_0 was selected to be at the EMR condition of the structure in order to optimize α_{nonlin}^{ME}, and correspondingly to decrease the equivalent magnetic noise floor. As a result, the signal to noise ratio (SNR) was significantly increased by a factor of 15 at f_0=EMR relative to f_0=1 kHz.

7.3.1 Measurement

The PMN-PT ME laminates were comprised of two tri-layers of magnetostrictive Metglas (Vacuumscheltze GmbH & Co. KG, Germany) sandwiching a piezoelectric PMN-PT (Ceracomp, Korean) core.[16] When an external magnetic field was applied, the Metglas layers generated a magnetic field induced strain via magnetostriction, resulting in a stress on the adjacent PMN-PT layers, which in turn produced a stress-induced electrical charge. Five PMN-PT fibers were used that had overall dimensions of $40\times10\times0.2$ mm^3. Both top and bottom surfaces of the core composites were fixed with two Kapton interdigitated copper electrodes layers (Smart materials, USA) using epoxy resin (Stycast 1264, USA). The copper electrodes had 500 μm wide digits spaced at 1.5 mm center-to-center to obtain the push-pull geometry. 25 μm thick Metglas foils were cut to have 10mm widths, similar to the core PMN-PT layer, and 100 mm lengths. Previous studies have shown this geometry to have the largest value of $\alpha_{\text{nonlin}}^{\text{ME}}$ due to magnetic flux concentration.[19] Six Metglas layers of such dimensions were then symmetrically attached to the two sides of the core composite using another epoxy resin (West system 206, USA). To minimize the epoxy thickness in-between the layers, the laminates were then pressed by a vacuum bag and cured for more than 24 hours at room temperature to finish fabrication of the ME laminates.

The laminates were wound with 200-turn windings, through which a H_{AC} signal was excited by a dynamic signal analyzer (SR-785, Stanford Research Systems, USA). This achieved an active modulation mode ME sensor, as shown in the inset of Figure 1. The active sensor unit was then placed into a Helmholtz coil driven by another signal generator with a low frequency incident signal H_{inc}. The induced voltages across the ID electrodes of the PMN-PT fibers at a modulation frequency of $f_0 \pm f_1$ were then measured by the SR-785 in response to H_{AC}=0.1 Oe at f_0=1kHz, and H_{inc}=0.0018 Oe at f_1=1 Hz. The Helmholtz coil together with the active sensor was placed between two poles of an electromagnet. Both DC and AC fields were directed along the longitudinal direction of the laminates, and measurements were performed as a function of dc magnetic bias with field strength of -30 Oe $\leq H_{\text{DC}} \leq$ 30 Oe.

Figure 7.7 shows $\alpha_{\text{nonlin}}^{\text{ME}}$ as a function of H_{DC} for different values of n stacked on both sides of the piezo-fiber core, where n was varied by successively peeling off layers.

From this figure, it can be seen that $\alpha_{\text{nonlin}}^{\text{ME}}$ was maximum at H_{DC}=0; decreased rapidly as H_{DC} was increased; reached a minimum value at a particular bias; and subsequently increased slightly reaching a second peak and then decreased to near zero as H_{DC} was further increased. One can also clearly see that the maximum value of $\alpha_{\text{nonlin}}^{\text{ME}}$ at H_{DC}=0 increased with decreasing number of Metglas layers until n=2. Moreover, the H_{DC} required for the second peak in $\alpha_{\text{nonlin}}^{\text{ME}}$ decreased with decreasing n. The enhancement in $\alpha_{\text{nonlin}}^{\text{ME}}$ for n=2 relative to n=6 is noteworthy, as prior studies of passive ME sensors have been focused on n=6 to achieve a maximum linear ME coefficient α^{ME}.[2, 20, 21] The value of $\alpha_{\text{nonlin}}^{\text{ME}}$ at H_{dc}=0 was determined to be 13 $\text{V}/(\text{cm}-\text{Oe}^2)$ for n=2, which represents an improvement of 6 times over previously reported values.[14]

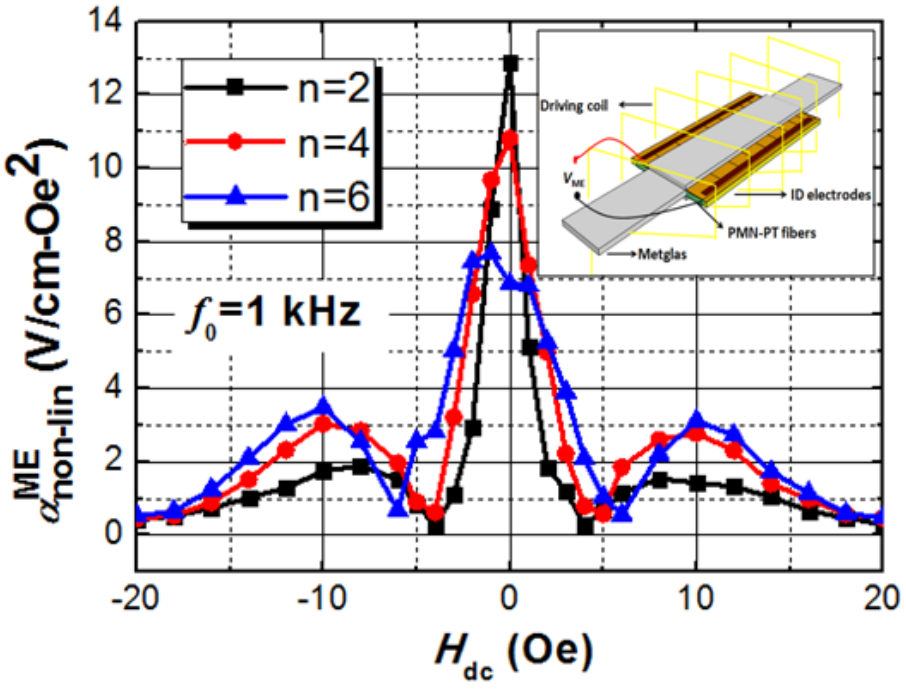

Figure 7.7 Non-linear ME coefficient $\alpha_{\text{nonlin}}^{\text{ME}}$ as a function of H_{DC} for various PMN-PT fiber-Metglas laminate composites under f_1=1 Hz. The numbers show the number (n) of Metglas layers stacked on both sides of the piezo-fibers, where n was varied by successively peeling off layers. The inset shows schematic diagram of the proposed Metglas/PMN-PT composites with driving coil.

7.3.2 Analysis and discussion

Figure 7.8 (a) shows the linear ME voltage coefficient α^{ME} for the same structures for different values of n. α^{ME} was measured using a lock-in amplifier, as a function of H_{DC} and in response to H_{AC}=1 Oe at f=1 kHz that was driven by a Helmholtz coil. With increasing H_{DC}, α^{ME} increased quickly from zero at H_{DC}=0 to a maximum value at a particular H_{DC} (which is referred as H_{optim}), and then declined to zero for $H_{DC}\geq$ 20 Oe. Such a thickness fraction-dependent α^{ME} for bimorph heterostructures has previously been shown.[1, 20, 22] Please note that the H_{optim}, where α^{ME} had maximum values for various n, were nearly equal to the bias at which α_{nonlin}^{ME} was minimum (see Fig. 1). Figure 7.8 (b) shows the derivative values of ME coefficient $div(\alpha^{ME})$ as a function of H_{DC}. A previous study[19] has indicated that α_{nonlin}^{ME} is dependent on the derivative of the piezomagnetic strain and should be proportional to $div(\alpha^{ME})$, which is consistent with data of Fig. 1 and 2(b). In these figures, one can clearly see that n=2 has the largest maximum $div(\alpha^{ME})$ value at H_{DC}=0,that the required H_{DC} decreased with decreasing n reaching a minimum value near H_{DC} =5 Oe, and that a second peak occured near $H_{DC}\sim$ 10 Oe.

Figure 7.8 (c) shows the magnetization (M) for various n as a function of magnetic field applied along the longitudinal direction. These data were obtained by using a vibrating sample magnetometer (VSM). The in-plane *M-H* behaviors for n=2, 4, 6 show that the required H_{DC} increased as n was increased. Thus, the linear magnetic susceptibility (χ_m) defined as the differential of the magnetization with magnetic bias ($\partial M/\partial H$), is the slope of the *M-H* curves. In this figure, the slope of the *M-H* curves can be seen to increase with decreasing n. χ_m has a significant effect on the relaxation factor k, which is proportional to the piezomagnetic coefficient d_{33}^m, given as[23]

$$k = \frac{3\chi_m}{M_s} and\ k \sim d_{33}^m ; \qquad (7.4)$$

where M_s is the saturation magnetization. The value of χ_m increased with decreasing n, resulting in an increase of k at a constant M_s and a subsequently enhanced value of d_{33}^m. Recently, it has been reported that α_{nonlin}^{ME} is highly dependent on the derivative of the

piezomagnetic strain coefficient, $\alpha_{\text{nonlin}}^{\text{ME}} \propto \partial d_{33}^{m}/\partial H$.[19, 24] As a consequence, the value of $\alpha_{\text{nonlin}}^{\text{ME}}$ increased with decreasing n as evidenced in Figure 7.7.

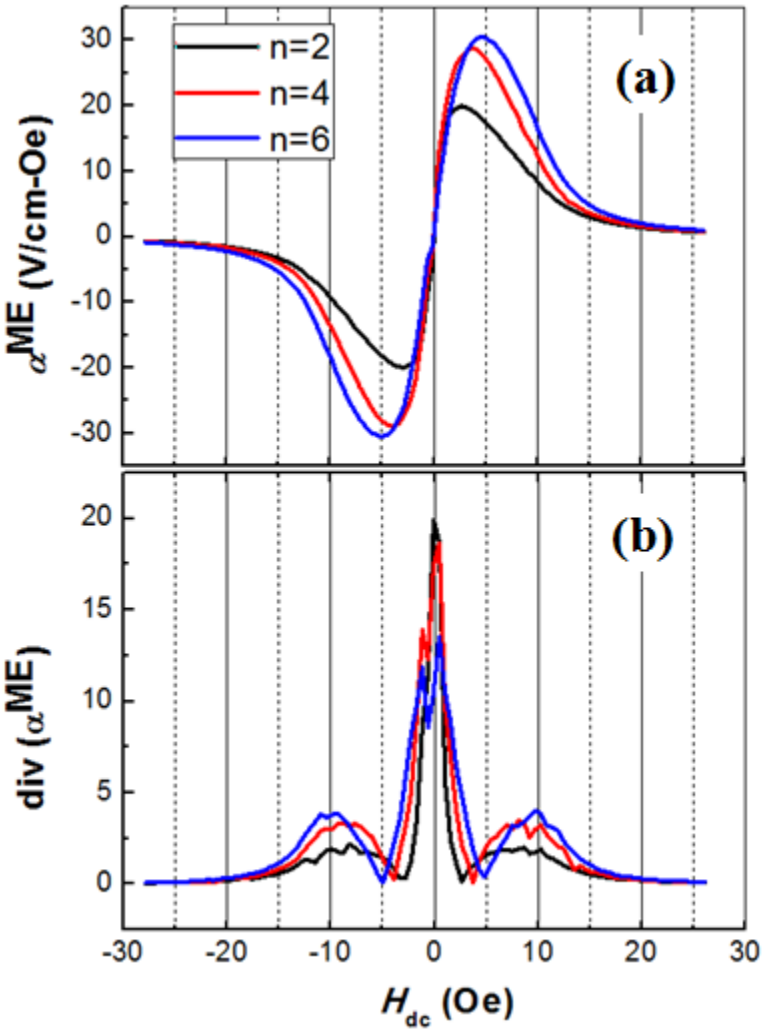

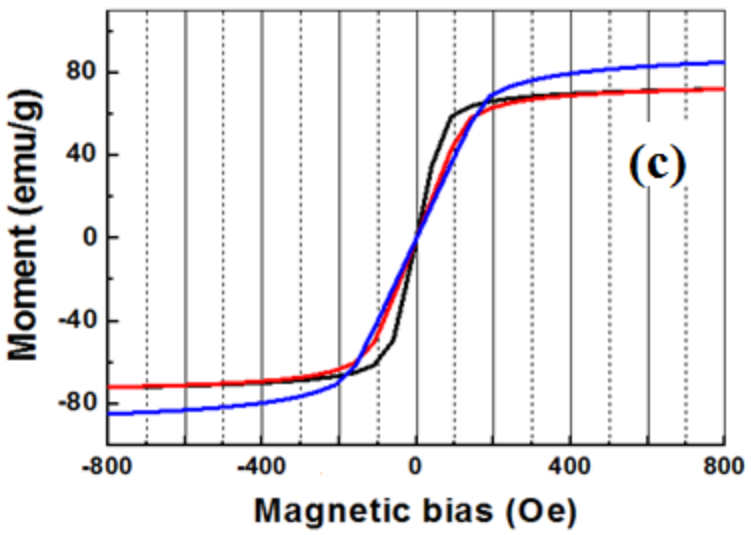

Figure 7.8 (a) ME voltage coefficient α^{ME} as a function of H_{DC} for various PMN-PT/Metglas laminates with different Metglas layers; (b) derivative values of ME coefficient $div(\alpha^{ME})$ as a function of H_{dc}; and (c) magnetization (M) of various Metglas layers as a function of magnetic field applied along the longitudinal direction.

The demodulated signal at f_1=1 Hz was then measured by a SR-785 dynamic signal analyzer, where the modulation signal ($f_0 \pm f_1$) was multiplied again by the driving signal (f_0) using a SR-850 lock-in amplifier. Figure 7.9 (a) shows the demodulated signal for a ME structure with n=2. These data were measured in response to an increasing H_{inc} between 2 nT to 90 nT at f_1=1 Hz, where H_{AC} was fixed at f_0=1 kHz. In this figure, it can be seen with increasing H_{inc}that the demodulated signal increased linearly with a transfer function of 3.7 V/Oe, as shown in Figure 7.9 (b). Further increase in the drive signal frequency to f_0=10 kHz and 24.2 kHz (i.e., the EMR) resulted in transfer functions of 5.3 V/Oe and 33.4 V/Oe respectively, shown in Figure 7.9 (b). These data were taken at a constant driving signal of H_{AC} =70 nT under H_{DC}=0. A tuning resistor was utilized to cancel the inductance of the driving coil, maintaining a stable magnetic field amplitude that was independent of frequency f_0. As shown in Fig. 7.9 (c), a significantly increased modulation transfer ability at f_0=24.2 kHz was observed, which can be attributed to the high value of α_{nonlin}^{ME}=100 $V/(cm - Oe^2)$ at H_{DC}=0 under the drive conditions. Clearly, the frequency transfer ability is dependent on the non-linear ME coefficient.

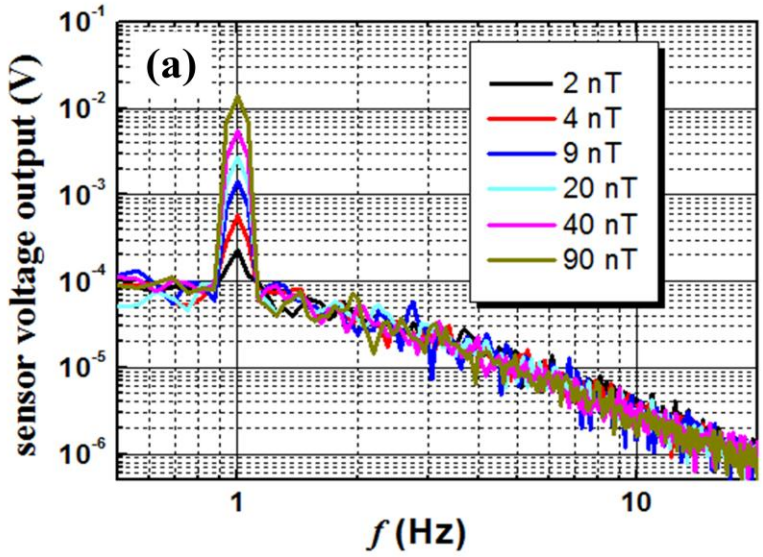
(a)
2 nT
4 nT
9 nT
20 nT
40 nT
90 nT
sensor voltage output (V)
10^{-1}
10^{-2}
10^{-3}
10^{-4}
10^{-5}
10^{-6}
1
10
f (Hz)

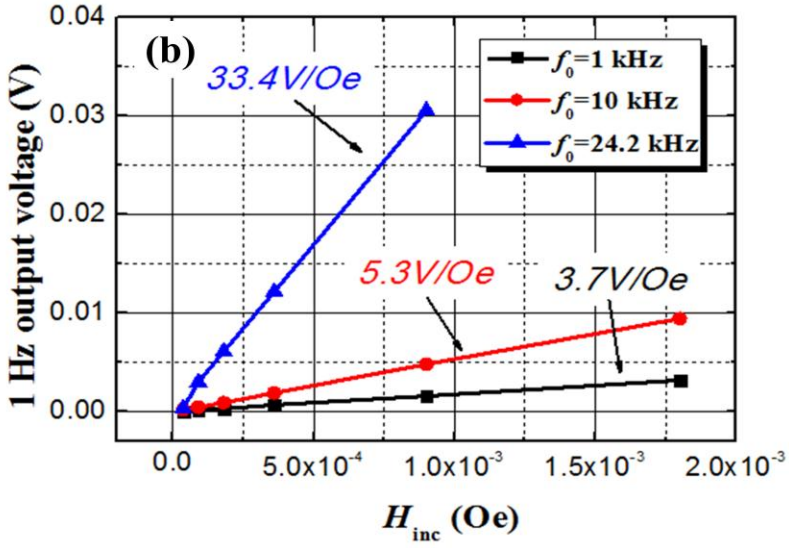
(b)
33.4V/Oe
5.3V/Oe
3.7V/Oe
f_0=1 kHz
f_0=10 kHz
f_0=24.2 kHz
1 Hz output voltage (V)
0.04
0.03
0.02
0.01
0.00
0.0
5.0x10^{-4}
1.0x10^{-3}
1.5x10^{-3}
2.0x10^{-3}
H_{inc} (Oe)

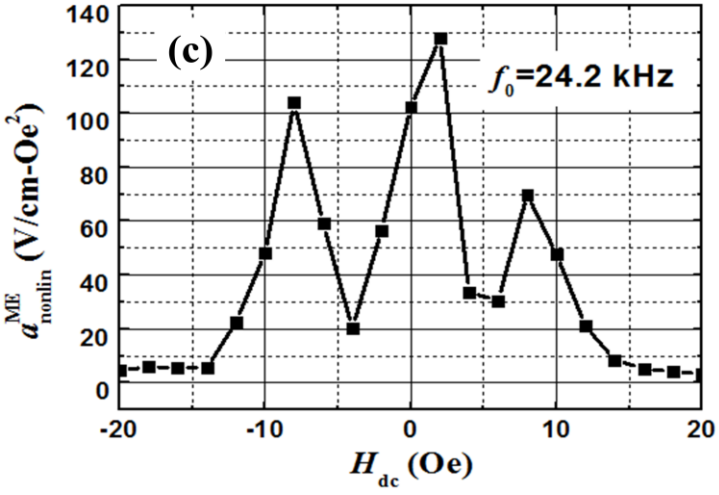
(c)
f_0=24.2 kHz
a^{ME}_{nonlin} (V/cm-Oe^2)
140
120
100
80
60
40
20
0
-20
-10
0
10
20
H_{dc} (Oe)

Figure 7.9 (a) Signal for a structure with n=2 in response 2≤ H_{inc}≤ 90 nT at f_1=1 Hz under zero DC bias, where H_{AC}=70 nT at f_0=1 kHz; (b) linear frequency modulation transfer function of 3.7 V/Oe, 5.3 V/Oe and 33.4 V/Oe for f_0=1, 10 and 24.2 kHz (EMR of the laminates); (c) non-linear ME coefficient α_{nonlin}^{ME} as a function of H_{DC} for Metglas/PMN-PT laminate composites with n=2 for f_1=24.2 Hz.

The voltage spectrum noise density of the demodulated signal was then measured using a SR-785 in unit of V/√Hz. These data were obtained in response to a fixed drive signal of H_{AC} =70 nT at different frequencies of f_0=1, 10 and 24.2 kHz. Upon applying the transfer function, the equivalent magnetic noise spectrum can be converted into unit of T/√Hz, as follows

$$Equivalentmagnticnoise\left(\frac{T}{\sqrt{Hz}}\right)=\frac{voltagenoise\left(\frac{V}{\sqrt{Hz}}\right)}{transferfunction\left(\frac{V}{Oe}\right)}\times 10^{-4}\,. \quad (7.5)$$

Figure 7.10 shows a representative equivalent magnetic noise spectrum. In this figure, the noise floor can be seen to be about 0.2 nT/√Hz at 1 Hz for f_0=24.2 kHz, which was much lower than that of 3 nT/√Hz for f_0=1 kHz. This decrease in the equivalent magnetic noise floor is a direct consequence of the use of a high driving frequency (at f_0) which can effectively transfer a low frequency target signal (f_1) to higher frequencies ($f_0 \pm f_1$), where the noise floor is much lower. It should be noted that these measurements were performed using a constant incident signal of H_{inc}=18 nT at f_1=1 Hz, as can be identified in the signal strengths to be constant as f_0 was varied in Fig. 7.10. The constant signal strength and reduced noise floor together resulted in an increased signal-to-noise ratio (SNR) at f_0=24.2 kHz. The SNR reached values of 300, which were significantly higher than SNR=20 and 100 for f_0=1 and 10 kHz. A higher value of SNR offers the potential to allow detection of much weaker magnetic fields. Thus, the enhanced SNR found by optimizing f_0 to be close to the EMR condition of the ME laminates offers promise for active mode ME sensor applications, which takes advantage of the enhanced values of $\alpha_{\mathrm{nonlin}}^{\mathrm{ME}}$ using the optimized thickness ratio and EMR drive (see Figs. 7.9(c) and 7.10). Significantly lower equivalent magnetic noise floors have been obtained in this study, consistent with predictions in [12].

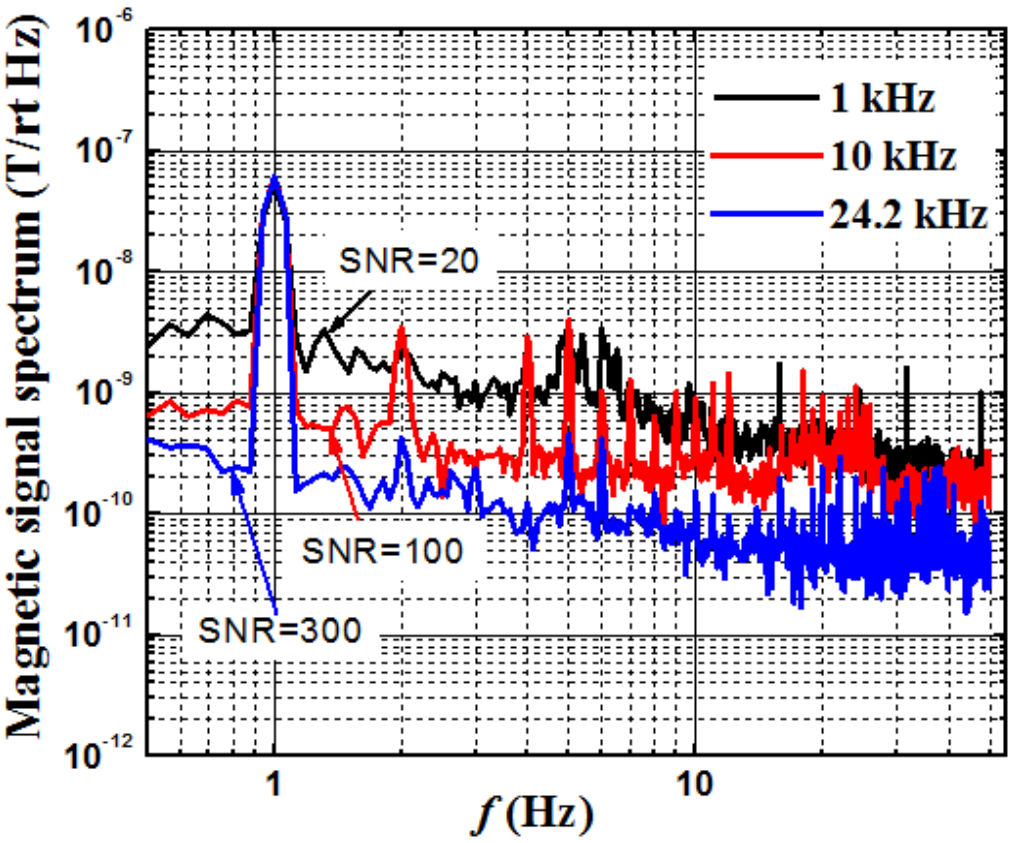

Figure 7.10 Equivalent magnetic noise spectrum for a magnetic signal at 1 Hz, after applying modulation transfer functions at various driving frequencies at f_0=1, 10 and 24.2 kHz. The noise floor can be seen to be 0.2 nT/√Hz at 1 Hz for f_0=24.2 kHz. When f_0=24.2 kHz, the highest signal to noise ratio was reached with SNR=300, compared to SNR=20 and 100 for f_0=1 and 10 kHz. This offers the potential to allow detection of weaker magnetic fields.

7.3.3 Summary of this section

In summary, a decrease in the number of Metglas layers has been shown to result in an enhancement in the non-linear ME coefficient at H_{DC}=0 for Metglas/PMN-PT based laminate composites. Using a drive signal at f_0=1 kHz, a high value of $\alpha_{\text{nonlin}}^{\text{ME}}$=13 $\text{V}/(\text{cm}-\text{Oe}^2)$ was obtained for n=2, which was further increased to $\alpha_{\text{nonlin}}^{\text{ME}}$=100 $\text{V}/(\text{cm}-\text{Oe}^2)$ at f_0=EMR. These findings demonstrate much higher frequency modulation efficiencies with SNR=300 and lower noise floors.

References:

[1] Y. Wang, J. Gao, M. Li, D. Hasanyan, Y. Shen, J. Li, *et al.*, "Ultralow equivalent magnetic noise in a magnetoelectric Metglas/Mn-doped Pb(Mg1/3Nb2/3)O3-PbTiO3 heterostructure," *Applied Physics Letters*, vol. 101, p. 022903, 2012.

[2] J. Gao, Z. Wang, Y. Shen, M. Li, Y. Wang, P. Finkel, *et al.*, "Self-powered low noise magnetic sensor," *Materials Letters*, vol. 82, pp. 178-180, 2012.

[3] J. Zhai, Z. Xing, S. Dong, J. Li, and D. Viehland, "Magnetoelectric Laminate Composites: An Overview," *Journal of the American Ceramic Society*, vol. 91, pp. 351-358, 2008.

[4] J. Ma, J. Hu, Z. Li, and C. W. Nan, "Recent progress in multiferroic magnetoelectric composites: from bulk to thin films," *Adv Mater*, vol. 23, pp. 1062-87, Mar 4 2011.

[5] C.-W. Nan, M. I. Bichurin, S. Dong, D. Viehland, and G. Srinivasan, "Multiferroic magnetoelectric composites: Historical perspective, status, and future directions," *Journal of Applied Physics*, vol. 103, p. 031101, 2008.

[6] Y. Shen, J. Gao, Y. Wang, J. Li, and D. Viehland, "Thermal stability of magnetoelectric sensors," *Applied Physics Letters*, vol. 100, p. 173505, 2012.

[7] Y. Shen, J. Gao, D. Hasanyan, Y. Wang, M. Li, J. Li, *et al.*, "Investigation of vehicle induced magnetic anomaly by triple-axis magnetoelectric sensors," *Smart Materials and Structures*, vol. 21, p. 115007, 2012.

[8] S. M. Gillette, A. L. Geiler, D. Gray, D. Viehland, C. Vittoria, and V. G. Harris, "Improved Sensitivity and Noise in Magneto-Electric Magnetic Field Sensors by Use of Modulated AC Magnetostriction," *IEEE Magnetics Letters*, vol. 2, pp. 2500104-, 2011.

[9] J. Petrie, D. Gray, D. Viehland, G. Sreenivasulu, G. Srinivasan, S. Mandal, *et al.*, "Shifting the operating frequency of magnetoelectric sensors," *Journal of Applied Physics*, vol. 111, p. 07C714, 2012.

[10] X. Zhuang, M. L. C. Sing, C. Cordier, S. Saez, C. Dolabdjian, L. Shen, *et al.*, "Evaluation of Applied Axial Field Modulation Technique on ME Sensor Input Equivalent Magnetic Noise Rejection," *IEEE Sensors*, vol. 11, pp. 2266-2272, 2011.

[11] J. Gao, Y. Shen, P. Finkel, J. Blottman, J. Li, and D. Viehland, "Geomagnetic field tuned frequency multiplication in Metglas/Pb(Zr, Ti)O3 heterostructure," *Materials Letters*, vol. 88, pp. 47-50, 2012.

[12] J. Ma, Z. Li, Y. Lin, and C. W. Nan, "A novel frequency multiplier based on magnetoelectric laminate," *Journal of Magnetism and Magnetic Materials*, vol. 323, pp. 101-103, 2011.

[13] W. Zhang, G. Yin, J. Cao, J. Bai, and F. Wei, "Frequency multiplying behavior in a magnetoelectric unimorph," *Applied Physics Letters*, vol. 100, p. 032903, 2012.

[14] L. Shen, M. Li, J. Gao, Y. Shen, J. F. Li, D. Viehland, *et al.*, "Magnetoelectric nonlinearity in magnetoelectric laminate sensors," *Journal of Applied Physics*, vol. 110, p. 114510, 2011.

[15] T.-Z. Wang and Y.-H. Zhou, "A theoretical study of nonlinear magnetoelectric effect in magnetostrictive–piezoelectric trilayer," *Composite Structures*, vol. 93, pp. 1485-1492, 2011.

[16] S. Dong, J. Zhai, J. Li, and D. Viehland, "Near-ideal magnetoelectricity in high-permeability magnetostrictive/piezofiber laminates with a (2-1) connectivity," *Applied Physics Letters*, vol. 89, p. 252904, 2006.

[17] M. Li, D. Berry, J. Das, D. Gray, J. Li, D. Viehland, *et al.*, "Enhanced Sensitivity and Reduced Noise Floor in Magnetoelectric Laminate Sensors by an Improved Lamination Process," *Journal of the American Ceramic Society*, vol. 94, pp. 3738–3741, 2011.

[18] S. Dong, J. Zhai, F. Bai, J.-F. Li, and D. Viehland, "Push-pull mode magnetostrictive/piezoelectric laminate composite with an enhanced magnetoelectric voltage coefficient," *Applied Physics Letters*, vol. 87, p. 062502, 2005.

[19] Y. Shen, J. Gao, Y. Wang, P. Finkel, J. Li, and D. Viehland, "Piezomagnetic strain-dependent non-linear magnetoelectric response enhancement by flux concentration effect " *Applied Physics Letters*, vol. 102, p. 172904, 2013.

[20] J. Das, J. Gao, Z. Xing, J. F. Li, and D. Viehland, "Enhancement in the field sensitivity of magnetoelectric laminate heterostructures," *Applied Physics Letters*, vol. 95, p. 092501, 2009.

[21] Y. Wang, D. Gray, D. Berry, J. Gao, M. Li, J. Li, *et al.*, "An Extremely Low Equivalent Magnetic Noise Magnetoelectric Sensor," *Advanced Materials*, vol. 23, pp. 4111-4114, 2011.

[22] F. Fang, C. Zhao, and W. Yang, "Thickness effects on magnetoelectric coupling for Metglas/PZT/Metglas laminates," *Science China Physics, Mechanics and Astronomy*, vol. 54, pp. 581-585, 2011.
[23] X. J. Zheng and X. E. Liu, "A nonlinear constitutive model for Terfenol-D rods," *Journal of Applied Physics*, vol. 97, p. 053901, 2005.
[24] D. A. Burdin, D. V. Chashin, N. A. Ekonomov, Y. K. Fetisov, L. Y. Fetisov, G. Sreenivasulu, *et al.*, "Resonance mixing of alternating current magnetic fields in a multiferroic composite," *Journal of Applied Physics*, vol. 113, p. 033902, 2013.